

Design of High-density Transformers for High-frequency High-power Converters

by

Wei Shen

Dissertation submitted to the faculty of the Virginia Polytechnic Institute and State University in partial fulfillment of the requirements for the degree of

Doctor of Philosophy

In

Electrical Engineering

Dr. Dushan Boroyevich	Committee Co-Chair
Dr. Fred Wang	Committee Co-Chair
Dr. Jacobus Daniel van Wyk	Committee Member
Dr. Guo-Quan Lu	Committee Member
Dr. Yilu Liu	Committee Member

July, 2006

Blacksburg, Virginia

Keywords: High-frequency Transformer, High power density, Core loss calculation, Leakage inductance calculation, Transformer optimal design

Design of High-density Transformers for High-frequency High-power Converters

Wei Shen

ABSTRACT

Moore's Law has been used to describe and predict the blossom of IC industries, so increasing the data density is clearly the ultimate goal of all technological development. If the power density of power electronics converters can be analogized to the data density of IC's, then power density is a critical indicator and inherent driving force to the development of power electronics. Increasing the power density while reducing or keeping the cost would allow power electronics to be used in more applications.

One of the design challenges of the high-density power converter design is to have high-density magnetic components which are usually the most bulky parts in a converter. Increasing the switching frequency to shrink the passive component size is the biggest contribution towards increasing power density. However, two factors, losses and parasitics, loom and compromise the effect. Losses of high-frequency magnetic components are complicated due to the eddy current effect in magnetic cores and copper windings. Parasitics of magnetic components, including leakage inductances and winding capacitances, can significantly change converter behavior. Therefore, modeling loss and parasitic mechanism and control them for certain design are major challenges and need to be explored extensively.

In this dissertation, the abovementioned issues of high-frequency transformers are explored, particularly in regards to high-power converter applications. Loss calculations accommodating resonant operating waveform and Litz wire windings are explored. Leakage inductance modeling for large-number-of-stand Litz wire windings is proposed. The optimal design procedure based on the models is developed.

Acknowledgements

I owe an enormous debt of gratitude to my advisor, Dr. Dushan Boroyevich, for his support and guidance during my study. His profound knowledge, masterly creative thinking, and sense of humor have been my source of inspiration through out this work.

To Dr. Fred Wang, my co-advisor, I want to express my sincere appreciation to him for his instruction, time, and patience. His gentle personality and rigorous attitude toward research will benefit my career as well as my personal life. Most importantly, I have learned motivation and confidence from them. I am very lucky to have both professors as mentors during my time in CPES.

I would like to express my appreciation to my committee member, Dr. van Wyk, who is such an elegant and admirable professor. I enjoyed each of our meetings and always learned more from him. I would also like to thank my other committee members Dr. Yilu Liu and Dr. Guo-Quan Lu for always helping and encouraging me.

I would also like to thank all my colleagues in CPES for their help, mentorship, and friendship. I cherish the wonderful time that we worked together. Although this is not a complete list, I must mention some of those who made valuable input to my work. They are Dr. Bing Lu, Dr. Qian Liu, Dr. Gang Chen, Dr. Lingyin Zhao, Dr. Rengang Chen, Dr. Wei Dong, Dr. Shuo Wang, Dr. Ming Xu, Jerry Francis, Tim Thacker, Arnedo Luis, Dianbo Fu, Chuanyun Wang, Jinggen Qian, Liyu Yang, Manjin Xie, Yu Meng, Chucheng Xiao, Dr. Wenduo Liu, Michele Lim, Jing Xu, Yang Liang, Yan Jiang, Sebastian Rosado, Xiangfei Ma, Dr. Jinghong Guo, Dr. Zhenxian Liang, Dr. Yingfeng Pang, Dr. Luisa Coppola, and so many others. The last but not the least, I want to thank group members of the ARL project: Hongfang Wang, Honggang Sheng, Dr. Xigen Zhou, Dr. Xu Yang, Yonghan Kang, Brayn Charboneau, Dr. Yunqing Pei, and Dr. Ning Zhu.

I would like to thank the administrative staff members, Marianne Hawthorne, Robert Martin, Teresa Shaw, Trish Rose, Elizabeth Tranter, Michelle Czamanske, Dan Huff, who always smiled at me and helped me to get things done smoothly.

This work made use of ERC Shared Facilities supported by the National Science Foundation under Award Number EEC-9731677.

I dedicate this achievement to my wife Shen Wang

It would not have been possible without your support, encouragement and love. Thank you for being with me for the whole five years of study.

Also to my parents

Mr. Hancal Shen and Ms. Xiangdai Yang

Table of Contents

ABSTRACT	ii
Acknowledgements	iii
Chapter 1 Introduction	1
1.1. Background	1
1.2. Literature Review	3
1.2.1. Low power & Ultra-high frequency applications	4
1.2.2. High power & mid-frequency applications	5
1.2.3. Mid-power & High-frequency applications	6
1.2.4. Summaries	7
1.3. Research Scope and Challenges	8
1.3.1. Research scope	8
1.3.2. Research challenges	9
1.4. Dissertation Organization	10
Chapter 2 Nanocrystalline Material Characterization	12
2.1. Conventional high-frequency magnetic materials	13
2.1.1. Magnetic material introduction	13
2.1.2. Characteristics of conventional ferri- and ferro-materials	15
2.1.3. Ferrites	15
2.1.4. Amorphous metals	18
2.1.5. Superalloy	20
2.2. Characteristics of nanocrystalline materials	21
2.2.1. B/H curve	23
2.2.2. Loss performance	26
2.2.3. Temperature dependence performance	28
2.2.4. Cut core issues	29
2.3. Summaries	34
Chapter 3 Loss Calculation and Verification	37
3.1. Core loss calculation	38
3.1.1. Calculation method survey	38

3.1.2.	Proposed loss calculation method	41
3.2.	Core loss measurement and verification	52
3.2.1.	Error analysis	53
3.2.2.	Loss verification for STS waveforms	58
3.2.3.	Summaries on core loss calculation	66
3.3.	Winding loss calculation	66
3.3.1.	AC resistance of Litz wire windings.....	67
3.3.2.	Litz wire optimal design	71
3.4.	Summaries	73
Chapter 4	Parasitic Calculation	74
4.1.	Leakage inductance calculation.....	74
4.1.1.	Leakage inductance calculation method survey	75
4.1.2.	Proposed leakage inductance calculation method.....	78
4.1.3.	Verifications.....	86
4.2.	Winding capacitance calculation.....	87
4.2.1.	Simplified energy base calculation method	88
4.2.2.	Transformer winding capacitance calculation	90
4.3.	Summaries	92
Chapter 5	The PRC System Case Study.....	93
5.1.	Transformer specifications of the PRC operation	94
5.1.1.	PRC operation analysis.....	96
5.1.2.	Transformer parameter determination	99
5.2.	Transformer minimum-size design procedure.....	102
5.2.1.	Consideration of variable frequency effect.....	102
5.2.2.	Minimum-size Design procedure.....	105
5.3.	Prototyping and Testing Results.....	108
5.4.	Summaries	114
Chapter 6	Transformer Scaling Discussions	115
6.1.	General scaling relationship	116
6.1.1.	Size scaling	119
6.1.2.	Frequency scaling	123

6.1.3. Discussions	125
6.2. Power rating scaling for variable core dimensions.....	126
6.2.1. C-core characterization	126
6.2.2. PRC scaling designs.....	127
6.3. Summaries	133
Chapter 7 Conclusions and Future Work	135
7.1. Conclusions	135
7.2. Future Work	136
7.2.1. Improve the Litz wire winding leakage inductance modeling.....	136
7.2.2. Extend the modeling and design work to EMI filter.....	137
References.....	138
Appendix I Arbitrary Waveform Generation.....	151
Appendix II Minimum-size Transformer Design Program	155
Appendix III C-core Shape Characteristic	161

Table of Figures

Fig. 1-1 Status of the $P \cdot f$ (W*Hz) of power electronics converters based on different semiconductor materials and devices.....	2
Fig. 1-2 A typical charger converter system.....	8
Fig. 1-3 Transformer characteristics and technologies.....	9
Fig. 2-1 Ferrite 3F3 core loss density at 25 °C [2-8].....	16
Fig. 2-2 Ferrite 3F3 complex permeability as a function of frequency [2-8].....	16
Fig. 2-3 Ferrite 3F3 B/H curve (top), initial permeability (middle) and loss density (bottom) as the function of temperature [2-8].....	18
Fig. 2-4 Typical Fe- and Co-based amorphous materials core loss density at 25 °C [2-11].....	19
Fig. 2-5 Amorphous 2605-3A and 2714A impedance permeability as a function of frequency [2-11].....	20
Fig. 2-6 Loss density of Supermalloy [2-13].....	21
Fig. 2-7 Typical initial permeability and saturation flux density for soft magnetic materials [2-16].....	22
Fig. 2-8 The relation between coercivity and grain size of different ferromagnetic materials.....	22
Fig. 2-9 B/H curve measurement setup.....	23
Fig. 2-10 B/H loop measured for FT-3M under 60 Hz.....	25
Fig. 2-11 Incremental permeability of the Finemet material.....	25
Fig. 2-12 B/H loops of the Finemet material under different frequencies.....	26
Fig. 2-13 Core loss density in mW/cm^3 of the Finemet material.....	27
Fig. 2-14 Complex permeability as the function of frequency for the Finemet material @ 0.1 T.....	28
Fig. 2-15 60 Hz B/H major and minor loops of the Finemet material under different temperature.....	29
Fig. 2-16 Flux density @ $H=3A/m$ variation percentage (left) and initial permeability variation percentage (right) as the function of the core temperature.....	29
Fig. 2-17 Core loss density as the function of the core temperature.....	29
Fig. 2-18 Finemet material C-core B/H loops (50 kHz) as the function of the length of air gap.....	31
Fig. 2-19 Core loss density of Finemet material and cut core using same material.....	32
Fig. 2-20 Core loss density as the function of the air gap length under frequency 20kHz (top), 50kHz (middle), and 100kHz (bottom).....	33
Fig. 2-21 Development road map for different soft magnetic materials.....	34
Fig. 2-22 Core loss density comparison of typical magnetic materials.....	35
Fig. 3-1 Voltage and flux of square and sinusoidal waveform.....	42
Fig. 3-2 Normalized flux density of triangle and sinusoidal waveforms.....	43
Fig. 3-3 Voltage and flux of the transform under a simplified STS waveform.....	45
Fig. 3-4 STS waveform with different shape and same peak flux level.....	47
Fig. 3-5 Loss calculated by different methods for the STS waveforms.....	48
Fig. 3-6 Calculated equivalent frequency by MSE for the STS waveforms.....	48

Fig. 3-7 The PRC system for studying.....	49
Fig. 3-8 The transformer waveform of PRC with capacitor filter	50
Fig. 3-9 Variable duty cycle quasi-square voltage and corresponding flux waveforms	52
Fig. 3-10 The electrical core loss measurement setup	53
Fig. 3-11 The measured voltage and current under different frequencies	56
Fig. 3-12 The core loss measurement winding resistance	57
Fig. 3-13 The equivalent circuit of the core loss measurement setup.....	57
Fig. 3-14 Simulated current (top) and voltage (bottom) waveforms w/wo parasitics	58
Fig. 3-15 Generated STS waveforms (100 kHz)	60
Fig. 3-16 Core loss density of FT-3M nanocrystalline under STS waveforms (100 kHz).....	61
Fig. 3-17 Measured and calculated Core loss density of under STS waveforms (100 kHz and 0.4 T)	62
Fig. 3-18 Measured voltage and current for triangle excitation (100 kHz) (left) and the corresponding B/H curve (right).....	63
Fig. 3-19 Measured core loss density for triangle, square, and sine waveforms (100 kHz).....	63
Fig. 3-20 Transformer waveform for the PRC circuit with resonant frequency 205 kHz and variable switching frequency 100 kHz (left) and 200 kHz (right)	64
Fig. 3-21 Core loss density of 100 kHz sine, square, and PRC waveforms	64
Fig. 3-22 Voltage and current waveforms of 100 kHz sine, square, and PRC waveform	65
Fig. 3-23 B/H loops of 100 kHz sine, square, and PRC waveforms.....	66
Fig. 3-24 Normalized resistance of Litz wire windings for 1 layer (upper) and 4 layers (lower)	69
Fig. 3-25 AC/DC resistance ratio of Litz wire windings for 1 layer (upper) and 4 layers (lower)	71
Fig. 4-1 Full bridge PWM converter (left) and V_{ds1} under different leakage values (right)	75
Fig. 4-2 Leakage field distribution of a pot core transformer	76
Fig. 4-3 Typical two-winding transformer structure and corresponding coordination notation	79
Fig. 4-4 Illustration and cross-section of a current-carrying semi-infinite plate	80
Fig. 4-5 Skin effect on magnetic field distribution (left) and current density distribution (right).....	82
Fig. 4-6 Illustration and cross-section of a current-carrying semi-infinite plate in a parallel field	82
Fig. 4-7 Proximity effect on magnetic field distribution (left) and current density distribution (right).....	83
Fig. 4-8 Eddy current effect on magnetic field distribution (right) of a two winding transformer (left).....	84
Fig. 4-9 Litz wire approximation	86
Fig. 4-10 Leakage inductance by the proposed method (blue solid), the simplified method (pink solid), and measurement (black dots).....	87

Fig. 4-11 Illustration of two adjacent winding layers	89
Fig. 4-12 Winding structures – wave wiring (left) and leap wiring (right)	90
Fig. 4-13 Transformer terminal voltages (a) high-frequency equivalent circuit (b).	91
Fig. 5-1 The three-level PRC converter for pulse power applications	95
Fig. 5-2 Capacitive filter half bridge PRC converter and resonant voltage and current	97
Fig. 5-3 Capacitive filter half bridge PRC converter normalized output characteristic	98
Fig. 5-4 Capacitive filter half bridge PRC converter normalized gain curve	99
Fig. 5-5 Hybrid charging schemes	100
Fig. 5-6 Capacitive filter half bridge PRC converter normalized gain curve	101
Fig. 5-7 30 kW hybrid charging trajectory	102
Fig. 5-8 Operating frequency (left) and $V \cdot S$ (right) of the application	103
Fig. 5-9 Calculated core loss profile within one charging	104
Fig. 5-10 Minimum size transformer design procedure	105
Fig. 5-11 Core loss (left) and winding loss (right) as function of flux density	106
Fig. 5-12 Optimal flux density for minimum total loss	107
Fig. 5-13 Total losses of the 30 kW transformer using different C-cores	107
Fig. 5-14 Transformer prototype structure	109
Fig. 5-15 30 kW ferrite core (left) and FT-3M nanocrystalline core (right) transformer prototypes	110
Fig. 5-16 30 kW PRC system with the nanocrystalline transformer	110
Fig. 5-17 Measured transformer primary voltage and current waveforms of the PRC during charging (current channels with 1 A/V conversion ratio)	111
Fig. 5-18 The thermal network of the nanocrystalline transformer	112
Fig. 5-19 Calculated (top) and measured (bottom) temperature rises of the transformer prototype for one charging operation	113
Fig. 5-20 Winding (top) and core (bottom) temperature rises of the transformer prototype for continuous charging operation	113
Fig. 6-1 Normalized transformer power density as function of SF ($y=1$, $m=1$, $f=10\text{kHz}$, Finemet FT-3M with $\alpha = 1.62$ and $\beta = 1.98$)	119
Fig. 6-2 Normalized transformer power density as function of SF ($y=0.5$, $m=1$, $f=10\text{kHz}$, Finemet FT-3M with $\alpha = 1.62$ and $\beta = 1.98$)	120
Fig. 6-3 Normalized transformer power density as function of SF ($y=1$, $m=1$, $f=10\text{kHz}$, Ferrite P with $\alpha = 1.36$ and $\beta = 2.86$)	121
Fig. 6-4 Normalized transformer power density as function of SF ($y=0.5$, $m=1$, $f=10\text{kHz}$, Ferrite P with $\alpha = 1.36$ and $\beta = 2.86$)	121
Fig. 6-5 Normalized transformer power density as function of SF ($m=1$, $f=100\text{kHz}$, Ferrite P with $\alpha = 1.36$ and $\beta = 2.86$)	122
Fig. 6-6 Normalized transformer power density as function of f ($y=1$, $m=1$, $SF=1$, Finemet FT-3M with $\alpha = 1.62$ and $\beta = 1.98$)	123
Fig. 6-7 Normalized transformer power density as function of f ($y=0.5$, $m=1$, $SF=1$, Finemet FT-3M with $\alpha = 1.62$ and $\beta = 1.98$)	124
Fig. 6-8 Normalized transformer power density as function of f ($y=1$, $m=1$, $SF=1$, Ferrite P with $\alpha = 1.36$ and $\beta = 2.86$)	124

Fig. 6-9 Normalized transformer power density as function of f ($y=0.5$, $m=1$, $SF=1$, Ferrite P with $\alpha = 1.36$ and $\beta = 2.86$).....	125
Fig. 6-10 The C-core dimensions for scale design	126
Fig. 6-11 C-core window (left) and core (right) exposed area to volume ratios.....	127
Fig. 6-12 Calculated power densities of PRC transformers under different frequencies and power ratings, using ferrite P (a), Finemet FT-3M (b), Supermalloy (c), and Amorphous 2705M (d) as transformer cores	130
Fig. 6-13 Calculated power densities of PRC transformers under different frequencies and power ratings, using Finemet FT-3M as transformer cores..	132
Fig. 6-14 Calculated power densities of PRC transformers for 200 kHz, using Finemet FT-3M and Ferrite P as transformer cores.....	133
Fig. 7-1 Cylindrical coordinate consideration of the leakage field.....	137

List of Tables

Table 1-1 Transformer design status.....	7
Table 2-1 Ferrites typical properties at 25°C	16
Table 2-2 Amorphous material typical properties at 25°C [2-11]	19
Table 2-3 Superalloy material typical properties at 25°C [2-13].....	21
Table 2-4 Magnetic material characteristic comparison.....	36
Table 5-1 System Specifications.....	94
Table 5-2 PRC operation mode analysis.....	97
Table 5-3 Transformer design specs and parameters.....	109
Table 6-1 PRC specifications for different ratings and frequencies	128
Table 6-2 Magnetic material characteristics	128
Table 6-3 Transformer scaling-design results for different materials	129
Table 6-4 Transformer scaling-design results for the integrated scheme	131

Chapter 1 Introduction

Transformer design is not a new topic, and the corresponding studies have been conducted along the development of the power systems and power conversion technologies. This work focuses on the high density transformer design for high-frequency and high-power applications. In this chapter, a background description and review will help to define this work and its novelty. Furthermore, we will identify challenges related to the transformer design of the interested frequency and power ranges.

1.1. Background

The apparatus Michael Faraday constructed in 1831 contained all the basic elements of transformers: two independent coils and a closed iron core. Since then, transformers have come into our ordinary lives as an essential part of AC lighting systems [1-1]. Power transformers, including transmission and distribution ones, usually have efficiency close to 100%. The development of cheaper and more reliable transformers is the goal of the power system industry.

Power electronics converters mainly employ transformers, for the purposes of galvanic isolation and voltage level changing, which are quite similar to the power system requirements. However, transformers for switching mode converters have distinct characteristics, like high operating frequencies, non-sinusoidal waveforms, and predominantly compact sizes. In practice, the transformer is a complex component, often at the heart of circuit performance. The design and performance of the transformer itself requires a deeper understanding of electromagnetism [1-2].

Together with other passive components, transformers dominate the size of the power circuit [1-3]. For the past two decades, high power density has been the main theme to the power electronics development in distributed power systems, vehicular electric systems, and consumer apparatus [1-4]. Increasing frequency that is driven by the desire to shrink passive size, in turn imposes the investigation on the design of high frequency passives, especially transformers and inductors. With the elevated frequencies of operation come new challenges and development that is required of the magnetic

components. These are primarily concerned with the increase in losses as well as the desire to minimize volume and footprint. Parasitic elements of magnetic components would affect the converter operation more and more as the frequency gets higher and higher.

Although transformer design seems a mature technology that has not changed radically compared to semiconductor devices, the development of the high frequency transformer is far from well understood by average practice. Sophisticated electromagnetic analysis, highly non-linear magnetic material characteristics, and difficulties on experimental verifications acutely mystify the design of the high frequency transformer. We have seen switching frequencies gradually rise from the tens of kilohertz range to the mega hertz range. The power frequency product of semiconductor devices has been a good indicator to evaluate progress and status of power electronics converter systems in the past. At present the silicon-based device technology appears to have stabilized around 10^9 watts-hertz, as in Fig. 1-1 [1-5]. The converter power frequency products frontline would be pushed even forward, with the availability of SiC-based devices. Transformer design would face the application with higher frequency and/or higher power rating than is today's practice.

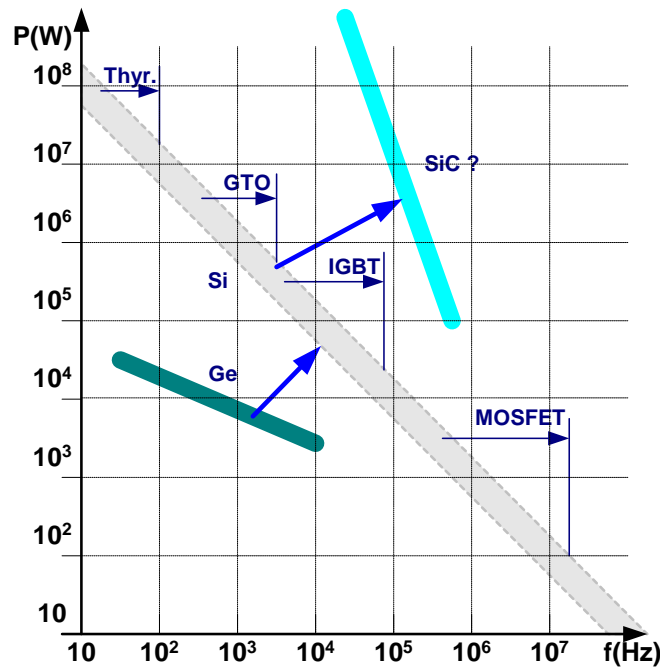


Fig. 1-1 Status of the $P \cdot f$ (W*Hz) of power electronics converters based on different semiconductor materials and devices

Similar to the advancement of the semiconductor devices, the improvement of the magnetic material and even the invention of new material have been pursued unceasingly. Low loss, high saturation induction, and high operation temperature are desired characteristics of the magnetic material for high frequency high power transformers. The developed better materials will influence the transformer design correspondingly. Technologies based on existing materials should be revisited and modified to be applied to the forthcoming materials.

In industry practice, the system operating frequency is determined by active switches or arbitrarily, and the transformer design will be an afterthought. Due to the inherent non-linearity of the magnetic circuit, any simple proportional scaling prediction could be way off the realistic situation. As the driving force, the size reduction of the transformer needs to be characterized and formulated, so that it can be integrated into the converter system design. Only after realizing that, the optimal system design could be obtained and the material and technology barriers could be identified of any particular converter system.

It is so important that we have a clear understanding of the high density transformer design for high frequency high power converter systems. Therefore, the literature review in the next session will show the state-of-the-art status of high frequency transformer design, and will help to determine the challenges and research topics of this work.

1.2. Literature Review

Transformers for power electronics converters are so varied that it is hard to make comparison without categorizing them according to applications. Power converters nowadays can be anywhere from couple watts mega watts, with switching frequency up to several mega hertz. These features are mainly determined by the kind of semiconductor devices employed by the converter. Therefore, the literature survey of transformer is conducted in three categories: 1) the low power (<1 kW) & Ultra-high frequency (>1 MHz) range that is for purely MOSFET based converters; 2) the high power (>10 kW) & mid frequency (<100 kHz) range that is dominated by IGBT and Thyristor type devices; 3) the mid power (1~10 kW) and high frequency (100~1 MHz)

range that is the field filled with IGBT and MOSFET both. These three categories together show the front line of existing silicon-based device technology, and the transformers employed by these converters include the state-of-the-art designs.

The emerging semiconductor technology, like SiC devices, will bring the power electronics converter into new field of applications. The high power (10~100 kW) and high frequency (100 kHz~1 MHz) converters actually have already been seen in vehicular and aircraft applications. Transformers falling in this range are the interested topic of research.

1.2.1. Low power & Ultra-high frequency applications

In telecom and computer products, switching mode power supplies have been designed to run above megahertz to increase power density and reduce foot print. For switching frequency beyond megahertz, switching losses contribute the majority part of the active losses. MOSFET devices are optimized to switch up to megahertz range while keeping loss generation low. As the switching frequency has increased to the megahertz range, magnetic design issues have been extensively explored [1-6]-[1-8] for low-power applications under 1 kW. It can be imagined that core and winding loss calculations are critical to this frequency range. Parasitic modeling receives the same attention, because the transformer behavior and performance are highly affected by the leakage inductance and stray capacitance.

Goldberg [1-6] had used Ni-Zn ferrite materials pot core and planar spiral windings for a 50 W transformer running between 1 and 10 MHz. He went through loss and leakage inductance calculations with considering skin effects. A design program was developed to search for the minimum footprint of the transformer. His pioneering work demonstrated the possibility, but it has more academic influence and only applies to very low power applications. In 1992, K. Ngo [1-7] developed a 2 MHz 100 W transformer with similar pot ferrite core and planar PCB windings.

P. D. Evans [1-8] claimed that the conventional E and planar core shapes are not satisfactory at MHz frequency range, so a toroidal core transformer was proposed with copper wires soldered on a substrate as windings. Their key idea was to fully realize the interleaved winding structure to cancel the proximity effect. However, no core loss and parasitic calculation methods are reported in this work.

In 2002, J. T. Strydom [1-9] reported an edge-cutting work on transformer development – 1 MHz 1 kW integrated passive module. Fundamentally, there is no difference on the planar structure and loss calculation considerations between this work and the Goldberg's. The inductance and capacitance calculations are critical, since they are designed to participate in the resonant converter operation. Other work also recently demonstrated 1 MHz 1 kW resonant converters for telecom power module, with both integrated planar [1-27] and discrete E core [1-28] transformers. Low loss ferrite is the choice for the core material.

It can be concluded that planar structures are prevailing for magnetic components falling in this range because of their low profile, easy manufacturability, and good heat removal. Ferrites are the exclusive core material, since they have lowest loss density. The disadvantage of low saturation induction does not bother the designer, since the designed flux level is usually much lower than the saturation level. Correspondingly, high-frequency loss calculations considering eddy current effects are applied to both magnetic cores and spiral windings. Parasitic effects are modeled into lumped equivalent circuit components. However, the planar structure and its corresponding sets of analysis can hardly be applied to a magnetic component with a higher power rating. To have the PCB winding present acceptable loss, we have to choose larger copper area for higher power applications, which will result in larger footprints. Although the interleaving winding scheme could reduce the AC resistance to certain degree, it is still quite impractical to have planar spiral windings for high current at high frequency.

1.2.2. High power & mid-frequency applications

Vehicular and aircraft power systems employ more and more power electronics converters which have typical power rating of tens kilowatts. MOSFET switches do not have advantages in this range. Since IGBT's dominate applications that are above the ten kilowatts range, the corresponding magnetics employed operates below 100 kHz. Frequencies between 20 and 50 kHz are typical to these applications, and power ratings higher than 10 kW can be categorized into this range.

Kheraluwala [1-10] proposed a novel coaxial wound transformer for 50 kHz and 50 kW dual active bridge DC/DC converter systems. Stemmed from the idea of reducing leakage and increasing coupling between primary and secondary windings, the coaxial

transformer employs a bunch of toroidal cores and has coaxial type wires wound across them. The coaxial wire is composed of outer copper tube and inner Litz wires for different windings, respectively. The leakage inductance calculation is explored for this particular structure.

J. C. Forthergill [1-11] developed a high voltage (50 kV) transformer for an electrostatic precipitator power supply, and insulation and electrostatic analysis are the major contribution of this work. No special considerations of loss and parasitic calculation have been discussed for this 25 kHz and 25 kV (pulsed-power) transformer.

Heinemann [1-12] described a 350 kW transformer for a 10 kHz dual active bridge DC/DC converter system. Nanocrystalline material wound core and coaxial cables are adopted to construct the transformer. Frequency dependent winding resistance and leakage inductance have been calculated. An active cooling scheme was implemented inside the winding. 330 kW and 20 kHz nanocrystalline cut-core transformers have developed for accelerator klystron radio frequency amplifier power systems recently [1-13], which are the biggest nanocrystalline core reported so far.

Instead of planar structures, high power transformers usually have cable or Litz wire windings, and ferromagnetic materials are used to achieve higher density. The accurate and convenient loss and parasitic calculation methods are lack for all the abovementioned transformers. Another interesting point is that nanocrystalline magnetic material has been applied to achieve higher density.

1.2.3. Mid-power & High-frequency applications

For applications of several kilo-watts and several hundreds kilo-hertz, IGBT and MOSEFT are both candidates to the converter power stage [1-14]. With the advancement of semiconductor devices and the application of soft-switching techniques, several-kilowatt converters running at more than 100 kHz have been realized. Transformers are a critical part of the circuit.

From Coonrod [1-15] to Petkov [1-16], high-frequency transformer design procedure has been studied. Core loss and winding loss are modeled and optimally allocated during the design. Simple thermal models have been employed to complete the design loop. Ferrite cores are the primary choice, and Litz wire or foil windings are popular, for this power and frequency range. Transformer prototypes falling in this range

can be found in high-frequency resonant DC/DC converter applications already [1-17]-[1-18].

1.2.4. Summaries

Table 1-1 Transformer design status

	Ultra-high-frequency Range (1 MHz - 10 MHz)	High-frequency Range (100 kHz - 1 MHz)	Mid-frequency Range (10 kHz - 100 kHz)
Low power range (< 1 kW)	<p>Goldberg (1989): Ni-Zn ferrite gapped pot core, Planar spiral windings, 5-10 MHz, 50 W, Resonant forward converter</p> <p>Ngo (1992): Pot core, Planar spiral windings, 2-5 MHz, 100 W</p> <p>Evans (1995): Toroidal core, copper wires soldered on substrate metallisation as windings, 2 MHz, 150 W</p> <p>J. T. Strydom (2002): Integrated planar core, spiral windings L-C-T transformer, 1 MHz, 1 kW, Asymmetrical half-bridge resonant converter</p>		
Mid power range (1~10 kW)		<p>Coonrod (1986), Ferrite toroidal core, magnet wire windings, 100~300 kHz, Half-bridge converters</p> <p>Petkov (1996), Freeite PM core, magnet wire windings, 100 kHz, 2.6 kW, Microwave heating supply</p> <p>Canales (2003), Ferrite E core, Litz wire windings, 745 kHz, 2.75 kW, Three-level resonant converters</p> <p>Biela (2004), Integrated transformer, ferrite E core, foil windings, 300~600, kHz, 3 kW, Resonant converters</p>	
High power range (> 10 kW)	<p>???</p>	<p>✓</p>	<p>Kheraluwala (1992), Ferrite toroidal core, coaxial windings (primary tube and secondary Litz), 50 kHz, 50 kW, Dual active bridge converter</p> <p>J. C. Fothergill (2001), Ferrite C-core, solid magnet wire windings, 25 kHz, 25 kW, 50 kV, Full IGBT bridge converter</p> <p>L. Heinemann (2002), Nanocrystalline wound core, coaxial cable windings (inner aluminum tube and outer braided copper), 10 kHz, 350 kW, 15 kV, Dual active full bridge</p> <p>Reass (2003), Nanocrystalline cut-core, 20 kHz, 380 kW, poly-phase resonant converter</p>

We have already reviewed the front line of the transformer design status, from both the frequency and power rating points-of-view. This is tabulated in Table 1-1. As the advancement of semiconductor devices, the converter operation will go into the blank area of even higher frequency and/or higher power rating. Therefore, the corresponding transformer design has to cater to the need. Since not all of the technologies established

in the past could be directly transferred to the new applications, we need to explore the possible issues related to the new applications.

1.3. Research Scope and Challenges

1.3.1. Research scope

As high-temperature switching devices such as SiC switches and diodes exemplify, higher-rating and higher switching-frequency converters are expected to become practical [1-19]-[1-20]. The requirement that converters operate in the high-power (> 10 kW) and high-frequency (100 kHz~1 MHz) range has already been perceptible, especially in pulsed-power power supplies [1-21], vehicular power systems [1-22]-[1-23], and distributed and alternative power source applications [1-24]-[1-26].

Therefore, inspired by the development of SiC devices, power converters would run at above hundred of kilohertz with power rating of the tens of kilowatts. The major driving force is the density requirement. Passive sizes will be reduced by elevating operating frequency. Resonant operation and soft switching schemes will be essential to this frequency and power range. The typical topology with transformer is the DC/DC full bridge converters, as shown in Fig. 1-2.

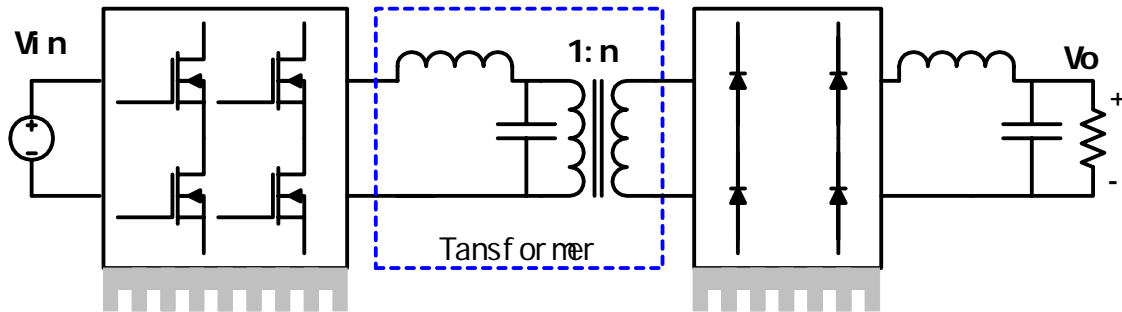


Fig. 1-2 A typical charger converter system

So the design and development of transformers employed by the converter would be challenging. As the research topic, the design issues of high density transformer for applications with the frequency (100~1 MHz) and power rating (10~500 kW) will be investigated. Transformer prototypes for a parallel resonant converter (PRC) charger will be developed and tested.

1.3.2. Research challenges

According to the survey, we can summarize the transformer for high frequency, high power applications would have the features shown in Fig. 1-3, like resonant operation waveforms, Litz wire windings, high operating temperature, and low loss. The corresponding design technologies projected are summarized and listed in Fig. 1-3.

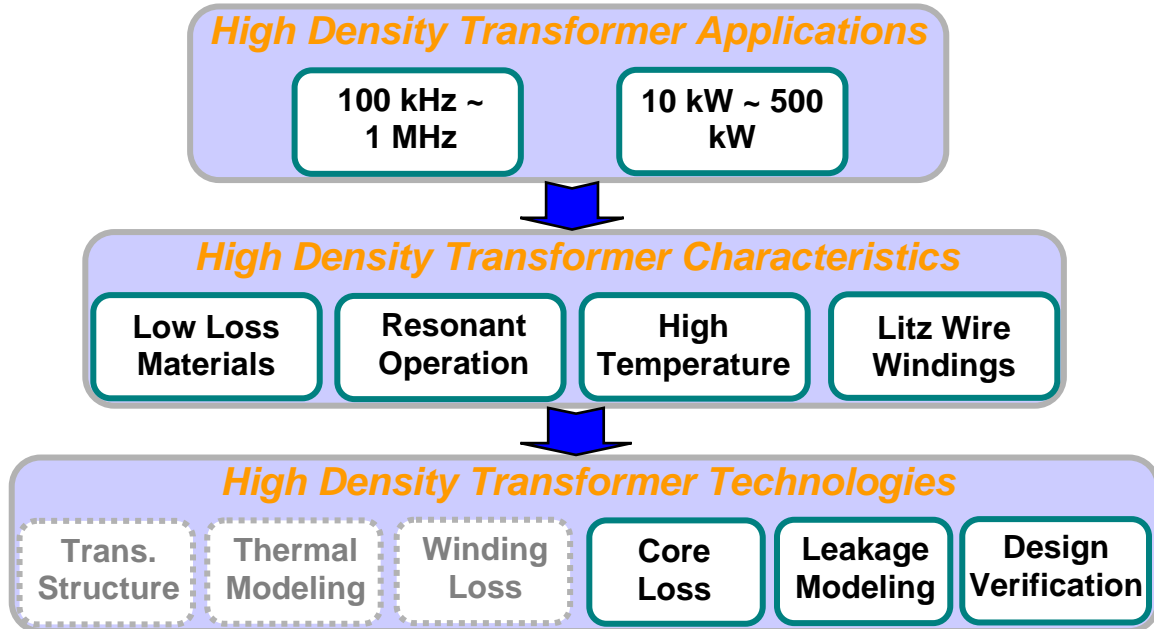


Fig. 1-3 Transformer characteristics and technologies

Among all transformer design issues, the following three aspects have been identified as the unique and challenging to the high density transformer in the range of interests.

a) *Core loss calculation*

The resonant and soft-switching techniques adopted to reduce the switching losses impose some unique requirements onto the magnetic design. One is the fact that the voltage and current waveforms applied to the magnetic components are not a square shape, as they are in PWM converters.

b) *Leakage inductance modeling*

The second important issue is that parasitic parameters of the magnetic components need to be modeled clearly, since they would be one of the key components in determining a circuit's operation conditions. The Litz wire winding has complex

leakage field distribution, and the frequency dependent leakage inductance should be modeled with considering eddy current effects.

c) Nanocrystalline material characterization

Ferrites might not be the only core material candidate, due to their low saturation and operating temperature. High density transformer design opens the possibility of utilization of high saturation flux density ferro-magnetic materials in high frequency applications. Nanocrystalline material, as the best combination of low loss and high saturation, has gained acceptance in mid-frequency range, and needs to be characterized for high-frequency range.

The following section will show the detailed structure of this dissertation.

1.4. Dissertation Organization

This dissertation presents high density transformer design and optimization for high-power high-frequency converter applications. The identified development barriers are studied. First, the nanocrystalline material is characterized for the high frequency and high temperature operations. Second, the core loss calculation method is proposed for the resonant operation waveforms and the nanocrystalline material. Third, 1D leakage inductance modeling of Litz wire windings is developed. After technologies developed, experimental results of a case study and possible scaling considerations are presented. The briefs of each chapter are shown as follows:

In **Chapter 2**, nanocrystalline magnetic materials frequency dependant and temperature dependent performance are characterized through experimental results, and are compared to the corresponding characteristics of popular ferri- and ferro-magnetic materials. Cut-core effects on core loss are calibrated and analyzed, so practical core preparation issues are discussed for applying the nanocrystalline materials as high power transformer cores.

A core loss calculation method has been proposed to tackle the non-PWM voltage waveform applications, which is described in **Chapter 3**. The proposed method can predict core loss under soft-switching and resonant operating waveforms, with better accuracy and easier implementation.

The leakage inductance calculation for Litz wire windings has been proposed in this work. The closed-form solutions for leakage inductance are derived in **Chapter 4**. FEA methods are avoided in this case.

In **Chapter 5**, these techniques are applied to a PRC converter system, and several designs are generated. Prototypes are built and tested in the PRC system, to verify the design procedure.

Further discussions on scaling design of the transformer are shown in **Chapter 6**. These are important to converter system level optimization.

Finally conclusions of this work are drawn in **Chapter 7**. Future work has been identified based on the achievement and insight understandings of the topic.

Chapter 2 Nanocrystalline Material Characterization

The magnetic material selection for high density transformer design is critical. The characteristics of magnetic materials have to be understood, and compromises have to be made according to the particular application. As identified in the literature review, ferromagnetic materials are adopted for high-power, high-frequency transformer cores, due to their higher saturation induction level than ferrites. Particularly, nanocrystalline materials which can be categorized as ferromagnetics present low loss and high saturation level. However, the nanocrystalline materials have mainly been used for EMI chokes and mid-frequency transformers, and their high-frequency and high temperature characteristics are not provided by manufacturers. To use the potentially suitable nanocrystalline material for the high frequency high power transformer cores, we need to characterize the material up to frequency of several hundred kilo-hertz and temperature beyond 100 °C.

In this chapter, the typical high-frequency magnetic materials, including ferrites, amorphous metals, and Permalloy, are reviewed first, and their loss and saturation performance will be compared to the corresponding characteristics of the nanocrystalline material. Through measuring B-H loops of the nanocrystalline material, we can obtain loss density saturation induction, and permeability of the material as the function of the frequency and temperature.

Similar to amorphous materials, the nanocrystalline material is in the form of thin tape which is too brittle to be used for transformer core without going through impregnation and annealing core preparing processes. Cut-core scheme is preferred by the high-power transformer manufacturing, but cutting would introduce more preparing processes. Performance, especially the loss density of the core is different from the original nanocrystalline material. It is hard to analytically model all these core-preparing effect on the core loss density variation. Therefore, we want to go through the characterization procedure of the cut core made of the nanocrystalline material, to find out the core preparation effects.

2.1. Conventional high-frequency magnetic materials

2.1.1. Magnetic material introduction

We always expect that there could be a kind of “perfect” magnetic material with low loss, high saturation density, and high permeability. We can use it as cores of high-frequency transformers, which will have a small size and a high efficiency. In reality, there is no such a “perfect” material existing, so we have to select suitable ones for particular applications. This should be based on the understanding and characterization of different soft magnetic materials. Typical magnetic materials for high frequency transformers are explored in this chapter, and the nanocrystalline material is selected due to its superior loss and saturation characteristics.

Magnetic materials have been so extensively used in a diverse range of applications, that the advancement and optimal utilization of magnetic materials would significantly improve our lives. Magnetic materials are classified in terms of their magnetic properties and their uses. If a material is easily magnetized and demagnetized then it is referred to as a *soft magnetic material*, whereas if it is difficult to demagnetize then it is referred to as a *hard* (or *permanent*) *magnetic material*. Materials in between hard and soft are almost exclusively used as recording media and have no other general term to describe them [2-1].

1600:	Dr. William Gilbert published the first systematic experiments on magnetism in " <i>De Magnete</i> " (" <i>On the Magnet</i> ").
1819:	Oerstead accidentally made the connection between magnetism and electricity discovering that a current carrying wire deflected a compass needle.
1825:	Sturgeon invented the electromagnet.
1880:	Warburg produced the first hysteresis loop for iron.
1895:	The Curie law was proposed.
1905:	Langevin first explained the theory of diamagnetism and paramagnetism.
1906:	Weiss proposed ferromagnetic theory.
1920's:	The physics of magnetism was developed with theories involving electron spins and exchange interactions; the beginnings of quantum mechanics.

The earliest observations of magnetism can be traced back to the Greek philosopher *Thales* in the 6th Century B.C [2-2]. However, it was not until 1600 that the modern understanding of magnetism began [2-3]. In the following table, we can briefly list out scientists and milestone events significantly influencing the evolution history of magnetic material [2-4].

Transformers and inductors, as energy transmission and storage elements in power electronic converters, usually utilize soft magnetic materials as cores. The soft magnetic material cores perform the crucial task of concentrating and shaping magnetic flux. As power electronics designers, we need to be familiar with the properties of different kinds of soft magnetic materials, and should be able to choose suitable materials to fulfill specification for certain applications [2-5].

“Most of pure elements in the periodic table are either *diamagnetical* or *paramagnetical* at room temperature. Since they present very small magnetism under the influence of an applied field, they normally are termed as *non-magnetic* [2-26]”. Another type of magnetism is called *antiferromagnetism*, and the only pure element presenting this characteristic is *Cr* in natural environment. *Fe*, *Co*, and *Ni* are called *ferromagnetics*, because very high levels of magnetism can be observed if we apply a field to these materials. Actually, pure single element ferromagnetic materials are seldom seen as magnets or cores in practical applications, and alloys composed of these elements and other ingredients are more widely used. Therefore, all of these alloys are also categorized as *ferromagnetics*. The last type of magnetic material is classified as *ferrimagnetic*. Although they cannot be observed in any pure element, they can be found in compounds, such as the mixed oxides, known as ferrites [2-6].

In general ferrimagnetics exhibit better loss performance but lower saturation flux density, compared with ferromagnetics. Therefore, material researchers are trying to improve both types of materials, such as, ferrites, amorphous, and silicon steel. Meanwhile, the efforts to discover new materials are ongoing.

Characteristics of typical ferrites and amorphous will be discussed in the next section. As a new magnetic material, nanocrystalline material will be characterized, and the advantages and disadvantages will be summarized. Among all electrical, magnetic,

and mechanical properties, the following characteristics of soft magnetics are of interests and can help us to select a suitable one for certain application:

- * Core loss density (specific core loss) in W/kg (W/cm^3);
- * Saturation flux density in *Tesla*;
- * Relative permeability;
- * Temperature characteristics.

2.1.2. Characteristics of conventional ferri- and ferro-materials

One decade ago, ferrites and amorphous were the only choices for high-frequency applications, due to their relatively low core loss density. We will examine them in detail from a high-frequency operation perspective.

2.1.3. Ferrites

Since the 1950's, ferrite materials have been developed for high-frequency applications because of their high electrical resistivity and low eddy current losses. The breadth of application of ferrites in electronic circuitry continues to grow. The wide range of possible geometries, the continuing improvements in the material characteristics and their relative cost-effectiveness make ferrite components the choice for both conventional and innovative applications [2-7].

Ferrite is a class of ceramic material with a cubic crystalline structure; the chemical formula $MOFe_2O_3$, where Fe_2O_3 is iron oxide and MO refers to a combination of two or more divalent metal (i.e. *Zinc*, *Nickel*, *Manganese* and *Copper*) oxides. The addition of such metal oxides in various amounts allows the creation of many different materials whose properties can be tailored for a variety of uses. Ferrite components are pressed from a powdered precursor and then sintered (fired) in a kiln. The mechanical and electromagnetic properties of the ferrite are heavily affected by the sintering process which is time-temperature-atmosphere dependent.

The typical properties of *MnZn* and *NiZn* ferrites, according to data from *Ferroxcube* (previous *Philips*), are listed in Table 2-1. The saturation flux density ranges from 0.3~0.5 Tesla normally, and permeability varies from thousands to several tens of thousands. Typically, *NiZn* ferrites have lower saturation flux density and better loss

performance, compared to the *MnZn* ones. Therefore, *NiZn* ferrites have been used for ultra-high frequency applications.

Table 2-1 Ferrites typical properties at 25°C

Grade/Category	B_{sat} (T)	μ_i	ρ ($\Omega \cdot m$)	T_c ($^{\circ}C$)	Thermal conductivity (W/(m·K))
3F3 (MnZn)	0.45	2000	2	220	3.5~5
3C94 (MnZn)	0.45	2300	5	220	3.5~5
3F45 (MnZn)	0.5	900	10	300	3.5~5
4B1 (NiZn)	0.35	250	10^5	250	3.5~5
4F1 (NiZn)	0.35	80	10^5	260	3.5~5

As the operating frequency increases, the core loss density of ferrites will increase as shown in Fig. 2-1, and permeability will reduce as shown in Fig. 2-2 . These two effects must be considered for high-frequency transformer designs, since both of them could cause the designed transformer failure.

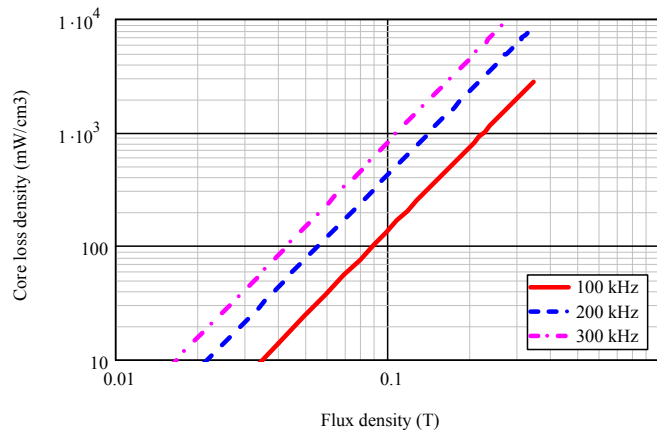


Fig. 2-1 Ferrite 3F3 core loss density at 25 °C [2-8]

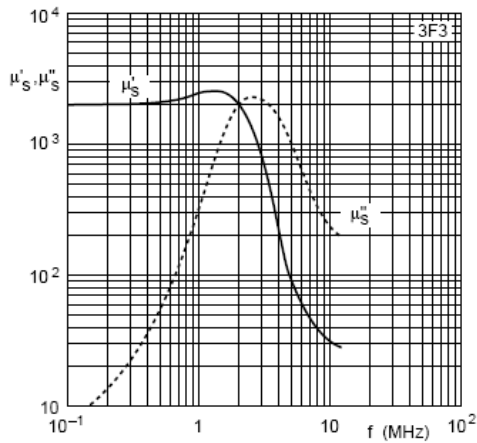
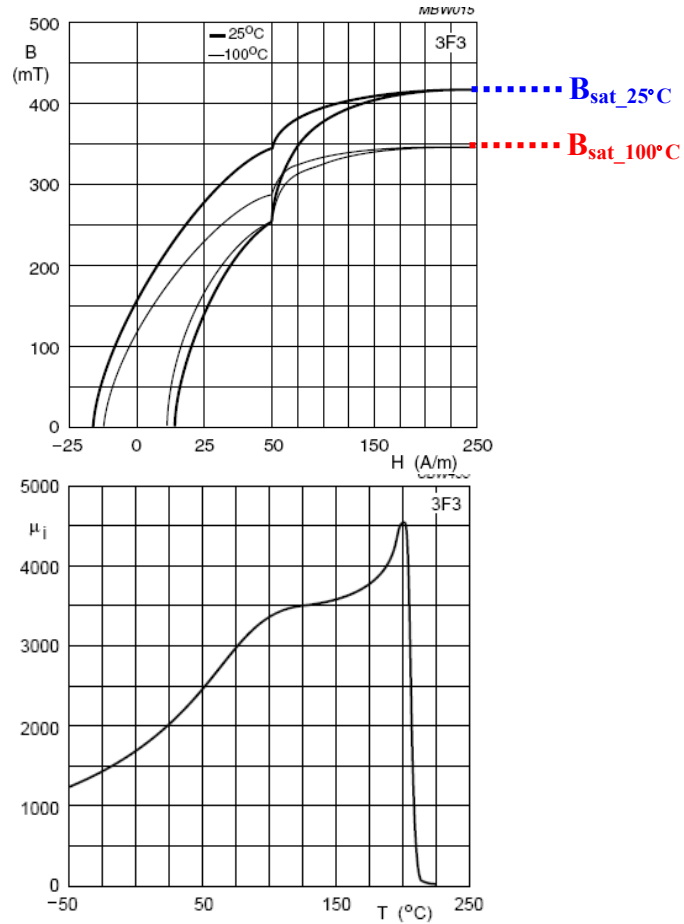


Fig. 2-2 Ferrite 3F3 complex permeability as a function of frequency [2-8]

The operating temperature of the ferrite should be below the Curie temperature where the magnetic material loses magnetic characteristics suddenly. Normally, the maximum continuous operating temperature of ferrites is below 125 °C. The development of high temperature ferrite (300 °C) has gained interests [2-9], since the high temperature semiconductor devices like *SiC* was introduced. Within the specified temperature range, temperature dependency of ferrite characteristics concerns designers. Fig. 2-3 shows the saturation flux density, initial permeability and core loss density variations of ferrite 3F3 under different temperatures.



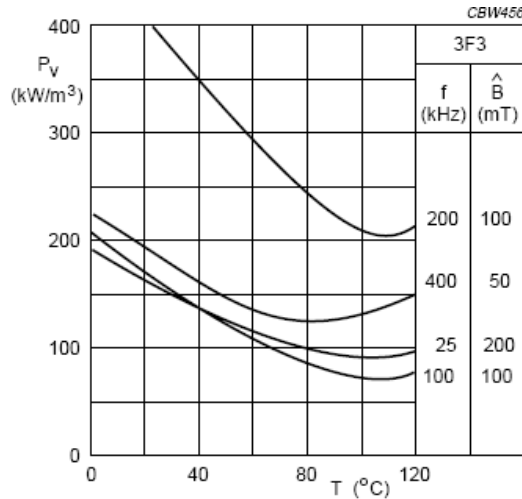


Fig. 2-3 Ferrite 3F3 B/H curve (top), initial permeability (middle) and loss density (bottom) as the function of temperature [2-8]

The reduction of saturation flux density under higher temperature would consequently result in more margins for a particular design. The permeability variation can cause an inductance change, which will affect the circuit operation. The more sophisticated issue is the loss variation along the temperature. The design would be iteration process indeed, since we have to calculate losses under an assumed temperature, and then calculate temperature induced by the amount of loss obtained, and so on. Therefore, all of the abovementioned temperature dependent issues of ferrites actually inherently limit the feasibility of ferrites of high-frequency high density applications.

2.1.4. Amorphous metals

Ferrites have quite low losses at high frequency, but at the sacrifice of saturation flux density. Ferromagnetic materials were too lossy to be used for application above tens kilo-hertz, until the advent of rapid solidification technology (*RST*) in 1970s. Amorphous metals produced by *RST* have markedly improved properties.

By quenching the alloy melt at rates of the order 10^6 K/s, the nucleation and growth of crystals are suppressed. The result is a solid ensemble of atoms that may justly be termed an amorphous metal or metallic glass. Amorphous metals have higher concentration of magnetic species than ferrites, promoting high saturation. They also exhibit lower coercivity due to the absence of metallurgical defects related to crystalline structure, have a higher electrical resistivity which requires thinner gauge tape for the

higher frequency, if they are compared with conventional ferromagnetic crystalline materials [2-10].

The typical properties of Fe-based and Co-based amorphous metals, according to data from *Metglas* (previous *Allied Signals*), are listed in Table 2-2. The saturation flux density ranges from 0.5~1.8 Tesla normally, and permeability varies from tens to hundreds of thousands [2-11].

Table 2-2 Amorphous material typical properties at 25°C [2-11]

Grade/Category	B _{sat} (T)	μ _i	ρ (Ω·m)	T _c (°C)	Thermal conductivity (W/(m·K))
2605CO (Fe(Co))	1.8	400,000	1.23*10 ⁻⁶	415	9
2605S-3A (Fe(Cr))	1.41	35,000	1.38*10 ⁻⁶	358	9
2826MB (FeNi)	0.88	800,000	1.38*10 ⁻⁶	353	-
2705M (Co)	0.77	600,000	1.36*10 ⁻⁶	365	9
2714A (Co)	0.57	1000,000	1.42*10 ⁻⁶	225	-

As shown in Fig. 2-4, Fe-based amorphous material (*Metglas 2605SA1*) exhibits a higher loss density than *Co*-based amorphous (*Metglas 2705M*), which is similar to *MnZn* ferrite *3F3*. Similar to ferrites, permeability of amorphous materials will reduce as frequency increases, shown in Fig. 2-5.

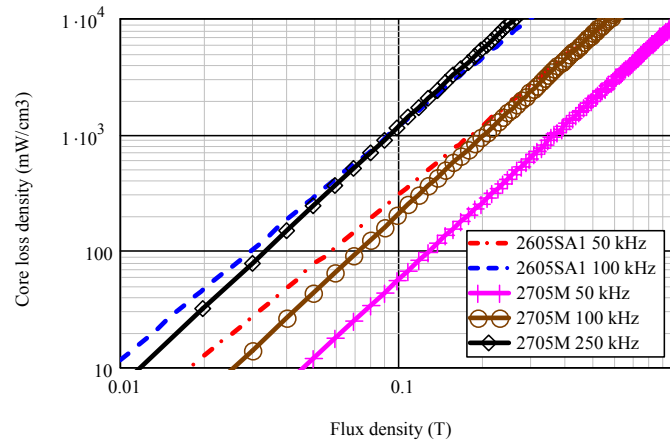


Fig. 2-4 Typical Fe- and Co-based amorphous materials core loss density at 25 °C [2-11]

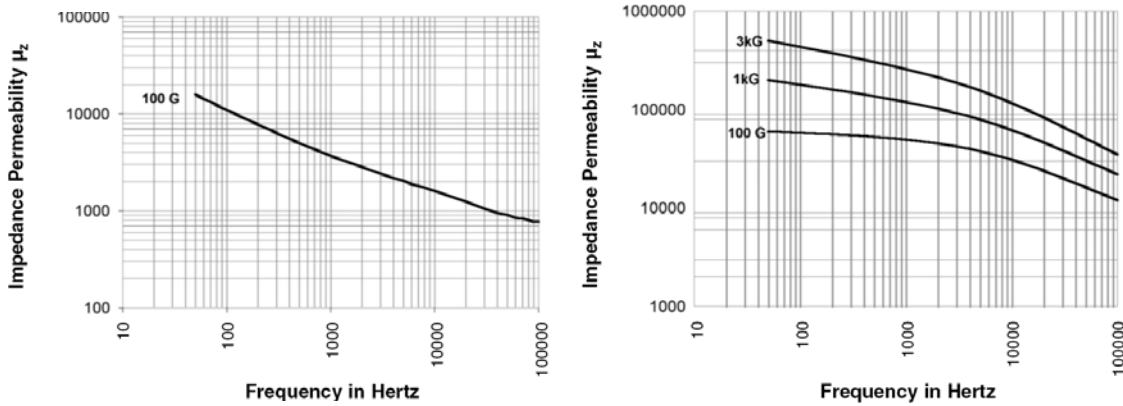


Fig. 2-5 Amorphous 2605-3A and 2714A impedance permeability as a function of frequency [2-11]

The maximum allowed continuous operating temperatures of amorphous magnetic cores are determined mainly by insulation materials, which are applied between amorphous material layers. Amorphous metals also have temperature dependent characteristics to which a designer must pay respects. Since amorphous materials have a much higher permeability than ferrites, we can suppress the temperature dependency by introducing air gaps into the magnetic loop.

2.1.5. Supermalloy

One of the early major applications of magnetic devices was the use of transformers in electrical power distribution and telecommunications. In the realm of power distribution, power transfer efficiency is a critical factor. Some ferromagnetic materials lose energy to heat from the physical expansion and contraction of the material, which caused by the magnetic field. This phenomenon, when a material changes physical dimension by an applied magnetic field, is called magnetostriction. A nickel-iron alloy ($Ni_{81}Fe_{19}$) is found to have essentially zero magnetostriction, and is widely used as a transformer core material. Permalloy is the common name for approximately 80-20 nickel-iron alloys, and the name appears to have been coined (or trademarked) by *Westinghouse* in approximately 1910 [2-12].

Supermalloy has an improved loss characteristic over Permalloy materials, which target a higher operating frequency. It is manufactured to develop the ultimate in high initial permeability and low losses. Initial permeability ranges from 40,000 to 100,000 while the coercive force is about 1/3 that of Permalloy. Supermalloy is very useful in ultra-sensitive transformers, especially pulse transformers, and ultra-sensitive magnetic

amplifiers where low loss is mandatory. The composition of Supermalloy is 79%Ni-15%Fe-5%Mo. The type thickness of the raw material normally in 0.0005”~0.004”, and strip wound cores with case or encapsulation or cut cores can be prepared for the final use. The basic magnetic characteristics are listed in Table 2-3, for Supermalloy.

Table 2-3 Supermalloy material typical properties at 25°C [2-13]

Grade/Category	B_{sat} (T)	μ_i	ρ ($\Omega \cdot \text{m}$)	T_c ($^{\circ}\text{C}$)	Density (kg/m^3)
Supermalloy	0.66~0.75	20,000	$0.57 \cdot 10^{-6}$	430	$8.72 \cdot 10^3$

The core loss density of the Supermalloy is plotted in Fig. 2-6, according to the data from Magnetic Metals [2-13].

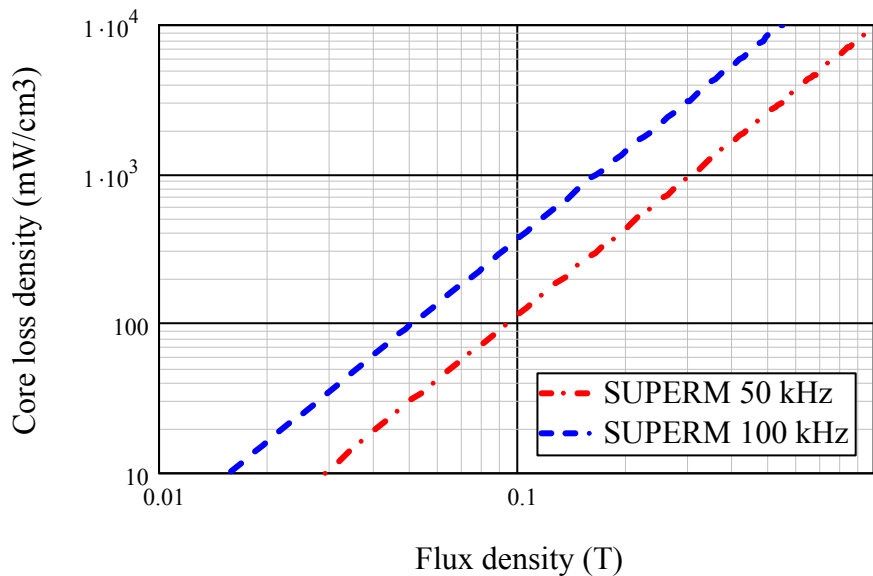


Fig. 2-6 Loss density of Supermalloy [2-13]

2.2. Characteristics of nanocrystalline materials

In 1988, Yoshizawa, etc, [2-14] introduced a new class of iron based alloys, named nanocrystalline, which exhibit superior soft magnetic behavior. Another group of Japanese scientists also found a similar type of magnetic material in 1991 [2-15]. The properties were a unique combination of the low losses, high permeability and near zero magnetostriction. Compared with all previously-known soft magnetic materials, nanocrystalline type materials have higher products of relative permeability and saturation flux density, as in Fig. 2-7. The higher the value of the product is the smaller size and lighter weight of magnetic components will be used for certain applications.

Certainly, good high frequency behavior, low losses and the good thermal stability are also important factors to affect the component density.

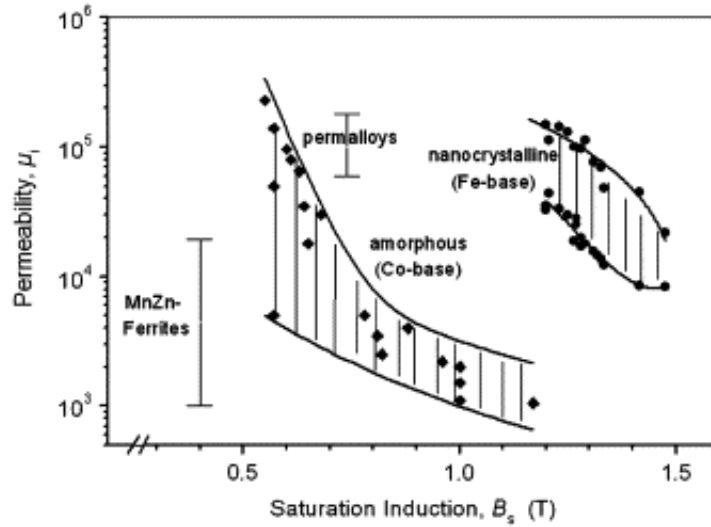


Fig. 2-7 Typical initial permeability and saturation flux density for soft magnetic materials [2-16]

“The fact that an extremely fine grained structure leads to good magnetic properties actually came as a surprise, since for conventional crystalline magnetic materials the coercivity increases with decreasing grain size, as illustrated in Fig. 2-8. Yet excellent soft magnetic properties are re-established when the grain size is below about 20 nm.” Somehow, the nanocrystalline materials are thought fit the blank between the amorphous and crystalline materials [2-17].

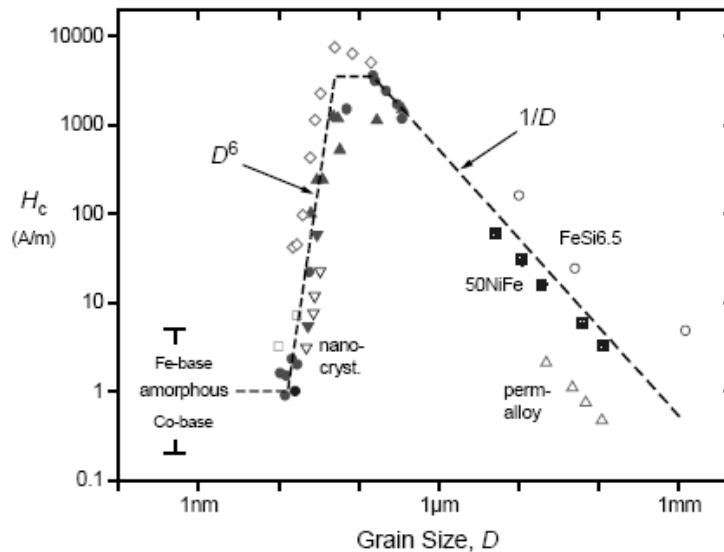


Fig. 2-8 The relation between coercivity and grain size of different ferromagnetic materials

Typical and so-far optimal nanocrystalline material composition is *Fe-Si-B-Nb-Cu*, which is also adopted by two major commercial nanocrystalline materials, *Hitachi Finemet®* $Fe_{73.5}Si_{13.5}B_9Nb_3Cu_1$ [2-18] and *Vacumschmelze Vitroperm®* $Fe_{73.5}Si_{15.5}B_7Nb_3Cu_1$ [2-19]. “Nanocrystalline materials are prepared based on amorphous precursors, and the nanocrystalline state is achieved by annealing at a temperature typically between 500 and 600 °C; this leads to primary crystallization. The resulting microstructure is characterized by randomly oriented, ultra fine grains of *Fe-Si* with a typical grain size 10-15 nm embedded in a residual amorphous matrix which occupies about 20-30% of the volume and separates the crystallites at a distance of about 1-2 nm. These features are the basis for the excellent soft magnetic properties indicated by high values of initial permeability of about 10^5 and correspondingly low coercivity of less than 1A/m.” [2-17]

The concerned properties of nanocrystalline materials are characterized in the following section, based on the material *Finemet®* from Hitachi.

2.2.1. B/H curve

The most important characteristics of soft magnetic materials are saturation induction B_s , relative permeability μ_r , coercivity H_c , and core loss density P_c , all of which can be visualized in the B/H curve of the material. To characterize the nanocrystalline material, the test circuitry shown in Fig. 2-9 has been setup [2-20].

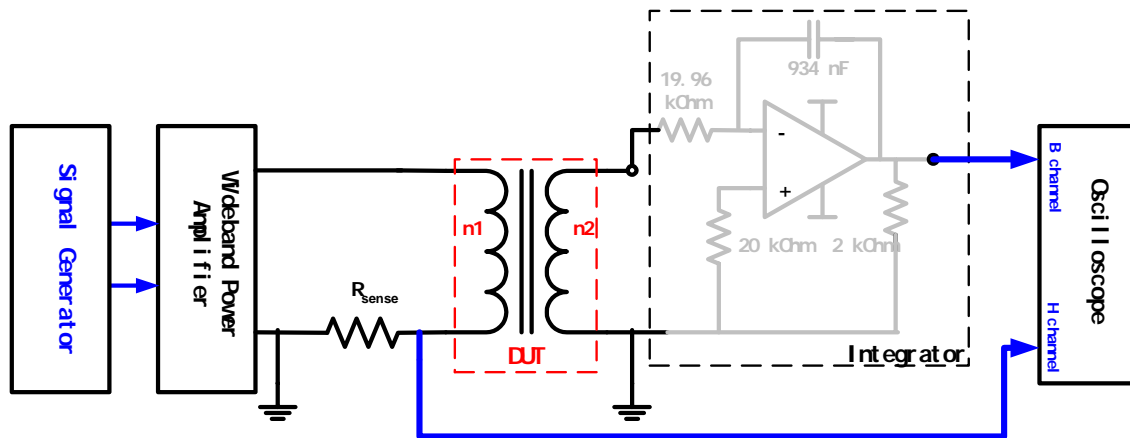


Fig. 2-9 B/H curve measurement setup

Two close coupled windings are wound onto a toroidal core, which is made of the nanocrystalline material, *Finemet®*, to be characterized. A sinusoidal signal is applied to

the primary winding through a wideband power amplifier, and induced voltage on the secondary winding is fed into an integrator, the flux density inside the material can be obtained. In practical, the flux compensation has to be considered, since the captured voltage initial value could be any point between plus and minus maximum [2-21]. There is a constant offset error at the output of the integrator due to the initial value of the voltage waveform $V \cdot \sin(\omega t + \varphi)$, i.e. taking $\varphi = 0$ as the starting point. The output of the integrator will have a DC offset as $\frac{V}{\omega}$.

$$B = \frac{\int v(t) \cdot dt}{n_2 \cdot A_c} \quad (2-1)$$

Exciting current is picked up using a sensing resistor, and magnetic field intensity is calculated by:

$$H = \frac{n_1 \cdot i}{l_c} \quad (2-2)$$

Where A_c notes a cross-section area of the DUT core, and l_c is the magnetic length. The measured B/H loop curve under 60 Hz and 25 °C of Finemet® is shown in Fig. 2-10. With exciting level increases, the DUT core is finally driven into saturation, so a series of minor and major B/H loops are recorded. Due to the output current limit of the amplifier and the size of the DUT core used in the test, the maximum magnetic field density obtained is around 5 A/m. Therefore, the real saturation flux density cannot be read directly, but it is clear that the material can hardly be used beyond 1 Tesla for transformer or inductor applications. Residual flux density is 0.8 Tesla, and coercivity is about 1.2 A/m, as shown in Fig. 2-10.

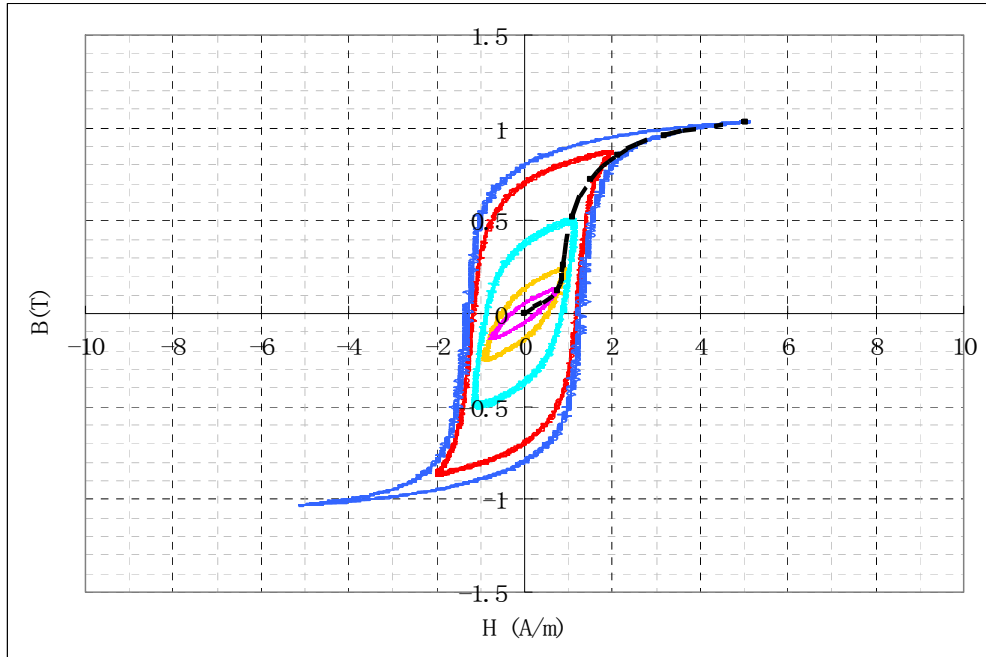


Fig. 2-10 B/H loop measured for FT-3M under 60 Hz

The interpretation of the measured B/H curves will give us a deeper understanding of the magnetization process of the nanocrystalline material. The black dotted curve (normal magnetization curve) connecting all tips of B/H loops clearly shows three magnetization scopes: initial magnetization, which happens below 0.1 Tesla, then irreversible magnetization with a much higher incremental permeability, and finally rotation magnetization before saturation. The corresponding incremental permeability can be obtained based on the normal magnetization curve, and is plotted against the magnetic field strength, as shown in Fig. 2-11.

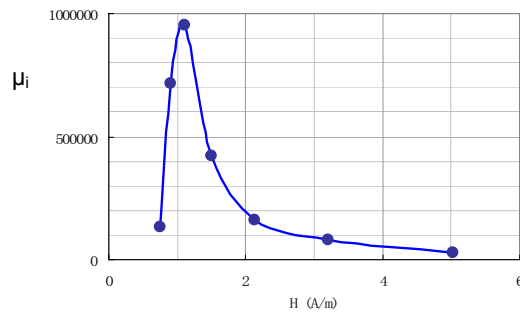


Fig. 2-11 Incremental permeability of the Finemet material

2.2.2. Loss performance

As one of the most important indicators to evaluate a soft magnetic material, core loss density can be obtained through the measured B/H loops. Since core loss is the function of frequency and flux density, the B/H loops of the material is measured with exciting frequency changing from 60 Hz to 100 kHz, and flux levels up to saturation B_s , as shown in Fig. 2-12. It is as expected that loss will increase as frequency increases, because of the effect of the eddy current inside the core. We can accept the assumption that the loss under 60 Hz is mainly hysteresis loss, according to many previous works.

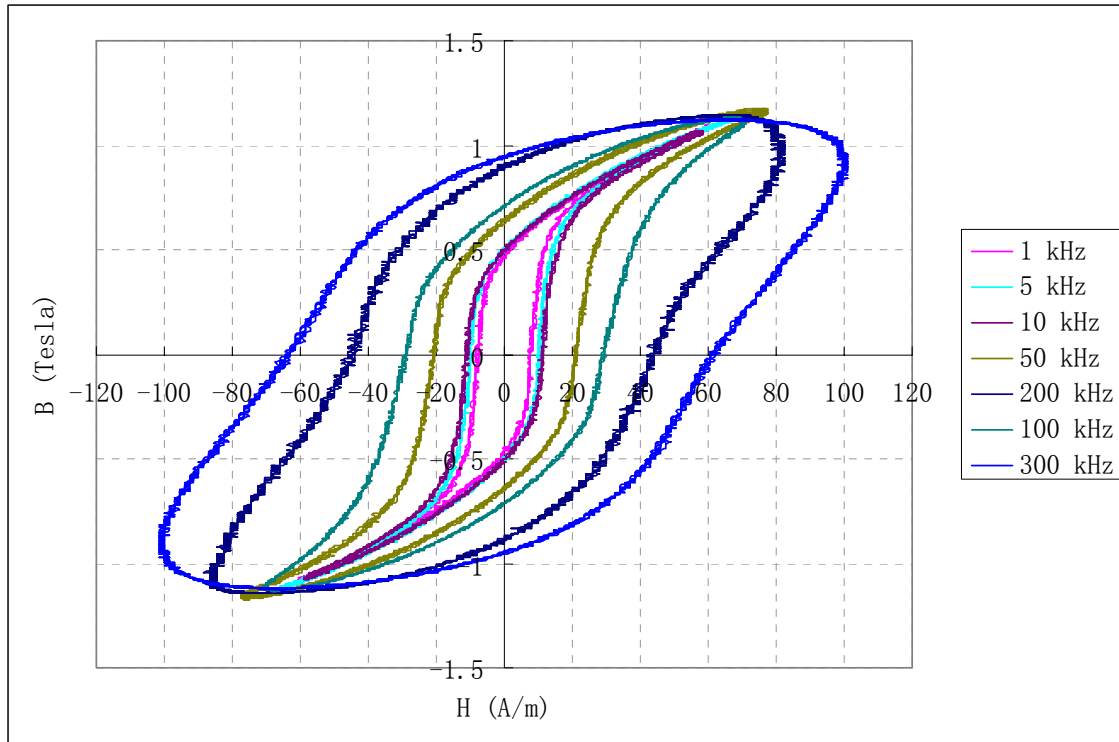


Fig. 2-12 B/H loops of the Finemet material under different frequencies

The enclosed area by the B/H loop represents the energy during each cycle trapped in the unit volume of the magnetic core. This energy is finally dissipated as heat loss. Therefore, we can calculate the loss density of the magnetic material as, with N samples of data within one cycle:

$$P_{cv} = f \cdot \int H \cdot dB = f \cdot \sum_0^N \{H(i) \cdot [B(i) - B(i-1)]\} \quad (2-3)$$

The calculated core loss density P_c , in mW/cm^3 , of the Finemet material is plotted against flux density and frequency in Fig. 2-13.

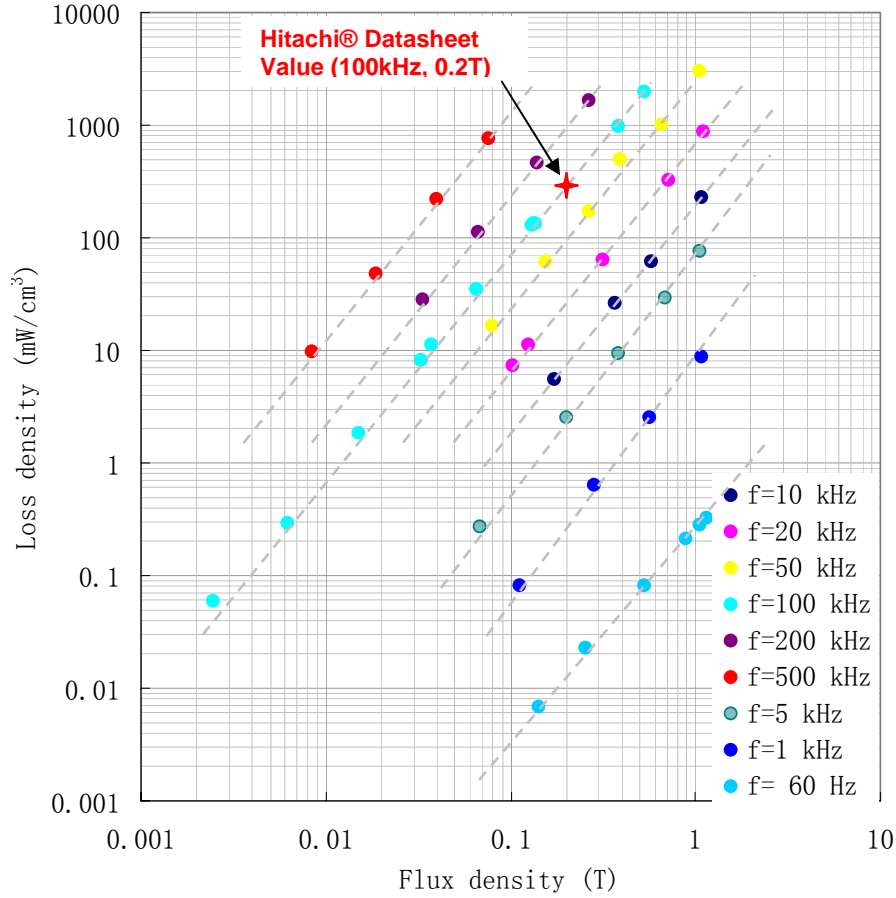


Fig. 2-13 Core loss density in mW/cm³ of the Finemet material

Another way to interpret the loss characteristic of the magnetic material is the complex permeability, $\mu = \mu' - j \cdot \mu''$, with an imaginary part representing loss and a real part for inductance. The complex permeability is very explicit for inductor and choke designs. To obtain the complex permeability (also termed as impedance permeability), the above measured current and voltage waveforms of the core can be processed as:

$$L = \frac{V_{\max}}{\omega \cdot I_{\max}} = \mu \cdot \mu_0 \cdot \frac{n_1^2 \cdot A_c}{l_c} \quad (2-4)$$

$$\Rightarrow \mu = \frac{V_{\max} \cdot l_c}{\mu_0 \cdot \omega \cdot I_{\max} \cdot n_1^2 \cdot A_c} \quad (2-5)$$

$$\mu' = \mu \cdot \sin(\varphi) \quad \mu'' = \mu \cdot \cos(\varphi) \quad (2-6)$$

φ is the angle of the voltage leading the current waveform. Basically, each set of complex permeability values are function of both frequency and exciting flux level. Loss and inductance are both affected by measurement flux level, so it is important to plot the

complex permeability frequency dependence at the same flux level. In our measurement, it is important to keep the measuring flux level low, so distortions of the current and voltage waveforms will not affect the calculation. The calculated complex permeability of the Finemet material at 0.1 Tesla is plotted in Fig. 2-14.

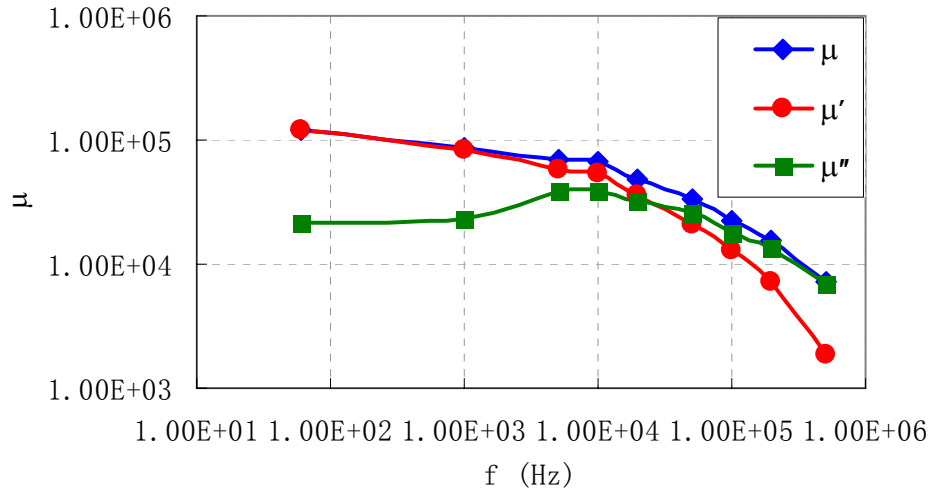


Fig. 2-14 Complex permeability as the function of frequency for the Finemet material @ 0.1 T

2.2.3. Temperature dependence performance

To characterize the temperature dependency of the nanocrystalline material, the DUT core has been put inside a temperature chamber. While monitoring the surface temperature of the DUT core, we measure the B/H loops at 60 Hz excitation from 25 °C to 150 °C, as shown in Fig. 2-15. By observing the curves, we find that the saturation flux density decreases as temperature increases. The percentage of flux level change at magnetic field density $H = 3 \text{ A/m}$ is plotted and shown in Fig. 2-16. According to the measured data, the maximum allowed flux density reduces 15% at 150 °C, if it is compared to the value at 25 °C, which must be considered for the transformer and inductor design of high temperature operations. Another interesting observation is that the coercivity H_c does not change between 25 °C and 100 °C. For temperatures above 100 °C, H_c increase and B_s reduces. The reduction on the initial permeability is also very obvious as illustrated by the minor loops in Fig. 2-15. This is another important point to which the designer should pay attention.

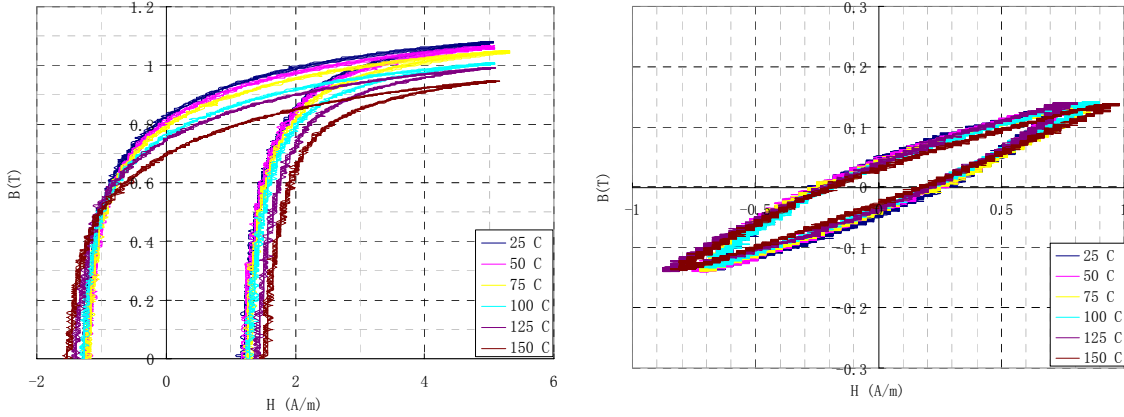


Fig. 2-15 60 Hz B/H major and minor loops of the Finemet material under different temperature

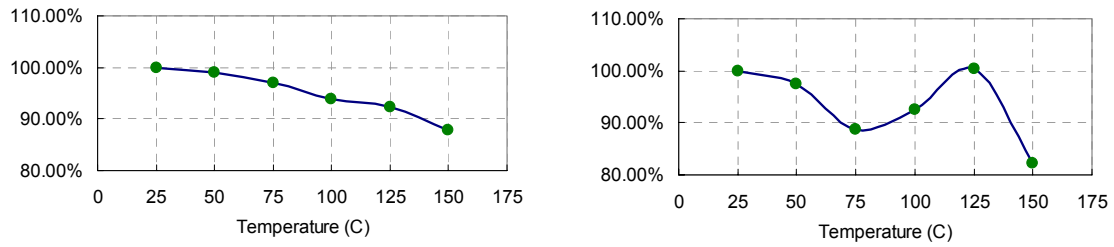


Fig. 2-16 Flux density @ H=3A/m variation percentage (left) and initial permeability variation percentage (right) as the function of the core temperature

The core loss density as the function of temperature is shown in Fig. 2-17. At different flux levels, the core loss has a different temperature dependency.

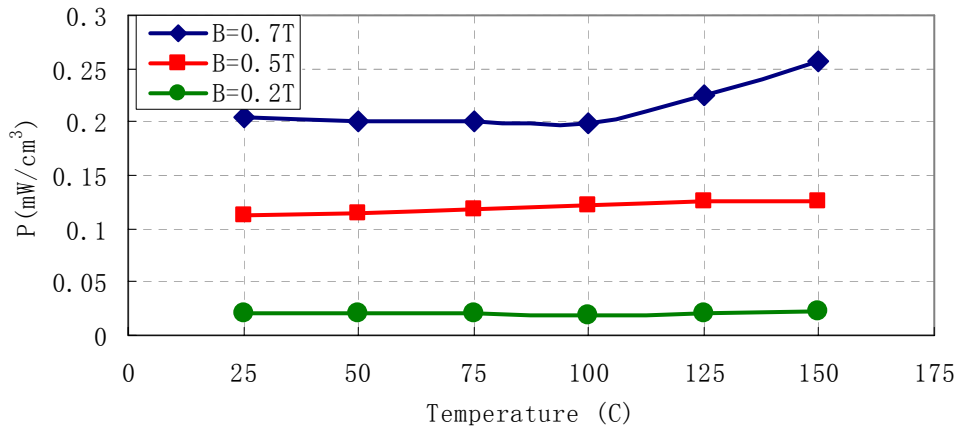


Fig. 2-17 Core loss density as the function of the core temperature

2.2.4. Cut core issues

Similar to amorphous metals, the nanocrystalline material is in the shape of a thin tape, which is the result of the rapid solidification process. After annealing, the tape is very brittle and hard to handle, so there are several ways to assembly the thin tape into

different shapes of cores to meet different application requirements. For common-mode chokes and small power transformers that do not require air gaps, cased toroidal cores would be the most convenient solution. Metal or nylon cases enclosing a roll of nanocrystalline material tape actually can act as winding bobbins. In this manner, the magnetic performance of the nanocrystalline material could be maintained at the most extension. However, the toroidal core cannot include air gap and is hard to be applied to high power transformers [2-22].

Air gaps are required to store energy for inductors and sometimes transformers. Besides, a tiny air gap will improve the operating ruggedness of the magnetic component. First, gapping the core would prevent saturations. A higher DC current value can be sustained by the transformer. Secondly, the gapping effect would reduce the sensitivity of permeability to the temperature variation. However, a gap would reduce the magnetizing inductance of the transformer, which means more loss to the circuit, and cause more winding losses due to fringing field around the gap. Therefore, we only want to introduce a very small gap into the magnetic path formed by the core, which can be realized by using cut core structures [2-23].

Nanocrystalline materials are inherently brittle and hard to cut, so the preparation of cut cores needs special care. Usually, nanocrystalline tapes are wound into the expected shape, and the core is impregnated by an insulation resin. Stress is induced during the casting process, so the molded core needs to be annealed to release the stress. Up to this stage, the core can be machined and cut into halves, and a special treatment is required to improve the smoothness of the cutting surface and remove the short circuit between tape layers. As we can see, the magnetic properties of the material would be changed due to these processes. We cannot rely on the material characteristics obtained any more, so, the characteristics of cut cores are investigated to provide insight into the transformer design based on cut cores.

To study the effect of air gaps, C-cores made of the same Finemet nanocrystalline material are prepared and put into the test circuit shown in Fig. 2-9. In Fig. 2-18, B/H loops of the C-core are shown as the function of the length of air gaps in the core pair, under 50 kHz sine wave excitation. The length of the air gaps varies from around 30 μm to 300 μm , and it is clear that the gapping would reduce both permeability and residual

flux density. For the C-core used for this demonstration, the minimum achievable air gap length is $L_{g0} = \frac{36}{2} \mu\text{m}$, which is mainly determined by the quality of the cutting and grinding processes during the C-core preparation.

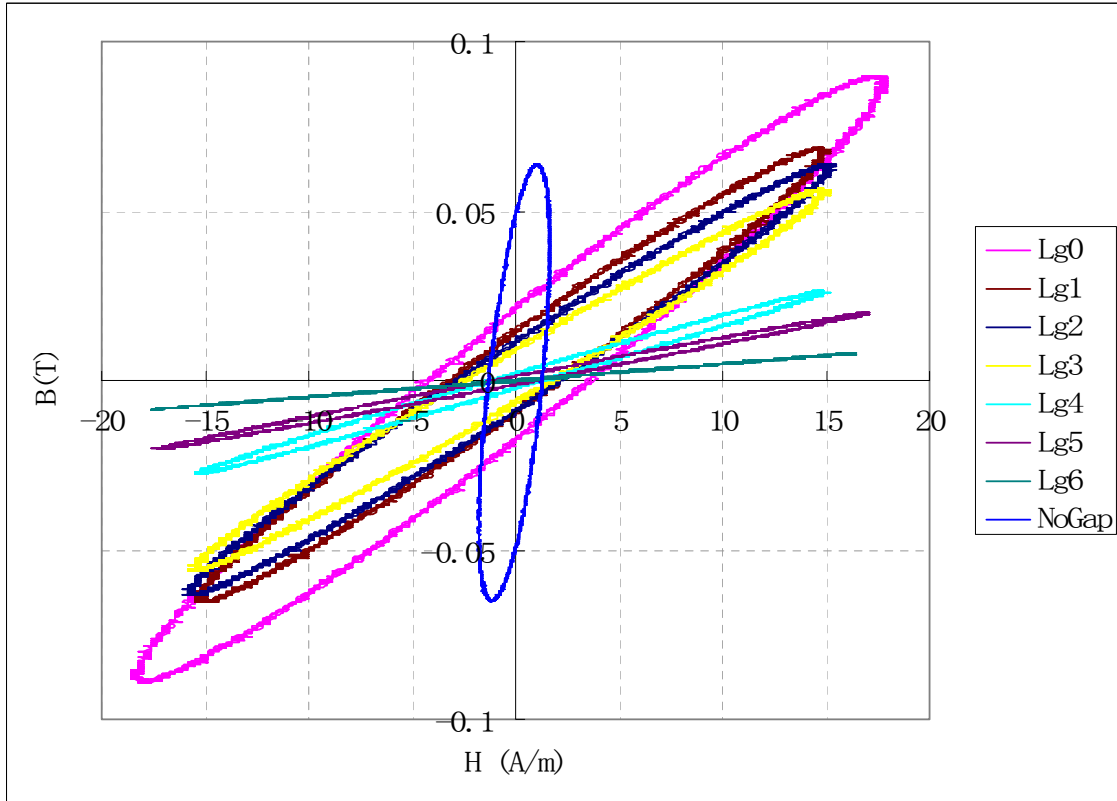


Fig. 2-18 Finemet material C-core B/H loops (50 kHz) as the function of the length of air gap

The relationship between air gap length and effective permeability can be derived as:

$$NI = H_{core} \cdot l_c + H_{gap} \cdot l_g = \frac{B}{\mu_0} \left(\frac{l_c}{\mu_r} + l_g \right) = \frac{B \cdot l_c}{\mu_0 \cdot \mu_e}$$

$$\Rightarrow l_g = l_c \cdot \left(\frac{1}{\mu_e} + \frac{1}{\mu_r} \right) \quad (2-7)$$

Similar to the core loss characterization of the Finemet material, B/H loops are measured for the C-core with the minimum air gap length, $L_{g0} = \frac{36}{2} \mu\text{m}$. Core loss density of the cut core can be calculated using equation (2-3), and correspondingly compared to the data of the material.

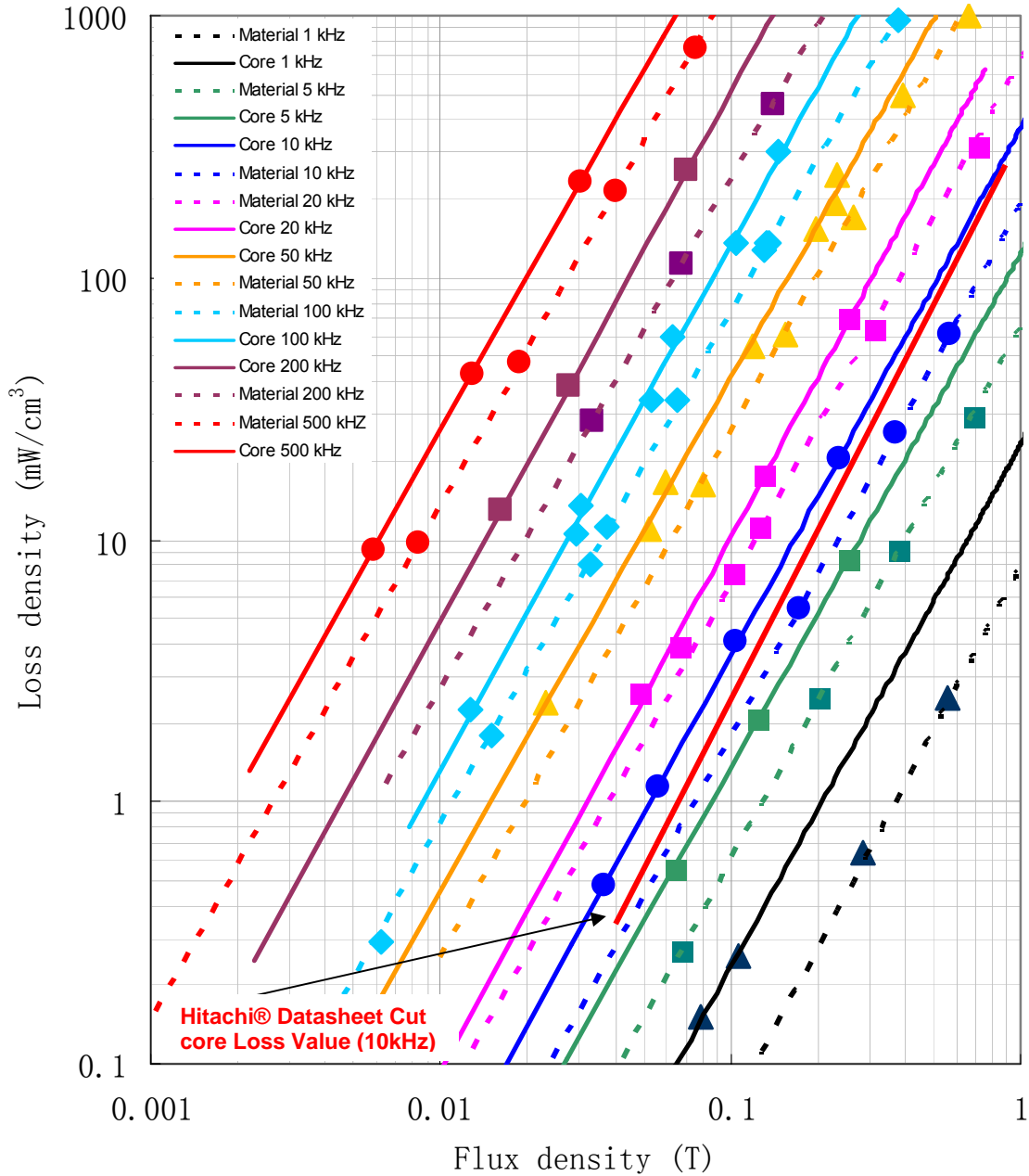


Fig. 2-19 Core loss density of Finemet material and cut core using same material

Compared to the nanocrystalline material, the C-core made of the material has a higher core loss density at corresponding flux density and frequency. As discussed in other literature, this is mainly caused by stress induced during the impregnating, cutting, and grinding process. Another reason could be the damage of insulation layers of nanocrystalline tapes, which would increase eddy current losses. Steinmetz equations are derived based on the measured core loss in Fig. 2-9. The cutting core effect can be read quantitatively then.

$$P_{v_material} = 3.935 * f^{1.585} * B^{1.88} \tag{2-8}$$

$$P_{v_core} = 8 * f^{1.621} * B^{1.982} \tag{2-9}$$

When the gap length is varied from 18 μm to 160 μm , core loss densities are measured for different frequency, as shown in Fig. 2-20. For the gap length range analyzed, we can see that the increase of core loss density is not proportional and can be omitted.

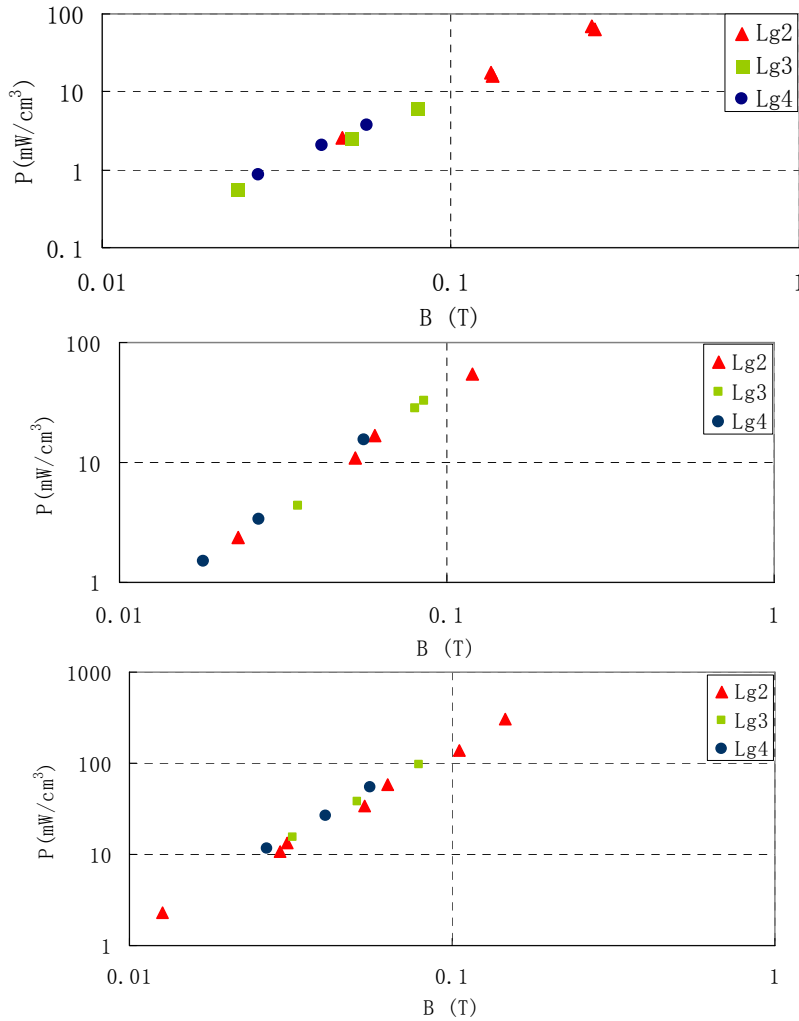


Fig. 2-20 Core loss density as the function of the air gap length under frequency 20kHz (top), 50kHz (middle), and 100kHz (bottom)

2.3. Summaries

The development of a soft magnetic material can be summarized from the high frequency performance perspective, as illustrated in Fig. 2-21. Each kind of material has been improved on its high frequency performance through changing ingredients, controlling process quality, and so on. Basically, the loss density is the most important index to high frequency transformer applications. It is hard to find a material with all aspects superior to the others, so trade-offs have to be considered by the designer. In general, rapid quench technology brings the birth of amorphous materials, which is a revolution to the soft magnetic material development. The nanocrystalline material is prepared through annealing the amorphous precursor, and this is another leap in the magnetic material development. The corresponding breakthroughs in magnetic performance are the benefits.

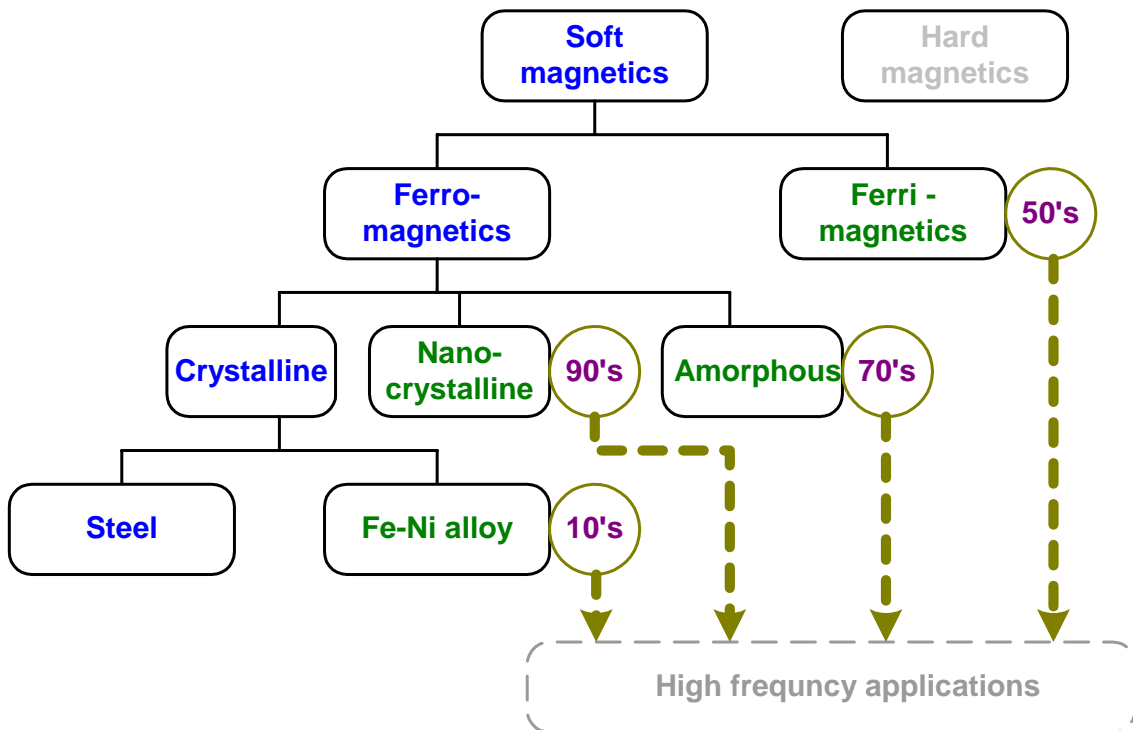


Fig. 2-21 Development road map for different soft magnetic materials

With all the data shown in this chapter for several typical soft magnetic materials, we can compare their performance for high frequency high power applications. In Fig. 2-22, core loss densities (in mW/cm³) of ferrite (*3F3*), amorphous (*Metglas 2605SA* and *2705*), Supermalloy, and nanocrystalline (*FT-3M*) are shown. *Finemet FT-3M* is clearly

less lossy than Fe-based amorphous **2605SA**, by about ten times for all flux density range, and it is superior to the MnZn ferrite **3F3** for flux density beyond 0.04 Tesla. Another group of loss densities of cut cores made of the **Finemet** material are also shown in the figure, which have higher losses than the corresponding material. According to the measurement, the nanocrystalline cut core still has a better loss performance than the ferrite because the flux density is higher than 0.1 Tesla. Since cut cores would improve the transformer operation ruggedness, we can sometimes tolerate a core loss increase.

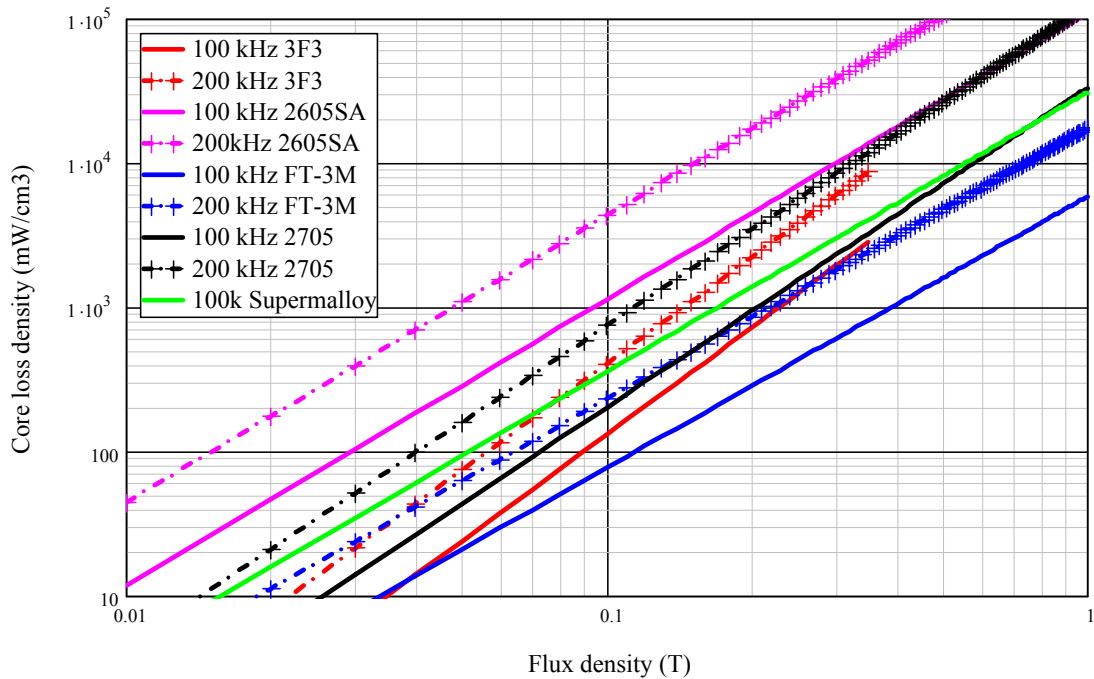


Fig. 2-22 Core loss density comparison of typical magnetic materials

Other characteristic comparisons are listed in Table 2-4. Here we can see that the Finemet material has a higher saturation flux density and less temperature dependence than the other materials. The designer can choose a higher operating flux density to make the transformer size smaller, and with nanocrystalline materials just fit the niche. The maximum continuous operating temperature of the FT-3M nanocrystalline material is 150 °C which is normally high enough to industrial applications. Since the temperature of the transformer usually are designed similar to the other components in the system that will seldom exceed 150 °C. The maximum operating temperature of the material is mainly determined by the core casting material, and this can be improved by changing the

casting material into the one with higher thermal grades, or using metallic casing for wound cores.

Table 2-4 Magnetic material characteristic comparison

Characteristics\Material	Finemet FT-3M	Ferrite 3F3	Supermalloy	Amorphous 2605SA
Saturation flux density B_{sat} (T)	1.23	0.45	0.79~0.87	1.57
Curie temperature T_c ($^{\circ}$ C)	570	200	430	392
Max. operation temp. ($^{\circ}$ C)	150	120	125	150
$B_{sat}(100^{\circ}$ C)/ $B_{sat}(25^{\circ}$ C)	91.7%	82.5%	-	-
μ (100° C)/ μ (25° C)	Within $\pm 10\%$	170%	-	-

By looking at the characteristics shown above, we can conclude that the nanocrystalline material is superior to the ferrites and amorphous materials for high-frequency high-power applications. The introduction of nanocrystalline magnetic materials with relatively low loss density, high saturation flux density, and high Curie temperature has shown promise for significantly improved magnetics design. They have gained quick acceptance in filter applications [2-24], and also have been used in transformers, even at very high power levels [2-25]. However, the frequencies of these high power transformers are generally around 20 kHz.

Chapter 3 Loss Calculation and Verification

Ideally, the size of the transformer used to transfer a certain amount of power is only limited by the saturation flux density of the core material. Realistically, however, the density achieved is much lower than the ideal value, because of losses in the wires and cores. Temperature rises under certain cooling schemes and/or efficiency requirements would be used as design criteria, both of which would limit the allowed loss for a particular design. Therefore, the understanding and modeling of winding loss and core loss would be the fundamental knowledge needed to obtain an optimal transformer design [3-1].

The challenging aspects of core loss calculation all stem from lack of a microscopic physical magnetization model, although significant advancements on domain wall theory have been made by physicists [3-2]. Steinmetz coefficients have been introduced [3-3] to correlate the core loss with corresponding operation frequency and peak flux values, and they can be obtained from experimental results under certain exciting waveform. Some methods have been proposed to deal with arbitrary operation waveforms, but they mainly focus on PWM hard switching operation waveforms [3-4]-[3-7]. As soft switching and resonant converters are suitable to high-frequency high-power applications, the core loss calculation method that is applicable to these waveforms is needed. The potential method also has to be compatible with nanocrystalline materials which could replace ferrites and amorphous metals for certain applications.

Eddy current effects would cause the winding AC resistance to be much higher than its DC value, as the frequency of the current flowing through the winding increases [3-1]. Calculation of winding loss, with considering skin and proximity effects, is highly influenced by winding and core geometry, wire type, and winding arrangement. Therefore, Finite Element Analysis (FEA) field solvers are usually required when taking 3-D or 2-D field distribution into consideration. However, the FEA methods are hardly applicable to Litz wires with huge numbers of strands, which is necessary to high power large current applications. Drawing, meshing, and computing are all too time consumed to be conducted for the purpose of Litz wire winding loss calculation.

3.1. Core loss calculation

3.1.1. Calculation method survey

The physical origin of core losses is the energy consumed to damp the domain wall movement by eddy currents and spin relaxation. Detailed knowledge about the origin of core losses does not provide a practical means for calculating losses. In general, the rather chaotic time and space distribution of the magnetization changes is unknown and cannot be described exactly. Furthermore, the manufacturer's datasheets only provide core loss for sine wave excitations, and most power electronics applications have a non-sine waveform.

To work around this lack of a microscopic physical remagnetization model, several macroscopic and empirical approaches have been formulated. Generally, they can be categorized into two groups: the loss-separation approach and empirical equations.

a) *Loss separation method*

The loss-separation approach [3-8] calculates the total core loss separately by three parts, as static hysteresis loss, dynamic eddy current loss which includes classic eddy current loss and excess eddy current loss, as in equation (3-1).

$$P_{v_core} = P_h + P_d = P_h + \underbrace{P_c + P_e}_{\text{dynamic eddy current loss}} \quad (3-1)$$

The physical reason for such decomposition is that the hysteresis loss originates from the discontinuous character of the magnetization process at a very microscopic scale, whereas the dynamic eddy current loss is associated with the macroscopic large-scale behavior of the magnetic domain structure. The separation method seems to provide the solution to the core loss calculation of arbitrary field waveforms. Hysteresis loss is only determined by the operating flux density peak value and frequency, but not the function of waveform shapes. The per unit volume hysteresis loss is equal to f times of static B/H loop area, as in (3-2). The static B/H loop can be obtained from measurement or Jiles-Atherton [3-9] and Preisach's models [3-10]. The dynamic eddy current loss can be calculated by introducing bulk resistivity of the magnetic material, as in (3-3) with d for material thickness and ρ for resistivity. However, results from the sum of (3-2) and (3-3) usually do not match with the measurement, so the excess eddy current loss is

introduced to count for the difference, but with very limited understanding of the mechanism. According to Bertotti [3-6], a wide variety of ferromagnetic materials show the relationship as in (3-4), with C_1 as the suitable constant characterizing the material.

$$P_h = f \cdot \int H \cdot dB \quad (3-2)$$

$$P_c = \frac{(\pi \cdot B_{\max} \cdot f \cdot d)^2}{6\rho} \quad (3-3)$$

$$P_e = C_1 \cdot (B_{\max} \cdot f)^{3/2} \quad (3-3)$$

The major drawback of this method is that it requires extensive measurements and parameter extraction with a given material. This is impractical for designers who normally have limited resources and knowledge of the material.

b) *Empirical method*

Another major group of core loss calculation methods is based on measurement observations. One of the advantages of these methods is easy to use, especially to designers who do not have much expertise on magnetism. Lacking of physical bases, empirical methods are usually applicable to particular material and operating conditions. As one of the empirical methods, Steinmetz equation (3-5) has proven to be a useful tool for the calculation of core loss.

$$P_{v_core} = K * f^\alpha * B^\beta \quad (3-5)$$

Where K , α , and β are determined by the material characteristic and usually obtained from the manufacturer's datasheet. For different magnetic materials, we extract different values. The Steinmetz equation is basically curve-fitting of measured core loss density under sinusoidal magnetization waveform. Therefore, it can be extracted from data provided by manufacturers, and without knowing the detailed material characteristics. However, the advantage of this method could also be a demerit due to the lack of physical background. It is almost impossible to represent the complex relationship among loss, flux density and frequency by such explicit exponential functions. Therefore, a set of Steinmetz equations have to be used to fit experimental results, each of which may only be valid for a part of whole frequency and/or flux density ranges.

Another problem with the Steinmetz equation is the limitation on waveform. The original Steinmetz equation (OSE) and the corresponding set of parameters are only valid

for a sinusoidal exciting condition. There is no direct and clear way to extend the Steinmetz equation to arbitrary operating waveforms, which is what mainly concerns us here.

Intuitively, people [3-11]-[3-12] have tried to apply a Fourier transform to any arbitrary waveform to obtain a series of sine wave. OSE could then be applied to each frequency component. However, the summation of calculated losses of each frequency is not the total core loss, because there is no orthogonality between different orders of harmonics existing. Also it is not universally appropriate to apply the Fourier transform to a magnetic component, which is nonlinear inherently.

The Modified Steinmetz equation (MSE) [3-4] and Generalized Steinmetz equation (GSE) [3-5] have been proposed to extend this OSE to non-sinusoidal applications. As basis of their concepts, they both attempt to correlate the rate of change of flux density $\frac{dB}{dt}$ with the frequency f in the OSE. The core concept of MSE is that an equivalent frequency f_{eq} is introduced to replace the frequency f in the OSE, as shown in equation (3-6) for a waveform with N piecewise linear segments, and equation (3-7) for integral version.

$$f_{eq} = \frac{2}{\pi^2} * \sum_{k=2}^N \left(\frac{B_k - B_{k-1}}{B_{max} - B_{min}} \right)^2 \cdot \frac{1}{t_k - t_{k-1}} \quad (3-6)$$

$$f_{eq} = \frac{2}{(B_{max} - B_{min})^2 \pi^2} * \int_0^T \left(\frac{dB}{dt} \right)^2 \cdot dt \quad (3-7)$$

The basic assumption behind this derivation is the linearization of flux density, which means the average value of $\frac{dB}{dt}$ over a complete magnetization cycle can be obtained as equation (3-8). This simplified assumption makes the MSE method susceptible to rigorous mathematic derivation and generic applicability.

$$\dot{B} = \frac{1}{B_{max} - B_{min}} * \oint \frac{dB}{dt} \cdot dB = \frac{1}{B_{max} - B_{min}} * \int_0^T \left(\frac{dB}{dt} \right)^2 \cdot dt \quad (3-8)$$

GSE directly assumes that core loss per cycle per unit volume could be expressed as the equation (3-9), with α , and β having the same meaning as in equation (3-5).

$$E_{v_core} = K_1 * \left(\frac{dB}{dt} \right)^\alpha * B(t)^{\beta-\alpha} \quad (3-9)$$

Once the integral of the E_{v_core} over one cycle is calculated and the result of sinusoidal exciting waveform is correlated to OSE (3-5), the coefficient K_I is derived as:

$$K_I = \frac{K}{(2\pi)^{\alpha-1} \int_0^{2\pi} |\cos\theta|^\alpha \cdot |\sin\theta|^{\beta-\alpha} \cdot d\theta} \quad (3-10)$$

The validation of GSE actually requires that a particular waveform of $\mathbf{B}(t)$, such that the derivation $\frac{dB}{dt}$ can be expressed in the format of $Coefficient \cdot B(t) \cdot f$, which is true for sinusoidal and linear waveforms only. Although most of power electronics applications do present sinusoidal and linear waveforms or combinations of them, this method has not been proven that it can be applied generally. Another drawback of this method is that the derivation of K_I could be quite complicated for certain waveforms; pre-programmed tools are necessary to cope with complex waveform applications.

Both of them claim that core loss due to non-sinusoidal excitations can be predicted with acceptable accuracy. In particular, typical PWM quasi-square waveforms have been studied and verified. However, according to the above discussions, both MSE and GSE have to be checked before they are applied to certain application, for example, particular flux waveforms and soft magnetic materials which have different Steinmetz coefficients α and β . Especially for soft switching and resonant operation converters, the magnetic flux waveform is different from ones with PWM converters. The applicability of the MSE and GSE to new magnetic materials other than ferrites and amorphous, such as nanocrystalline materials, also needs to be checked.

3.1.2. Proposed loss calculation method

As discussed above, the loss separation method is based on physical interpretation of magnetization, but the calculation of the excess eddy current loss makes the method too complicated to be adopted for engineering purposes. Empirical methods, including MSE and GSE, is less material parameter involved, and have been verified for PWM (square) waveforms with acceptable accuracy. For resonant and soft switching operation waveforms which are much more popular for high-frequency high-power applications than PWM waveforms, we still need to discover the appropriate core loss calculation method. The developed method should be straightforward to most power converter design engineers and quite accurate, and at least on conservative side, for core loss

calculation. Here, we propose to modify the Steinmetz equation based on the flux waveform coefficient concept, so the core loss due to non-sinusoidal waveforms can be correlated to the Steinmetz equation.

a) *Waveform-coefficient Steinmetz Equation (WcSE) method*

We first examine the flux waveform of the sinusoidal and square operating voltages, as shown in Fig. 3-1. If the maximum flux densities are the same, the sinusoidal flux encloses the triangular flux wave, which is excited by the square wave with amplitude of $\frac{2}{\pi}$ times of the sinusoidal one. Here the sinusoidal peak voltage is assumed to be a unit, and the induced flux density of the sine wave is also normalized. Therefore, the square waveform has a voltage amplitude of $\frac{2}{\pi}$, and flux density peak value as 1.

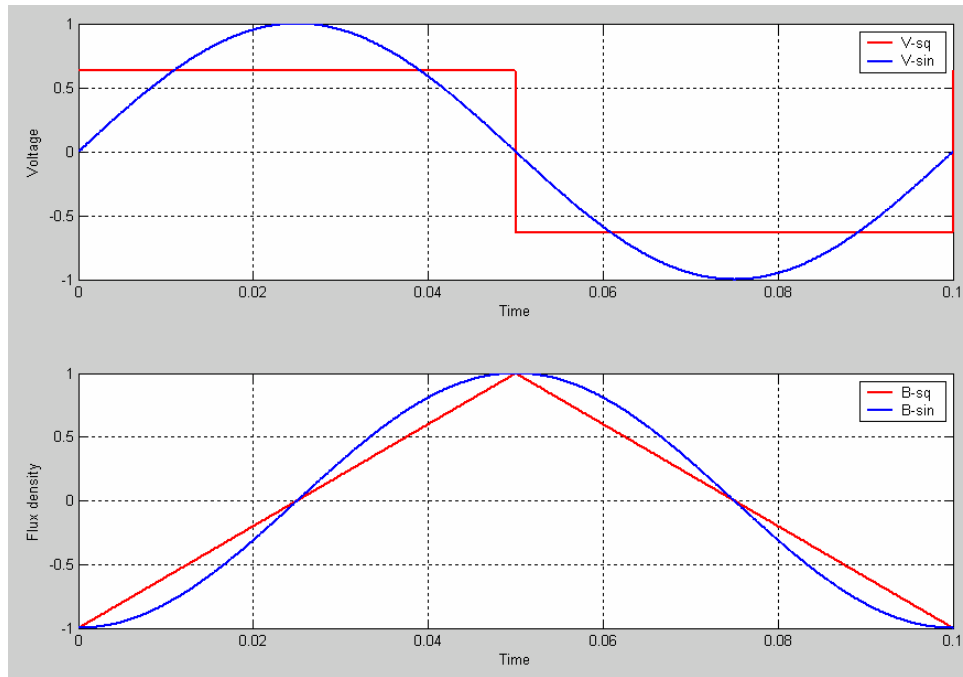


Fig. 3-1 Voltage and flux of square and sinusoidal waveform

A concept of the “flux waveform coefficient” has been introduced here, which basically attempts to correlate the non-sinusoidal waveforms to the sinusoidal one with the same peak flux density, through calculating the “area” of the flux waveform. For the sinusoidal flux waveform, the integral of the half cycle is derived.

$$W_{\sin e} = \frac{1}{T \cdot B} \int_0^{T/2} B \cdot \sin(\omega t) \cdot dt = \frac{2}{\pi} \quad (3-11)$$

Similarly, we can find out the waveform factor of the triangular flux waveform, which is shown in (3-12).

$$W_{sq} = \frac{4}{T \cdot B} \int_0^{T/4} \frac{4B \cdot t}{T} \cdot dt = \frac{1}{2} \quad (3-12)$$

Therefore, the flux waveform coefficient, FWC, of the square voltage waveform (triangular flux waveform) can be defined as:

$$FWC_{sq} = \frac{W_{sq}}{W_{sine}} = \frac{\pi}{4} \quad (3-13)$$

With β as the Steinmetz coefficient in (3-5), we can calculate the core loss of certain material under square exciting voltage waveform as:

$$P_{v_core} = FWC_{sq} \cdot K \cdot f^\alpha \cdot B^\beta \quad (3-14)$$

A similar procedure can be applied to the triangular voltage waveform, which will generate a parabola flux density waveform, as illustrated in Fig. 3-2. Again, we will discuss the core loss difference of these two kinds of waveforms with the same peak flux density. It is clearly shown that the triangular waveform will have a larger core loss, compared to its sine counterpart.

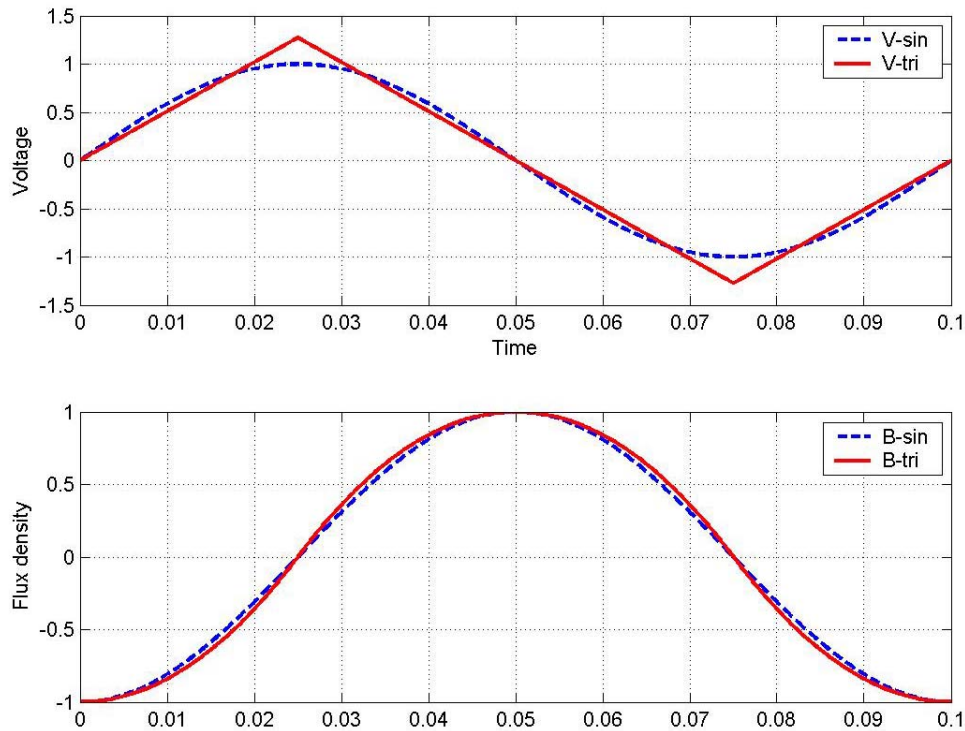


Fig. 3-2 Normalized flux density of triangle and sinusoidal waveforms

We can find out the waveform factor of the parabola flux waveform, which is shown in (3-15).

$$W_{tri} = \frac{2}{T \cdot B} \int_0^{T/2} B \cdot \left[1 - \frac{16}{T^2} \cdot \left(t - \frac{T}{4} \right)^2 \right] \cdot dt = \frac{2}{3} \quad (3-15)$$

Therefore, the flux waveform coefficient, **FWC**, of the triangular voltage waveform (parabola flux waveform) can be defined as:

$$FWC_{tri} = \frac{W_{tri}}{W_{\sin e}} = \frac{\pi}{3} \quad (3-16)$$

This waveform coefficient shows that the core loss by the triangle voltage will be slightly higher than the one by the sine wave. The measured results shown in the following section will verify the derivation.

So, using the information obtained from a datasheet and the flux waveform coefficient, we can calculate the core loss under non-sinusoidal waveforms. The flux waveform coefficient, **FWC**, is derived according to the detailed flux waveform. The sine waveform coefficient is used as a benchmark, since the available core loss data would be for the sine waveform. The propose WcSE method is still a kind of empirical based solution to this problem, since it is easy to use for design engineers who mostly do not have a sophisticated knowledge of materials, magnetization, and so on. To verify the concept and the proposed method, the follow case is constructed, and the WcSE is compared with MSE and GSE.

b) Sinusoidal transition square (STS) waveform verification

For many high-power, high-frequency applications, soft-switching techniques are adopted to reduce switching losses. Therefore, the operating voltage applied to the transformer could be like a “sinusoidal transition square” (STS) kind of waveform, which was either treated as a sine or trapezoidal waveform for the core loss calculation in previous works. Even though core losses calculated from these simplifications have been used for practical magnetic designs, there are still desires to refine the loss calculation. High-frequency high-power and high-density requirements would push engineers to cut off margins and reduce uncertainties.

To study the appropriate loss calculation method for soft switching operation conditions, a simplified STS kind of waveform is constructed, as shown in Fig. 3-3. The

corresponding flux density waveforms of the transformer core can be obtained as shown in Fig. 3-3. Characteristics of the STS waveform include the repetitive frequency of $f_0 = \frac{1}{T}$, the sinusoidal transition part has a frequency of f_{sine} , the peak value is V_{sine} , and the level of the voltage flat part is V_0 . Basic restrictions of the value selection of these parameters are $f_0 \leq f_{\text{sine}}$ and $V_0 \leq V_{\text{sine}}$. The ratios, $\frac{f_0}{f_{\text{sine}}}$ and $\frac{V_0}{V_{\text{sine}}}$, can be changed within the range of [0,1]. It should be noticed that the STS waveform becomes sinusoidal when the condition of $\frac{f_0}{f_{\text{sine}}} = 1$ and $\frac{V_0}{V_{\text{sine}}} = 1$ meet; it is like square one for the conditions of $\frac{f_0}{f_{\text{sine}}} \rightarrow 0$ and/or $\frac{V_0}{V_{\text{sine}}} \rightarrow 0$. Therefore, the constructed STS waveform is capable of checking the validation of core loss calculation method for different waveforms.

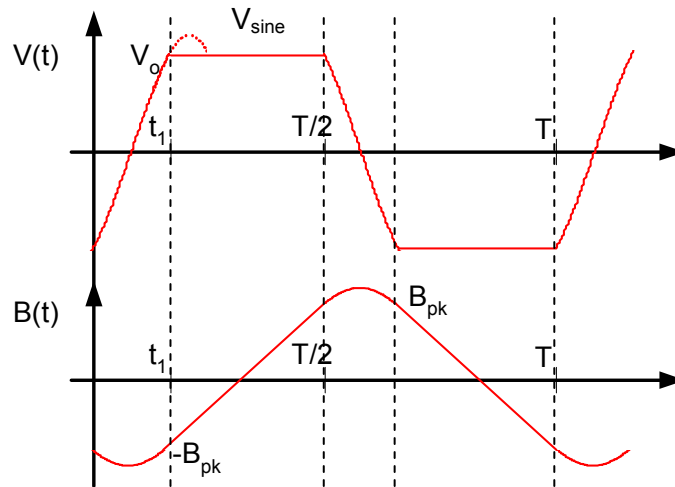


Fig. 3-3 Voltage and flux of the transform under a simplified STS waveform

To express the voltage waveform, we need to know the crossing-over moment of the sine and linear parts, t_1 , first. The value of t_1 can be obtained as:

$$t_1 = \frac{\arcsin\left(\frac{V_0}{V_{\text{sine}}}\right)}{\pi \cdot f_{\text{sine}}} \quad (3-15)$$

Segments of the voltage waveform are expressed in (3-16), and the corresponding flux density waveform, in the core with the cross-section area of A_c and nI turns of winding on it, can be derived as in (3-17).

$$V(t) = \begin{cases} V_{\sin e} \sin \left[\omega_{\sin e} \left(t - \frac{t_1}{2} \right) \right] & [0, t_1) \\ V_o & \left[\frac{t_1}{2}, \frac{T}{2} \right) \\ -V_{\sin e} \sin \left[\omega_{\sin e} \left(t - \frac{(t_1 + T)}{2} \right) \right] & \left[\frac{T}{2}, \frac{T}{2} + t_1 \right) \\ -V_o & \left[\frac{T}{2} + t_1, T \right) \end{cases} \quad (3-16)$$

$$B(t) = \frac{1}{nI \cdot Ac} \begin{cases} \frac{-V_{\sin e}}{\omega_{\sin e}} \cos \left[\omega_{\sin e} \left(t - \frac{t_1}{2} \right) \right] + \frac{V_{\sin e}}{\omega_{\sin e}} \cos \left(\frac{\omega_{\sin e} t_1}{2} \right) + \frac{V_o}{2} \left(t_1 - \frac{T}{2} \right) & [0, t_1) \\ V_o t - \frac{V_o}{2} \left(t_1 + \frac{T}{2} \right) & \left[\frac{t_1}{2}, \frac{T}{2} \right) \\ \frac{V_{\sin e}}{\omega_{\sin e}} \cos \left[\omega_{\sin e} \left(t - \frac{(t_1 + T)}{2} \right) \right] - \frac{V_{\sin e}}{\omega_{\sin e}} \cos \left(\frac{\omega_{\sin e} t_1}{2} \right) - \frac{V_o}{2} \left(t_1 - \frac{T}{2} \right) & \left[\frac{T}{2}, \frac{T}{2} + t_1 \right) \\ -V_o t + \frac{V_o}{2} \left(t_1 + \frac{3T}{2} \right) & \left[\frac{T}{2} + t_1, T \right) \end{cases} \quad (3-17)$$

From equation (3-17), we can find out the maximum flux density as expressed in (3-18). It is important to know the maximum flux density, since we want to compare the core loss calculation for different STS waveforms that present the same maximum flux density.

$$B_{pk} = \left| \frac{1}{nI \cdot Ac} \left[-\frac{V_{\sin e}}{\omega_{\sin e}} + \frac{V_{\sin e}}{\omega_{\sin e}} \cos \left(\frac{\omega_{\sin e} t_1}{2} \right) + \frac{V_o}{2} \left(t_1 - \frac{T}{2} \right) \right] \right| \quad (3-18)$$

Where, nI is the number of winding turns on the core, and Ac is the cross-section area of the core. For simplicity, both of them are set to unit here. Also the magnetic length and core volume of the core are set to unit, so the calculated core loss density is directly compared. We first let the ratios, $\frac{V_o}{V_{\sin e}} = 1$ and $\frac{f_0}{f_{\sin e}} = 1$, so we get a sine wave. As the $f_{\sin e}$ increases, we will have waveforms close to square wave, and it is necessary to reduce the ratio $\frac{V_o}{V_{\sin e}}$ to keep B_{pk} the same, as illustrated in Fig. 3-4.

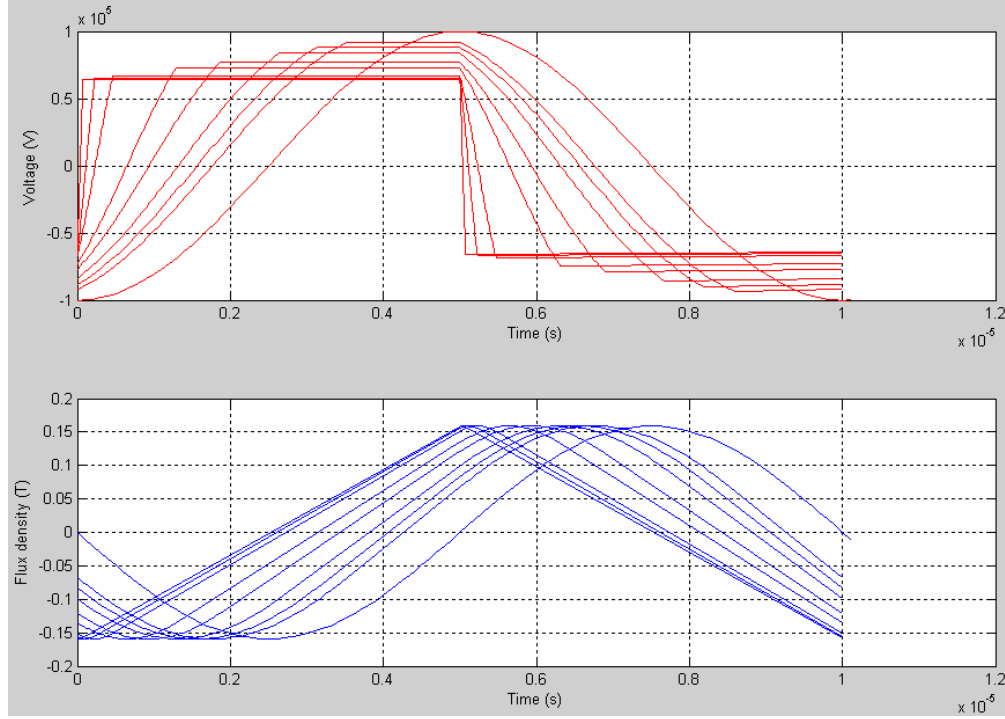


Fig. 3-4 STS waveform with different shape and same peak flux level

The proposed WcSE method is applied to these waveforms to calculate the core loss, and the results are compared with the ones obtained by MSE and GSE. For MSE, the equivalent frequency is calculated according to equation (3-19). For GSE, the coefficient K1 is calculated according (3-10).

$$f_{eq} = \frac{1}{2\pi^2} \cdot \frac{V_{\sin e}^2 \cdot t_1 - V_{\sin e}^2 \frac{\sin(2\omega_{\sin e} t_1)}{2\omega_{\sin e}} + V_o^2 (T - 2t_1)}{\left[-\frac{V_{\sin e}}{\omega_{\sin e}} + \frac{V_{\sin e}}{\omega_{\sin e}} \cos\left(\frac{\omega_{\sin e} t_1}{2}\right) + \frac{V_o}{2} \left(t_1 - \frac{T}{2}\right) \right]^2} \quad (3-19)$$

Then, core loss densities (in mW/cm³) are calculated for certain magnetic material, which has the Steinmetz coefficient as: $K = 0.0434$, $\alpha = 1.63$, and $\beta = 2.62$. The result comparison is plotted in Fig. 3-5. Here, all calculated losses are normalized to the value due to the sinusoidal waveform. As mentioned previously, $\frac{f_0}{f_{\sin e}} = 1$ means sinusoidal waveform, and $\frac{f_0}{f_{\sin e}}$ decrease when the STS waveform changes toward square waveform.

The equivalent frequency of the MSE method, according to (3-19), is calculated for the STS waveform. The ratio of $\frac{f_{eq}}{f_0}$ is plotted in Fig. 3-6. The result shows that the equivalent frequency does not monotonically decrease as the STS waveform comes close to the square shape. There is a sharp change when the waveform shape approaching sinusoidal, which means that the core loss would jump when the waveform shape has a tiny variation from the sinusoidal. Since the equivalent frequency is derived purely based on waveform shape, and has nothing to do with magnetic material loss characteristics, a monotonic change would be expected for a set of gradually changed waveforms.

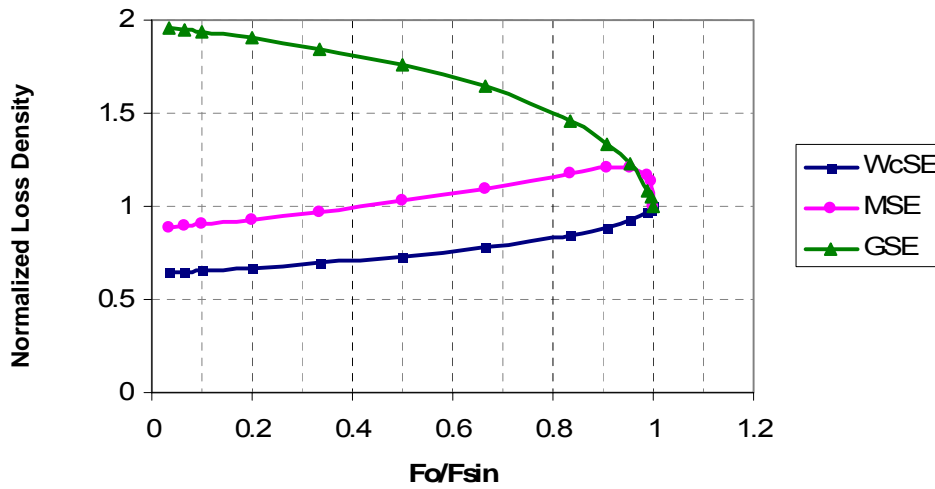


Fig. 3-5 Loss calculated by different methods for the STS waveforms

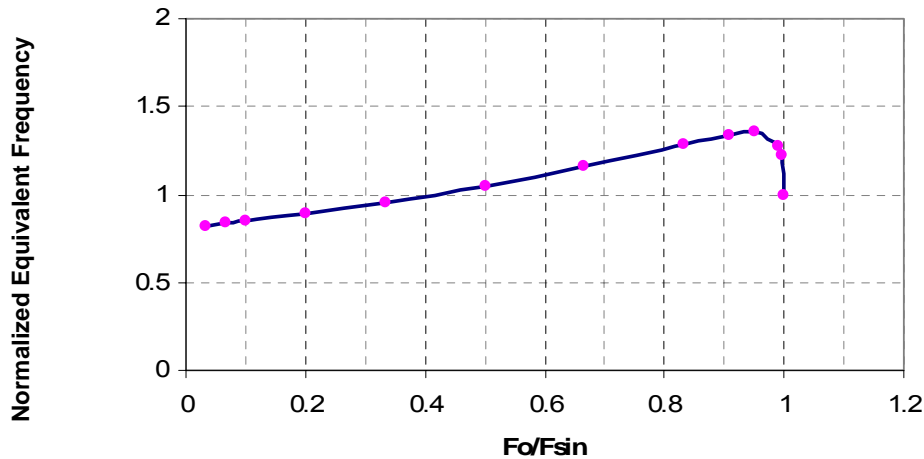


Fig. 3-6 Calculated equivalent frequency by MSE for the STS waveforms

It is clear that the core loss reduces, as the waveform becomes more like a square shape. WcSE predicts a monotonic reduction in the core loss, while the GSE shows incremental trends and MSE has the maximum core loss happening somewhere in between.

c) Parallel resonant converter (PRC) operation waveform verification

With the proposed method, we can calculate the core loss of a transformer operating in a parallel resonant converter (PRC) with a capacitor filter as a case study. The waveform for a transformer for this case is similar to the waveform constructed above, and they are both a kind of “sinusoidal transition square” waveform. The circuit is shown in Fig. 3-7, and the detailed operation of the converter can be found in reference [3-22]. We can find the expression of the voltage waveform that is applied on the transformer [3-13].

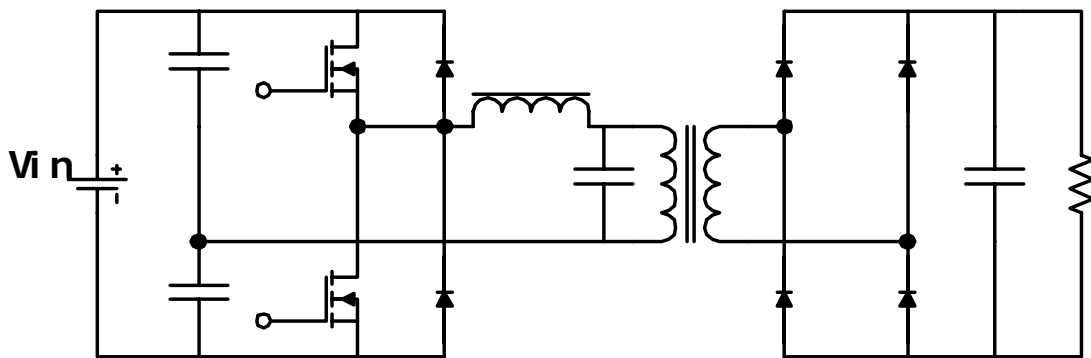


Fig. 3-7 The PRC system for studying

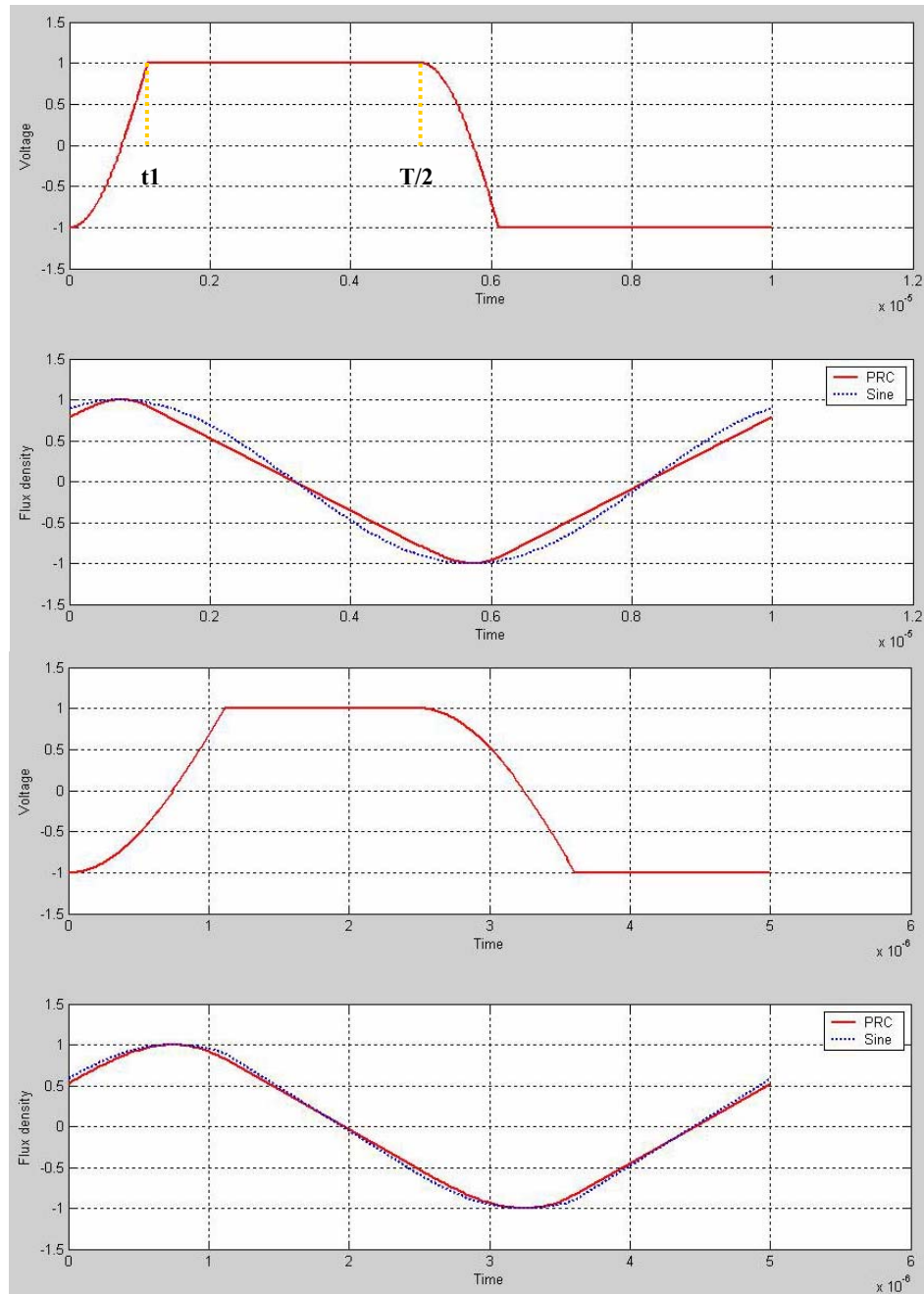


Fig. 3-8 The transformer waveform of PRC with capacitor filter

In Fig. 3-8, the normalized voltage and flux waveforms of the capacitive output filter PRC are shown for a different ratio between the resonant frequency and switching frequency. Also, the flux density waveforms are compared with the sinusoidal one with the same peak value, and it is clear that the PRC waveform is going to induce less core loss than sinusoidal waveforms.

$$V(t) = \begin{cases} V_g - (V_g + V_o) \cdot \cos(\omega_o t) & [0, t_1) \\ V_o & [t_1, T/2) \\ -V_g + (V_g + V_o) \cdot \cos\left(\omega_o\left(t - \frac{T}{2}\right)\right) & [T/2, T/2 + t_1) \\ -V_o & [T/2 + t_1, T) \end{cases} \quad (3-20)$$

Where V_g is half of the input voltage, V_o is the output voltage reflected back to the primary side, f_o is the resonant frequency, and $1/T$ is the switching frequency. The clamping time t_1 can be determined as:

$$t_1 = \frac{\arccos\left(\frac{V_g - V_o}{V_g + V_o}\right)}{\omega_o} \quad (3-21)$$

Similarly, the flux density by this exciting voltage can be derived as:

$$B(t) = \frac{1}{n1 \cdot Ac} \begin{cases} V_g t - \frac{V_g + V_o}{\omega_o} \sin(\omega_o t) - \frac{1}{2} \left[V_g t_1 - \frac{V_g + V_o}{\omega_o} \sin(\omega_o t_1) - V_o \left(t_1 - T/2 \right) \right] & [0, t_1) \\ V_o t + \frac{1}{2} \left[V_g t_1 - \frac{V_g + V_o}{\omega_o} \sin(\omega_o t_1) - V_o \left(t_1 + T/2 \right) \right] & [t_1, T/2) \\ -V_g t + \frac{V_g + V_o}{\omega_o} \sin\left(\omega_o\left(t - \frac{T}{2}\right)\right) + \frac{1}{2} \left[V_g t_1 - \frac{V_g + V_o}{\omega_o} \sin(\omega_o t_1) - V_o \left(t_1 - T/2 \right) \right] + V_g \cdot \frac{T}{2} & [T/2, T/2 + t_1) \\ -V_o t - \frac{1}{2} \left[V_g t_1 - \frac{V_g + V_o}{\omega_o} \sin(\omega_o t_1) - V_o \left(t_1 + 3T/2 \right) \right] & [T/2 + t_1, T) \end{cases} \quad (3-22)$$

The maximum flux density happens at the moment of $\frac{dB(t)}{dt} = V(t) = 0$, which is

$$t_{B_{pk}} = \frac{\arccos\left(\frac{V_g}{V_g + V_o}\right)}{\omega_o}. \text{ So the peak flux density can be found as:}$$

$$B_{pk} = \left| \frac{1}{n1 \cdot Ac} \left[V_g t_{B_{pk}} - \frac{V_g + V_o}{\omega_o} \sin(\omega_o t_{B_{pk}}) - \frac{1}{2} \left[V_g t_1 - \frac{V_g + V_o}{\omega_o} \sin(\omega_o t_1) - V_o \left(t_1 - T/2 \right) \right] \right] \right| \quad (3-23)$$

d) The WcSE method validation discussion

All the above discussions are about the fixed duty cycle waveforms (D=0.5), which are true for variable frequency controlled resonant converters. There are still a large number of high-frequency, high-power applications using PWM phase shift

operations, and the voltage waveform applied to the transformer then is variable duty cycle square wave. The waveform shown in Fig. 3-9 will be seen by the transformer.

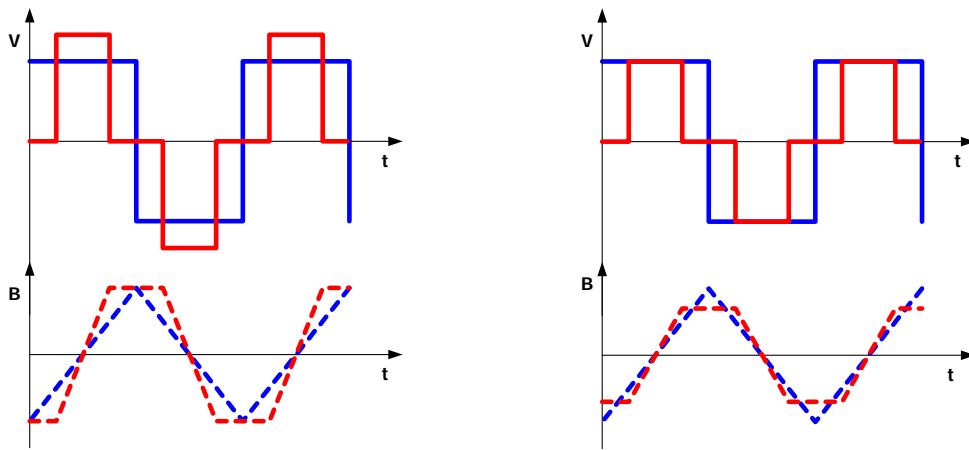


Fig. 3-9 Variable duty cycle quasi-square voltage and corresponding flux waveforms

If the peak flux density levels are kept the same during the comparison, we can easily conclude that the minimum core loss happens at $D = 0.5$, and increases as the duty cycle reduces. This phenomenon has been verified by many previous studies and experimental measurement. In the real converter operation, the rail voltage level is kept constant while the duty cycle is changed, so the peak flux density in the core is not kept the same anymore. The proposed WcSE method can still give a very explicit prediction whether the core loss is bigger or smaller than the case of $D = 0.5$.

If the soft-switching detailed waveform is included, WcSE can efficiently predict the corresponding core loss, through the explicit process. However, other methods like GSE and MSE will be too cumbersome to be applicable. This is the major advantage of the proposed WcSE method.

The application of the WcSE requires no minor loop appearing, which could be caused by overshooting in the circuit and resonant operation. It is still possible to isolate the effect of minor loops by estimating it separately.

3.2. Core loss measurement and verification

The core loss measurement has been challenging [3-14]-[3-16], especially for frequencies higher than tens of kilohertz and non-sinusoidal waveforms. The main reason for the difficulty is that we have to excite the core and measure the voltage and current

through the winding wound onto the DUT core. Flux density inside the core can only be calculated from the induced voltage through integration, so the leakage flux would cause an error. The biggest problem is still the loss measurement, which is under an almost 90 degree phase angle between the voltage and current. Therefore, the thermal measurement, or indirect measurement, has been proposed as the alternative way to the electrical measurement, whose typical setup is shown in Fig. 3-10. The fundamental principle of the thermal measurement is to have a precise indication of the heat flow out of the excited core, which should be put into a certain chamber with good heat insulation. It is clear that the thermal measurement method introduces a complicated apparatus structure, which basically transfers the error due to probes and oscilloscopes into one of heat leakage and thermal control units.

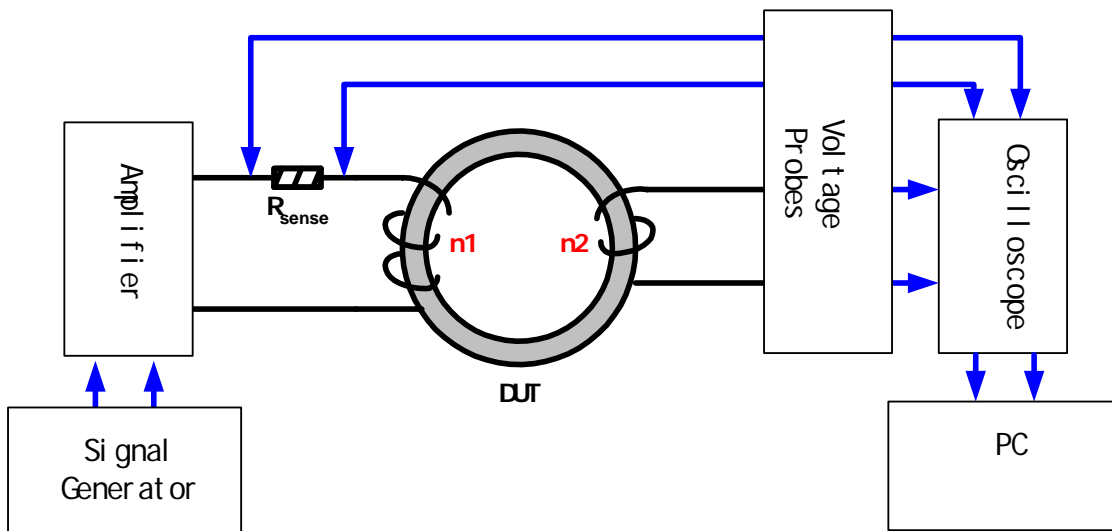


Fig. 3-10 The electrical core loss measurement setup

It is probably the only choice if we want to measure the core loss for very high frequencies above a mega-hertz. For the digital oscilloscope with a sampling frequency of 500 MHz, we still use the electrical method to measure the core loss for the special resonant operation waveforms of below 1 MHz. In the following section, the error and limitation of the electrical measurement method will be discussed.

3.2.1. Error analysis

Errors of the electrical core loss measurement would confine the applicable frequency range of the method. For power frequency or range below kilo hertz, the electrical measurement has been used and proven accurate [3-23]. However, our interests

focus on frequency above the hundred kilo hertz, so we need to be careful with the error analysis. There are several sources bringing errors to the measurement results, and they will be identified and analyzed separately [3-17].

a) *Oscilloscope accuracy*

A Tektronix TDS7104 digital oscilloscope is used for the test. It has an 8-bit ADC, and 11-bit accuracy with averaging mode. So, we assume the voltage measurement error is $\delta = 2^{-11} = 0.49\%$ at full scale. Therefore, the relative error of the worst case loss due to the voltage measurement is given by (3-24), which is less than 1% for the test results by the oscilloscope.

$$\left| \frac{\Delta P_{loss}}{P_{loss}} \right| = \left| \frac{\frac{N1}{N2} \cdot \frac{1}{M} \sum_{i=1}^M V_{li} \cdot (1 \pm \delta) \cdot \frac{V_{2i} \cdot (1 \pm \delta)}{R_{sense}}}{\frac{N1}{N2} \cdot \frac{1}{M} \sum_{i=1}^M V_{li} \cdot \frac{V_{2i}}{R_{sense}}} - 1 \right| = \left| (1 \pm \delta)^2 - 1 \right| \approx 2\delta \quad (3-24)$$

Besides the vertical error, there are time delay errors, which could be introduced by the differences between channels, the sensing resistor parasitic inductance, and so on. The tiny time difference could cause significant loss errors, due to the power factor angle $\theta \approx 90^\circ$. The analysis is shown here to quantify the impact on the final measurement result. The loss calculation under sinusoidal waveforms is expressed in (3-25), with θ representing the phase angle between voltage and current channels.

$$P_{loss} = \frac{N1}{N2} \cdot \frac{1}{M} \sum_{i=1}^M V_{1-pk} \cos(\omega t_i) \cdot \frac{V_{2-pk} \cos(\omega t_i + \theta)}{R_{sense}} \quad (3-25)$$

If some errors, $\Delta\theta$ is introduced into the measured phase angle between the voltage and current channels. Then the incremental loss due to this error can be calculated as:

$$\Delta P_{loss} = \frac{\partial P_{loss}}{\partial \theta} \cdot \Delta\theta \quad (3-26)$$

After putting (3-25) into (3-26), we can have the relative loss error as

$$\left| \frac{\Delta P_{loss}}{P_{loss}} \right| = \left| \frac{\Delta\theta \cdot \sum_{i=1}^M [\cancel{\cos(\omega t_i)} - \sin(\omega t_i) \cdot \cos \theta + \cos(\omega t_i) \cdot \cos(\omega t_i) \cdot \sin \theta]}{\sum_{i=1}^M [\cos(\omega t_i) \cdot \cos(\omega t_i) \cdot \cos \theta - \cancel{\cos(\omega t_i)} - \sin(\omega t_i) \cdot \sin \theta]} \right| = \Delta\theta \cdot \tan \theta \quad (3-27)$$

This means the relative error is a function of the absolute angle difference multiplied by the tangent of the power factor angle. The error is bigger for the same angle

difference when θ approaches 90 degree, which means the smaller core loss density of the certain magnetic material is, the poorer the accuracy of the loss measurement of the material. Another issue is that the absolute value of $\Delta\theta$ increases proportionally as the measured frequency increases, for about the same amount of time difference.

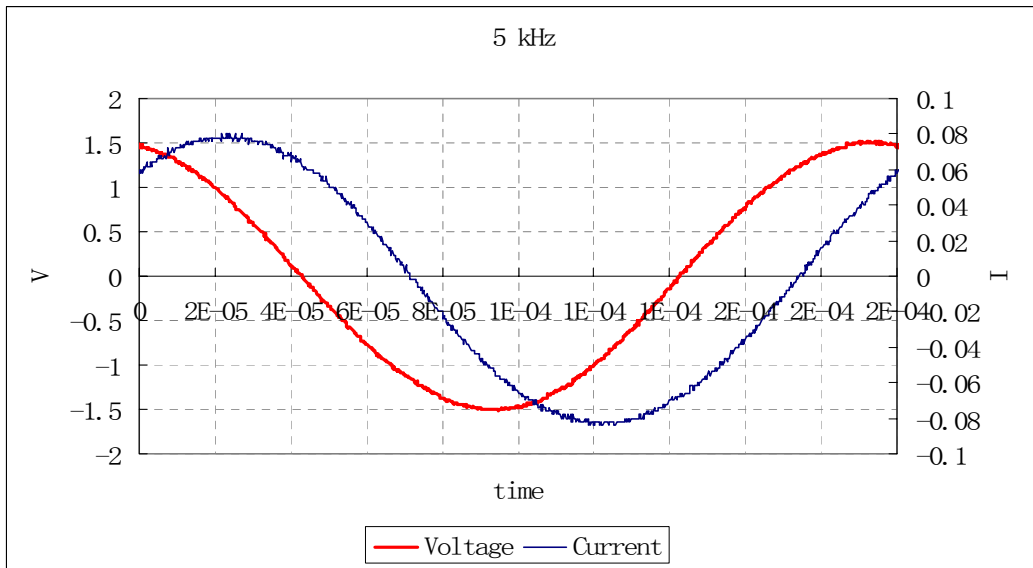
$$\Delta\theta = 360 \cdot \delta t \cdot f \tag{3-28}$$

However, the loss density will increase as the frequency increases for the magnetic material, which means the values of θ and $\tan\theta$ decrease. Therefore, the particular frequency limitation for a certain magnetic material should be determined by examining the results carefully. In Fig. 3-11, measurement results of voltage current for the nanocrystalline material are shown. The value of the power factor angle is about 50 degrees at a 5 kHz core loss measurement, so the allowed time difference for a 1% loss accuracy can be calculated according to (3-27) and (3-28).

$$\delta t \leq \frac{0.01}{\tan 50^\circ \cdot 360 \cdot 5000} = 4.7ns \tag{3-29}$$

Similarly, the power factor angle is about 20 degrees for the 500 kHz measurement. We can obtain the maximum allowed absolute time error for 1% accuracy as:

$$\delta t \leq \frac{0.01}{\tan 20^\circ \cdot 360 \cdot 500000} = 153ps \tag{3-30}$$



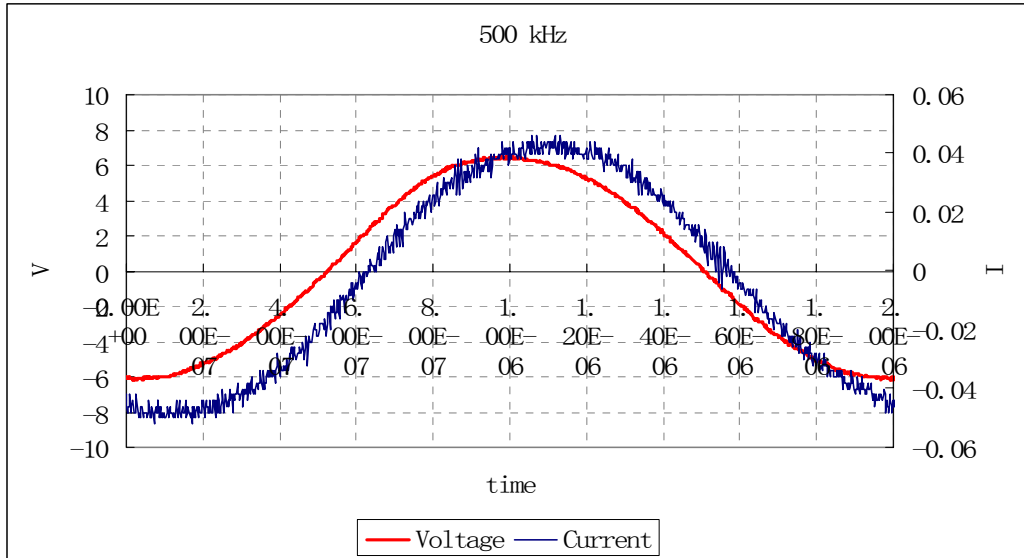


Fig. 3-11 The measured voltage and current under different frequencies

The oscilloscope has a trigger jitter that is typically at 8 ps, and the probe and channel difference can be calibrated. If we can control the phase angle introduced by the ESL of the sensing resistor to less than 0.02 degree, we achieve a 1% accuracy for the measurement up to 500 kHz. A possible low ESL sensing resistor candidate could be the one with 1 Ohm and 0.1 nH. The detailed calculation can just follow the above equations.

b) Winding loss

Apparently, the measured loss consists of a core loss and a winding loss, which is caused by magnetizing the current and winding resistance. Since both of them are inevitable to any measurement, we need to reduce the winding resistance. For all the tests conducted in this work, we use a Litz wire of 60*AWG38 for both all windings. Actually, the resistance of the winding wound on a wood bobbin with the same cross-section as the DUT core has been measured by the impedance analyzer.

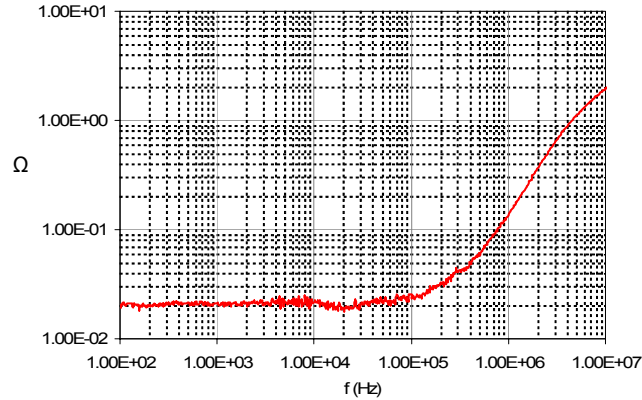


Fig. 3-12 The core loss measurement winding resistance

The resistance value is $43 \text{ m}\Omega$ at 500 kHz . So, the winding loss is 0.43 mW for the 100 mA exciting current, and the measured total loss is 252.6 mW at this flux level. The winding loss is only about 0.17% of the total measured loss. Anyway, the amount of the winding loss can always be subtracted from the measured total loss, for any frequency and exciting level.

c) *Winding parasitic effects*

Up to this stage, parasitics in the windings are not included in the analysis yet. This could be a limitation to extend the measurement method to high frequency. If non-sinusoidal waveforms are studied, the parasitic effect could loom and degrade the result accuracy, even for a relatively low frequency. Therefore, the winding leakage inductance and capacitance are included in the equivalent circuit, as shown in Fig. 3-13. All of parasitic values can be extracted from small signal measurement by the impedance analyzer.

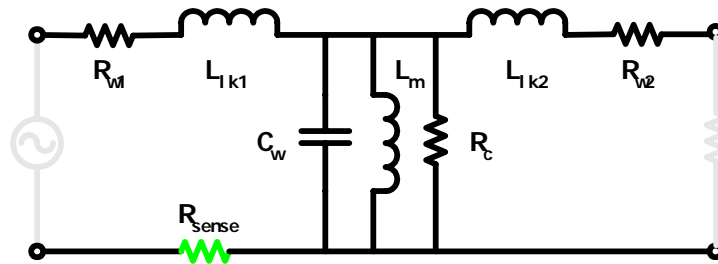


Fig. 3-13 The equivalent circuit of the core loss measurement setup

Actually, the measured loss is affected by the parasitics even under sinusoidal sources. If we apply a square waveform to the primary winding, the voltage and current

waveform are compared with the ones from the ideal circuit, in Fig. 3-14. Here, the winding parameters are assumed as: $L_{lk1} = L_{lk2} = 100nH$, $R_{w1} = R_{w2} = 100m\Omega$, $L_m = 60\mu H$, $C_w = 30pF$, and $R_c = 3000\Omega$ for 1 MHz square wave source. The distortion on both the current and voltage waveforms can be observed. Due to the hysteresis effects of the magnetic core, these overshootings would result in minor loops if we draw the B/H loops of the simulated waveforms. The measured core loss does not reflect the expected peak flux density value and the operating frequency only, for these minor loops cause extra losses.

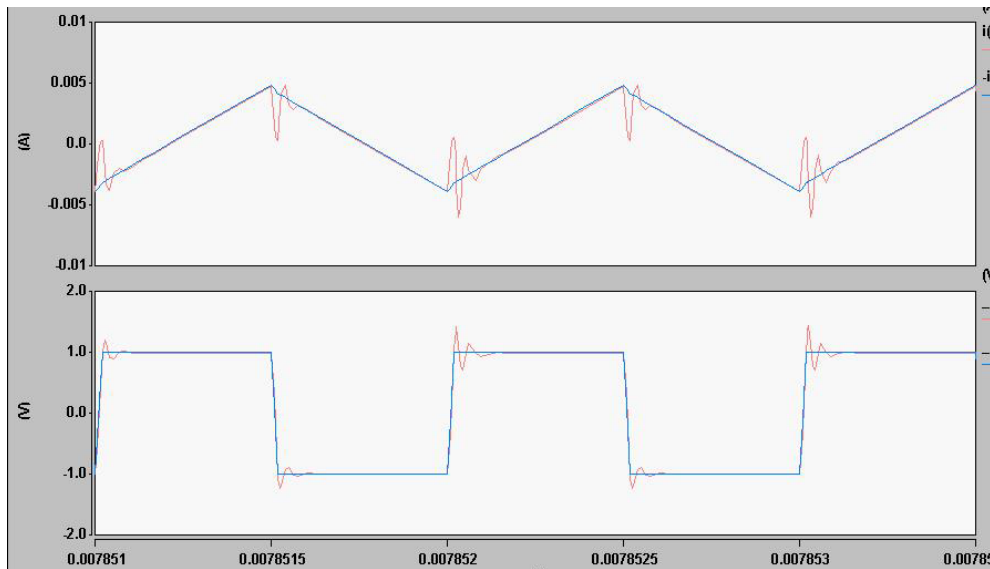


Fig. 3-14 Simulated current (top) and voltage (bottom) waveforms w/wo parasitics

Conclusively, we want the parasitic as small as possible. Reducing winding turns, improving coupling, and choosing a Litz wire would help to extend the measurement to the high frequency range. Because the real winding parasitics are much smaller than the assumed values above, our test results can be accurate up to 500 kHz.

3.2.2. Loss verification for STS waveforms

With the clear understanding of the limitation and error physics of the measurement method, we can perform the loss verification experiments using the setup shown in Fig. 3-10. Our first goal is to measure the core loss under the constructed STS waveforms, so we have to find the way to generate the dedicated waveform. So the generated waveform would be applied to the magnetic core through an amplifier. The function generator is the ideal candidate.

a) *Generating arbitrary waveforms*

To apply the interested STS waveform to a DUT core, we need to have the waveform generator, and then feed them to a wide bandwidth power amplifier. For the HP 33120a function generator, which has the capability of editing and downloading arbitrary waveform, we just create the desired STS waveform in Matlab, and transfer the data into the function generator through RS232 connection. The detailed programs are listed in *Appendix I*.

You can download between 8 and 16,000 points per waveform. The waveform can be downloaded as floating-point values or binary integer values. Use the DATA VOLATILE command to download floating-point values between -1 and +1. The downloaded waveform data is stored in the volatile memory, and will disappear after turning off the generator. Total 4 waveforms can be stored into the non-volatile memory of the function generator, so these four user-defined waveforms can be retracted any time through the arbitrary waveform list. When the waveform is selected as output, the frequency and amplitude parameters can be set to define the details of the waveform.

To connect the function generator to a computer or terminal, you must have the proper interface cable. Most computers and terminals are DTE (Data Terminal Equipment) devices. Since the function generator is also a DTE device, you must use a DTE-to-DTE interface cable. These cables are also called null-modem, modem-eliminator, or crossover cables. The interface cable must also have the proper connector on each end and the internal wiring must be correct. Connectors typically have 9 pins (DB-9 connector) or 25 pins (DB-25 connector) with a “male” or “female” pin configuration. A male connector has pins inside the connector shell and a female connector has holes inside the connector shell.

We connect the function generator to the RS-232 interface using the 9-pin (DB-9) serial connector on the rear panel. The function generator is configured as a DTE (Data Terminal Equipment) device. For all communications over the RS-232 interface, the function generator uses two handshake lines: DTR (Data Terminal Ready) on pin 4 and DSR (Data Set Ready) on pin 6. Configure the RS-232 interface using the parameters shown below. Use the front-panel I/O MENU to select the baud rate, parity, and number of data bits.

- * Baud Rate: 300, 600, 1200, 2400, 4800, or 9600 baud (factory setting)
 - * Parity and Data Bits: None / 8 data bits (factory setting), Even / 7 data bits, or Odd / 7 data bits
 - * Number of Start Bits: 1 bit (fixed)
 - * Number of Stop Bits: 2 bits (fixed)
- b) *STS waveform loss measurement*

The generated STS waveforms are shown in Fig. 3-15. The amplitude of the waveform is set to make the flux density induced the same. Here repetitive frequency is 100 kHz, and the pure sine waveform peak value is set to 1 V. These waveforms are fed into the wide-band amplifier, and then applied to the DUT core winding.

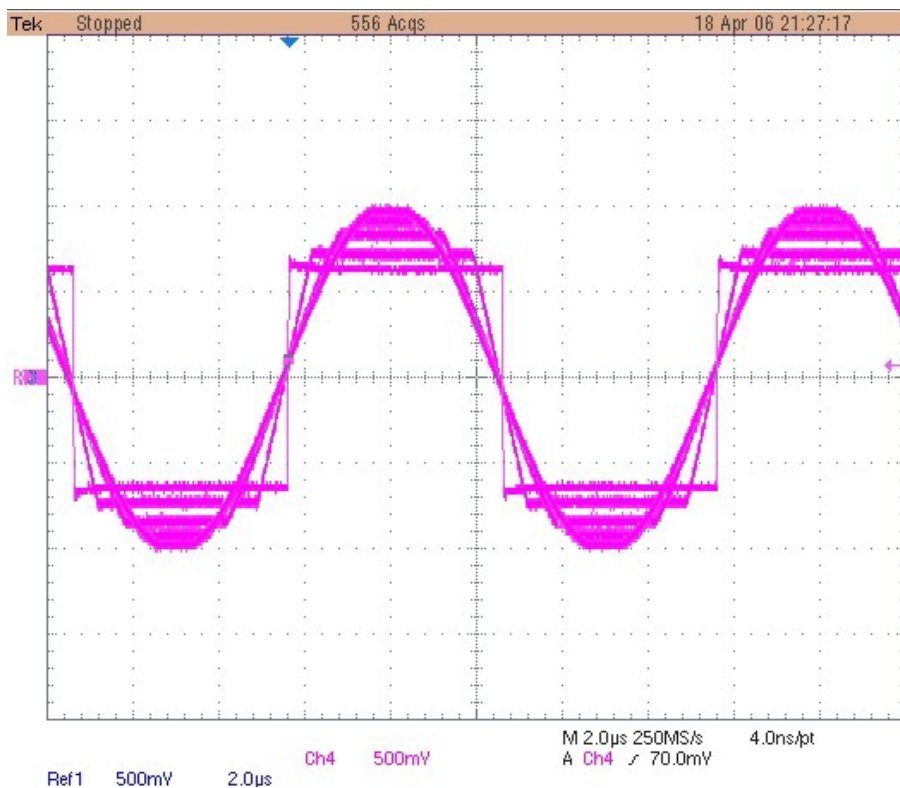


Fig. 3-15 Generated STS waveforms (100 kHz)

During the measurement, the core temperature is monitored and controlled at 25 °C. By using the electrical method discussed above, we can obtain the core loss density of the nanocrystalline material under the STS waveform excitation. From the result shown in Fig. 3-16, it is clear that the core loss decreases gradually as the waveform shape changes from sine to square gradually.

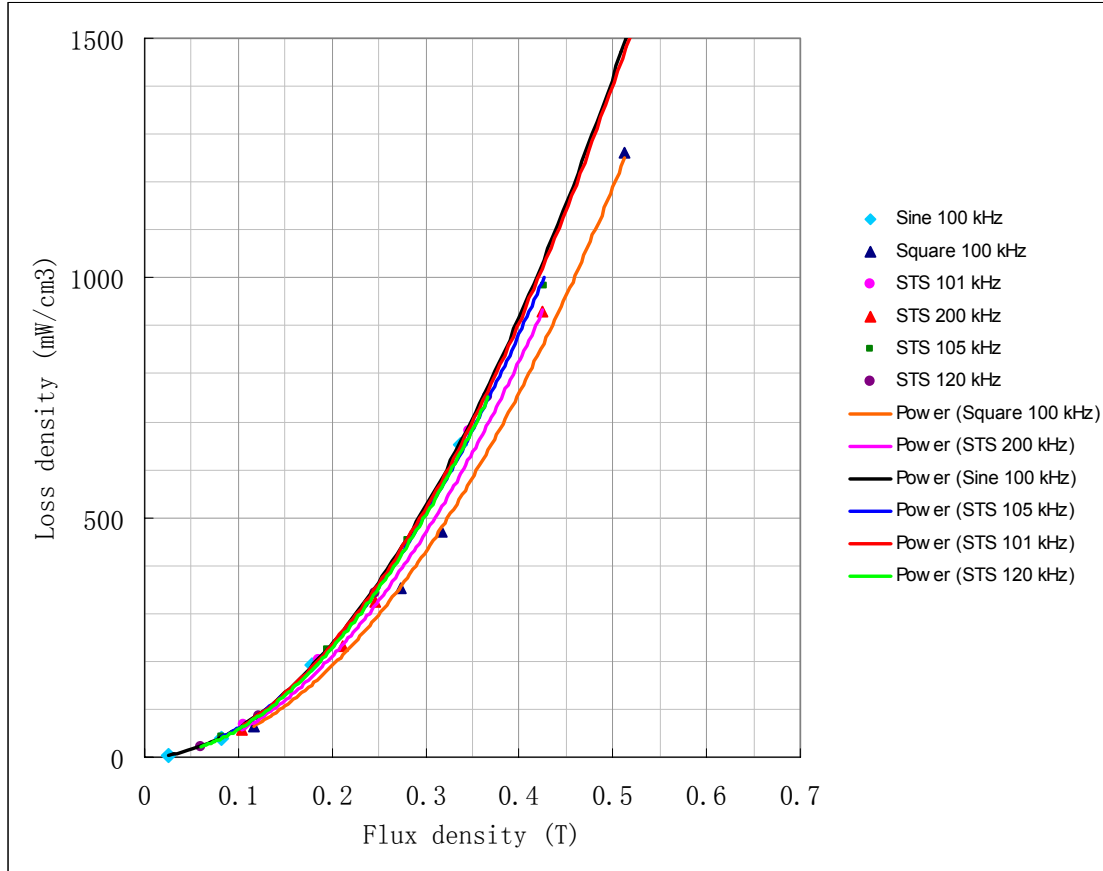


Fig. 3-16 Core loss density of FT-3M nanocrystalline under STS waveforms (100 kHz)

To observe the trend clearly, we read all core loss density values at 0.4 Tesla, and then they are plotted verse the frequency ratio $\frac{f_0}{f_{sine}}$ as shown in Fig. 3-17. The similar relationship can be observed for the other flux density values. For the gradually changed STS waveforms, the core loss decrease should be monotonic. Compared with the calculated result shown in Fig. 3-5, the measured core losses match with the result by the proposed WcSE method only. MSE predicts some peak values, which are not found in the measurement. GSE shows the totally wrong trend, which shows the core loss by square waveform is higher the sine waveform.

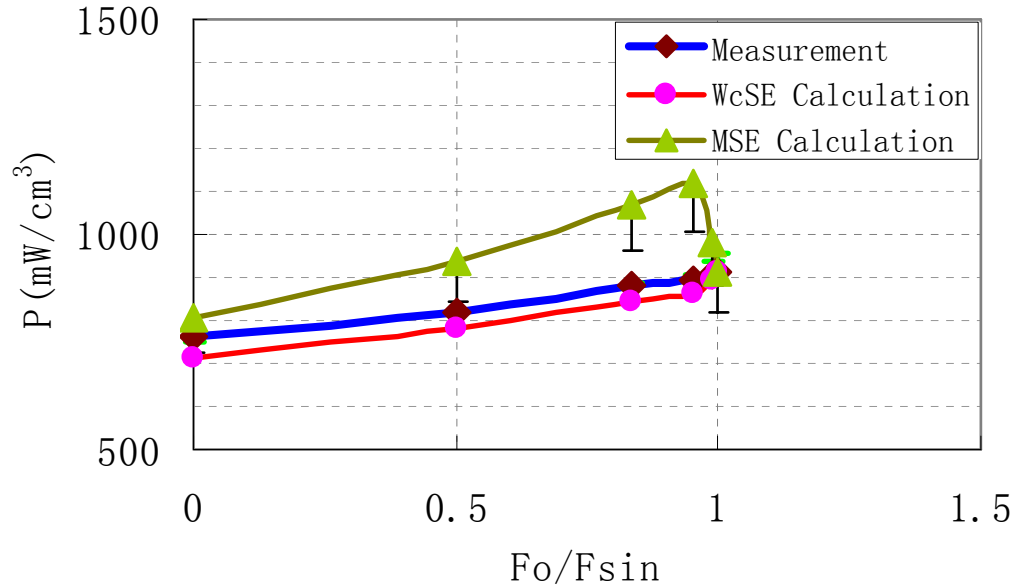


Fig. 3-17 Measured and calculated Core loss density of under STS waveforms (100 kHz and 0.4 T)

The proposed WcSE method predicts the loss closer to the measurement result when compared with the other two methods. Therefore, the WcSE method will be applied to the real waveform of the PRC with a capacitive filter converter system.

Besides the STS waveforms, the triangular and saw-tooth waveforms have been applied to the DUT core for core loss measurement. Different excitation levels are conducted, and the corresponding core loss density can be obtained and compared with the value of sine waveform, which is shown in Fig. 3-19. The measured core loss by the triangular waveform is about 5% higher, compared with the sine waveform results, and this is exactly the WcSE prediction, $\frac{\pi}{3}$. Similarly, the saw-tooth kind waveforms are also investigated, and the result shows the convergence of the WcSE method. Therefore, the measurement verification has shown the accuracy of the proposed WcSE method. Together with its explicit derivation, this method is quite suitable to the applications have soft-switching and resonant waveforms. However, it is not confined to the STS type waveform, it is also applicable to PWM waveforms.

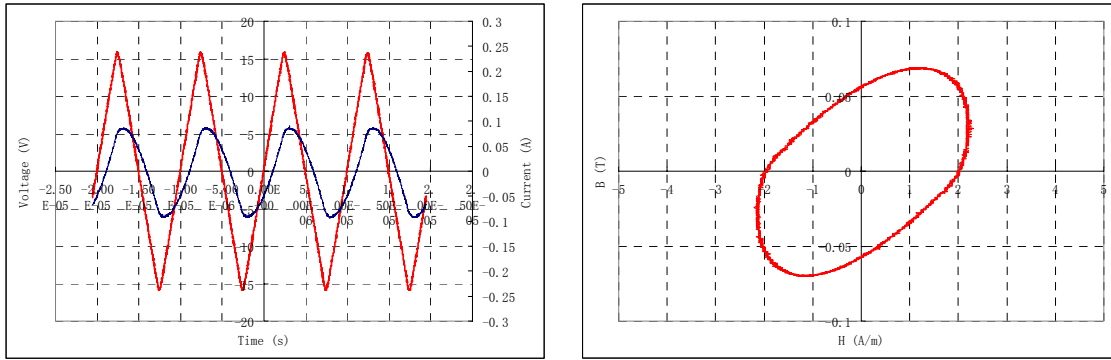


Fig. 3-18 Measured voltage and current for triangle excitation (100 kHz) (left) and the corresponding B/H curve (right)

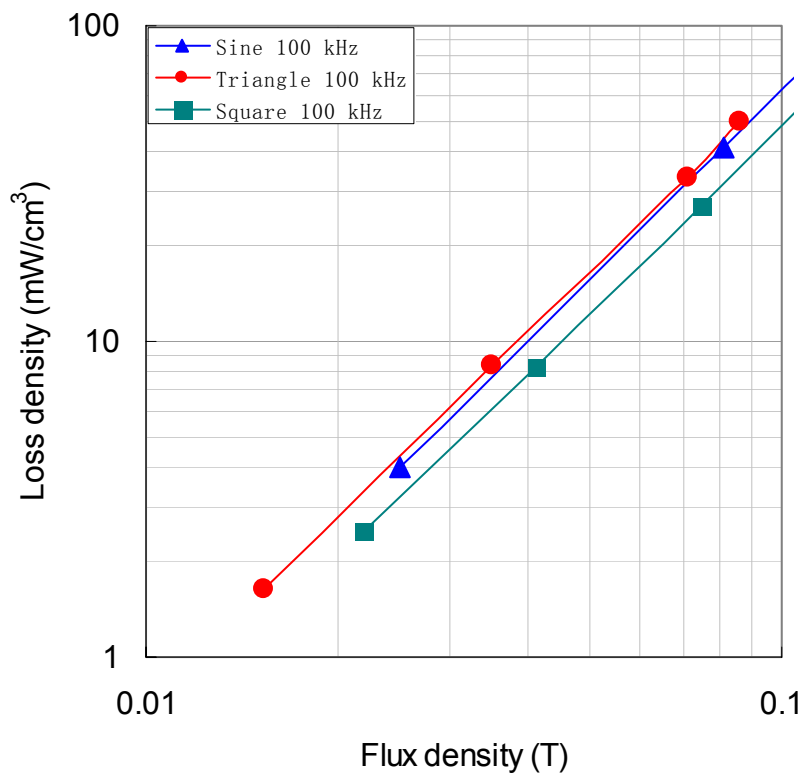


Fig. 3-19 Measured core loss density for triangle, square, and sine waveforms (100 kHz)

c) *PRC waveform core loss measurement*

The analyzed waveform of the PRC converter with capacitive filter is shown in Fig. 3-8. The same waveforms have been put into the function generator by the method introduced above. The waveform reflects the ratio of resonant frequency to switching frequency and input voltage to output voltage, but they are normalized during the realization of the waveform. The realized waveforms are shown in Fig. 3-20.

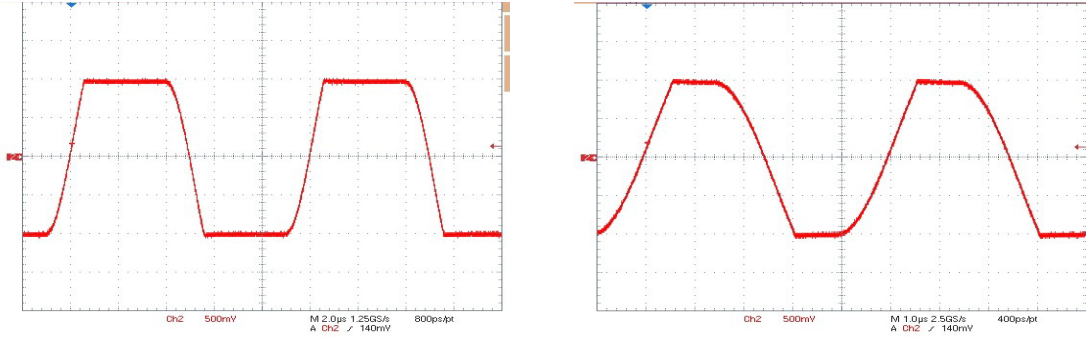


Fig. 3-20 Transformer waveform for the PRC circuit with resonant frequency 205 kHz and variable switching frequency 100 kHz (left) and 200 kHz (right)

Again, the constructed waveform has been applied to the nanocrystalline core. The measured core loss density is compared with sine and square waveforms with the same repetitive frequency, as shown in Fig. 3-21. As predicted by the WcSE method, the measured core loss of the losses by the PRC waveform locates between sine and square waveforms. The core loss is determined by the waveform shape in detail. However, the calculation method is the same for all of them.

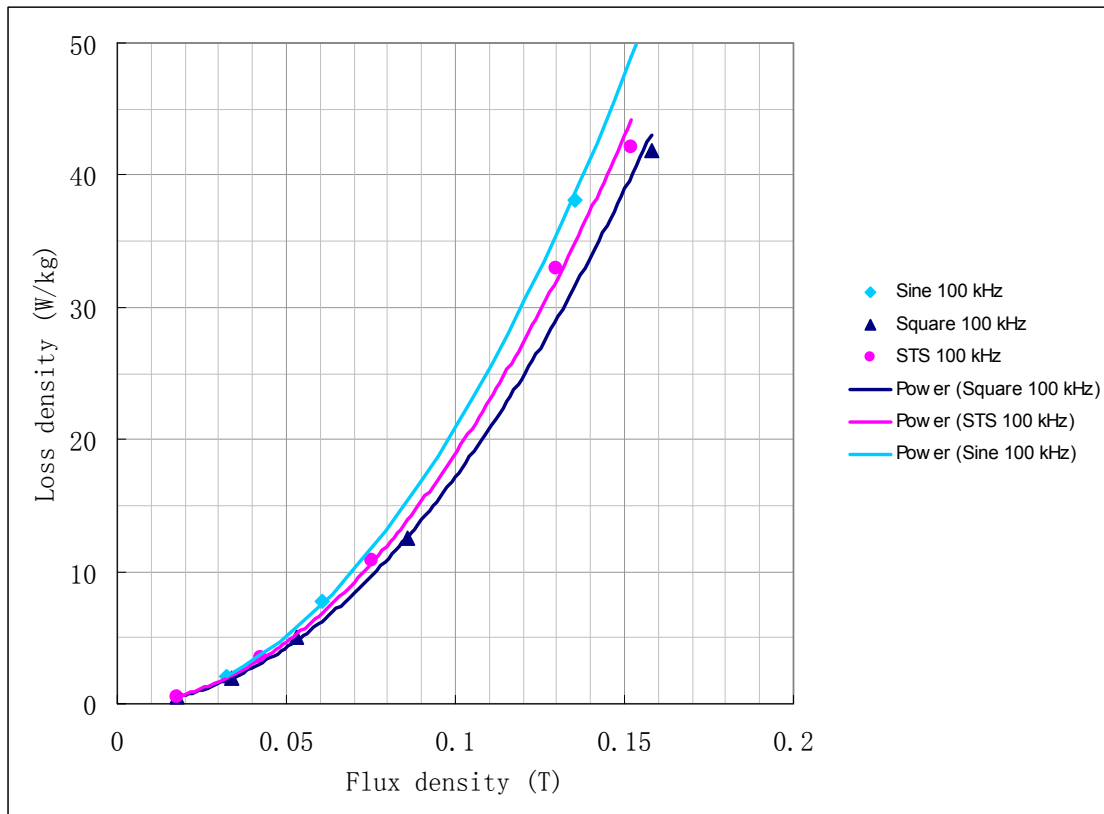


Fig. 3-21 Core loss density of 100 kHz sine, square, and PRC waveforms

We can examine the time domain waveforms of these three different waveforms to get a deeper feeling for the WcSE mechanism. The voltage and current waveforms are shown in Fig. 3-22, and the corresponding B/H loops are shown in Fig. 3-23. For the same flux density peak value, the B/H loop by square waveform has a smaller area enclosed as compared to the one of sine wave. The area by the PRC STS type waveform is in between area values of the sine and square waveforms.

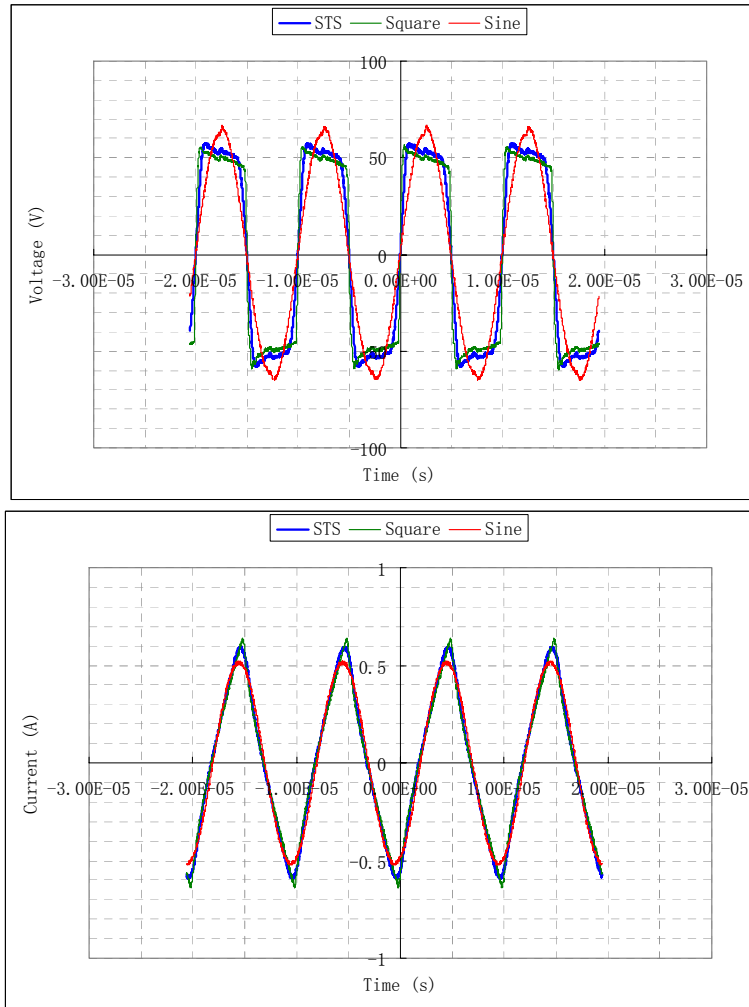


Fig. 3-22 Voltage and current waveforms of 100 kHz sine, square, and PRC waveform

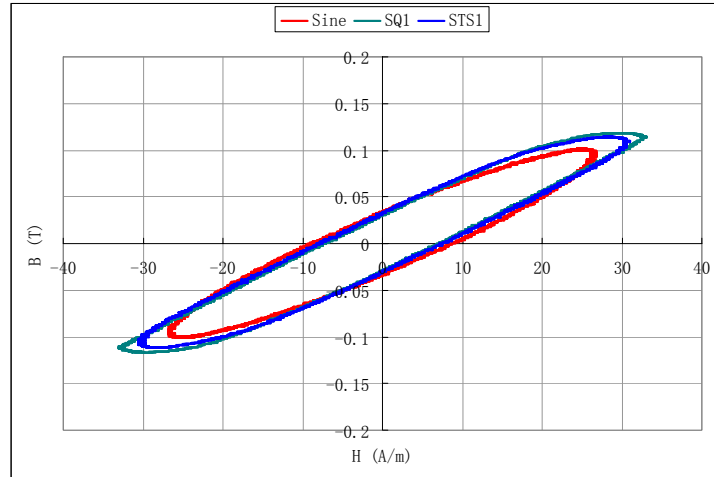


Fig. 3-23 B/H loops of 100 kHz sine, square, and PRC waveforms

3.2.3. Summaries on core loss calculation

The proposed core loss calculation method, WcSE, can predict the core loss by STS type of waveforms and for the nanocrystalline material, which has been verified by experimental results. This is important to soft switching and resonant operation applications, which have the STS type waveform, instead of sine or square waveforms, since both MSE and GSE methods give incorrect results. For high density requirements, the accurate calculation of the core loss would provide the possibility to cut the margin of over-design.

The WcSE method can be conveniently integrated into optimization programs when compared with MSE and GSE methods. The waveform coefficient, as the only change from the original SE, can easily be calculated even instantaneously. For a resonant converter running at variable frequency, the WcSE method can provide the accurate and easy way to calculate core losses.

3.3. Winding loss calculation

The transformer windings are formed by conductors in different shapes of plates, round wires, strand wires, and Litz wires. The resistance of the winding at a low frequency can be easily calculated as the following, with N for turn's number, ρ for conductor resistivity at certain temperature, MLT for mean length per turn, and A_w for conductor cross-section area.

$$R_{DC} = \frac{N \cdot \rho \cdot MLT}{A_w} \quad (3-31)$$

The winding loss is equal to the product of DC resistance and the current RMS square value, if the current waveform is DC or low frequency sinusoidal. However, for high frequency power electronics converter systems, skin and proximity effects cannot be omitted. Both of them change the current distribution inside the conductor, so the resistance is increased when compared with the DC value. Therefore, the challenge of calculating winding loss really means how to count the eddy current effect in the conductor. For an operating frequency above 100 kHz, eddy current losses would be the dominant part of the winding loss.

3.3.1. AC resistance of Litz wire windings

Researchers have been working on this issue continuously. As the first one to adapt this strictly one-dimensional solution for practical transformers, Ferreira [3-18] has further extended the Dowell's method [3-19] to round wires and proposed the orthogonal concept which ensures the skin and proximity effects can be calculated separately.

Normally foil plates or Litz wires would be adopted to reduce the high frequency winding losses. For high power applications, foil plates used to carry large amounts of current will result in an unrealistic width. Therefore, Litz wires, with many fine strands are chosen for the application. A Litz wire is supposed to cancel the proximity effect by external magnetic field, which ideally means the Litz wire put in a transpose field should be "transparent", and its AC resistance is only determined by the skin effect of each strand. However, there are still "local" proximity effects existing for each strand imposed by its surrounding strands.

Tourkhani [3-20] has modeled the winding loss of the round Litz wire in close-form equations, and it has been proved accurate and convenient to use. We adopt this method to calculate winding losses. In this method, the strand internal field distribution is simplified. It is shown that the eddy current effect would be the function of both strand number N_0 and winding layers m . The AC resistance of an N -turn Litz wire winding will be expressed as:

$$R_{AC} = \frac{\sqrt{2}N \cdot \rho}{\pi \cdot \delta \cdot N_0 \cdot d_{strand}} * \left(\frac{\frac{ber\left(\frac{y}{\sqrt{2}}\right) \cdot bei'\left(\frac{y}{\sqrt{2}}\right) - bei\left(\frac{y}{\sqrt{2}}\right) \cdot ber'\left(\frac{y}{\sqrt{2}}\right)}{ber'^2\left(\frac{y}{\sqrt{2}}\right) + bei'^2\left(\frac{y}{\sqrt{2}}\right)} - \frac{\frac{\pi^2 N_0 \eta}{24} \left(16 * m^2 - 1 + \frac{24}{\pi^2}\right) \frac{ber_2\left(\frac{y}{\sqrt{2}}\right) \cdot ber'\left(\frac{y}{\sqrt{2}}\right) - bei_2\left(\frac{y}{\sqrt{2}}\right) \cdot bei'\left(\frac{y}{\sqrt{2}}\right)}{ber^2\left(\frac{y}{\sqrt{2}}\right) + bei^2\left(\frac{y}{\sqrt{2}}\right)}}{\right)} \quad (3-32)$$

32)

Where $y = \frac{d_{strand}}{\delta}$ with d_{strand} for Litz wire strand diameter and $\delta = \sqrt{\frac{\rho_{cu}}{\pi \cdot f \cdot \mu_r \cdot \mu_0}}$

for skin depth. To simplify the analysis, R_{AC} can be normalized with respect to a base resistance.

$$R_b = \frac{N \cdot \rho_{cu}}{N_0 \cdot \pi \cdot \delta^2} \quad (3-33)$$

If K_r denotes the normalized values of R_{AC} , then we have:

$$K_r = \frac{\sqrt{2}}{y} * \left(\frac{\frac{ber\left(\frac{y}{\sqrt{2}}\right) \cdot bei'\left(\frac{y}{\sqrt{2}}\right) - bei\left(\frac{y}{\sqrt{2}}\right) \cdot ber'\left(\frac{y}{\sqrt{2}}\right)}{ber'^2\left(\frac{y}{\sqrt{2}}\right) + bei'^2\left(\frac{y}{\sqrt{2}}\right)} - \frac{\frac{\pi^2 N_0 \eta}{24} \left(16 * m^2 - 1 + \frac{24}{\pi^2}\right) \frac{ber_2\left(\frac{y}{\sqrt{2}}\right) \cdot ber'\left(\frac{y}{\sqrt{2}}\right) - bei_2\left(\frac{y}{\sqrt{2}}\right) \cdot bei'\left(\frac{y}{\sqrt{2}}\right)}{ber^2\left(\frac{y}{\sqrt{2}}\right) + bei^2\left(\frac{y}{\sqrt{2}}\right)}}{\right)} \quad (3-34)$$

The normalized AC resistance as the function of N_0 , y , and m is plotted in Fig. 3-24. It is shown that there are optimal values of y existing to minimize the winding loss under certain strand number and winding layer. There are trends that both larger number of strands and winding layers will make the AC resistance bigger, which can be explained by the proximity effect. The value of y is determined by the strand diameter and operating frequency. It is also important that we could not just follow some empirical rule of thumb to select wire gauge according to the frequency. The higher the strand number is, the smaller the optimal value of y , which indicates that thinner wire be used for higher power rating. In practical, the fill factor will reduce as more and thinner Litz wire strands are used, so DC resistance will increase due to the copper area reduction.

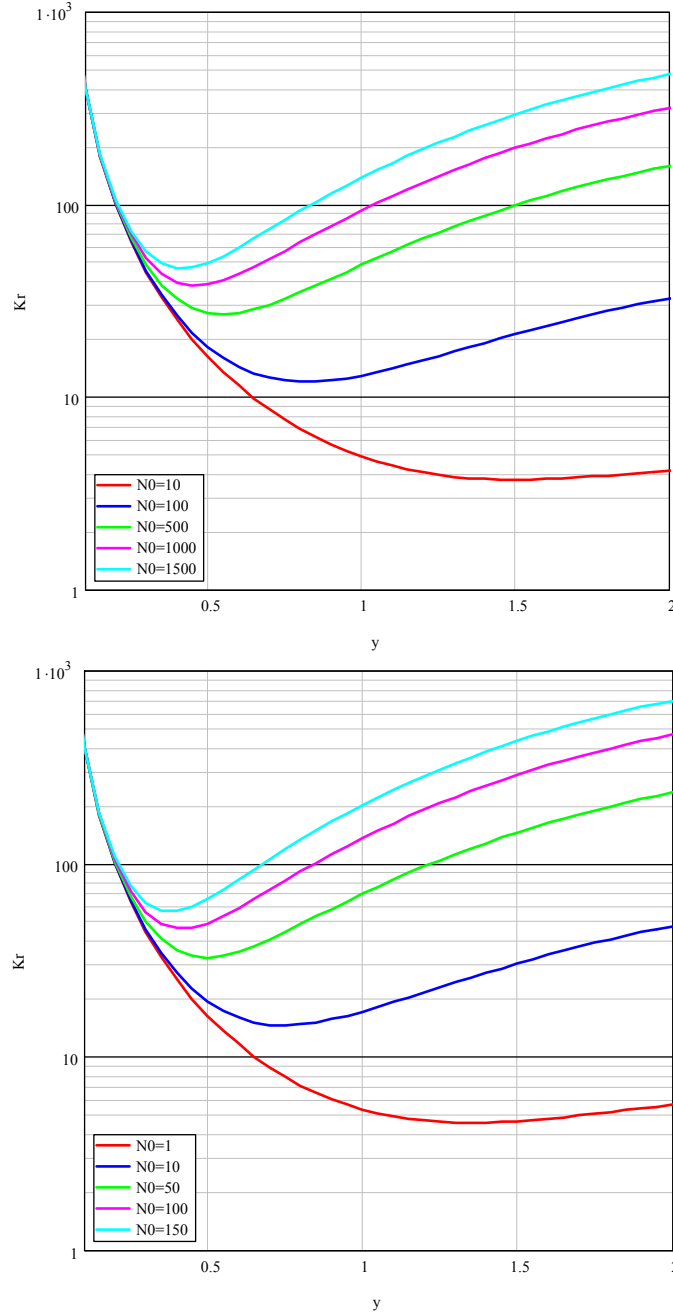


Fig. 3-24 Normalized resistance of Litz wire windings for 1 layer (upper) and 4 layers (lower)

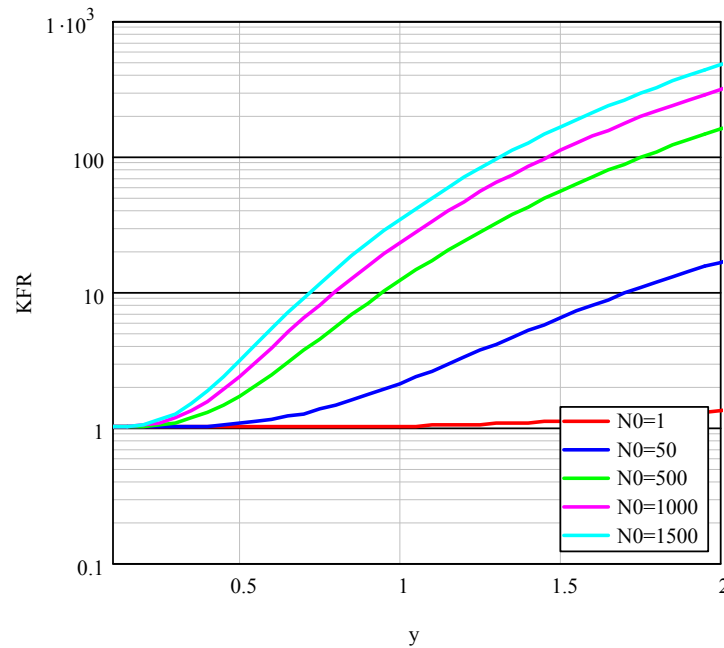
It is sometimes more convenient to use AC-to-DC resistance ratio representing the eddy current effect. The DC resistance of the Litz wire can be expressed as:

$$R_{DC} = \frac{4N \cdot \rho_{cu}}{N_0 \cdot \pi \cdot d_{strand}^2} \tag{3-35}$$

Using equation (3-35) and (3-32), we can have:

$$K_{FR} = \frac{y}{\sqrt{2}} * \left(\frac{ber\left(\frac{y}{\sqrt{2}}\right) \cdot bei'\left(\frac{y}{\sqrt{2}}\right) - bei\left(\frac{y}{\sqrt{2}}\right) \cdot ber'\left(\frac{y}{\sqrt{2}}\right)}{ber'^2\left(\frac{y}{\sqrt{2}}\right) + bei'^2\left(\frac{y}{\sqrt{2}}\right)} - \frac{\frac{\pi^2 N_0 \eta}{24} \left(16 * m^2 - 1 + \frac{24}{\pi^2}\right) \frac{ber_2\left(\frac{y}{\sqrt{2}}\right) \cdot ber'\left(\frac{y}{\sqrt{2}}\right) - bei_2\left(\frac{y}{\sqrt{2}}\right) \cdot bei'\left(\frac{y}{\sqrt{2}}\right)}{ber^2\left(\frac{y}{\sqrt{2}}\right) + bei^2\left(\frac{y}{\sqrt{2}}\right)} \right) \quad (3-36)$$

The ratio K_{FR} is plotted in Fig. 3-25 for different numbers of winding layers and Litz wire strands. As expected, the ratio will increase as y increases, but the relationship is not linear. One thing that needs to be noticed is we can not choose y to be an unlimited small value due to the practical manufacture and cost concerns on the strand. The effects of the strand number and winding layer are still salient.



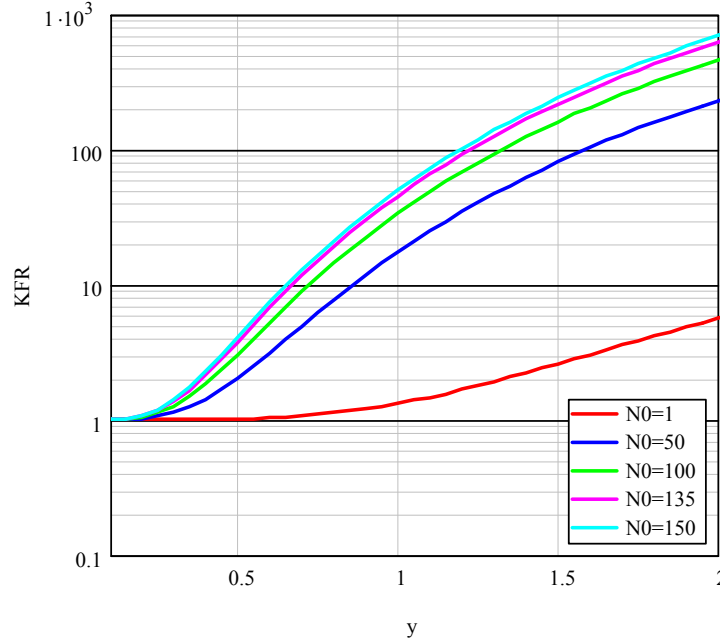


Fig. 3-25 AC/DC resistance ratio of Litz wire windings for 1 layer (upper) and 4 layers (lower)

So, the winding loss for any core selected can be expressed as a function of flux density B :

$$P_w = K_{FR} \cdot I_{pri}^2 \cdot \frac{\lambda^2 \cdot \rho_{cu} \cdot (MLT)}{4A_{window} \cdot k_u \cdot A_c^2} \cdot \left(\frac{1}{B}\right)^2 \quad (3-37)$$

Where, I_{pri} and λ for primary current and volt*sec; MLT , A_{window} , and A_c for mean-length-per-turn, window area, and leg cross-section area of certain core; ρ_{cu} representing copper resistivity under certain operating temperature. k_u is the fill factor which includes the Litz wire packing factor, and the core window utilization factors of bobbin, insulation, and manufacture effects. It has been proven that 0.2~0.4 would be reasonable for our power level.

3.3.2. Litz wire optimal design

From the above analysis of the Litz wire winding eddy current effect, we know that the AC-to-DC resistance ratio K_{FR} is the function of strand numbers and strand diameters for same winding layers and certain frequency. For a selected core window area and fixed fill factor, the larger diameter means fewer strands needed; on the other hand, we also can choose smaller wires with more strands. There should be an optimal selection of the Litz wire strand number and diameter. Sullivan [3-21] has addressed this

issue, but his eddy current effect consideration for the Litz wire is over simplified. With the help of equation (3-32), we will derive the optimal Litz wire strand number and diameter to realize the minimum loss, under certain frequency and core window selected.

The first relationship we can have is that the total copper area is fixed, if the core window has been selected and the fill factor is kept constant. So, we will have:

$$Const = N_0 \cdot d_{strand}^2 \quad (3-34)$$

So the DC resistance is fixed for the case discussed here. The minimum winding loss now can be translated into the minimum K_{FR} , which is expressed in (3-32).

Therefore, the optimal y_{op} is going to be found through having $\frac{\partial K_{FR}}{\partial y} = 0$:

$$y_{op} = 4 \cdot \sqrt[4]{\frac{3}{1 + \frac{\pi^2 \cdot N_0 \cdot \eta}{4} \cdot \left(16m^2 - 1 + \frac{24}{\pi^2}\right)}} \quad (3-35)$$

$$y_{op} = \frac{d_{strand}}{\delta} = d_{strand} \cdot \sqrt{\frac{\pi \cdot f \cdot \mu_r \cdot \mu_0}{\rho}} \quad (3-36)$$

Now we can determine the Litz wire parameters by combining equations (3-34), (3-35), and (3-36). For example, the Litz wire with 1500 strands should have $y_{op} = 0.446$ for a single layer winding, which means the strand diameter should be less than half of the skin depth of the given frequency. Another example is that $y_{op} = 0.405$ should be kept for 150 strands Litz wire in a 4-layer winding.

Since the above equations are non-linear, we can have a program to iterate the Litz wire parameters towards each given DC resistance which also means the given core window area.

There is an assumption, which may not hold true in realm, that the fill factor is constant, since it is also related to the Litz wire parameters. More strands and finer wire gauge both means more insulation occupation in the window. We do not take this into the analysis, because that will make the analysis result too complicit to be useful to the designer. Furthermore, the different empirical values of the fill factor can be used for different strand number ranges.

3.4. Summaries

For high-frequency, high power density transformer design, we need to accurately calculate the core and winding loss that determine the size of the transformer under certain thermal management condition. The resonant converter operation waveforms and Litz wire windings enlarge the difficulty of calculation.

The WcSE method is proposed to calculate core loss for resonant operation waveforms. By directly observing the flux of different exciting voltage waveforms, we derive the Flux Waveform Coefficient (FWC) for each kind of waveform. After correlating the FWC of the arbitrary waveform to the one of sinusoidal waveform, we can find the coefficient of the WcSE and the core loss of the arbitrary waveform can be calculated based on the Steinmetz equation. The method has been verified for the resonant waveform by examining STS series waveforms. This is important to soft switching and resonant operation applications, which have the STS type waveform, instead of sine or square waveforms, since both MSE and GSE methods give incorrect results. For high density requirements, the accurate calculation of the core loss would provide the possibility to cut the margin of over-design.

The WcSE method can be conveniently integrated into optimization programs when compared with MSE and GSE methods. The waveform coefficient, as the only change from the original SE, can easily be calculated even instantaneously. For a resonant converter running at variable frequency, the WcSE method can provide the accurate and easy way to calculate core losses.

The Litz wire winding loss calculation is reviewed. Simplified leakage field distribution has been adopted by the method [3-20]. Based on the solution of the AC-to-DC resistance ratio of the Litz wire winding, the optimal selection of the Litz wire has been discussed, which have practical meaning to the designer.

Chapter 4 Parasitic Calculation

Leakage inductances and winding capacitances are inevitable characteristics of transformers, so they are called parasitic. They can significantly change converter behavior. The energy stored in these parasitic elements will cause extra losses and stress in semiconductor switches. Normally, small parasitic values are desired, which means they need to be controlled during the transformer design. The proper selection of the topology and switching scheme would reduce the affection by parasitics. From this perspective, we need to know the precise value of these parasitics, so the converter can be operated under certain switching moments utilizing the resonant frequency of the parasitic.

The calculation methods of leakage inductance and winding capacitance are discussed in this chapter. Since numerical methods are not flexible enough to be included into the design procedure, the analytical methods are developed here for parasitic calculations.

4.1. Leakage inductance calculation

Leakage inductance is one of the important design parameters of a high-frequency transformer. Leakage inductance plays a very important role in pulse-width-modulated (PWM) converters, limiting the upper frequency of operation. In switched-mode converters, the leakage inductance causes undesirable voltage spikes that can damage circuit components [4-1]. For the PWM full bridge converter shown in Fig. 4-1, the effect on the switch voltage stress is demonstrated. Here it clearly shows that the voltage ringing is more severe as the leakage inductance of the transformer increases. The overshoot voltage could destroy the semiconductor devices, and the extra losses due to the ringing would reduce the system efficiency. Therefore, the leakage inductance needs to be controlled in the transformer design.

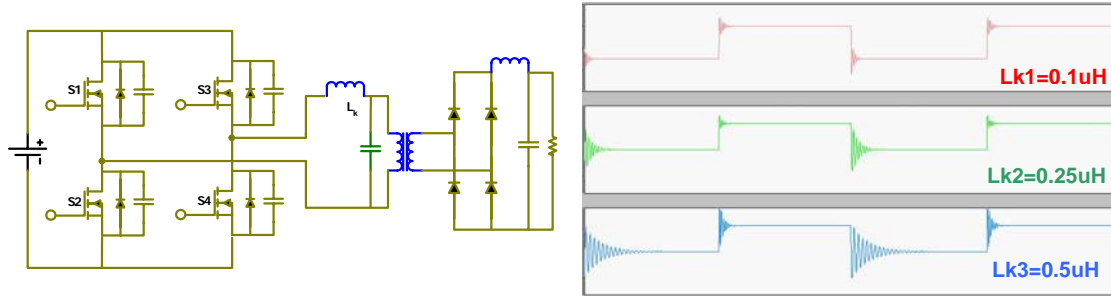


Fig. 4-1 Full bridge PWM converter (left) and V_{ds1} under different leakage values (right)

Since it is difficult to have small leakage values, especially for high power applications, soft switching and resonant operation schemes have been proposed to absorb the inevitable leakage inductance [4-2]-[4-4]. In these cases, the leakage inductor participates in the circuit operation, through resonating with certain capacitance along or together with extra inductors.

From the discussions above, we can conclude that accurate calculation of leakage inductance is critical to high power density converters. The leakage inductance is actually a lumped equivalent representation of the energy stored in the leakage field, which consists of the portion of the magnetic flux not linking both primary and secondary windings. Therefore, the calculation of the leakage inductance can be performed as:

$$W = \frac{1}{2} L_{lk} I^2 = \frac{1}{2} \mu_0 \int_V H^2 dV \quad (4-1)$$

The distribution of leakage field could be very complicated, due to the eddy current effects inside the winding conductors. The situation is even worse, when the Litz wire is adopted for the winding. In many previous works, researchers have tried to tackle this problem, and they will be reviewed in the next section.

4.1.1. Leakage inductance calculation method survey

a) Simplified 1-D calculation

The well known way to calculate leakage inductance assumes that the current distribution in the winding is linear and the core permeability is infinite [4-5]. The magnetic field in the winding space is assumed to be parallel to the leg of the transformer core. We can simplify this field distribution as a one-dimensional problem, as shown in Fig. 4-2. The 1-D leakage field distribution, $H_z(r)$ is shown in the cross-section of the

pot-core transformer. The leakage inductance of unit winding length can be obtained through putting the $H_z(r)$ expression into equation (4-1).

$$\frac{L_{lk}}{l_w} = \frac{\mu_0 \cdot N_1^2 \cdot b_w}{3} \quad (4-2)$$

Where, b_w is the core window width and l_w is mean length of the winding. This equation can be used for other types of cores and winding structures, with the validation of the assumptions. Even for the transformer with perfect fit structure, this method is only accurate for low frequencies, since it omits high-frequency eddy current effects inside the transformer winding conductors.

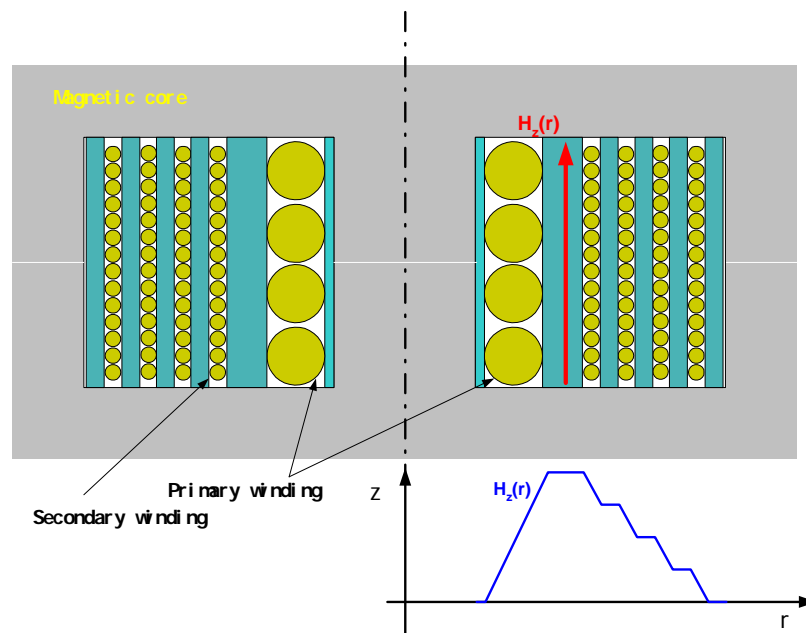


Fig. 4-2 Leakage field distribution of a pot core transformer

b) Numerical methods

The numerical method is powerful to count complex structure and asymmetrical problems. Significant research has been done to analyze and model eddy current effects in transformers. Skutt [4-6] applied 3-D Finite Element Analysis method to a high-power (500 W) planar winding transformer. The impact that the secondary winding terminations have on the leakage characteristics of the device is examined. It is shown that the effective inductance the transformer presents to the circuit can be several times of the inductance calculated or measured based on an ideal short-circuited winding. This is a perfect example where 1-D simplification cannot hold due to the structure. In this case,

the sophisticated FEA calculation is performed initially to identify the discrepancy between ideal calculation and the real situation. However, the FEA calculation needs expensive computation resources and the most important issue is that it is hard to integrate into a design procedure.

Instead of working in frequency domain, the method by Lopera [4-7] is constructed in time domain. 1-D distributions of magnetic and electric fields are assumed, and from Maxwell's equations an equivalent electric circuit is easily obtained. This equivalent circuit can be included in analog simulators (Spice, Saber ...). The leakage inductance calculated by this method represents eddy current effects, but it is hard to apply the method to Litz wire windings, because of its inherent 1-D plate structure basis.

To capture all the irregularities of the leakage field distribution due to edge effects and asymmetries, FEA is probably the only appropriate way to calculate leakage inductance, but the lengthy computation makes it unsuitable to be integrated into the design procedure. Another drawback of the numerical method is that the Litz wire, especially the one with many strands, is hard to depict and calculate. The radial and azimuthal transposition of strands in the Litz wire actually requires 3-D solvers. It is impractical to calculate detailed field distribution of each tiny strand and to sum them up in order to obtain the macro winding inductance. The FEA method is really insufficient because of the number of strands and the small diameter of each strand. The high frequency requires that each strand be very thin, while the high power means that more strands are needed; thus these requirements make the FEA method impractical.

c) Close-form methods considering eddy current effects

The closed-form expression of leakage inductances is preferable for power electronics designers. Dowell [4-8] did pioneering work on including high-frequency eddy current effects into 1-D impedance solutions, and Venkatraman [4-9] expanded the method to non-sinusoidal waveforms. This particular approach, being one dimensional in rectangular coordinates, is in principal applicable to foil conductors having a magnetic field parallel to the conductor surface, and is therefore subject to certain restrictions:

Magnetizing current of transformers cannot be included, as it results in a magnetic field component that is not parallel to the foil conductor surface. Even when considering transformers with negligible magnetizing current, it should be realized that, strictly

speaking, the analysis is valid for infinitely long solenoid windings. When the windings fill the window length completely, or if the distance between primary and secondary is small, the resultant field approaches that of infinite solenoid windings.

Error is introduced by replacing round conductors with square-shaped conductors of an equal cross-sectional area. At DC, the resistances are equal, although at high frequencies, the square representation of round conductors becomes inaccurate.

Another shortcoming is that the method cannot be applied to stranded or Litz wire windings, since it requires the series connection of conductors carrying same current. The parallel conductor in stranded wires would not have the same current flowing, due to the eddy current effects.

Different kinds of transformer structures have been explored for the past two decades. Hurley [4-13] thoroughly derived leakage inductance calculation for toroidal ferrite core transformers. The method is generic for windings with or without magnetic core, but it is too complicated to be applied to Litz wire windings. Goldberg [4-14] studied planar pot core transformers; and more general structures (Pot or EE core with cylindrical windings) were considered by Niemela [4-15].

For high-frequency high-power transformers, Litz wires are used to reduce the winding loss. Ideally, there should be only a skin effect and no proximity effects due to the adoption of the Litz wire, so the current distribution, and correspondingly the leakage field distribution, should be easier to derive. However, the Litz wire is still not immune to the proximity effect because of its local field created by neighboring strands within one bundle. No method has been developed to calculate the leakage inductance for Litz wire winding transformers. Although Cheng [4-16] considered the stranded wire and applied the Dowell method to obtain the frequency-dependant leakage inductance, there is no clear analysis of the Litz wire mechanism and the limitations of the method.

4.1.2. Proposed leakage inductance calculation method

A closed-form method is proposed here to overcome the problem. To calculate unit length leakage inductance of the high-power high-frequency transformers, we first divide the leakage inductance into two parts - one part is frequency-independent components and the other is frequency-dependent components. The first part is mainly due to the stored energy in the interlayer and inter-strand gaps. The latter part of the

leakage inductance is due to the flux crossing the winding conductors. The electric potential is produced according to the Faraday's Law, and correspondingly eddy current generated in the conductor, which would change the field distribution inside the conductor space. The computation of the frequency-independent component is simple. The frequency-dependent component is the theme of the work as it affects the performance of a transformer significantly, and will be discussed in detail.

a) *1-D structure eddy current effects*

The typical transformer structure is revisited here, as in Fig. 4-3. The coordinate system will be used for all discussions in this chapter. Several assumptions will make the analysis explicit but without losing much generalness and accuracy.

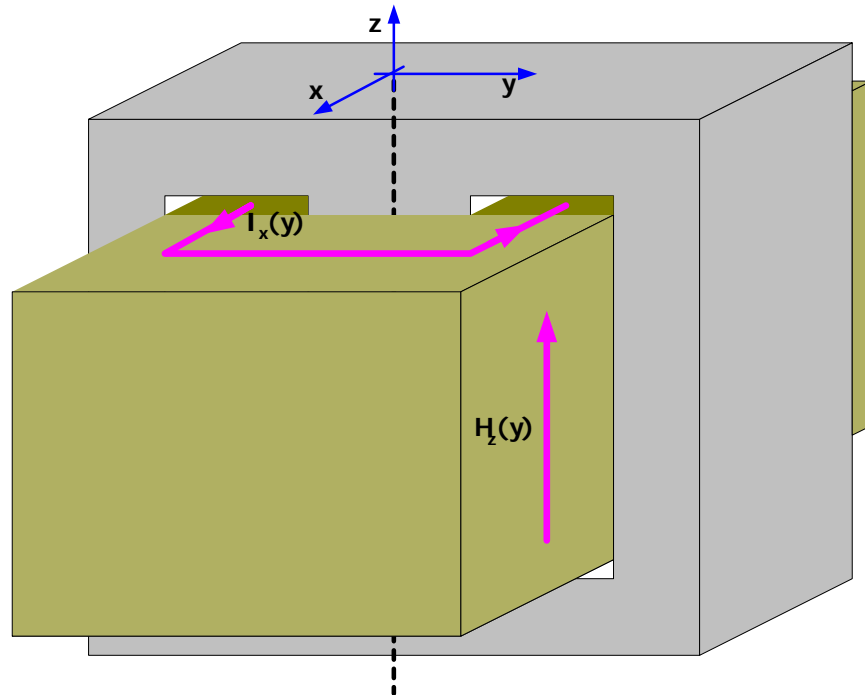


Fig. 4-3 Typical two-winding transformer structure and corresponding coordination notation

The first assumption is that the foil winding is under consideration. If compactly wound wire winding is the case, all wires in the same layer could be treated as a plate with the same area and width (in y direction), but an equivalent height (in z direction). The second assumption is that permeability of the core is infinite, so that the magnetizing current is neglect. This will ensure the leakage field in the winding would be parallel to the legs. The third assumption is that the current distribution is unchanged for each whole

turn, which means the edge effect of the hang-out portion of the winding is omitted. The current and field distribution for the winding portion within the core window is calculated, and the result is multiplied by the mean turn length to get the overall inductance of the winding. All of these assumptions will bring in errors to some extent, but the analysis is greatly simplified. Actually, for high-power transformer applications, these assumptions are acceptable and realistic.

With the abovementioned assumptions made, the eddy current effect of the transformer winding can be analyzed. Both skin and proximity effects change the MMF field distribution. We can look at the skin effect and the proximity effect separately.

If the transformer shown in Fig. 4-3 is cut along the x - y plane, we can consider the winding conductor as a semi-infinite current-carrying plate of thickness $2b$ in y direction, and width h in z direction, as illustrated in Fig. 4-4. Here, we consider the skin effect only, so a unit current I flow through the plate in x direction. The magnetic field in z direction will be induced. We want to find out the current density and magnetic field distribution along y direction inside the plate as, $H_z(y)$ and $J_x(y)$ [4-19].

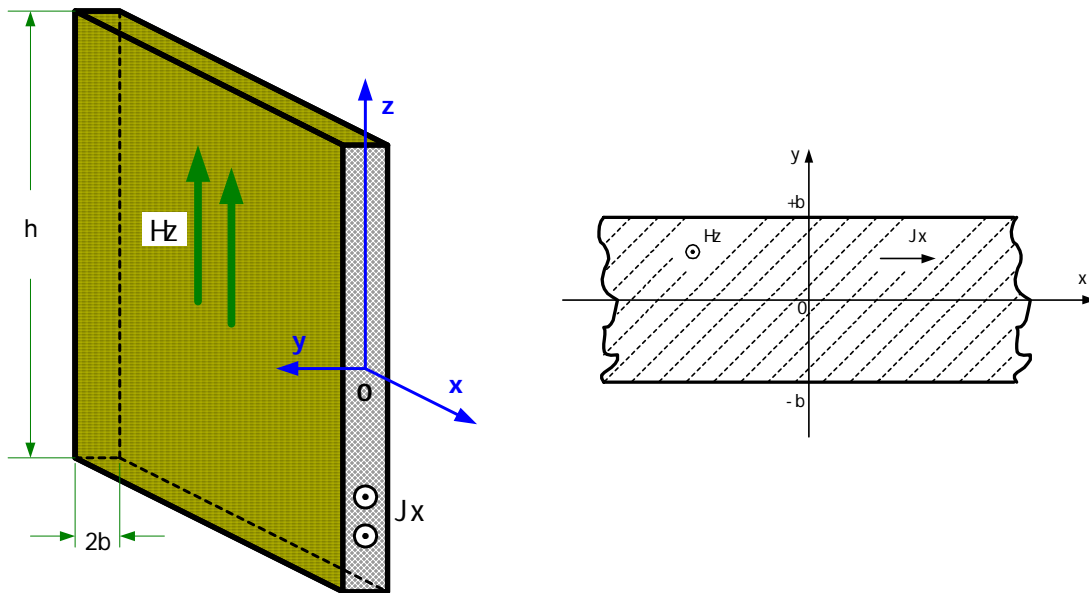


Fig. 4-4 Illustration and cross-section of a current-carrying semi-infinite plate

If the linear current distribution in the conductor plate is assumed, the ideal current density can be obtained as:

$$J_{x,av} = \frac{I}{4b \cdot h} \quad (4-3)$$

Now the Maxwell's equations are applied to the problem shown above [4-17], to obtain the skin effect. For conductor with conductivity σ , the sinusoidal current with frequency ω , and no displacement current considered, we can have the famous elliptic partial differential equation as (4-9).

$$\nabla \times E = -\frac{\partial B}{\partial t} = -\mu_r \cdot \mu_0 \frac{\partial H}{\partial t} = -j \cdot \mu_r \cdot \mu_0 \cdot \omega \cdot H \quad (4-4)$$

$$\nabla \times H = J + \epsilon_0 \frac{\partial E}{\partial t} \quad (4-5)$$

$$J = \sigma \cdot E \quad (4-6)$$

$$\nabla \times (\nabla \times H) = -j \cdot \sigma \cdot \mu_r \cdot \mu_0 \cdot \omega \cdot H \quad (4-7)$$

$$\nabla \cdot H = 0 \quad (4-8)$$

$$\nabla^2 H = \nabla \cdot H - \nabla \times (\nabla \times H) = j \cdot \sigma \cdot \mu_r \cdot \mu_0 \cdot \omega \cdot H \quad (4-9)$$

In the Cartesian coordinates, the diffusion equation in (4-9) is in the form of:

$$\nabla^2 H = \frac{\partial^2 H}{\partial x^2} + \frac{\partial^2 H}{\partial y^2} + \frac{\partial^2 H}{\partial z^2} = j \cdot \sigma \cdot \mu_r \cdot \mu_0 \cdot \omega \cdot H \quad (4-10)$$

According to the 1-D assumption made above and the boundary conditions, $H_{sk_z}(b) = -H_{sk_z}(-b) = \frac{I}{2h}$, the magnetic field can be solved as (4-11), which gives the description of the magnetic field distribution along the y -axis:

$$H_{sk_z}(y) = \frac{I}{2h} \cdot \frac{\sinh(\alpha y)}{\sinh(\alpha b)} \quad (4-11)$$

Where $\alpha^2 = j \cdot \sigma \cdot \mu_r \cdot \mu_0 \cdot \omega$, and $\alpha = \frac{1+j}{\delta}$, in which the skin depth is expressed as

$\delta = \sqrt{\frac{2}{\sigma \cdot \mu_r \cdot \mu_0 \cdot \omega}}$. The current density distribution can be obtained by putting (4-11) into

(4-5), and is expressed in (4-12).

$$J_{sk_x}(y) = \frac{\alpha \cdot I}{2h} \cdot \frac{\cosh(\alpha y)}{\sinh(\alpha b)} \quad (4-12)$$

The skin effects on current density and magnetic field distribution within the conductor plate space are shown in Fig. 4-5, for a 1 cm thick copper plate under different operating frequencies. It is clear that the current distribution is “crowding” beneath the surface, as it is called the skin effect. The higher the frequency is, the more severe the skin crowding degree is.

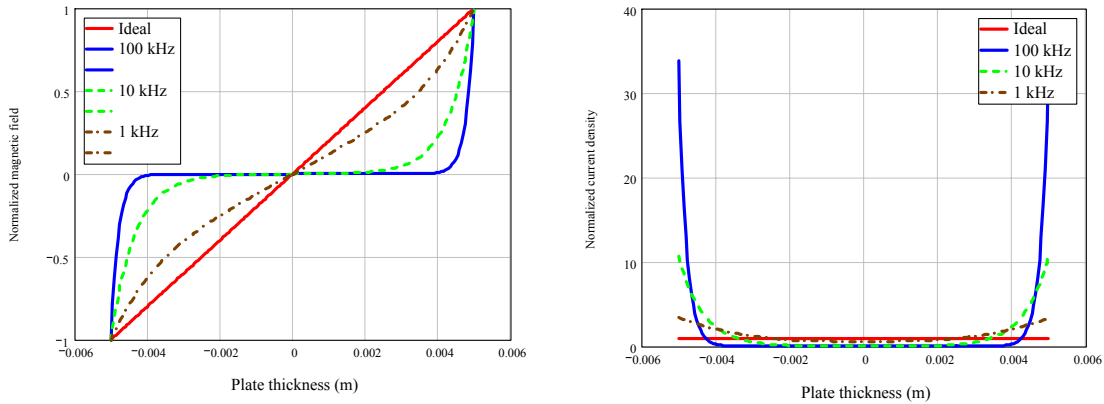


Fig. 4-5 Skin effect on magnetic field distribution (left) and current density distribution (right)

Similarly, the proximity effect of the transformer winding is analyzed. According to the 1-D assumption, the winding conductor is under the leakage magnetic field, which is parallel to its surface along the z direction, as illustrated in Fig. 4-6.

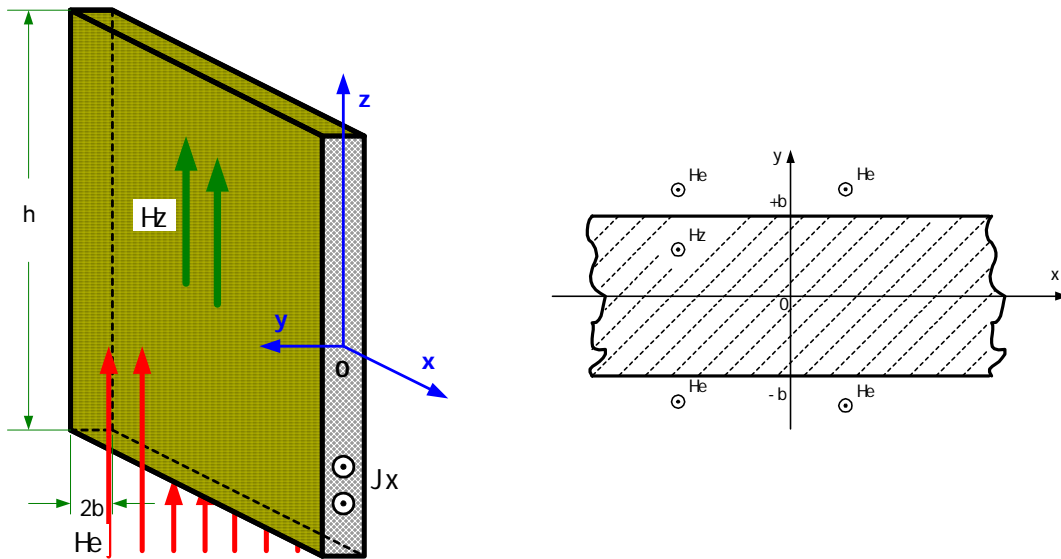


Fig. 4-6 Illustration and cross-section of a current-carrying semi-infinite plate in a parallel field

As we know, the conductor put in a varying magnetic field will generate voltage potential and then eddy current, which in turn creates an internal magnetic field to oppose the change of the external field. Therefore, we need to solve the magnetic field and current distributions inside the conductor space. Maxwell's equations are adopted again, and the same diffusion equation as (4-10) can be derived for the proximity effect. The solution to the equation would be different, due to different boundary conditions,

$H_z(b) = H_z(-b) = H_e$, the magnetic field can be solved as (4-13), which gives the description of magnetic field distribution along the y -axis:

$$H_{Pr_z}(y) = H_e \cdot \frac{\cosh(\alpha y)}{\cosh(\alpha b)} \quad (4-13)$$

The current density distribution can be obtained by putting (4-13) into (4-5), and is expressed in (4-14).

$$J_{Pr_x}(y) = \alpha \cdot H_e \cdot \frac{\sinh(\alpha y)}{\cosh(\alpha b)} \quad (4-14)$$

The proximity effects on current density and magnetic field distribution within the conductor plate space are shown in Fig. 4-7, for a 1 cm thick copper plate under 1 Tesla external magnetic field in different operating frequencies.

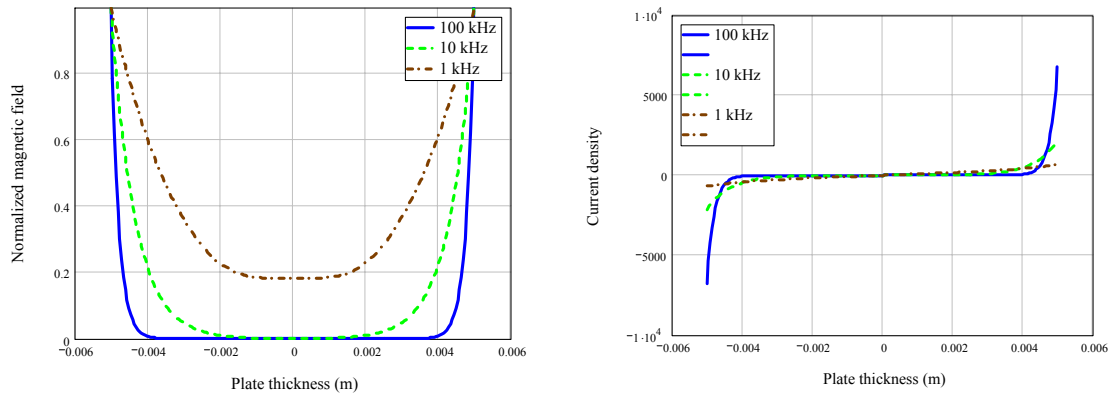


Fig. 4-7 Proximity effect on magnetic field distribution (left) and current density distribution (right)

Once the skin and proximity effects are known separately, we can apply them to a typical transformer winding configuration which has primary and secondary windings, as shown in Fig. 4-8. The normalized magnetic field distribution is plotted for different frequencies in Fig. 4-8. The eddy current would result in a smaller magnetic energy store which means smaller inductance in the conductor spaces, and the enclosed area decreases greatly as the conductor thickness to skin depth ratio, $\frac{b}{\delta}$, reaches 3.4. It is obvious that the simple 1-D calculation method would over predict the leakage inductance, even for the design which chooses the conductor thickness as two times that of the skin depth.

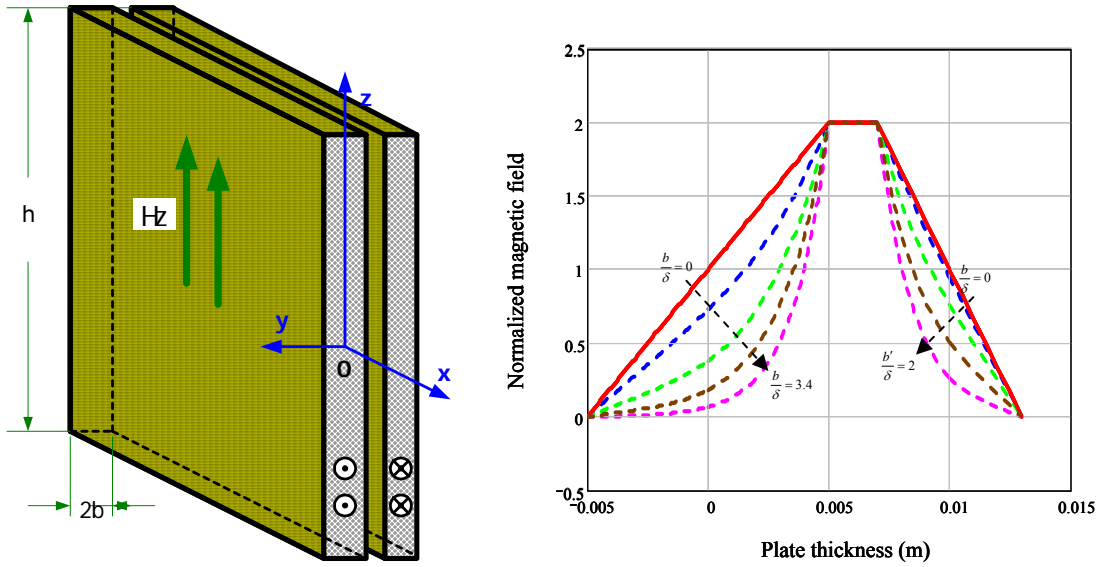


Fig. 4-8 Eddy current effect on magnetic field distribution (right) of a two winding transformer (left)

The ultimate objective is to find out the inductance, which is directly related to the total energy stored by the leakage field. Therefore, the power integral of magnetic field intensity is calculated. From the above analysis, the magnetic field distributions due to skin and proximity effects are calculated separately. The total leakage field energy can be calculated as described below. Since the integral of $\sinh \cdot \cosh$ is zero, the cross product items, $H_{Sk} \cdot H_{Pr}^*$ and $H_{Sk}^* \cdot H_{Pr}$ are gone for the final total energy calculated. This is called the orthogonality that exists between the skin and proximity effects under the condition shown above [4-18]. The greatness of this relationship is that we can now consider them separately, and the mathematic derivation would be simpler. If the applied field and current flowing directions are not perfectly perpendicular to each other, the orthogonal relationship is not valid any more.

$$\begin{aligned}
 W &= \frac{1}{2} \mu \int_V (H \cdot H^*) dV = \frac{1}{2} \mu \int_V ((H_s + H_p) \cdot (H_s^* + H_p^*)) dV \\
 &= \frac{1}{2} \mu \int_V (H_s \cdot H_s^* + H_p \cdot H_p^* + \cancel{H_s \cdot H_p^*} + \cancel{H_p \cdot H_s^*}) dV \\
 &= \frac{1}{2} \mu \int_V (|H_s|^2 + |H_p|^2) dV
 \end{aligned} \tag{4-15}$$

Fig. 4-5 and Fig. 4-7 clearly show the eddy current effect. Thus the calculated inductance from the linear magnetic field distribution, as for low frequency cases, would

be larger than the actual magnetic field distribution. This is the major motivation for considering eddy current effects into leakage calculation. Meanwhile, the winding loss at high frequency also is determined by the leakage field, so this is also fundamental to calculating the winding's AC resistance.

b) Litz wire effects

Litz wires are originally developed to result in lower ac resistances than solid wires. Eddy current effects drive the current through a solid wire close to the surface of the conductor at high operating frequencies. If a multi-strand conductor is used, the overall cross-sectional area is spread among several conductors with a small diameter. For this reason, a Litz wire would result in a more uniform current distribution across the wire section. Moreover, Litz wires are assembled so that each single strand, in the longitudinal development of the wire, occupies all the positions in the wire cross section. Therefore, not only the skin effect but also the proximity effect is drastically reduced [4-20]-[4-22].

However, the following limitations occur when using Litz wires: 1) the utilization of the winding space inside a bobbin width is reduced with respect to a solid wire. 2) The dc resistance of a Litz wire is larger than that of a solid wire with the same length and equivalent cross-sectional area because each strand path is longer than the average wire length.

c) Litz wire winding leakage inductance calculation

With the above derivations, we can now calculate the leakage inductance of the Litz wire, which ideally should present even current distribution among each strand. However, current distribution within each strand is still affected by the local skin effect of the individual stand and the local proximity effect of all its neighboring strands.

For high-power applications, the Litz wire used usually has a huge number of strands, so the Litz wire can be approximated by a square array of strands [3-20] without sacrificing accuracy. Furthermore, all strands in one row are packed into an equivalent copper plate. Therefore, the analysis that resulted during the above section can be adopted

here to solve the leakage inductance within Litz wire area. Each layer is combined into one solid foil as shown in Fig. 4-9.

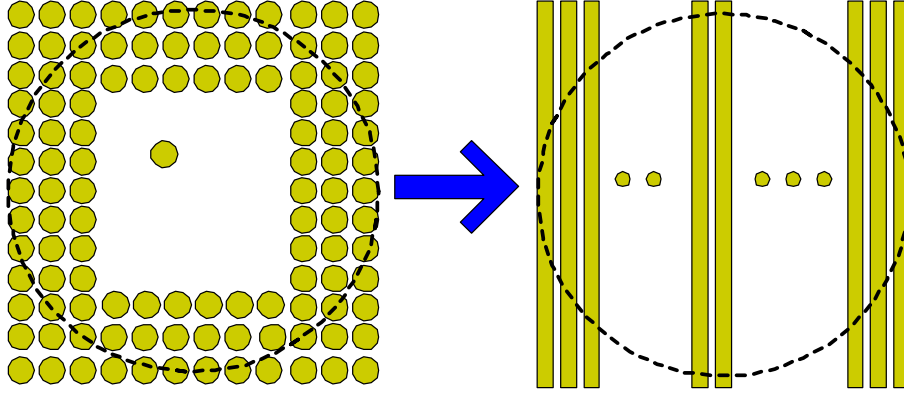


Fig. 4-9 Litz wire approximation

Therefore, the energy stored in the k_{th} layer can be derived as:

$$\begin{aligned}
 W_k &= \frac{1}{2} \mu \int_V \left(|H_s|^2 + |H_p|^2 \right) dV \\
 &= \frac{MLT \cdot h \cdot \delta}{2} \mu \left\{ \frac{2I^2}{h^2} \cdot \frac{\sinh \nu - \sin \nu}{\cosh \nu - \cos \nu} + \frac{2(k-1)^2 I^2}{h^2} \cdot \frac{\sinh \nu + \sin \nu}{\cosh \nu + \cos \nu} \right\} \\
 &= \frac{1}{2} \mu \int_0^h \left\{ \left| \frac{I}{h} \cdot \frac{\sinh(\alpha y)}{\sinh(\alpha h/2)} \right|^2 + \left| H_e \cdot \frac{\cosh(\alpha y)}{\cosh(\alpha h/2)} \right|^2 \right\} \cdot h \cdot MLT \cdot dy \quad (4-16)
 \end{aligned}$$

The leakage inductance can be calculated through summing all layers together.

$$\begin{aligned}
 L_{lk-w} &= \frac{2 \cdot MLT \cdot \delta}{m^2 h} \sum_{k=1}^m \mu \left\{ \frac{\sinh \nu - \sin \nu}{\cosh \nu - \cos \nu} + (k-1)^2 \cdot \frac{\sinh \nu + \sin \nu}{\cosh \nu + \cos \nu} \right\} \\
 &= \frac{2 \cdot MLT \cdot \mu \cdot \delta}{mh} \left\{ \frac{\sinh \nu - \sin \nu}{\cosh \nu - \cos \nu} + \frac{(2m-1)(m-1)}{6} \cdot \frac{\sinh \nu + \sin \nu}{\cosh \nu + \cos \nu} \right\} \quad (4-17)
 \end{aligned}$$

4.1.3. Verifications

One case study for the transformer using the Litz wire (1500 AWG38 strands) will be analyzed. A simplified 1D method generates only a frequency-independent result. The proposed method is more accurate, and avoids the time-consuming FEA method. The calculated leakage inductance by the proposed method and the simple method are shown in Fig. 4-10.

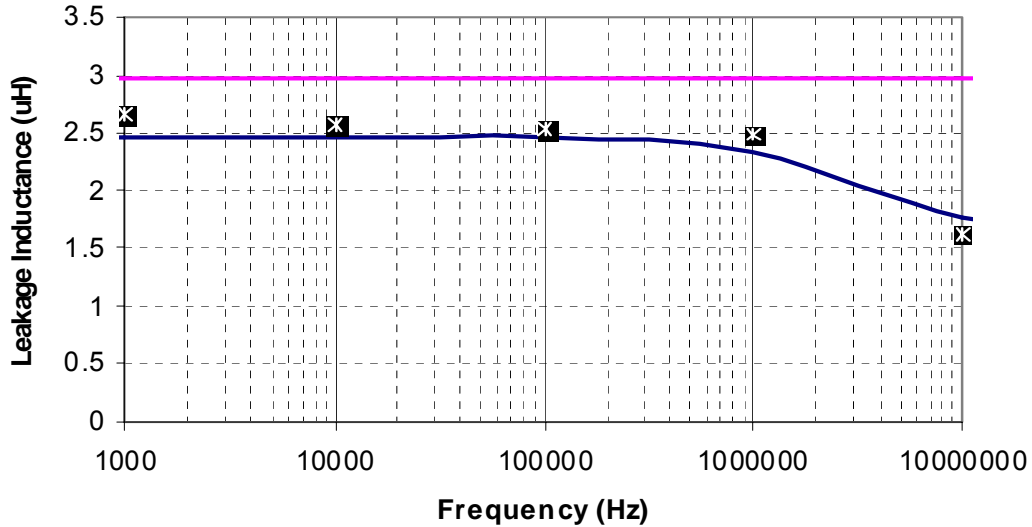


Fig. 4-10 Leakage inductance by the proposed method (blue solid), the simplified method (pink solid), and measurement (black dots)

4.2. Winding capacitance calculation

Winding capacitances, also generally defined as stray capacitances, of a transformer arise from the distributed electrical coupling between any two conductors in or around the transformer. Winding capacitances are all related to transformer windings, but not only between winding conductors. The capacitance, or the stored electrical energy, more precisely, could happen between the windings and magnetic cores, even transformer cases. They are heavily geometry-dependent and distributed in nature [4-23], and to most power converter applications, lumped models of winding capacitance are sufficient.

It has become widely aware that winding capacitances in high-frequency transformers have significant effects on the performance of the components as well as the entire power electronic systems. The winding capacitance results in current spikes and slow rise times which would cause more stress and loss on semiconductor switches. Furthermore, it is responsible for the propagation of conducted EMI noises in converter systems. Parallel resonant topologies can utilize the winding capacitance, which becomes a part of the resonant capacitance required for the operation. Therefore, a winding capacitance calculation is an important aspect of the transformer design.

Substantial attention has been drawn to the modeling of winding capacitance of transformers. Many techniques for the determination of the lumped winding capacitances in transformers have been proposed in literature. The main approaches can be categorized into three groups: **1)** experimental methods – the transformer is treated and measured as a single or two port network, and the lumped capacitances would be calculated according to the measured impedance together with inductances [4-24]-[4-25]. **2)** theoretical calculation based on the field analysis – sophisticated field distribution can be obtained on the detailed transformer winding geometries, and electrostatic energy in the structure would be integrated to have the lumped terminal capacitance [4-26]-[4-27]. **3)** analytical expressions – simplified electrostatic field analysis makes the closed-form solution to the equivalent lumped capacitance possible, for regular winding structures [4-28]-[4-29]. The fundamental equation of all energy base approaches is as:

$$W = \frac{1}{2} \iiint_v \varepsilon_r \cdot \varepsilon_0 \cdot E^2 \cdot dv = \frac{1}{2} \cdot C \cdot V^2 \quad (4-18)$$

To integrate the winding capacitance calculation into the transformer design procedure, we prefer the method of having analytical expressions and acceptable accuracy. 2-D or 3-D field analysis approaches could give accurate results, but definitely require a great amount of information about the geometry and boundary conditions. It is not possible to include this into design iterations, due to its extensive computation resource requirements. The simplified energy-base approach could be the candidate, if the electric field distributions are regular in the transformer, which requires that distances between the windings should be much smaller than the height of windings.

4.2.1. Simplified energy base calculation method

Since voltages induced in all the turns of a given winding layer are identical, the potential varies linearly from one end of the layer to the other, as illustrated in Fig. 4-11. To make the example general, three independent voltages are defined between the four terminals. Therefore, we can find out the 1-D electrical field distribution between the two layers as:

$$E_x(y) = \frac{1}{d} \cdot \left(\frac{V_2 \cdot y}{h} + V_3 - \frac{V_1 \cdot y}{h} \right) \quad (4-19)$$

Now, the energy stored between two layers which have a unit length can be expressed as, if the dielectric material in between has permittivity of ϵ_r :

$$W = \frac{1}{2} \int_0^h \epsilon_r \cdot \epsilon_0 \cdot E_x(y)^2 \cdot dy \cdot d = \frac{\epsilon_r \cdot \epsilon_0 \cdot d}{2} \cdot \int_0^h E_x(y)^2 \cdot dy \quad (4-20)$$

After putting (4-19) into (4-20), we can obtain the relationship between the energy and the terminal voltages as:

$$W = \frac{C_0}{2} \cdot \left(\frac{V_1^2}{3} + \frac{V_2^2}{3} + V_3^2 - \frac{2V_1 \cdot V_2}{3} + V_3 \cdot V_2 - V_3 \cdot V_1 \right) \quad (4-21)$$

We can note $C_0 = \frac{\epsilon_r \cdot \epsilon_0 \cdot h}{d}$ which can be looked as the structure capacitance formed by the two conductor layers.

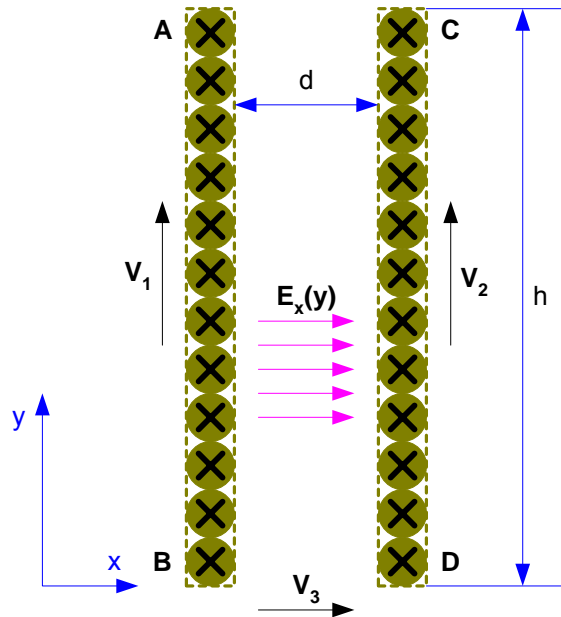


Fig. 4-11 Illustration of two adjacent winding layers

We can apply this general structure to the particular transformer windings to calculate capacitance. First we will determine the connection between the two layers, and correspondingly correlate terminal voltages with the particular values. After multiplying the length of the winding turns, we will have a total of the electrostatic energy stored, as a function of the terminal voltages. The corresponding capacitance can be obtained by the relationship in (4-18). Two of the most popular winding structures are shown in Fig. 4-12. For the wave-type winding, we can correlate the terminal voltages as:

$$V_1 = -V_2 = \frac{1}{n} V_{winding}, \quad V_3 = 0 \quad (4-22)$$

Similarly, the leap-type winding has the relationship like:

$$V_1 = V_2 = \frac{1}{n} V_{winding}, \quad V_3 = -\frac{1}{n} V_{winding} \quad (4-23)$$

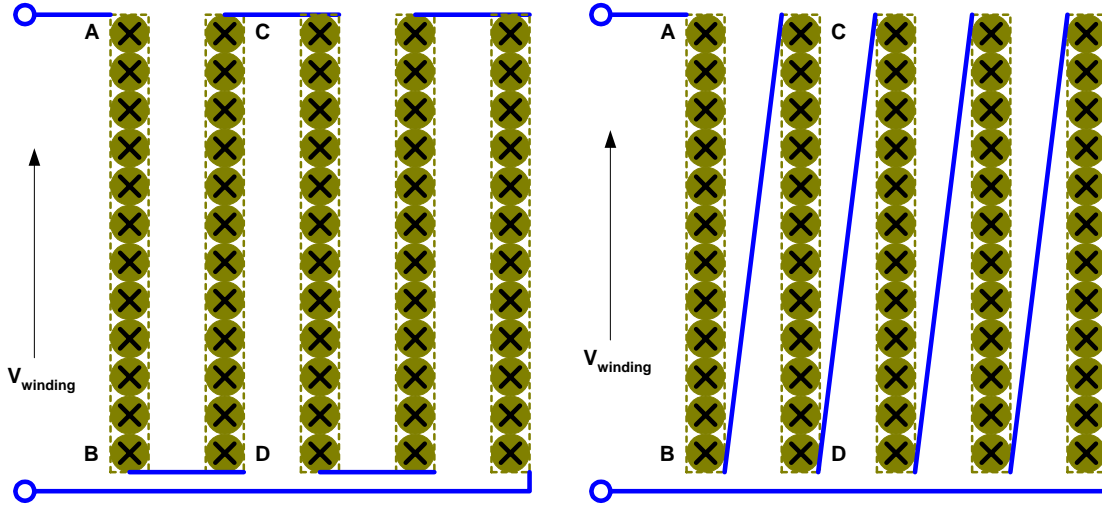


Fig. 4-12 Winding structures – wave wiring (left) and leap wiring (right)

The above discussion is valid for the situation of parallel flat winding layers. If the winding is cylindrical, or the curvedness of the winding can not be omitted, the equation (4-21) still holds true, except the structure capacitance is expressed as:

$$C_0 = \frac{2\pi \cdot \varepsilon_r \cdot \varepsilon_0 \cdot h}{\ln(r_2 / r_1)} \quad (4-24)$$

4.2.2. Transformer winding capacitance calculation

With the energy based method discussed above, we can calculate the winding capacitance of a magnetic core transformer. For a transformer with secondary floating, three terminal voltages can be defined as shown in Fig. 4-13 (a). As in equation (4-25), the total electrostatic energy stored in the transformer could be expressed in six items, which correspond to all capacitance between any two terminals.

$$W = \frac{1}{2} \cdot (C_{11} \cdot V_1^2 + C_{22} \cdot V_2^2 + C_{33} \cdot V_3^2 + 2C_{12} \cdot V_1 V_2 + 2C_{23} \cdot V_3 V_2 + 2C_{13} \cdot V_3 V_1) \quad (4-25)$$

However, these three voltages are not independent, and we can determine the voltage between primary and secondary windings V_3 as the function of primary and secondary terminal voltages V_1 and V_2 .

$$V_3 = -\frac{C_{13} \cdot V_1 + C_{23} \cdot V_2}{C_{33}}, \quad (4-26)$$

So, the high-frequency equivalent circuit of the transformer can be drawn as in Fig. 4-13 (b). If winding resistances are omitted for the analysis, we can have the energy stored in transformer expressed as:

$$W = \frac{1}{2} \cdot \left(C_1 \cdot V_1^2 + C_2 \cdot \left(\frac{V_2}{n'} \right)^2 + C_3 \cdot \left(V_1 - \frac{V_2}{n'} \right)^2 \right) \quad (4-27)$$

Through comparing equation (4-27) and (4-25) with (4-26), we can derive the lumped equivalent capacitances as:

$$C_1 = C_{11} - \frac{C_{13}^2}{C_{33}}$$

$$C_2 = n'^2 \cdot \left(C_{22} - \frac{C_{23}^2}{C_{33}} \right) \quad (4-28)$$

$$C_3 = -n' \cdot \left(C_{12} - \frac{C_{23} \cdot C_{13}}{C_{33}} \right)$$

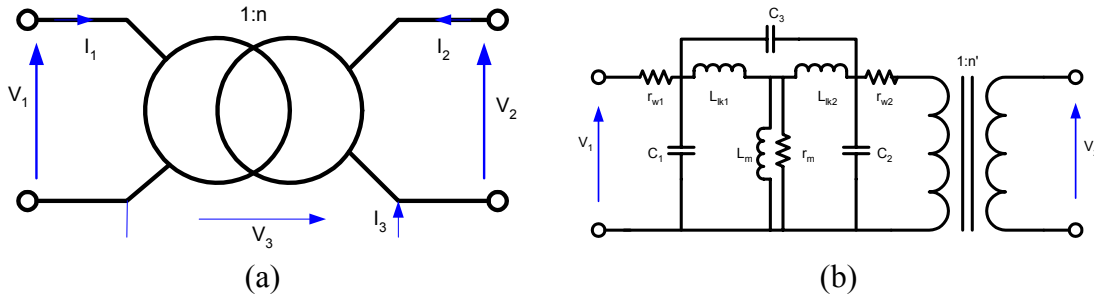


Fig. 4-13 Transformer terminal voltages (a) high-frequency equivalent circuit (b)

Actually, we can further reduce three equivalent lumped capacitors into one, by expressing secondary voltage with primary one, or vice versa. Although it is true from an energy storage point of view, the distributed characteristic of the winding capacitance makes the equivalent circuit capable of representing the transformer behavior to a high frequency range. Another point is that the transformer turns ratio in Fig. 4-13 (b) is the real ratio between the primary and secondary turn numbers, but it is not equal to the voltage ratio. Especially for resonant converter applications, leakage inductances cause a voltage drop, which cannot be omitted.

The magnetic core would have certain voltage potential, if the material is conductive, like most ferro-magnetic materials. Usually the core will be grounded just

like the primary winding. Winding capacitance of non-conductive magnetic core transformers would be complicated, and it is out of the scope of this thesis.

If other winding connection configurations are adopted, such as, common ground for primary and secondary windings, we just need to find out the value of V_3 and correlate equation (4-27) with (4-25).

4.3. Summaries

The 1-D energy-based leakage inductance calculation method has been proposed, with considering Litz wire eddy current effect. To find out closed-form solution of the transformer leakage field, Litz wire strands are equivalent into parallel plates which are along the core leg axis. Then the skin and proximity effects are calculated in the 1D rectangular coordinate system. The energy stored in the transformer window can be integrated, and the corresponding leakage inductance can be obtained. The calculation has been verified by the measurement results, and the transformer with the expected leakage inductance also is put into the PRC system.

Winding capacitance calculation is also based on the 1D static electric field assumption. The total stored electric energy in the transformer is related to the terminal voltages, and the corresponding lumped capacitances can be obtained.

The major advantage of the 1D parasitic modeling is that the parasitic calculation can be integrated into the transformer design iteration, which is quite important to the high frequency, high power applications. The tedious FEA methods could be avoided. The analytical method used here is limited to the certain regular structures, and the edge effect of the field distribution cannot be considered. The trade-off between accuracy and convenience in use can be evaluated for particular transformer application. For the typical high power transformer structure, the proposed method can provide satisfied parasitic results.

Both leakage inductance and winding capacitance calculation methods are heavily related to the insulation material characteristics, transformer geometry and manufacturing process. Therefore, the calculation results should be correlated to the prototype preparation for the first time.

Chapter 5 The PRC System Case Study

The transformers discussed in this work are for the DC-DC converter systems with power rating 10 kW above and operation frequency range between 100 kHz and 1 MHz. Among the traditional industrial applications, induction heating [5-1]-[5-2] and electric welding [5-3] are the fields employing or potentially expecting the high density transformers within those power and frequency ranges.

High voltage, pulse power converters would be another kind of application requiring high density isolation transformers, such as laser and plasma applications [5-4]-[5-6]. Step-up transformers with a larger turn's ratio could be the challenge to this type of system.

The development of more electric vehicles [5-7] and aircrafts [5-8] provide the prosperous stages of high density DC-DC converter systems for high-power, high-frequency operations. Apparently, power density is important due to the mobile nature of these applications. Transformers have always been one of the major barriers to improving the system power density.

As a typical study case, the transformer of a parallel resonant converter (PRC) charging system has been designed, developed and tested, to verify the proposed loss and parasitic calculation methods. Basically, the resonant inductance required for a 30 kW PRC module will be realized by the leakage inductance of the transformer. The winding capacitance of the transformer is way smaller than the required resonant capacitance, so winding capacitance will be absorbed by the extra capacitance. The nanocrystalline soft magnetic material is used as the transformer core. The pulsed power nature of the PRC system has been considered during the transformer design, since the thermal capacitances of transformer core and windings are effective on temperature rises. Through varying C-core dimensions, we can obtain the minimum size design of the transformer. The minimum-size transformer design procedure is programmed and applied to the prototype development. The experimental results of prototyping transformers are reported.

5.1. Transformer specifications of the PRC operation

U.S. Army Research Lab (ARL) is interested in developing a high density, high power, and high voltage DC/DC converter. This type of converter system will be used in pulsed power applications to charge high-energy capacitor banks. The primary technical challenge is to achieve the power density goal under a harsh environmental condition. Table 5-1 shows the main specifications for the target converter system. Here we can find

out the equivalent load capacitance as: $C = \frac{2 * 15 * 10^3}{(10 * 10^3)^2} = 0.3mF$.

Table 5-1 System Specifications

Parameter	Specification
Input voltage	600 VDC
Output voltage	10 kVDC
Output power	30kW
Efficiency	> 80%
Thermal management	65 °C
Load	15 kJ capacitor bank

Based on the topology literature survey, it can be summarized that phase shift ZVS PWM and resonant converters are the most popular topologies for high voltage, high power capacitor charging power supplies. Non-isolation topology, such as boost converter is seldom found for this application. It is partly due to the extremely high voltage gain which requires near unit duty cycle ($D = 0.94$). The major reason behind the selection of transformer-isolated topologies is the idea of better utilization of the semiconductor devices. With transformers, primary switches see lower input voltage and higher currents, while switches on the secondary side would block high output voltage and carry smaller currents.

For isolation topology, the high voltage high power capability transformer is considered the most critical part of the whole system. In order to shrink the transformer volume, the high frequency operation is preferable. Zero voltage (ZVS) and zero current (ZCS) switching can effectively reduce the switching loss and therefore will be adopted.

Both the phase shift PWM and the resonant converters can realize the ZVS and ZCS operation [5-9]-[5-10].

To develop a high power-density 10kV 30kW pulse power converter module, we choose the three level parallel resonant converter (PRC) topology, as shown in Fig. 5-1 [5-11], running in zero-voltage switching (ZVS) mode. The MOSFETs are used as switching devices so the switching frequency can be pushed up to 200 kHz to shrink the size of the passive components including the isolation transformer. The transformer design objective is to achieve the highest power density possible, while the transformer operates within its thermal limits and its parasitics can be controlled precisely. With leakage inductances and winding capacitances predicible and controllable at the design stage, we can perform optimization not only of the transformer itself, but also of the converter system.

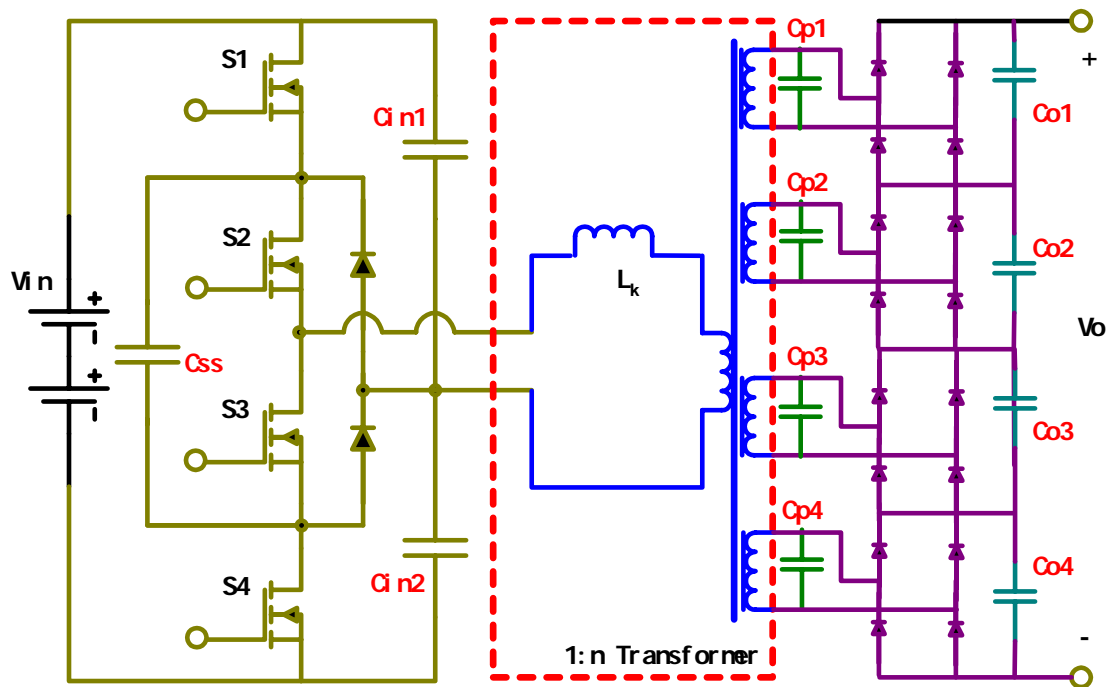


Fig. 5-1 The three-level PRC converter for pulse power applications

For the given topology, the operating specifications and waveforms imposed on the transformer would be derived in the subsequent section. Instead of using cut-and-try methods, we first solve the circuit state variables to analyze the converter operation, and then the specifications of the transformer are determined according to design of the converter.

5.1.1. PRC operation analysis

To analyze the operation of the PRC shown in Fig. 5-1, we can simplify and redraw the circuit as in Fig. 5-2, without changing the major characteristics. Putting the resonant capacitor on the primary side would cause the transformer's primary current to be different from the case of the resonant capacitor on the secondary. We can use the inductor current i_L , which is actually the transformer's primary current. If the resonant inductance is fully realized by the leakage inductance of the transformer, then the voltage waveform applied to the primary winding would be different from the secondary voltage which is actually shown in Fig. 5-2 as V_{cp} . Since the leakage inductance of the transformer is distributed in windings and insulation layers, the real volt*second applied to the core would not be the same as V_{cp} . However, the leakage inductance derived in this work is a lumped representative of the total energy stored in the transformer, the typical waveform of V_{cp} is still used for the core loss calculation during the transformer design in this section.

The first harmonic [5-13] and steady-state [5-12] analysis approaches have been proposed for the PRC operation. The converter should be designed always running at the CCM ZVS condition, so the typical resonant voltage and current waveforms are shown in Fig. 5-2, and the detailed operation subintervals are listed in Table 5-2. Two moments, t_{a1} and t_{a2} , and two current values, $i_L(0)$ and $i_L(t_{a2})$, are key parameters to describe the operation. They can be found by matching the steady-state boundary conditions.

$$\left\{ \begin{array}{l} \omega_0 \cdot (t_{a2} - t_{a1}) = \arccos \left(\frac{V_g - V_s - V_0 + 2V_{D2}/n}{V_g - V_s + V_0 + 2V_{D2}/n} \right) \\ i_L(t_{a2}) = \frac{1}{Z_0} [V_g - V_s + (V_0 + 2V_{D2})/n] \cdot \sin \omega_0(t - t_{a1}) \\ i_L(0) = -i_L(t_{a2}) - [V_g - V_s - (V_0 + 2V_{D2})/n] \cdot (\frac{T_s}{2} - t_{a2})/L \\ i_L(0) = -[V_g - V_s + (V_0 + 2V_{D2})/n] \cdot t_{a1}/L \end{array} \right. \quad (5-1)$$

Where V_s is the switch voltage drop, V_{D1} is the freewheeling diode voltage drop, V_{D2} is the rectifier diode voltage drop, in the PRC circuit.

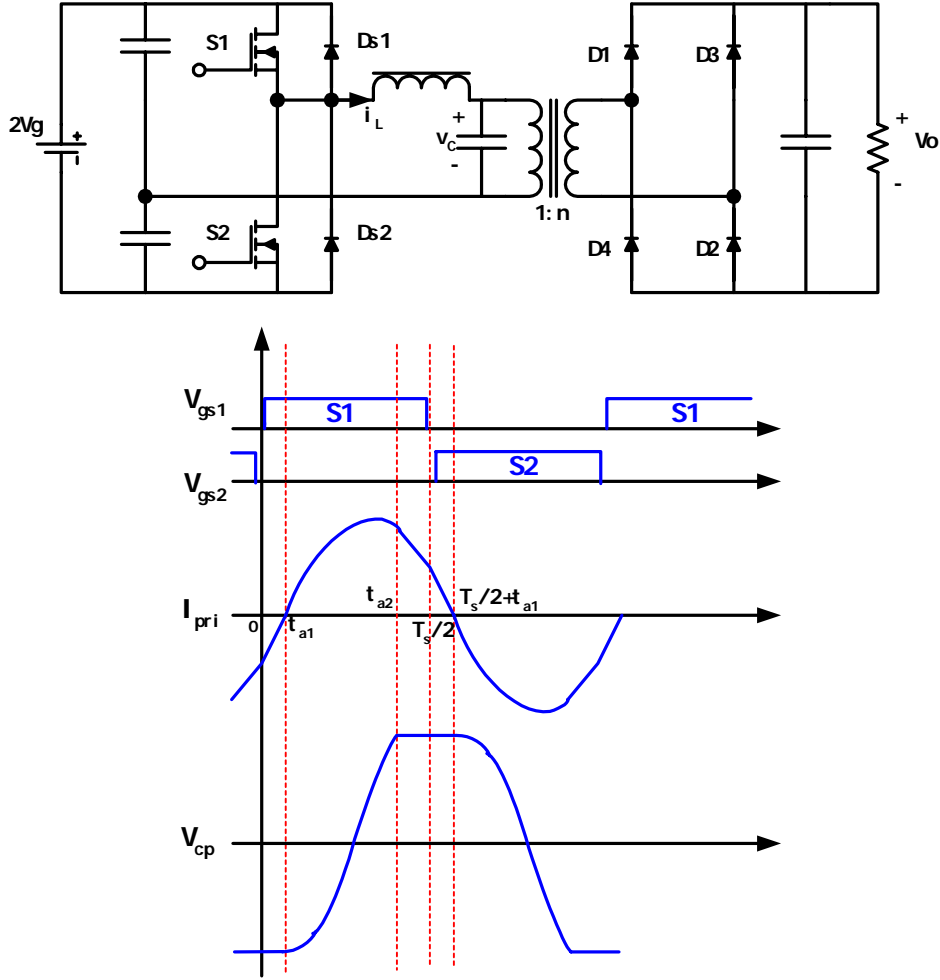


Fig. 5-2 Capacitive filter half bridge PRC converter and resonant voltage and current

Table 5-2 PRC operation mode analysis

Operation intervals	Equivalent circuit	Resonant voltage and current expressions
Circulating stage: [0 t _{a1}]		$i_L(t) = i_L(0) + [V_g + V_{D1} + (V_o + 2V_{D2})/n] \cdot t/L$ $v_C(t) = -(V_o + 2V_{D2})/n$
Resonant stage: [t _{a1} t _{a2}]		$i_L(t) = \frac{1}{Z_0} [V_g - V_s + (V_o + 2V_{D2})/n] \cdot \sin \omega_0(t - t_{a1})$ $v_C(t) = V_g - V_o - [V_g - V_s + (V_o + 2V_{D2})/n] \cdot \cos \omega_0(t - t_{a1})$
Delivery stage: [t _{a2} T _s /2]		$i_L(t) = i_L(t_{a2}) + [V_g - V_s - (V_o + 2V_{D2})/n] \cdot (t - t_{a2})/L$ $v_C(t) = (V_o + 2V_{D2})/n$

The analysis is normalized so that it may be applicable to any specified set of values for operating conditions. All secondary values are also converted to primary side.

The base values are chosen as:

$$\left\{ \begin{array}{l} V_{base} = V_g \\ R_{base} = Z_0 = \sqrt{\frac{L}{C}} \\ I_{base} = \frac{V_g}{Z_0} \\ \omega_{base} = \omega_0 = \frac{1}{\sqrt{L \cdot C}} \end{array} \right. \quad (5-2)$$

The steady state operation of the PRC converter can now be fully described. First the output current can be derived as:

$$n \cdot I = \frac{2}{T_s} \cdot \left[- \int_0^{t_{a1}} i_L(t) \cdot dt + \int_{t_{a2}}^{T_s/2} i_L(t) \cdot dt \right] \quad (5-3)$$

Then, the normalized output current can be expressed as the function of the normalized output voltage M and frequency F . Therefore, the PRC output characteristic can be plotted in Fig. 5-3.

$$J = \frac{2\pi}{F} \left\{ \begin{array}{l} \left[(1+M) \cdot \left[(1-M) \cdot \left(\frac{\pi}{F} - \arccos\left(\frac{1-M}{1+M}\right) \right)^2 / 2 + (1+M) \cdot \left(\frac{\pi}{F} - \arccos\left(\frac{1-M}{1+M}\right) \right) \cdot \sin \arccos\left(\frac{1-M}{1+M}\right) \right] \right] \\ - \left[(1+M) \cdot \sin \arccos\left(\frac{1-M}{1+M}\right) \right]^2 / 2 \end{array} \right\} \quad (5-3)$$

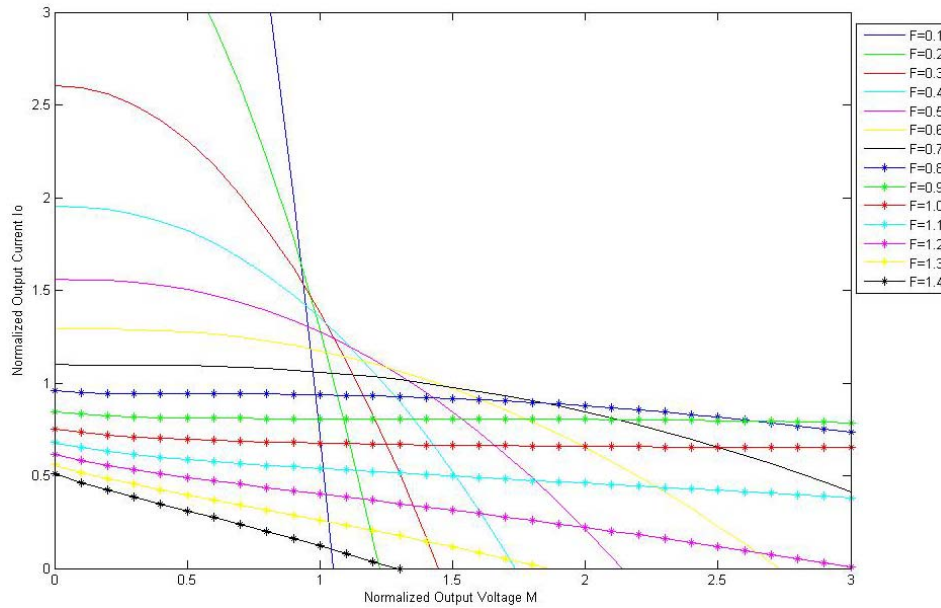


Fig. 5-3 Capacitive filter half bridge PRC converter normalized output characteristic

The PRC converter performs a like current source for the normalized frequency higher than 0.8. This characteristic makes it suitable for charging applications where the output current needs to be controlled. It is also possible to picture the converter performance in another way; a voltage gain curve. Here the quality factor is $Q = \frac{Z_0}{R_l}$ which has a clear meaning for resistive loads.

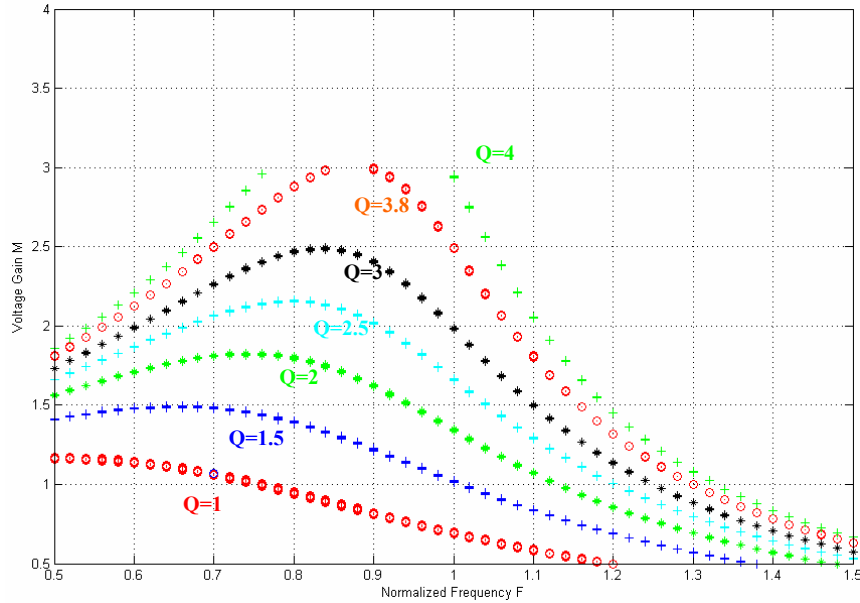


Fig. 5-4 Capacitive filter half bridge PRC converter normalized gain curve

5.1.2. Transformer parameter determination

According to the given specification, we need to design the PRC to charge a 0.3 mF capacitor within 0.55 s up to 10 kV. It can be derived that the charging current should be $0.3 \cdot 10^{-3} \cdot 10 \cdot 10^3 / 0.55 = 5.5$ A, if the constant current charging is applied. But the peak output power will be 55 kW at the end of the charging. Therefore, hybrid charging schemes are adopted, which combine constant current and constant power charging, as shown in Fig. 5-5. The current value at the initial constant portion must be bigger than 5.5 A, to ensure the charging time requirement. The upper limit of the current should be the rectifier diode rating and certain margins.

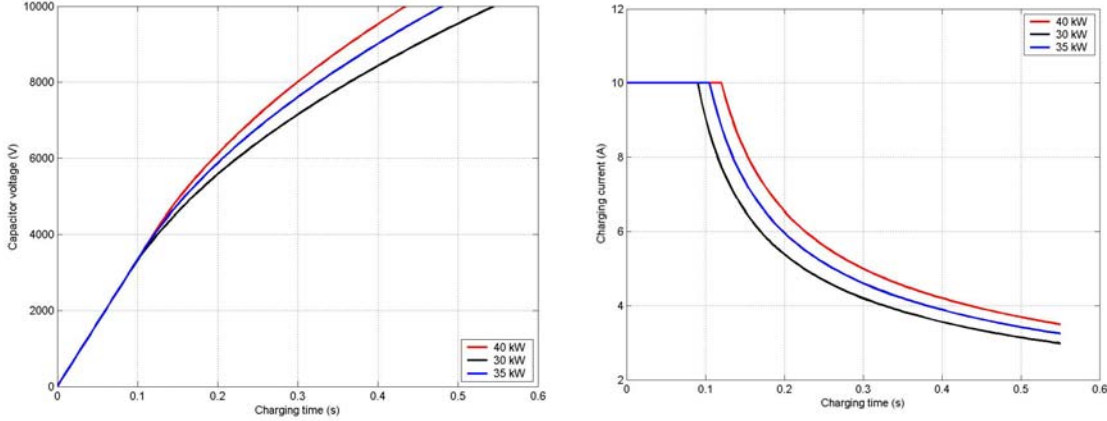


Fig. 5-5 Hybrid charging schemes

After determining the charging scheme, we design the PRC converter to make sure it can output the required currents and voltages by certain kinds of control. We need to normalize the load capacitor power rating by equation (5-4), so that we can compare it with the converter output characteristic in Fig. 5-3.

$$P_{base} = V_{base} \cdot I_{base} = \frac{V_g^2}{Z_0} \quad (5-4)$$

In Fig. 5-6, 30 kW constant power charging trajectories are plotted along with the normalized PRC converter output characteristic, for a different value of Z_0 . It indicates that the converter cannot charge the load capacitor with 30 kW constant power in certain regions, if we choose $Z_0 = 5$. On the other hand, we do not want Z_0 to be too small, which means a large amount of circulating energy in the PRC converter. Therefore, the cutting-edge value, $Z_0 = 3.8$, has been chosen for 30 kW constant power charging. Together with the pre-selected resonant frequency $f_0 = 200$ kHz, we can fully determine the resonant tank values as:

$$\begin{cases} \sqrt{L/C} = 3.8 \\ \frac{1}{\sqrt{L \cdot C}} = 2\pi * 200 * 10^3 \end{cases} \Rightarrow \begin{cases} L = 3\mu H \\ C = 211nF \end{cases} \quad (5-5)$$

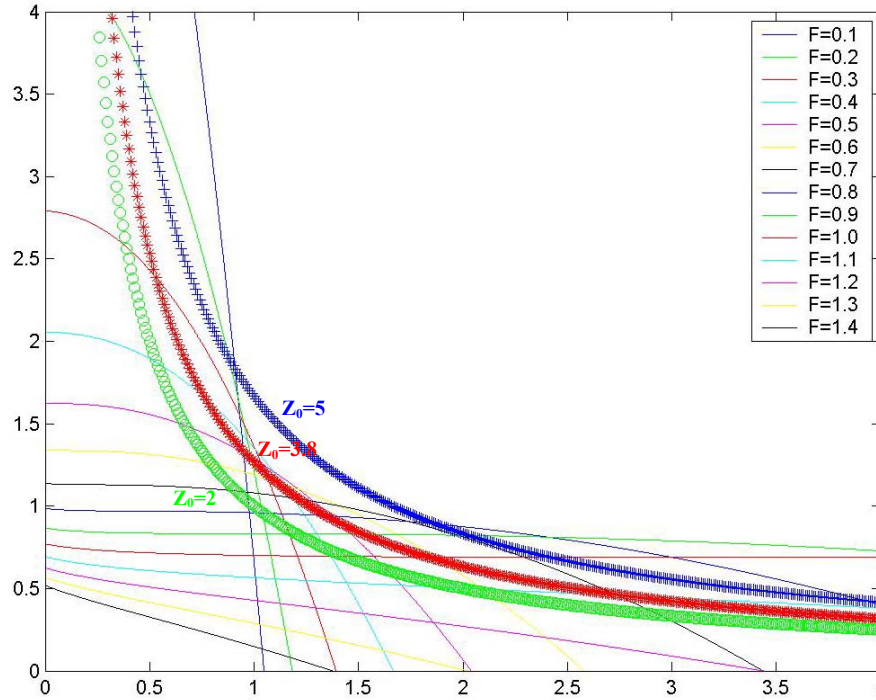


Fig. 5-6 Capacitive filter half bridge PRC converter normalized gain curve

Since normalized curves are used, we just need to command the PRC to operate along the red curve shown in Fig. 5-6. However, we need to determine the transformer turn's ratio, which will correlate the normalized voltage gain and the x-axis with real output voltage. For example, if we choose the transformer ratio as $n = 11$, the output

voltage 10 kV will be correlated to $M = \frac{V_{out}}{n \cdot V_g} = \frac{10000}{11 \cdot 300} = 3.03$.

Correspondingly, the normalized initial constant charging current value can be found as $J = \frac{I_{ch} \cdot n \cdot Z_0}{V_g} = \frac{10 \cdot 11 \cdot 3.8}{300} = 1.4$. So, we can find out the whole charging trajectory on the PRC output curves. The voltage-to-frequency relationship can be read from the plot, and the control can be made according to it.

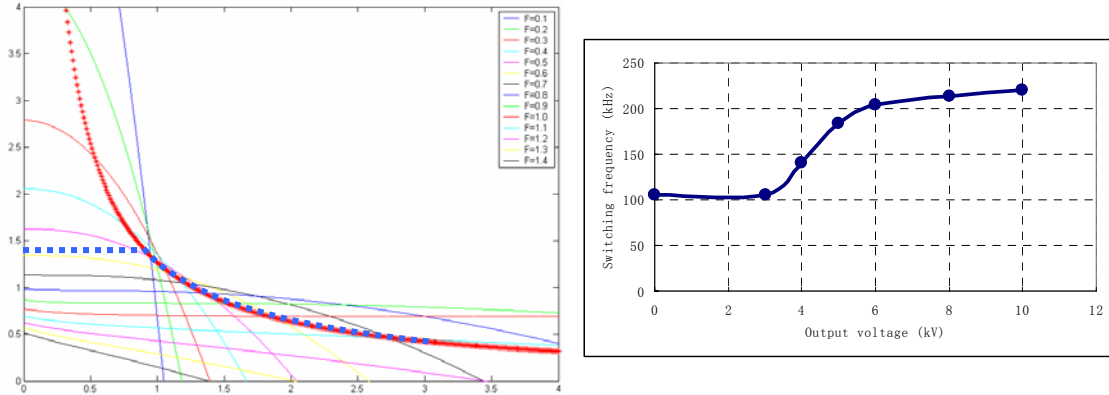


Fig. 5-7 30 kW hybrid charging trajectory

Until now, the PRC converter have been designed to fulfill the charging requirements, and the transformer specifications, including turn's ratio, operating frequency, voltage and current waveforms have been determined. In the next section, the design procedure will be explored, for the given specification here.

5.2. Transformer minimum-size design procedure

Several previous works have reported findings regarding optimal high-frequency transformer design [5-14]-[5-18], but none of them can be directly applied to the PRC charging application. The resonant voltage waveforms need to be considered of core loss calculation, and leakage inductance calculation of Litz wire winding has to be included in the design procedure. Therefore, the minimum-size design procedure of the 30 kW PRC charger system is discussed in this chapter.

5.2.1. Consideration of variable frequency effect

One of the major challenges that the resonant converter operation imposes on transformer designs is the varying operating frequency. Usually, the transformer design needs to consider the worst case: the highest operation frequency and maximum volt*second requirements. This would result in over-design, since the highest operation frequency usually does not coincide with the highest volt*second requirement.

Winding loss is impacted by the varying frequency. The eddy current and proximity effects are all functions of frequency, and winding AC resistance will increase as frequency increases. For our case, the RMS value of transformer winding current decreases, because of the constant-power control scheme chosen, while frequency

increases within one operating pulse. Therefore, winding loss does not vary much within one operating pulse, and we can choose the wire gauge according to the maximum operating frequency.

For core design, we must know both the frequency and volt*second varying profile within one operating pulse. As shown in Fig. 5-8, the maximum operating frequency, which is three times that of the lowest frequency, happens at the end of the charging cycle, and the maximum volt*second applied to the transformer appears near the starting point.

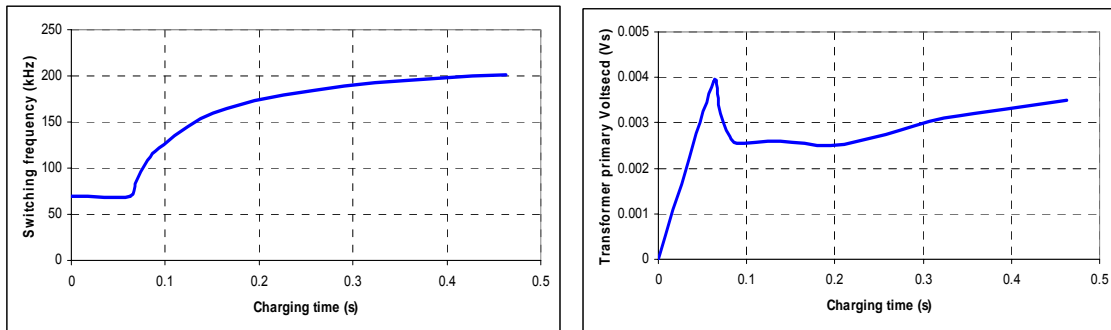


Fig. 5-8 Operating frequency (left) and V*S (right) of the application

Knowing frequency and volt*second applied to the transformer, we can calculate the core losses of a certain design (detailed core loss calculation can be found in next section), as in Fig. 5-9. The transformer core loss will vary along with the charging period, as a function of frequency and flux density. For 30kW power rating, the transformer thermal time constant is much larger than the pulse time, so we can use an equivalent “quasi-average” core loss which can cause the same temperature rise as the time-varying loss, within one charging cycle.

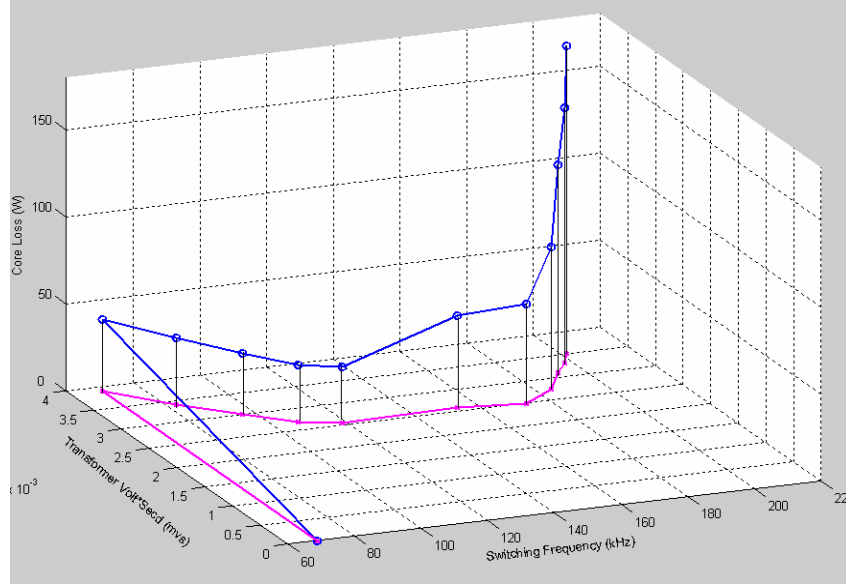


Fig. 5-9 Calculated core loss profile within one charging

The “quasi-average” core loss within one charging can be derived, with frequency and volt*second being noted as $f(t)$ and $\lambda(t)$:

$$\begin{aligned} \bar{P}_c &= \frac{\int_0^{T_{charge}} P_c(t) \cdot dt}{T_{charge}} = \frac{V_c \cdot \int_0^{T_{charge}} K \cdot f(t)^\alpha \cdot \Delta B(t)^\beta \cdot dt}{T_{charge}} \\ &= \frac{K \cdot V_c}{(2n \cdot A_c)^\beta \cdot T_{charge}} \cdot \int_0^{T_{charge}} f(t)^\alpha \cdot \lambda(t)^\beta \cdot dt \end{aligned} \quad (5-6)$$

Based on the derived “quasi-average” core loss, the core design can be treated as conventional fixed-frequency, fixed-voltage operation design. First, the maximum volt*second, λ_{max} , is assumed to be applied for a whole charging cycle, since the design transformer would not saturate for all charging points by doing this. Then, we can obtain an equivalent switching frequency, which would generate the “quasi-average” core loss for the fixed flux density chosen.

$$f_{eq-fixed} = \left[\frac{\int_0^{T_{charge}} f(t)^\alpha \cdot \lambda(t)^\beta \cdot dt}{\lambda_{max}^\beta \cdot T_{charge}} \right]^{\frac{1}{\alpha}} \quad (5-7)$$

With all abovementioned, we can apply any conventional transformer design and optimization methods, for fixed frequency and voltage applications. The advantage of this transformation is that we do not over design the transformer as compared to the conservative method, which uses all the maximum values. Actually, the maximum value

design method will calculate the core loss at about 3.5 times that of the real average core loss for our application, which results in a much bigger core design.

5.2.2. Minimum-size Design procedure

Fig. 5-10 illustrates the procedure for a minimum-size transformer design for a given application. Clearly the relationships between design variables, constraints, and conditions must be established for a successful design. The key relationships include the loss models and parasitic models discussed above, as well as the thermal model to be discussed later in the section.

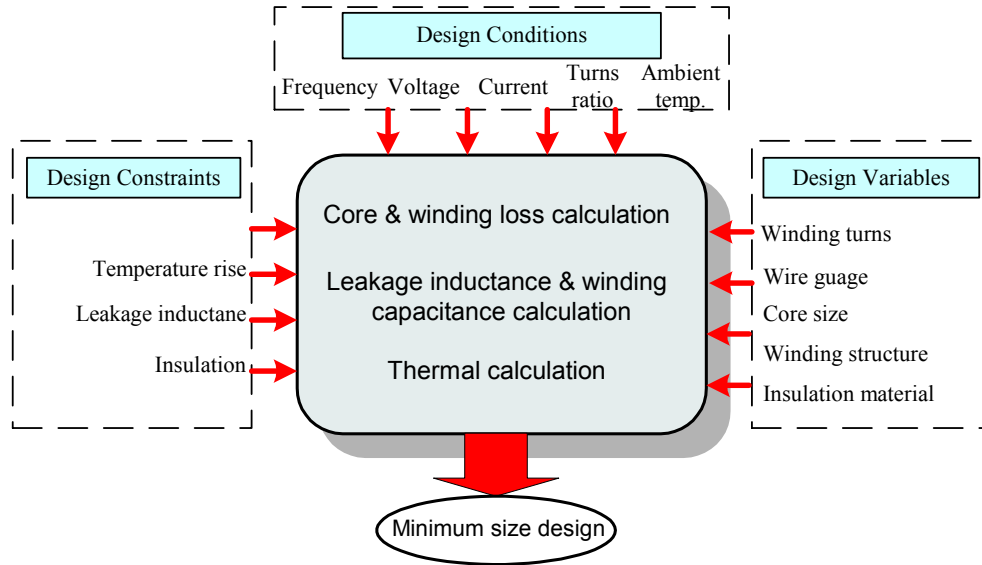


Fig. 5-10 Minimum size transformer design procedure

For a certain core, the core and winding loss can be expressed as the function of flux density if the operating conditions are given, as shown in Fig. 5-11. It is obvious that the core loss increases as the flux density increases. The opposite trend can be observed for the corresponding winding loss, since higher flux density means less turns and smaller resistance for the same core.

$$p_c = V_c * K * f_{eq-fixed}^\alpha * (\Delta B)^\beta \quad (5-8)$$

$$p_w = K_r \cdot I_{rms}^2 \cdot \frac{\lambda^2 \cdot \rho \cdot (MLT)}{4A_{window} \cdot K_u \cdot A_c^2} \cdot \left(\frac{1}{\Delta B}\right)^2 \quad (5-9)$$

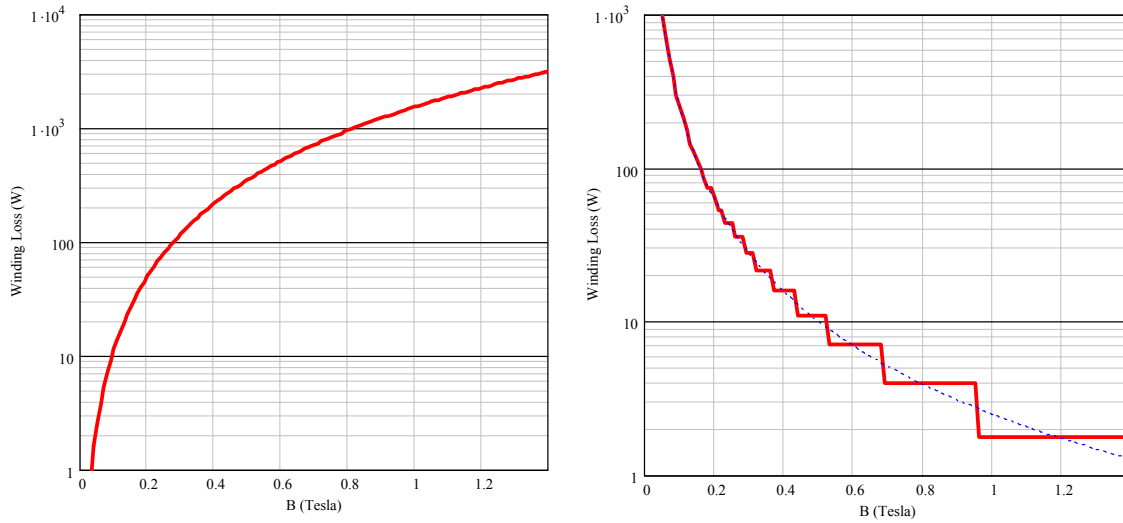


Fig. 5-11 Core loss (left) and winding loss (right) as function of flux density

When the dielectric loss is omitted, the total loss of the transformer can be obtained by adding the core loss and the winding loss together. Therefore, an optimal flux density can be found, for which the total loss is minimal. This means that with this core the minimum loss can be achieved if we design the core running at the B_{op} , as shown in Fig. 5-12. The optimal flux density B_{op} for each core can be found, under the minimum loss condition, $\frac{\partial p_{tot}}{\partial B_{pk}} = 0$. The most interesting aspect of this is that the optimal operating flux density does not necessarily happen at the point where core loss equals winding loss.

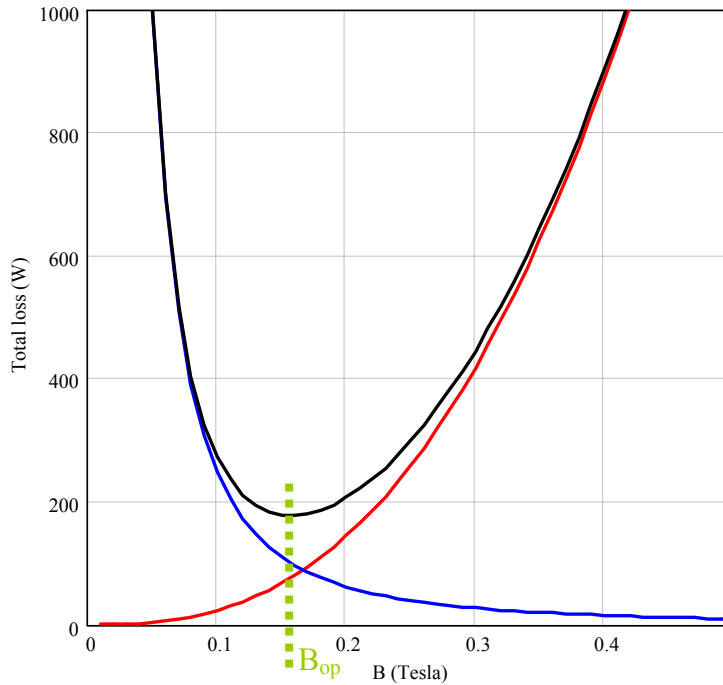


Fig. 5-12 Optimal flux density for minimum total loss

A set of total losses is shown in Fig. 5-13, for transformers using different FT-3M nanocrystalline C-cores (U-U cores) and application conditions listed in Table I. Since the C-core dimension can be changed continuously for a full customized design, we can achieve minimum size design.

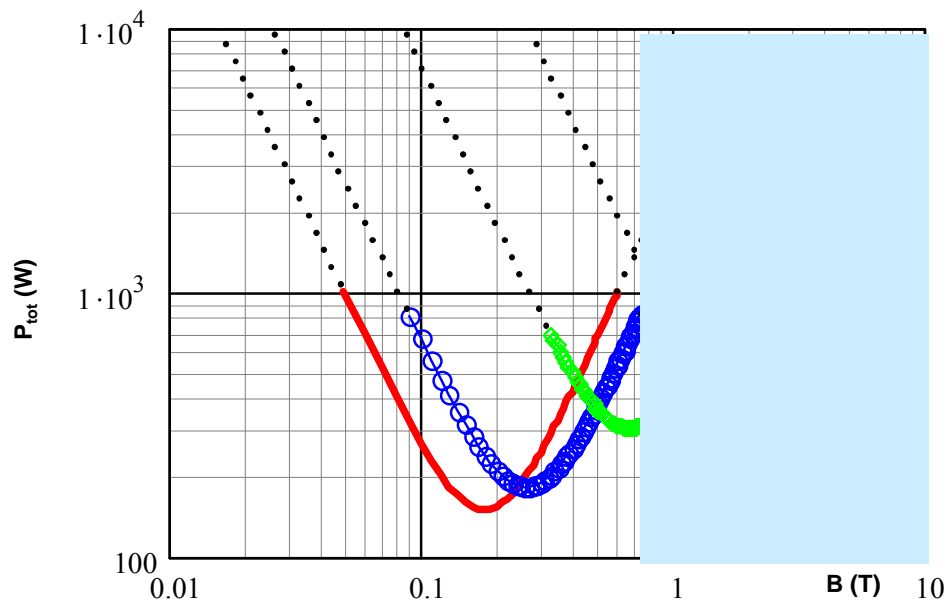


Fig. 5-13 Total losses of the 30 kW transformer using different C-cores

The design should avoid the shaded area to avoid saturation. For a given core, the valid design must also have a total loss below a certain limit to stay within the temperature limit. In Fig. 5-13, only the solid portion of the curves are valid for loss and temperature consideration. For a given core, through calculating conduction, convection, and radiation heat-transfer effects, we can determine the optimal loss for certain temperature rise requirement. Apparently, the thermal calculation is a process of iteration. Many 1-D transformer thermal models have been developed [1]-[2], and can be adopted for the design procedure.

Thus, Fig. 5-13 can be used to select the core and for the given core determine the optimal operating flux density for minimum loss. For example, we can use the U67/27/14 core running at 0.6 Tesla, with minimum 300W losses. For the same application, a design using U93/76/30 core at 0.3 Tesla would have a minimum 200W total losses. Within the temperature limit, the former core is preferred for its smaller size. Similar charts can be generated for other available cores and materials. The design results can be clearly compared.

In the optimization procedure, leakage inductance objective functions can also be set, in addition to total loss and temperature rise requirements.

5.3. Prototyping and Testing Results

Several transformer prototypes have been made for the 30 kW PRC charger. Nanocrystalline material cut cores and Litz wire windings are used for the prototypes. The structure of the transformer is illustrated in Fig. 5-14. Two sets of identical windings are put on each leg of the C-cores, so we can realize interleaving winding to reduce the eddy current effect. Actually, the resonant inductance is fully realized by the leakage inductance of the transformer, so the distance between primary and secondary is tuned to ensure the leakage inductance and the 10 kV insulation requirements can be satisfied.

The C-core is chosen mainly for availability and for better balanced secondary outputs, since we have multiple secondary outputs and they are required to be identical to reduce the mismatch effect on resonant operation. A small inevitable air gap is introduced, which can reduce the temperature dependence of the nanocrystalline material and improve saturation proneness.

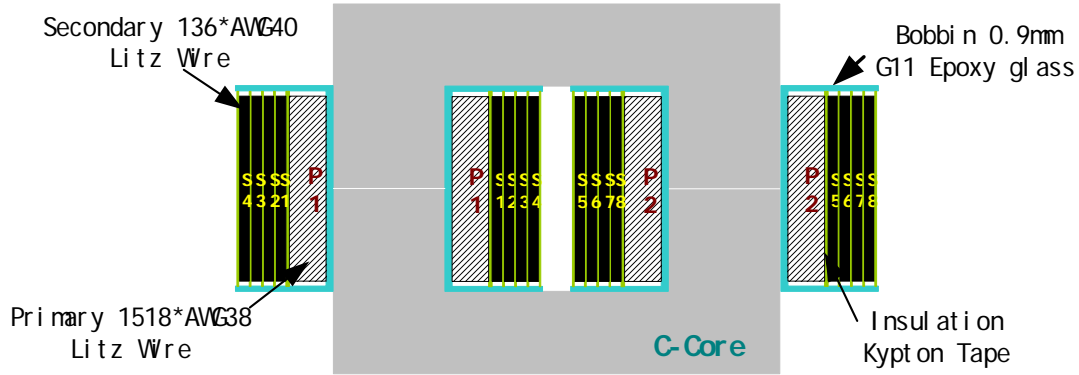


Fig. 5-14 Transformer prototype structure

Table 5-3 shows the transformer specifications and design results for the prototype transformer. For comparison purposes, a ferrite-based transformer is also designed and prototyped, together with a FT-3M nanocrystalline core based transformer. The design followed the procedure presented in the previous section. Clearly, the nanocrystalline core transformer (1064 W/in³) is considerably smaller than the ferrite one (341 W/in³) as shown also in Fig. 5-15. Note: the differences between single pulse temperature rises and continuous ones are due to thermal capacitance of transformer cores and windings.

Table 5-3 Transformer design specs and parameters

Conditions and constraints			
Primary voltage	280~325 V	Max. volt*sec	0.003 V*sec
Max. Secondary voltage	10 kV	Turns ratio	11
Max. Primary current	170 A	Frequency	79~200 kHz
Ambient temperature	65 °C		
Maximum temperature	120 °C		
Designed parameters			
	Ferrite (Magnetic P)	Nanocrystalline (FT-3M)	
C-Core	U93/76/16	2*U67/27/14	
Flux density	0.203 T	0.613 T	
Primary winding	22 turns	8 turns	
	2430*AWG38	1518*AWG38	
Secondary winding	240 turns	88 turns	
	370*AWG40	136*AWG40	
Core loss (average)	154 W	212 W	
Winding loss	217 W	391 W	
Core window fill factor	0.25	0.2	
Core T _{rise} (1 pulse)	2 °C	3 °C	
Winding T _{rise} (1 pulse)	8 °C	10 °C	
Temp. rise (continuous)	20 °C	55 °C	
Power density	341 W/in ³	1064 W/in ³	

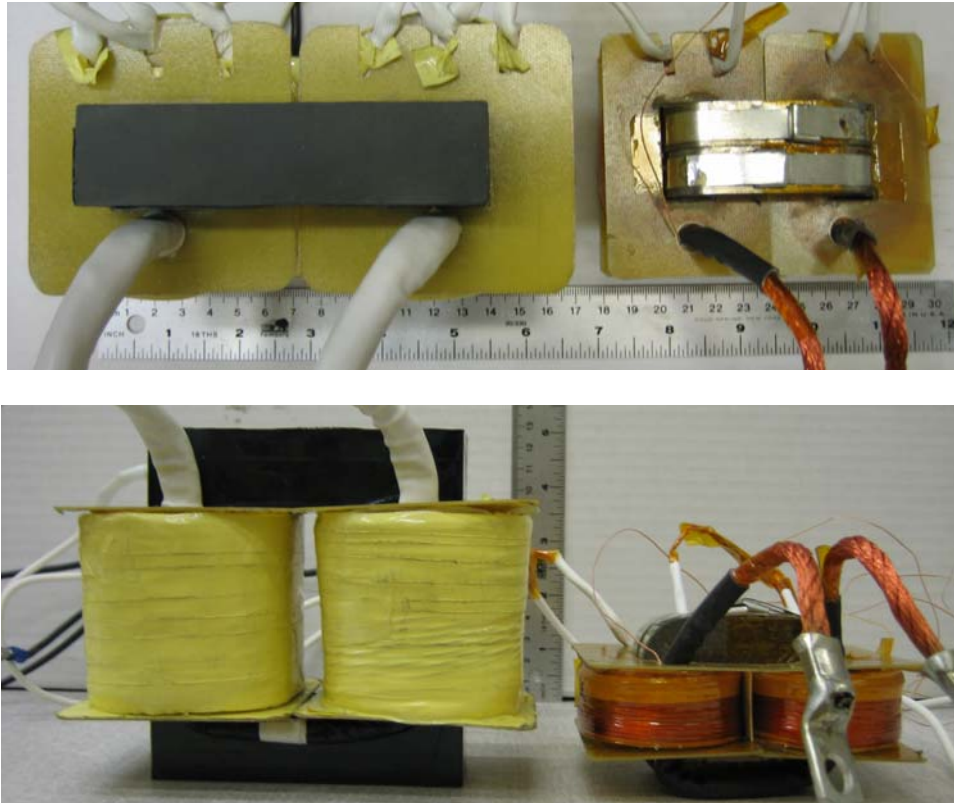


Fig. 5-15 30 kW ferrite core (left) and FT-3M nanocrystalline core (right) transformer prototypes



Fig. 5-16 30 kW PRC system with the nanocrystalline transformer

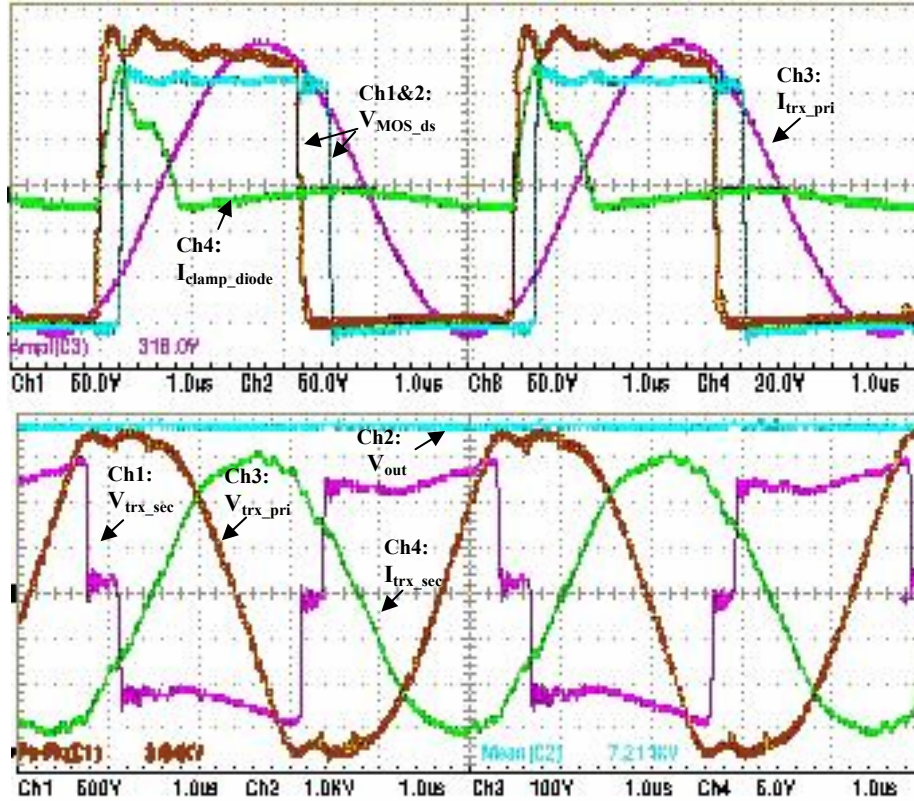


Fig. 5-17 Measured transformer primary voltage and current waveforms of the PRC during charging (current channels with 1 A/V conversion ratio)

The power density achievable is strongly related to the environmental and cooling condition, and in the case of the pulse power application, also the pulse duty cycle. Note in Table 5-3, both materials use the same temperature limit of 120°C for comparison, though the nanocrystalline core can probably have a higher temperature. The results also show that both the ferrite and nanocrystalline transformers have temperature margins, so theoretically smaller sizes can be achieved for both the designs. The ferrite design could also be improved more. In fact, if both designs would fully exploit thermal margins, 1000 W/in³ could be achieved for the ferrite and 1300 W/in³ for the nanocrystalline design. In practice, since the chosen ferrite has a minimum loss of around 80°C, out of concerns for practical converter applications, more margins are introduced in the prototypes. In any case, the nanocrystalline magnetic core will lead to a smaller transformer size. Another important consideration is the insulation requirement for the transformer. Both prototypes passed the DC high potential test at 15kV for 10kV maximum working voltage.

Both the ferrite and nanocrystalline transformers have been tested with PRC circuit as shown in Fig. 5-1. The prototype converter system with the nanocrystalline transformer is shown in Fig. 5-16. The PRC converter is tested up to full average power of 30kW at 220 kHz switching frequency, and the transformers worked as expected. The selected waveforms are shown in Fig. 5-17.

The thermal model of the transformer can be derived with considering natural convection heat transfer [5-19]. The thermal network of the transformer prototype is shown in Fig. 5-18. The thermal capacitances of core and windings have to be included for the pulsed power. The core loss and winding loss are applied separately to the thermal network, and two calculated temperature rises are obtained as shown in Fig. 5-19. The calculated temperature rises are verified by the measured results as in Fig. 5-19.

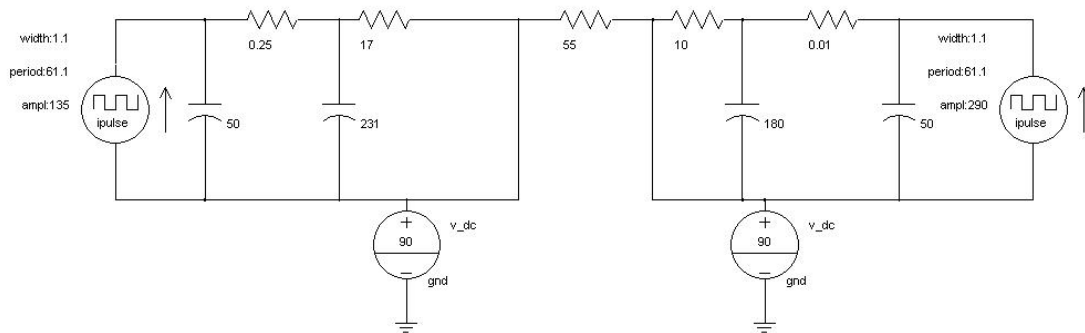


Fig. 5-18 The thermal network of the nanocrystalline transformer

For one charge cycle, the temperature rise of the transformer core and windings are below 5°C , under the ambient temperature 65°C . These are below and reasonably close to the expected values as shown in Table 5-3. For continuous charging, the steady state transformer core and winding temperature rises have been predicted using the same thermal network and losses. The results are shown in Fig. 5-20.

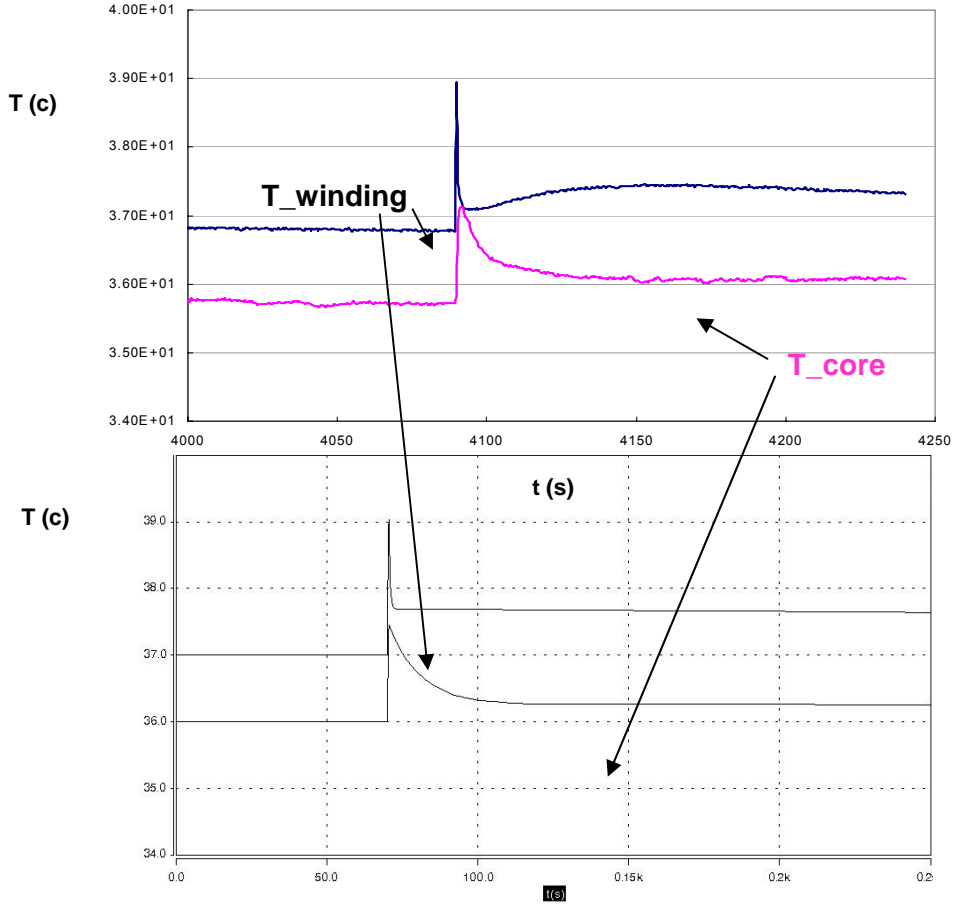


Fig. 5-19 Calculated (top) and measured (bottom) temperature rises of the transformer prototype for one charging operation

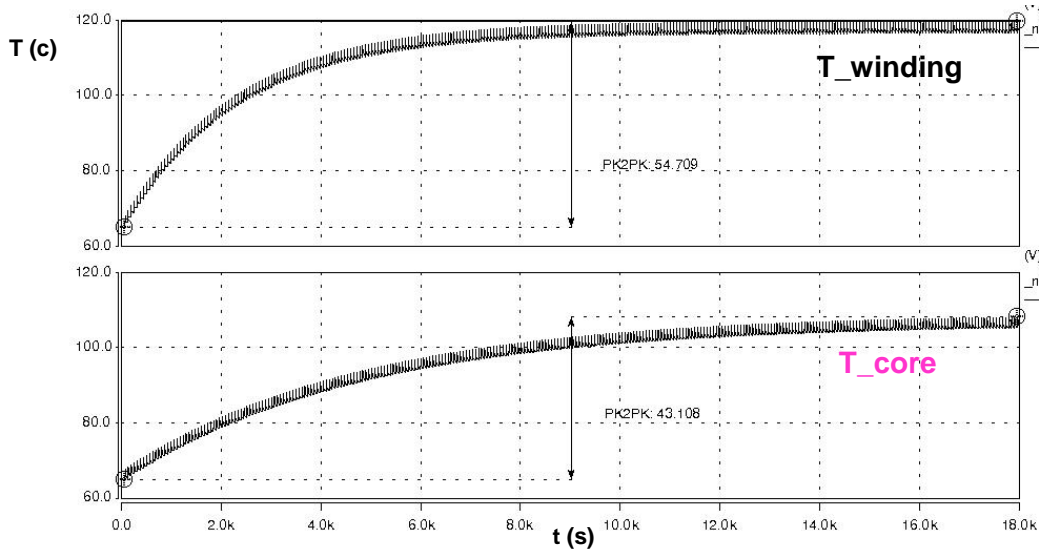


Fig. 5-20 Winding (top) and core (bottom) temperature rises of the transformer prototype for continuous charging operation

5.4. Summaries

The transformer parameter determination for the PRC system has been went through. Required voltage and current waveforms of the transformer have been derived through analytic equations. The transformer turn's ratio has been determined according to the resonant voltage gain selection. C-core with split-winding on both legs is the transformer structure.

A transformer with nanocrystalline core is developed for a 30 kW, 200 kHz resonant converter, and achieves a pulse power density of 1064 W/in³. Compared with other materials such as ferrite, nanocrystalline cores can lead to higher power density transformers because of their desirable characteristics of high saturation flux density, low loss, and low temperature dependence. For pulse power variable resonant converter applications, the transformer can be designed considering the maximum volt-seconds, a quasi-average frequency, together with other usual constraints.

The resonant inductance required for a 30 kW PRC module will be realized by the leakage inductance of the transformer. The winding capacitance of the transformer is way smaller than the required resonant capacitance, so winding capacitance will be absorbed by the extra capacitance. The pulsed power nature of the PRC system has been considered during the transformer design, since the thermal capacitances of transformer core and windings are effective on temperature rises. Through varying C-core dimensions, we can obtain the minimum size design of the transformer.

The prototype transformer has been tested by putting in the PRC charging module, and all electrical requirements have been fulfilled. Thermal and insulation of the transformer have been verified. Although the studied case is a pulsed power application, the development method proposed in this work can still be applied to the continuous operation converter systems. Apparently, the achievable power density of the continuous power would be smaller than the one shown here.

Chapter 6 Transformer Scaling Discussions

Since we always emphasize the desire for high-frequency converters, the power density of converters has been improved, mainly because of the size reduction on passive components. To transformers of a particular rating, volt*second decrease due to frequency increase would result in a smaller core size, but a counter force of loss density increases in both cores and windings would retard the trend. Therefore, the relationship between the transformer size and the operating frequency, together with active switch loss analysis, is important to the optimal system design.

The distributed power system (DPS) concept implies that ultimately the system should be composed of “optimal” modules that have optimal power ratings and operating frequencies. Most of previous literature [6-1]-[6-5] addresses this issue from the topologies, semiconductor devices, and control points of view. The passive component effects on modular system design are explored mainly for the particular applications with fixed power rating and frequency [6-6]-[6-7]. If the transformer design is treated as a post-process of the system level design, as it is now, then the system level design might only be local optimal.

Therefore, understanding and formulating high frequency transformer scaling trends are critical to the optimal system design. However, the relationship between the transformer size and operating conditions is highly non-linear, as discussed in previous chapters. This really discourages any attempts to integrate the transformer design into the system level design process. Effects of scaling high-frequency transformer parameters have been studied in previous work [6-8]-[6-9], for relatively small power rating (below several kilo-watts).

In this chapter, the design method discussed in the previous chapter will be applied to the PRC charging application example, for a varying power rating, switching frequency, and so on. Then results of the design program will be summarized, and the physical reasons behind the trend will be discussed. This analysis will provide the information to further improve the PRC charging system design.

6.1. General scaling relationship

To study the transformer scaling problem, we assume several conditions to be unchanged during the analysis. These assumptions will make the analysis feasible and the result explicit, while not affecting the fundamental relationship. Some of these assumptions will be taken away for the analysis of the PRC transformer scaling.

- * Core shape is kept unchanged. So, we can use a single dimension factor, SF , to proportionally scale the core. The second effect of this assumption is that the volume-to-surface ratio is proportional to the dimension scaling factor, $\frac{Vol}{A_{sur}} \propto SF$, for arbitrary core shapes. This assumption is not always true for realistic transformer designs, since different core shapes will have different volume-to-surface ratios. Therefore, this constraint will be released during the analysis of the PRC system.
- * Cooling condition is kept unchanged, and the expected temperature rise is also constant. Either natural or force convections are the major ways to transfer heat. According to the results in [6-10], the loss density is proportional to the reciprocal of the scaling factor, $p_v \propto \frac{1}{SF}$, in order for the constant temperature to rise. Again, this assumption is adopted based on the experimental observations and applied to simplify the analysis, but it will not confine the transformer cooling condition to the way discussed.
- * All packing and fill factors are kept unchanged. This means the manufacturing process variation and material tolerance are omitted. The insulation requirement is also assumed to be the same. However, the situation becomes complicated when Litz wires are taken into consideration. Increasing strands of the Litz wire will result in reducing values of fill factors, because more space is needed for insulation and position transposition. The Litz wire effect will be discussed in the section of PRC transformer scaling analysis.
- * Operating waveform shapes are unchanged, although some resonant converts might have the variable waveform shape, while the operating frequency changes. The particular PRC application will be discussed further in the following sections.

Starting from the transformer apparent power rating expression (6-1), the power density will be derived as the function of the frequency and scaling factor. The core dimension is scaled by the factor SF , and the eddy current effects of the Litz wire winding is represented by a variable K_{FR} , which has been given in Chapter 3.

$$S = V * I = (k_{wave} \cdot f \cdot N \cdot A_{core} \cdot B) * \left(\frac{A_{window} \cdot FF}{N} \cdot J \right) \quad (6-1)$$

$$= \{A_{core} \cdot A_{window}\} * \{k_{wave} \cdot FF \cdot f \cdot J \cdot B\}$$

$$P_{vc} = B^\beta * f^\alpha \propto \frac{1}{SF} \Rightarrow \quad (6-2)$$

$$B \propto SF^{-\frac{1}{\beta}} \cdot f^{-\frac{\alpha}{\beta}}$$

$$P_{vw} = K_{FR} * J^2 \propto \frac{1}{SF} \Rightarrow \quad (6-3)$$

$$J \propto SF^{-\frac{1}{2}} \cdot K_{FR}^{-\frac{1}{2}}$$

The term $A_{core} \cdot A_{window}$ in (6-1) represents the power handling capability of a core, and is proportional to SF^4 . k_{wave} and FF are the waveform shape coefficient and window fill factor. Putting (6-2) and (6-3) into (6-1), we can obtain the relationship as:

$$S(SF, f) \propto SF^{\frac{7}{2} - \frac{1}{\beta}} \cdot f^{1 - \frac{\alpha}{\beta}} \cdot K_{FR}^{-\frac{1}{2}} \quad (6-4)$$

$$S_v(SF, f) = \frac{S(SF, f)}{SF^3} \propto SF^{\frac{1}{2} - \frac{1}{\beta}} \cdot f^{1 - \frac{\alpha}{\beta}} \cdot K_{FR}^{-\frac{1}{2}} \quad (6-5)$$

As shown in (6-5), the power density of the transformer can be expressed as the function of the core magnetic material Steinmetz coefficients, size scaling factor, frequency, and winding AC-to-DC resistance ratio. The trend of power density can be plotted, as we scaling the core size and frequency.

The unique point here is to include the Litz wire winding eddy current effect in the scaling analysis, since this is the inevitable aspect of high frequency high power transformer. The variation of the eddy current effect is not explicit as transformer size and frequency is scaled. We have to express the AC-to-DC resistance K_{FR} as the function of the scaling factor and frequency.

The equation of the Litz wire winding K_{FR} is re-written here. For the winding with m layers and the Litz wire strand number N_0 , we can have:

$$K_{FR} = \frac{y}{\sqrt{2}} * \left(\frac{ber\left(\frac{y}{\sqrt{2}}\right) \cdot bei'\left(\frac{y}{\sqrt{2}}\right) - bei\left(\frac{y}{\sqrt{2}}\right) \cdot ber'\left(\frac{y}{\sqrt{2}}\right)}{ber'^2\left(\frac{y}{\sqrt{2}}\right) + bei'^2\left(\frac{y}{\sqrt{2}}\right)} + \frac{\pi^2 N_0 \eta \left(16 * m^2 - 1 + \frac{24}{\pi^2}\right) \frac{ber_2\left(\frac{y}{\sqrt{2}}\right) \cdot ber'\left(\frac{y}{\sqrt{2}}\right) - bei_2\left(\frac{y}{\sqrt{2}}\right) \cdot bei'\left(\frac{y}{\sqrt{2}}\right)}{ber^2\left(\frac{y}{\sqrt{2}}\right) + bei^2\left(\frac{y}{\sqrt{2}}\right)} \right) \quad (6-6)$$

The $y = \frac{d_{strand}}{\delta}$ is related to d_{strand} for Litz wire strand diameter and $\delta = \sqrt{\frac{\rho}{\pi f \mu}}$ for skin depth.

For all three unknowns in equation (6-6), strand diameter d_{strand} , strand number N_0 and winding layers m , we will find out their changing trend for transformer size and frequency scaling.

The winding layer number m is kept unchanged, since we can interleave multi-layer windings. This is close to the realistic consideration of transformer design. We always want to interleave primary and secondary windings that have multi layers. If the possibility of fill factor reduction is not counted, the variable, winding layer number m , can be excluded from the scaling analysis.

The product of $N_0 \cdot y^2$ representing copper area of the Litz wire winding will be scaled as the following equations. Equation (6-7) and (6-8) do not regulates the selection of strand number and diameter uniquely, unless the equation (3-35) is taken into the consideration. It means that we can always find out an optimal combination of strand number and diameter for any scaling step.

$$N_0 \cdot y^2 \propto SF^2 \quad (\text{for size scaling}) \quad (6-7)$$

$$N_0 \cdot y^2 \propto Const \quad (\text{for frequency scaling}) \quad (6-8)$$

On the other hand, we can follow another way to determine the value of strand number and diameter. The K_{FR} is in the form of Kevin functions of y , which is highly non-linear. To simplify the analysis at this stage, we can fix the value of y during the scaling. This also complies with the wire gauge selection philosophy, which usually suggests keeping the wire diameter as certain times of the skin depth.

After determining the strand number and diameter as the function of scaling factor and frequency, we can perform scaling to the transformer.

6.1.1. Size scaling

We consider the size scaling first for certain frequency. If the core is scaled by factor of SF , the window area will be SF^2 times of the original one. Since y is constant, d_{strand} is constant. Then strand numbers N_0 will be scaled by SF^2 . The power density trends as the function of the size scaling factor are plotted in Fig. 6-1 and Fig. 6-2, for different values of y .

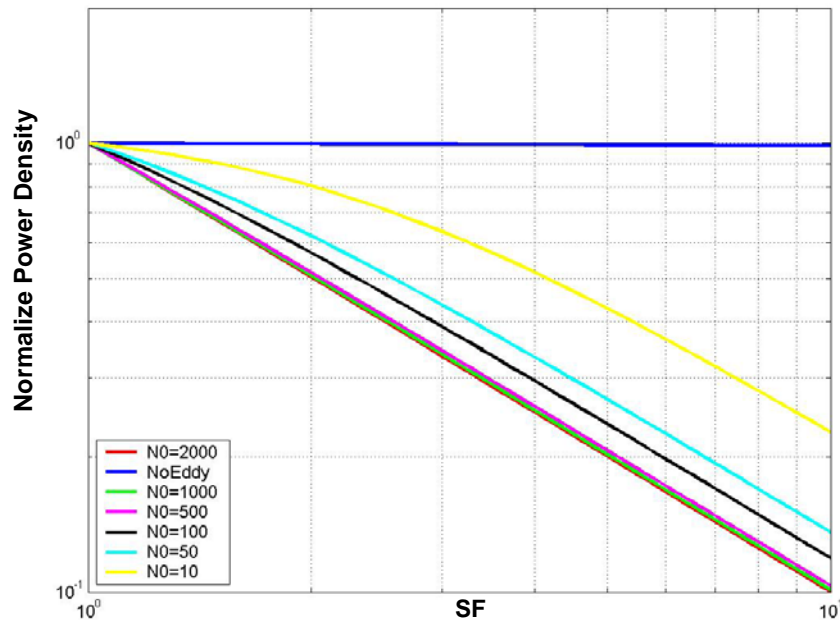


Fig. 6-1 Normalized transformer power density as function of SF ($y=1$, $m=1$, $f=10\text{kHz}$, Finemet FT-3M with $\alpha = 1.62$ and $\beta = 1.98$)

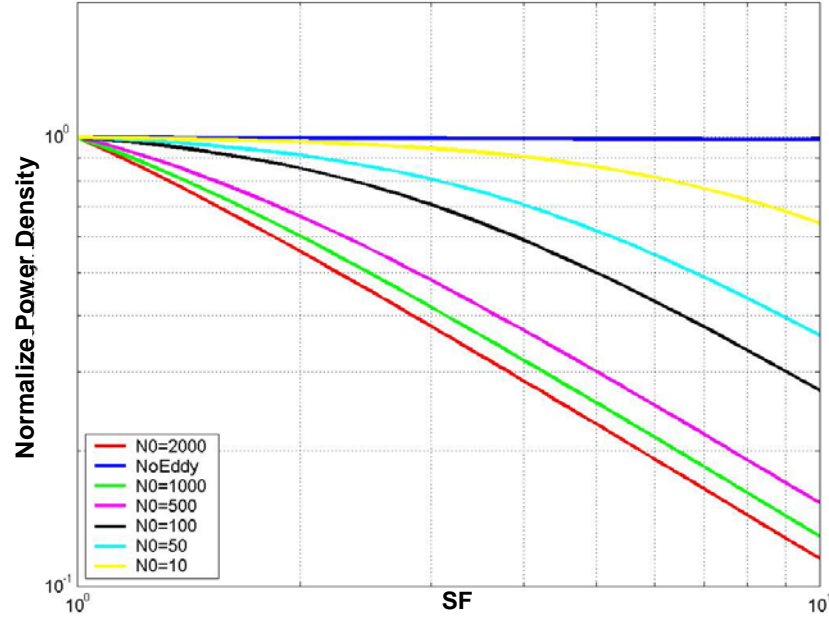


Fig. 6-2 Normalized transformer power density as function of SF ($\gamma=0.5$, $m=1$, $f=10\text{kHz}$, Finemet FT-3M with $\alpha = 1.62$ and $\beta = 1.98$)

The “NoEddy” lines in both figures indicate the power density trajectory without eddy current effect included for the nanocrystalline material, if the transformer size is scaled. Different strand numbers have been chosen as the starting point for the scaling design and the corresponding power density trajectory is plotted. Each curve means that the transformer power density will change if the strand number is scaled by SF^2 times. The bigger number N_0 is, the bigger power rating or higher frequency of the transformer is. Power density will drop quickly for large number of strands, and large number of strand diameter.

The above analysis is for Finemet FT-3M, which has the core loss Steinmetz equation coefficients as $\alpha = 1.3$ and $\beta = 1.98$. It is clear that the power density would reduce as the transformer size is scaled up. Since the Finemet Steinmetz coefficient $\beta < 2$, $\frac{1}{SF^2} \frac{1}{\beta}$ would decrease for the size scale-up. The eddy current coefficient K_R increases as SF increases, so the power density is further reduced by including the eddy current effect.

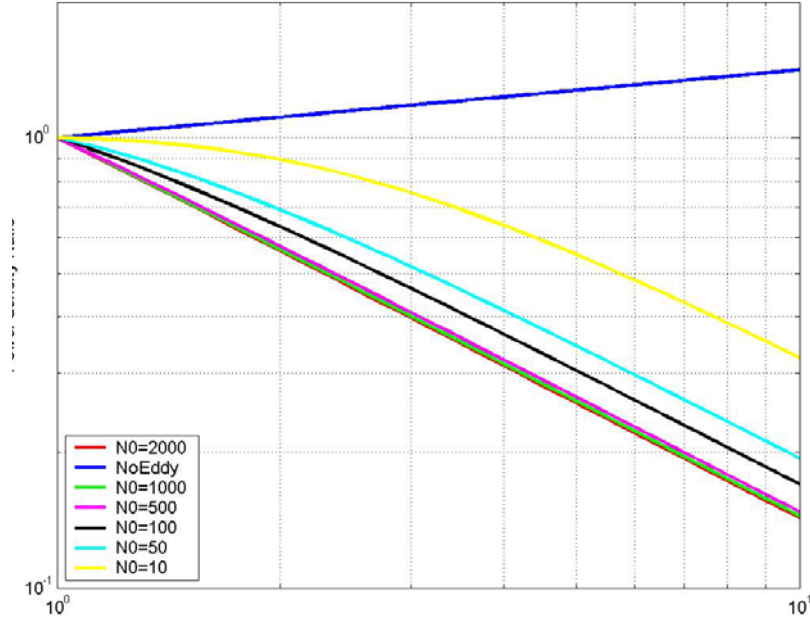


Fig. 6-3 Normalized transformer power density as function of SF ($y=1, m=1, f=10\text{kHz}$, Ferrite P with $\alpha = 1.36$ and $\beta = 2.86$)

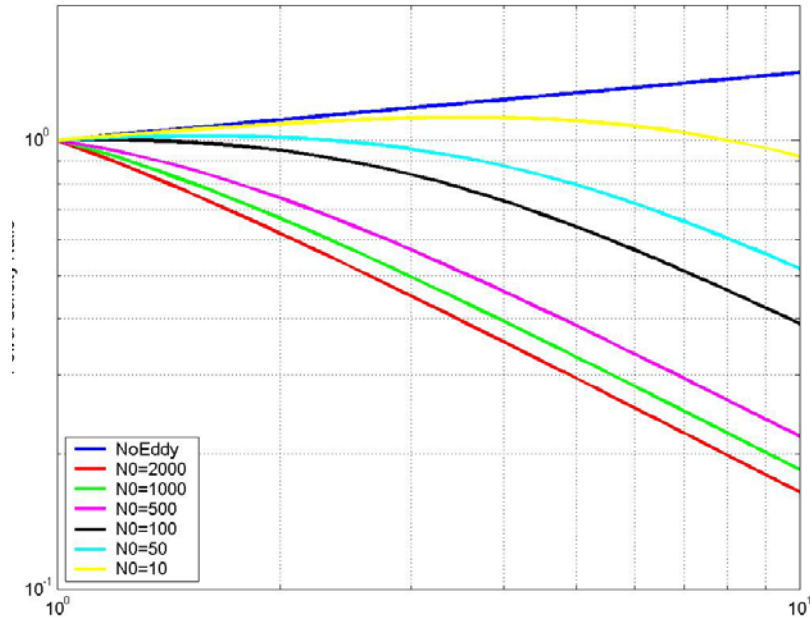


Fig. 6-4 Normalized transformer power density as function of SF ($y=0.5, m=1, f=10\text{kHz}$, Ferrite P with $\alpha = 1.36$ and $\beta = 2.86$)

Similarly, Ferrite P material with the core loss Steinmetz equation coefficients as $\alpha = 1.62$ and $\beta = 2.86$ is analyzed. We can observe peaks of the power density from Fig. 6-3 and Fig. 6-4. The position of the peak is affected by parameter y and N_0 .

If the optimal strand number and diameter are used along the scaling process, which means the value of y will be variable according to the number of strand. The transformer power density scaling can be performed as shown in Fig. 6-5. From the plot, we can see that the eddy current effect can be minimized by selecting optimal strand numbers and diameters ideally. However, the strand diameter cannot be too small and strand number cannot be too many in wire preparing practice. The value of y in the plot does not decrease below 0.16 for 100 kHz operating frequency, since the wire gauge has already reach AWG50. If the fill factor decrease due to the increase of strand number and decrease of strand diameter is counted, the scaling power density trajectory will drop at even smaller value of SF . All of these observations indicate that the size scaling is highly affected by eddy current effects, which is important to the high frequency high power applications.

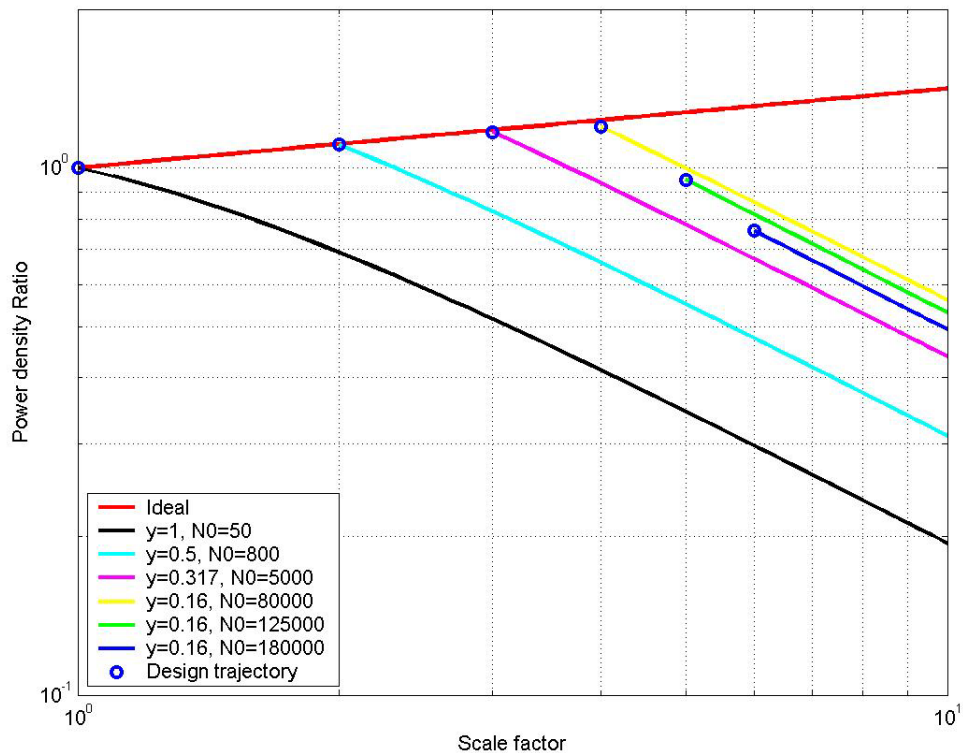


Fig. 6-5 Normalized transformer power density as function of SF ($m=1$, $f=100\text{kHz}$, Ferrite P with $\alpha = 1.36$ and $\beta = 2.86$)

6.1.2. Frequency scaling

By keeping $SF = 1$, we still want the condition $y = 1$ to simplify the analysis, so the strand diameter will be proportional to the skin depth of variable frequency, $d_{strand} \propto \frac{1}{\sqrt{f}}$.

Therefore, the strand numbers will be scaled by the factor of f . The normalized power density is plotted against frequency and strand number, as shown in Fig. 6-6 and Fig. 6-7 for Finemet, Fig. 6-8 and Fig. 6-9 for Ferrite P.

According to equation (6-5), the power density would increase with the frequency increase, if no eddy current effect is considered. This unbounded increase apparently violates the reality, and the high frequency would finally make the transformer density decrease. The eddy current effect would act as the counter-force, so peaks of power density should be determined at certain frequency. Obviously, the optimal frequency where the transformer density achieves a maximum is affected by parameter y and N_0 .

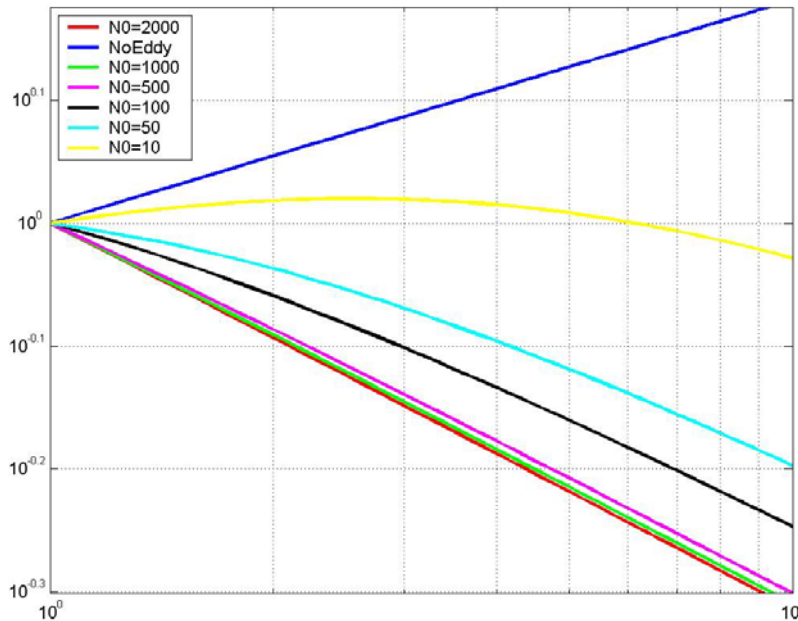


Fig. 6-6 Normalized transformer power density as function of f ($y=1, m=1, SF=1$, Finemet FT-3M with $\alpha = 1.62$ and $\beta = 1.98$)

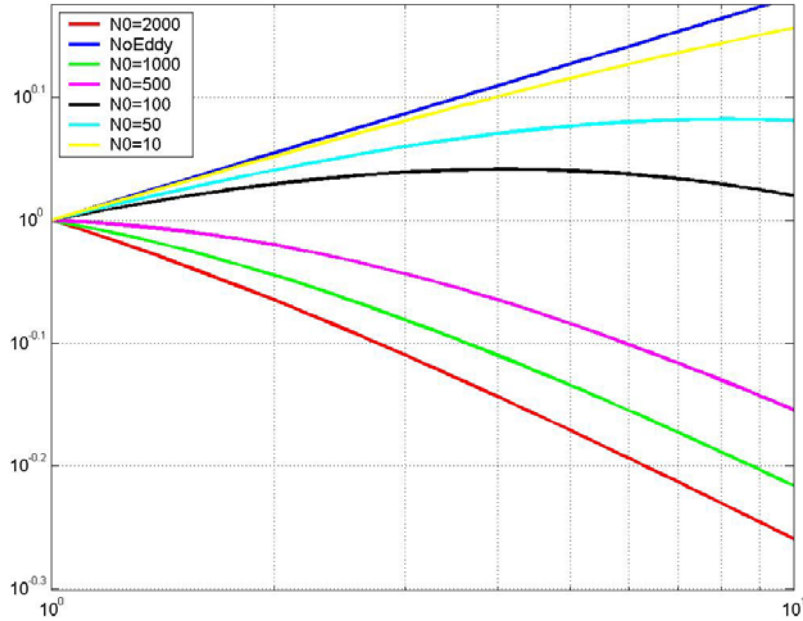


Fig. 6-7 Normalized transformer power density as function of f ($\gamma=0.5$, $m=1$, $SF=1$, Finemet FT-3M with $\alpha = 1.62$ and $\beta = 1.98$)

Ferrite P material shows the similar trend as the Finemet. While under the same conditions, the difference is that the ferrite would have the peak density happen at a higher frequency than Finemet. This is determined by the materials inherent characteristic.

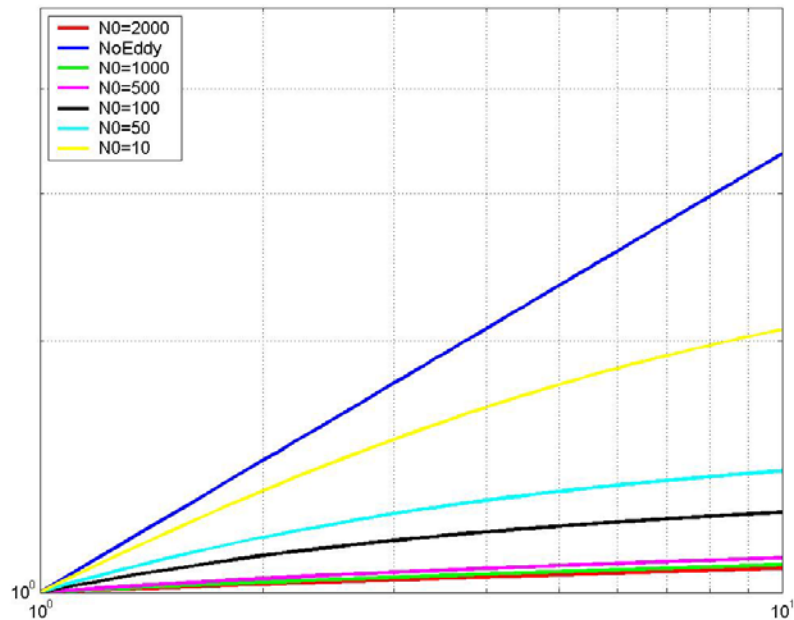


Fig. 6-8 Normalized transformer power density as function of f ($\gamma=1$, $m=1$, $SF=1$, Ferrite P with $\alpha = 1.36$ and $\beta = 2.86$)

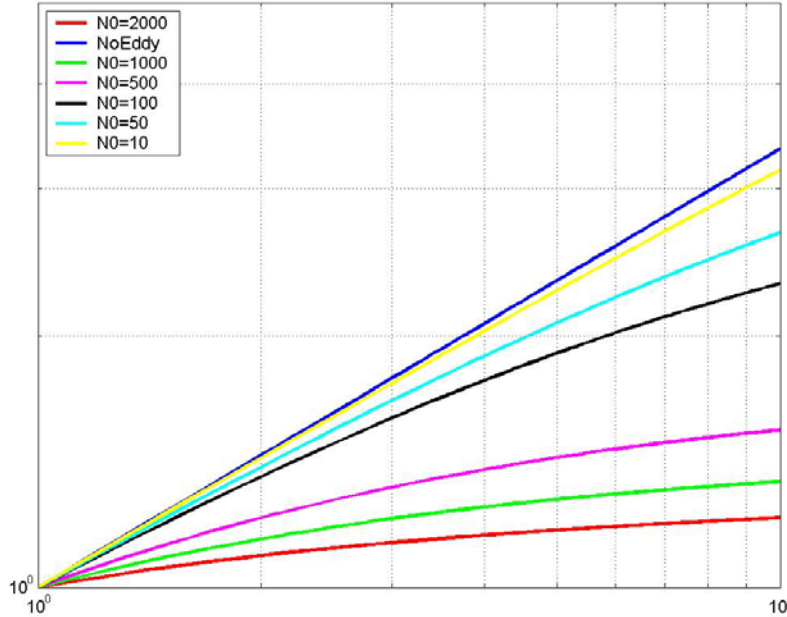


Fig. 6-9 Normalized transformer power density as function of f ($\gamma=0.5$, $m=1$, $SF=1$, Ferrite P with $\alpha = 1.36$ and $\beta = 2.86$)

6.1.3. Discussions

After summarizing all the above observations, we can conclude the following points as:

- * Eddy current effect increases when both size and frequency are scaled up, and its influence on transformer power density is negative.
- * Transformer density would not monotonically increase as frequency increases, so the optimal frequency can be found for certain conditions.
- * Finemet is not suitable for size scaling, while ferrite is. This is determined by the material loss characteristics.

However, the scaling analysis has limited instructive meaning to real transformer designs. First, the proportional size scaling is rarely applicable in real design, which may requires shape changing. Secondly, the power scaling discussed here is implied as coordinating with the core size scaling. For example, $SF = 2$ means core dimensions are doubled, so the voltage and current applied to the transformer are assumed to increase to certain degree. This is regulated by equations (6-2) and (6-3). In real applications, the power rating is changed by changing the voltage and the current to meet the load requirements, which is not the same as the situation discussed above.

6.2. Power rating scaling for variable core dimensions

We can take the abovementioned two aspects into the consideration, by using the PRC studied case as an example. Here, the power rating will be scaled by varying the current while keeping the voltage the same. The core shape can be varied, instead of proportionally scaling dimensions.

6.2.1. C-core characterization

In the real design, it is more convenient to have the core dimensions changed freely. For the C-core shown in Fig. 6-10, we define four variables to describe the core, a for leg width, d for leg thickness, b for window width, and h for window height. The windings are symmetrical on both legs, and they fully occupy the window.

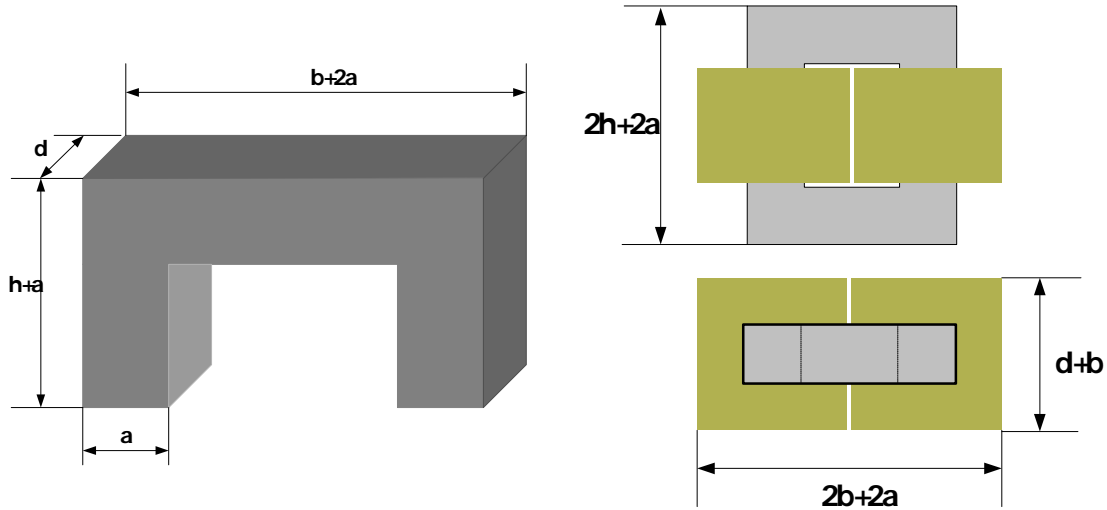


Fig. 6-10 The C-core dimensions for scale design

We can characterize the area-to-volume ratio of the C-core assembly, since it is important to the scaling design. The transformer volume can be expressed as (6-9), and correspondingly, the core and winding exposed surface areas are as in (6-10) and (6-11).

$$V = (2b + 2a) \cdot (d + b) \cdot (2h + 2a) \quad (6-9)$$

$$A_c = 4[(b + 2a + d) \cdot a + h \cdot (2d + 2a)] \quad (6-10)$$

$$A_w = 4[h \cdot (d + 3b + 2a)] \quad (6-11)$$

Therefore, the normalized area-to-volume ratios of the core and window are plotted and shown in Fig. 6-11. For $a = 1$, other dimension variables vary between

[0.1 10]. In the plot, x-axis and y-axis are for window width b and leg thickness d , Four 3-D curvy planes are for window height of 0.1, 0.5, 1, and 10, respectively.

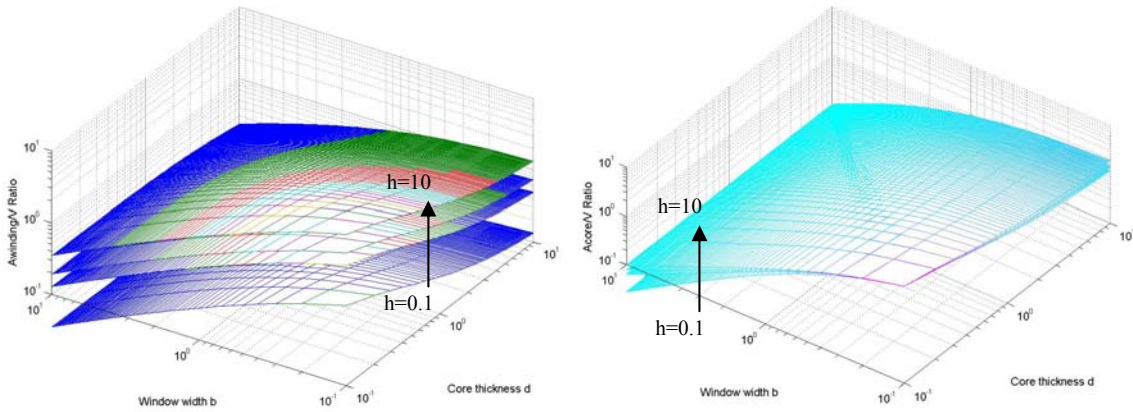


Fig. 6-11 C-core window (left) and core (right) exposed area to volume ratios

After examining the plots, we can conclude the following interesting and important design rules of the C-core transformer. To obtain the high area to volume ratios that are always preferred, we should have the C-core comply:

- Rule 1 – core window height h being as large as possible;
- Rule 2 – core leg thickness being equal or similar to window width, $d = b$;
- Rule 3 – core leg width a being as small as possible.

6.2.2. PRC scaling designs

The 30 kW PRC module running at 200 kHz has been developed to operate in parallel, and to fulfill the 150 kW load requirement. However, the power rating and operating frequency of the module has been determined by the loss of the active switches of the PRC, and the transformer is designed afterward. We want to include the transformer scaling effects into the system design in order to find the optimal power rating and frequency of each module.

The parallel architecture is adopted here, so input and output voltages of modules are kept unchanged. PRC is the topology of the module, so resonant tank values of the module for different power and frequency are scaled proportionally. The detailed specifications of the transformer for different rating and frequency are listed in Table 6-1. The transformers for these PRC modules have the same turns ratio (1:11), ambient temperature (65 °C), and allowed temperature rise (55 °C). Nanocrystalline magnetic material is used for the transformer core, and Litz wires for windings. We can realize the

resonant inductance by the leakage inductance, and in cases of low leakage inductance, the transformer design is also considered. Wind capacitances are so small compared with the expected resonant capacitances that they will not affect the transformer design under the discussed power and frequency ranges.

Table 6-1 PRC specifications for different ratings and frequencies

Power rating (kW) / Switching frequency (kHz)		10	15	30	37.5	50	75	100
		200	Max. transformer primary current (A)	57	85	170	220	295
300								
500								
200	Max. transformer volt*sec	0.003	0.003	0.003	0.003	0.003	0.003	0.003
300		0.002	0.002	0.002	0.002	0.002	0.002	0.002
500		0.0012	0.0012	0.0012	0.0012	0.0012	0.0012	0.0012
200	Resonant inductance (μH)	10.89	7.26	3.63	2.9	2.15	1.45	1.075
300		7.26	4.84	2.42	1.93	1.43	0.97	0.72
500		4.356	2.9	1.45	1.16	0.86	0.58	0.43
200	Resonant capacitance (nF)	48.3	72.5	145	181.2	241.7	362.5	483.3
300		32.2	48.3	96.7	120.8	161	241.7	322.2
500		19.3	29	58	72.5	96.7	145	193.3

Four soft magnetic materials, which are typical to high frequency applications, have been adopted for the scale-design discussion. The specific loss parameters of these materials are tabulated in Table 6-2.

Table 6-2 Magnetic material characteristics

Material name	B_{sat}/B_{max} (T)	Core loss density (mW/cm ³) $P_{v_core} = K * f^\alpha * B^\beta$	Manufacturer
Ferrite P	0.5/0.35	$K = 18.0921, \alpha = 1.63, \beta = 2.62$	Magnetics
Finemet FT-3M	1.23/0.8	$K = 8, \alpha = 1.621, \beta = 1.982$	Hitachi
Supermalloy	0.8/0.65	$K = 12.248, \alpha = 1.7, \beta = 1.937$	Magnetic Metals
Amorphous 2705M	0.77/0.55	$K = 5.6628, \alpha = 1.883, \beta = 2.215$	Metglas

a) *Free-style scaling design*

The design program has been run to search for maximum density design for each operating condition. The first group of results shows designs without considering the leakage inductance constraint. Design results are listed in Table 6-3.

The transformer operating flux density decreases when the power rating increases. This can be interpreted that the core loss density has to be reduced for a bigger core, due to a surface area/volume ratio reduction. At the same time, the winding turn's number is reduced, since we scaled the current up. All design results show that the narrow and high

window cores are preferred for all conditions, which is determined by the natural convection thermal management. The leakage inductance decreases as both power rating and frequency increase. All designs have the core and winding temperature rises close to the pre-set limits.

Table 6-3 Transformer scaling-design results for different materials

Material	Frequency (kHz)	Power rating (kW)	Core size (cm)				Bop (T)	n1	Ptot (w)	Llk (μH)	Trise_co (°c)	Trise_wd (°c)
			a	b	d	h						
Ferrite P	200	10	1.3	0.5	1.9	2.5	0.3572	17	229.4	0.224	53.8	54
		30	1.9	0.7	2.4	4.2	0.3631	9	570	0.0707	51.7	53.1
		50	2.2	1	2.3	6	0.3706	8	876	0.0614	54.2	54.7
		100	2.9	1.2	2.9	8.2	0.3576	5	1606.5	0.0268	54.1	51.6
	300	10	1.4	0.4	1	3.9	0.3571	20	315.1	0.1203	55	53.4
		30	1.7	0.6	1.1	9.4	0.3565	15	813.3	0.0511	42	55
		50	2	0.8	1.2	12.6	0.3472	12	1251.6	0.0383	46.9	54.7
		100	3.2	1	1.7	13.2	0.3064	6	2102.5	0.0169	51.9	54.8
	500	10	1.1	0.5	0.8	5	0.3099	22	350.2	0.1216	40.6	55
		30	2	0.7	0.9	8.6	0.2778	12	879.5	0.0442	46.2	54.4
		50	2.7	0.7	1.1	11.2	0.2525	8	1403.8	0.0188	48.3	54.9
		100	3.3	0.9	1.6	15.2	0.2273	5	2362.2	0.009	54.3	54.7
Finemet FT-3M	200	10	1	0.5	0.9	2.9	0.7939	21	252	0.1911	47.7	54.1
		30	1.4	0.8	1.1	5.8	0.6957	14	615.1	0.0934	54.3	54.9
		50	2	0.8	1.1	9	0.6198	11	1041.5	0.0439	54.2	54.2
		100	3.2	0.7	1.3	15.1	0.5151	7	2161.9	0.0124	54.8	54.9
	300	10	0.7	0.5	1.3	2.9	0.6105	18	286	0.1462	54.66	54.7
		30	0.9	0.7	2.6	4.9	0.4748	9	686.4	0.0509	54.7	54.8
		50	0.9	0.8	3.6	7.3	0.4409	7	1125.8	0.0298	54.4	54.3
		100	1.2	1	5.7	9.1	0.3655	4	1993	0.0145	55	55
	500	10	0.7	0.4	1.2	4.5	0.3968	18	357.54	0.0694	54.6	53.7
		30	0.7	0.7	3.7	5.2	0.3309	7	831.7	0.0352	54.1	54.6
		50	0.8	0.9	5	6.4	0.3	5	1279.1	0.0247	54.9	54.8
		100	1.1	1.2	7.4	8.1	0.2457	3	2203.9	0.0135	55	54.4
Super-alloy	200	10	1.1	0.5	0.7	4.8	0.573	34	380.3	0.29	54.4	54.8
		30	2.1	0.6	1	8.4	0.4202	17	971.7	0.08	54	54.7
		50	3	0.6	0.9	13.5	0.3968	14	1759.9	0.0411	54.4	54.8
		100	4.2	0.9	1.2	16.9	0.3307	9	2956.1	0.0285	54.9	54.9
	300	10	1.5	0.5	0.5	5.4	0.4167	32	486	0.2482	54.9	54.4
		30	2.4	0.6	0.9	9.7	0.2894	16	1169	0.0647	54.3	54.7
		50	3.3	0.7	1.1	11.9	0.2504	11	1835.6	0.038	54.7	54.9
		100	4.4	1.1	1.6	14.5	0.02029	7	2953	0.0276	55	54.7
	500	10	1.7	0.4	0.4	8.1	0.2757	32	668.1	0.1324	54.7	54.5
		30	2.5	0.6	0.8	12.8	0.1875	16	1437.7	0.049	54.4	54.9
		50	3.4	0.7	1	15.8	0.1604	11	2236.6	0.0286	54.3	54.8
		100	4.2	1.2	1.6	18.4	0.1276	7	3376.2	0.0234	54.9	55
Amorph. 2705M	200	10	1.1	0.4	0.7	5.9	0.5411	36	386.6	0.2024	45.6	54.8
		30	2	0.6	0.8	9.9	0.4688	20	968.6	0.0863	50	54.8
		50	2.8	0.7	0.8	13.2	0.4464	15	1607.5	0.0537	52.3	55
		100	4	0.8	1.3	16	0.3606	8	2726.5	0.0204	54.6	54.6
	300	10	1.2	0.5	0.5	6.8	0.4274	39	467.1	0.2577	51.4	54.8
		30	2	0.7	0.8	10.7	0.3289	19	1068.3	0.0866	52.3	54.8
		50	2.9	0.7	0.8	15.4	0.3079	14	1861.4	0.0411	53.8	54.7
		100	3.5	0.9	1.5	19.2	0.2381	8	2865	0.0185	54.2	54.8
	500	10	1.3	0.4	0.5	9.2	0.2637	35	584.9	0.1227	50.3	54.9
		30	1.9	0.7	0.9	12.8	0.2064	17	1210.7	0.0579	54.1	54.8
		50	2.6	0.7	1.2	16.3	0.1748	11	1893.6	0.0245	53.5	54.9
		100	4.2	1	1.6	17.3	0.1488	6	3163.4	0.0148	54.9	54.7

The power density trends of four materials are plotted in Fig. 6-12. Several interesting points have been observed:

- ✧ Finemet core transformer will have highest power density, due to its high saturation flux density and low loss density.
- ✧ Frequency scale-up will increase power density for Ferrite and Finemet, when the power rating decrease.
- ✧ Supermalloy and amorphous core transformers will have smaller density, when the power rating and frequency increase.
- ✧ The general trend analyzed in the last section for the fixed core shape would be the specific situation of the result shown here.

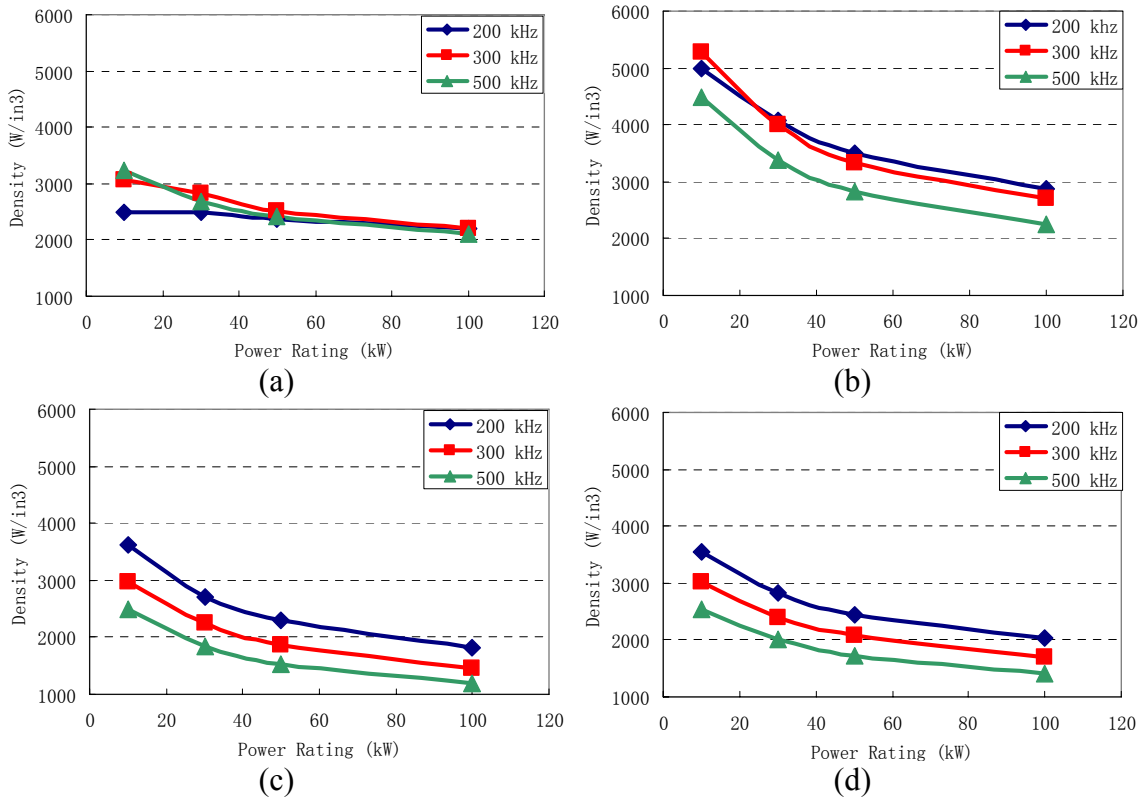


Fig. 6-12 Calculated power densities of PRC transformers under different frequencies and power ratings, using ferrite P (a), Finemet FT-3M (b), Supermalloy (c), and Amorphous 2705M (d) as transformer cores

b) Leakage integrated scaling design

Another transformer development strategy for the PRC application is that we can utilize the leakage inductance of the transformer as the resonant inductance of the PRC operation, with values tabulated in Table 6-1. The leakage inductance calculation will be

included in the design program, so the effect of this extra constraint to the transformer design will be investigated in this section. Detailed design results considering leakage inductance are listed in Table 6-4.

All leakage inductances are controlled within $\pm 5\%$ of the required resonant inductance values. Meanwhile, temperature rises are close to their limits. We can conclude that the optimal core dimensions have been achieved for the integrated transformer scheme. The core shape is different from the one preferred by the free style designs. The width of the core windows is now bigger than the height, to fulfill the leakage requirement. So, the wide core window would provide enough insulation space between windings. The free style design results have a much narrower core window, which is not suitable for a high voltage application. The core thickness is large to meet the flux density requirement. The final height of the transformer is much smaller, compared with the ones by the free style design; and the footprint is close to square. All these features are favorable to converter system assembly.

Table 6-4 Transformer scaling-design results for the integrated scheme

Material	Frequency (kHz)	Power rating (kW)	Core size (cm)				Bop (T)	n1	Ptot (w)	Llk (μ H)	Trise_co ($^{\circ}$ C)	Trise_wd ($^{\circ}$ C)
			a	b	d	h						
Finemet FT-3M	200	10	0.4	3.4	2.2	0.9	0.8117	21	239.69	10.4678	53.3	54.82
		30	0.4	4.6	3.7	2	0.7796	13	577.19	3.5413	54.61	52.93
		50	0.7	5.9	5.6	1.8	0.5466	7	788.69	2.0519	52.98	53.87
		100	0.8	7.2	7.3	2.9	0.5137	5	1394.5	1	54.6	54.4
	300	10	0.3	3.5	4.1	0.8	0.5807	14	270.66	7.094	53.65	52.4
		30	0.5	4.7	4.7	1.7	0.4728	9	592.76	2.3217	53.76	52.78
		50	0.7	5.6	5	2.3	0.4082	7	877.1	1.4118	54.46	54.36
		100	1.1	7.2	7.2	2.8	0.3157	4	1443.7	0.6678	54.7	55
	500	10	0.3	3.3	3.8	1	0.4049	13	300.32	4.3218	54.4	53.7
		30	0.8	4.5	3.4	1.9	0.2757	8	616.62	1.381	54.5	54.5
		50	0.7	5.3	5.2	2.7	0.2747	6	974.7	0.8288	55	54.6
		100	1.1	6.6	6.2	3.9	0.2199	4	1620.3	0.3941	54.8	54.8

The transformer power densities are plotted in Fig. 6-13. We can observe two points from the curves. First, the power density of the integrated transformer scheme is lower than the corresponding free style one shown in Fig. 6-12, which is under the same operating conditions. The solid volume sum of one low leakage transformer and an inductor could be smaller than the volume of an integrated transformer. However, connection space and form factor mismatch between the transformer and inductor could cause lots space, and might make the final assembly volume of the discrete scheme bigger.

Second, increasing frequency and power rating will make the power density decrease, for the ranges explored. This is also different from the free style design results, which show that 300 kHz could have a bigger power density for power ratings smaller than 30 kW. The eddy current effect retards the benefit of frequency increase which can reduce the volt*second applied to the transformer.

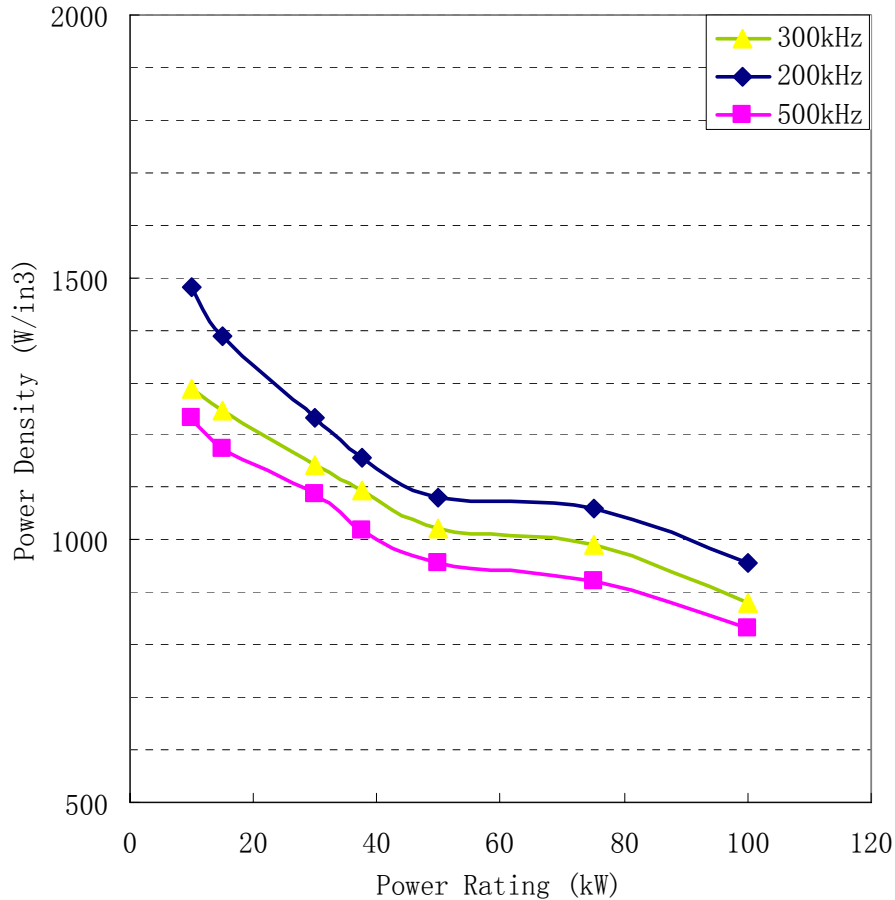


Fig. 6-13 Calculated power densities of PRC transformers under different frequencies and power ratings, using Finemet FT-3M as transformer cores

The calculation has also been performed for the Ferrite P core material, and the transformer power densities are compared to Finemet core ones, as shown in Fig. 6-14. Finemet can give us a higher density, especially for lower power ratings, and it would be similar to the Ferrite at 100 kW.

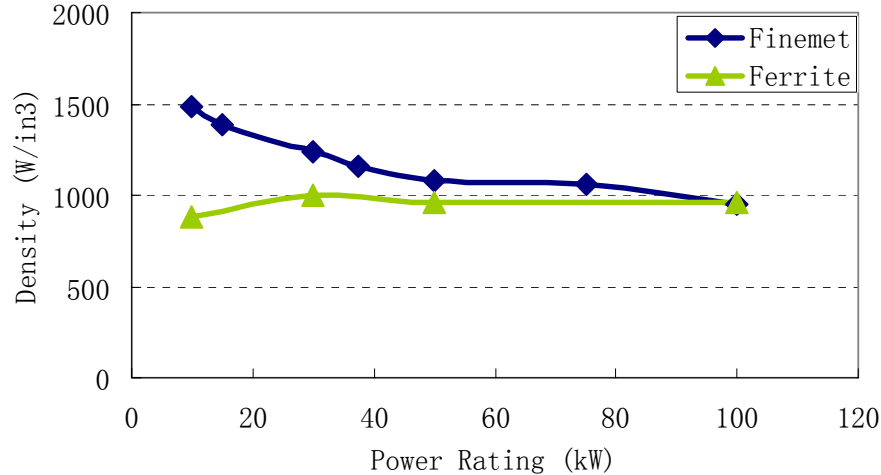


Fig. 6-14 Calculated power densities of PRC transformers for 200 kHz, using Finemet FT-3M and Ferrite P as transformer cores

6.3. Summaries

The eddy current effect of the Litz wire winding has been included into the transformer scaling analysis, which is unique and important to high power high frequency transformers. Results show that the eddy current effect affects the power density increase. Simply scaling power or frequency up might not guarantee higher power density, since the eddy current effect becomes more severe for both higher frequency and higher power rating. This makes sense, if we consider the unlimited power density increase due to the frequency increase impractical.

Based on the understanding of general scaling relationship of high frequency, high power transformers, we perform the power rating and frequency scaling to the PRC charging system particularly. Different magnetic materials have been investigated for different power ratings and frequencies. From the power density point of view, Finemet core material is better than other soft magnetic materials like ferrite, amorphous, and Supermalloy, for the pulse-power PRC application. For the Finemet material, the highest power density happens at 300 kHz and 10 kW. Higher frequency might not bring the higher power density, at the studied power rating range. This is instructive to the transformer design, but the system operating frequency and power rating also need to consider other components like active switched and passive filters.

One important issue should never be omitted is that all above scaling designs consider the transformer cores and windings as homogeneous heat source, which means the thermal conductivities of cores and windings are assumed infinity. This is obvious not the practical case; and actually the temperature distribution inside cores and windings would be more uneven for large geometries. Having thermal resistance representing the material thermal conductivity in the thermal model would make the scaling analysis extremely difficult. One way to reduce the affection is to scale down from a well-designed transformer, so, in that way, the temperature distribution might not be worse.

This analysis can be considered together with active component designs, to determine the system level optimal frequency and power rating. Instead of guessing transformer dimensions and power density in vein, we can roughly predict the trend of the power density changes under certain given operating conditions.

Chapter 7 Conclusions and Future Work

7.1. Conclusions

The design issues of high-density transformer for high-frequency high-power resonant converters have been studied in this work, and several critical technical barriers have been identified and solved. Prototype transformer for a 30 kW PRC charging converter has been developed and tested in-circuit. The proposed modeling and calculation methods have been verified. The followings are the detailed achievements and contributions.

Nanocrystalline material characterizations: Through measuring B-H curves, we calibrate the high frequency and high temperature performance of the nanocrystalline material. Beyond the material, cut core issues, which are inevitable to high power transformer development have also been characterized. The loss increase due to the cut-core preparation process has been considered into the loss calculation coefficient. According to characteristics shown above, we can conclude that the nanocrystalline material is superior to ferrites and amorphous materials for high-frequency high-power applications. The introduction of nanocrystalline magnetic materials with relatively low loss density, high saturation flux density, and high Curie temperature has shown promise for high density magnetics design.

Core loss calculation method: The proposed core loss calculation method, WcSE, can predict the core loss by the STS type of waveforms and for the nanocrystalline material, which has been verified by experimental results. This is important to soft switching and resonant operation applications, which have STS type waveforms, instead of sine or square waveforms, since both MSE and GSE methods give the incorrect results. For high density requirements, the accurate calculation of the core loss would provide the possibility to cut the margin of over-design.

As compared to the MSE and GSE methods, it is quite convenient to integrate the WcSE method into optimization programs. The waveform coefficient, as the only change from the original SE, can easily be calculated even instantaneously. For a resonant

converter running at variable frequency, the WcSE method can provide the accurate and easy way to calculate core losses.

Leakage inductance calculation: The 1-D energy-based calculation methods for leakage inductance and winding capacitance are proposed. The frequency dependent leakage inductances of prototypes have verified the model. Litz wire effect has been included, and the leakage field has been modeled and solved using 1D assumption.

Minimum-size transformer design procedure: With considering loss and parasitic calculations, a program has been developed to find out the minimum size transformer needed for certain operating conditions. The studied case is the 30 kW PRC converter system, and prototypes have been developed and tested.

Scaling designs: This analysis can be considered together with active component designs, to determine the system level optimal frequency and power rating. Instead of guessing transformer dimensions and power density in vein, we can roughly predict the trend of these power density changes under certain given operating conditions.

7.2. Future Work

7.2.1. Improve the Litz wire winding leakage inductance modeling

The leakage inductance modeling presented in Chapter 4 is based on the assumption that the round Litz wire could be considered as multi parallel plates; so a 1D solution in Cartesian coordinate system is ready. The major drawback of this assumption is that the Litz wire principle is violated. The radial and azimuthal transposition of strands will ensure the cancellation of proximity effect induced by the transverse external field.

If the 1D solution of the leakage field is still preferred, the application of a cylindrical coordinate system to the Litz wire is necessary, as shown in Fig. 7-1. Without the parallel plate requirement, the irregularity of the leakage field distribution could be taken into consideration. To each strand inside the Litz wire, there are two external magnetic fields, which are induced by other layers of the winding and other strands inside the same Litz wire. The magnetic field inside the Litz wire can be calculated, and the energy stored can be integrated.

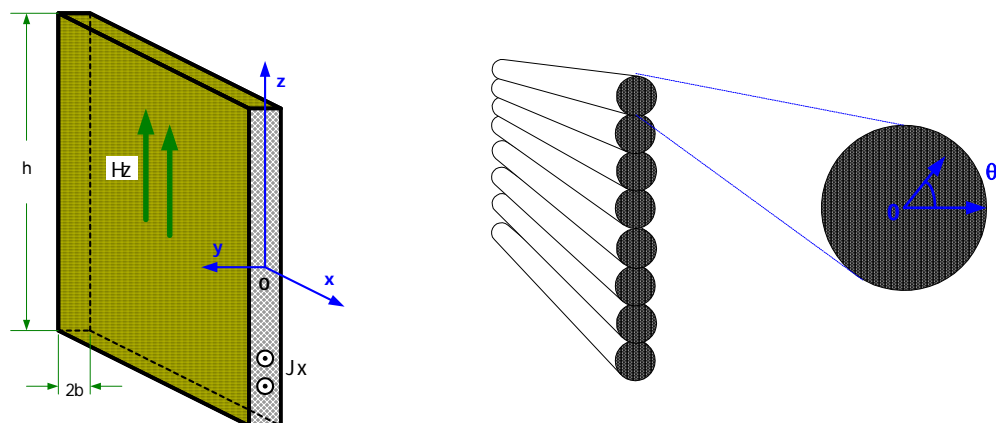


Fig. 7-1 Cylindrical coordinate consideration of the leakage field

7.2.2. Extend the modeling and design work to EMI filter

As EMI regulations cover products more and more stringently, EMI filters are required to confine the noise generation level. However, the EMI filter could be a major part of the total cost and size.

The EMI filter is designed for certain noise source characteristics, such as noise level and source impedance. The designed filter would have a minimum cost or size. An optimization design procedure should be developed. The filter attenuation calculation based on the datasheet and minimum measurement of material and components is required. High frequency attenuation prediction requires information on the filter component parasitic, such as common-mode choke core loss, self inductance, leakage inductance, winding capacitance, and winding loss. CM choke is a special type of transformer, and saturation and loss calculations are necessary.

A design program has been developed to consider ferrite materials. The need to extend to other magnetic materials, such as nanocrystalline material, has already been seen. Preliminary work on modeling has also been integrated into the program. After refining the model based on the knowledge obtained in this dissertation, we could build more filter prototypes to verify the model.

References

- [1-1] S. Jeszenszky, “History of transformers”, IEEE Power Engineering Review, Vol. 16, 1996, pp. 9-12.
- [1-2] P. D. Evans and B. Heffernan, “Electromagnetic considerations in power electronic converters”, Proceedings of the IEEE, Vol.89, 2001, pp. 864-875.
- [1-3] J. D. van Wyk, F. C. Lee, and D. Boroyevich, “Power electronics technology: present trends and future developments”, Proceedings of the IEEE, vol. 89, June 2001, pp. 799-802.
- [1-4] A. W. Lotfi, and M. A. Wilkowski, “Issues and advances in high-frequency magnetics for switching power supplies”, IEEE Proceedings of the IEEE, Vol. 89, June, 2001, pp.833-845.
- [1-5] J. D. van Wyk, and F.C. Lee, “Power electronics technology at the dawn of the new millennium – status and future,” Power Electronics Specialists Conference, 1999. PESC 99. 30th Annual IEEE Volume 1, 27 June-1 July 1999 Page(s):3 – 12.
- [1-6] A. F. Goldberg, J. G. Kassakian, and M. F. Schlecht, “Issues related to 1-10-MHz transformer design”, IEEE Transactions on Power Electronics, Vol. 4, No. 1, Jan. 1989, pp. 113-123.
- [1-7] K. D T. Ngo, R. P. Alley, “A. J. Yerman, R. J. Charles, and M. H. Kuo, “Design issues for the transformer in a low-voltage power supply with high efficiency and high power density”, IEEE Transactions on Power Electronics, Vol. 7, Jul. 1992, pp. 592 –600.
- [1-8] P. D. Evans, “Multi megahertz transformers”, Industry Applications Conference, 1995. Thirtieth IAS Annual Meeting, IAS '95, Volume 1, 8-12 Oct. 1995 Page(s):824 – 832.
- [1-9] J. T. Strydom, J. D. van Wyk, C. K. Campbell, J. A. Ferreira, M. F. K. Holm, “Packaging of an integrated planar power passive module for a power electronics converter: a 1 MHz case study”, IEEE Transactions on Components and Packaging Technologies, Vol. 25, June 2002 pp. 260 – 265.

-
- [1-10] M. H. Kheraluwala, D. W. Novotny, and D. M. Divan, "Coaxially wounded transformers for high-power high-frequency applications", IEEE Transactions on Power Electronics, Vol. 7, Jan. 1992, pp. 54-62.
- [1-11] J. C. Forthergill, P. W. Devine, and P. W. Lefley, "Novel prototype design for a transformer for high voltage, high frequency, high power use", IEEE Transactions on Power Delivery, Vol. 16, 2001, pp. 89-98.
- [1-12] L. Heinemann, "An actively cooled high power, high frequency transformer with high insulation capability", APEC 2002, pp.: 352-357.
- [1-13] W. A. Reass, D. M. Baca, J. D. Doss, R. F. Gribble, "Design technology of high-voltage multi-megawatt polyphase resonant converter modulators", IECON '03, Nov. 2003, pp.: 96 – 101
- [1-14] P. L. Hower, "power semiconductor devices: an overview", Proceedings of the IEEE, Vol. 86, 2001. pp. 335-342.
- [1-15] N. Coonrod, "Transformer computer design aid for high frequency switching power supplies," IEEE Transactions on Power Electronics, pp. 248-256, Oct. 1986.
- [1-16] R. Petkov, "Optimal design of a high-power high-frequency transformer", IEEE Transactions on Power Electronics, Vol. 11, No. 1, Jan. 1996, pp. 33-42.
- [1-17] F. Canales, P. Barbosa, C. Aguilar, F. C. Lee, "A high-power-density DC/DC converter for high-power distributed power systems", Power Electronics Specialist Conference, 2003. PESC '03. Volume 1, 15-19 June 2003 pp.11 – 18.
- [1-18] J. Biela, J. W. Kolar, "Electromagnetic integration of high power resonant circuits comprising high leakage inductance transformers", PESC 04, 2004, pp. 4537 – 4545.
- [1-19] M. Bhatnagar, B. J. Baliga, "Comparison of 6H-SiC, 3C-SiC, and Si for power devices", Electron Devices, IEEE Transactions on, Vol. 40, 1993, pp. 645 – 655.
- [1-20] J. B. Baliga, "Power ICs in the saddle", Spectrum, IEEE Volume 32, Issue 7, July 1995 Page(s):34 - 40, 45-9.
- [1-21] M. A. Kempkes, J. A. Casey, M. P. J. Gaudreau, T. A. Hawkey, I.S. Roth, "Solid-state modulators for commercial pulsed power systems", Power Modulator Symposium, 2002 and 2002 High-Voltage Workshop, 2002. pp. 689 – 693.

- [1-22] J. G. Kassakian, J. M. Miller, N. Traub, “Automotive electronics power up”, IEEE Spectrum, Vol. 37, 2000, pp. 34 – 39.
- [1-23] M. Gerber, J. A. Ferreira, I. W. Hofsjager, and N. Seliger, “High temperature high power density packaging for automotive applications” IEEE PESC 2003, pp. 425-430.
- [1-24] F. Blaabjerg, Z. Chen, and S. B. Kjaer, “Power electronics as efficient interface in dispersed power generation systems”, IEEE Trans. On Power Electronics, Vol. 19, Sept. 2004, pp. 1184-1194.
- [1-25] F. C. Lee, P. Barbosa, P. Xu, J. Zhang, B. Yang, and F. Canales, “Topologies and design considerations for distributed power system applications”, Proceedings of the IEEE, Vol. 86, 2001. pp. 939-950.
- [1-26] J. G. Kassakian, M. F. Schlecht, “High-frequency high-density converters for distributed power supply systems”, Proceedings of the IEEE, Vol. 76, 1988, pp. 362 – 376.
- [1-27] Wenduo Liu; J. D. van Wyk, “Design of integrated LLCT module for LLC resonant converter”, APEC 2005, Vol. 1, 6-10 March 2005, pp. 362 – 368.
- [1-28] B. Lu, W. Liu, Y. Liang, F. C. Lee, and J. D. van Wyk, “Optimal Design Methodology for LLC Resonant Converter”, APEC '06, pp.533 – 538.

-
- [2-1] E. F. Gordon, "Soft Magnetic Materials", IEEE Proceedings of the IEEE, Vol. 78, June, 1990, pp.947-972.
- [2-2] H. W. Meyer, "A history of electricity and magnetism", Cambridge, Mass., MIT Press, 1971.
- [2-3] E. Feldtkeller, "100 years' magnetic contributions to electrical engineering", Magnetics, IEEE Transactions on, Vol. 20, Nov 1984, pp. 2057 – 2090.
- [2-4] K.J. Overshott, "Magnetism : it is permanent", IEE PROCEEDINGS-A, Vol. 138, 1991, pp. 22-30.
- [2-5] W. T. McLyman, "Magnetic core selection for transformer and inductors", New York: Marcel Dekker, 1978.
- [2-6] Chih Wen Chen, "Magnetism and Metallurgy of Soft Magnetic Materials", Courier Dover Publications, 1986.
- [2-7] Ernst Albers-Schoenberg, "Ferrites", Journal of the American Ceramic Society, Vol. 41, November 1958, pp. 484-489.
- [2-8] Ferroxcube, "Data sheets - Soft ferrite products and accessories" <http://www.ferroxcube.com/>.
- [2-9] R. Spyker, J. Huth, I. Mehdi, A. Brockschmidt, "300C ferrite material for high temperature magnetics", PESC 2004, pp. 155 – 160.
- [2-10] K. J. Overshott, "Amorphous Ribbon Materials and Their Possibilities", Electron Power. Vol. 25, No. 5, pp. 347-350. May 1979.
- [2-11] Metglas, "Data sheets – Magnetic alloy", <http://www.metglas.com/>.
- [2-12] G. Chin, "Review of magnetic properties of Fe-Ni alloys", Magnetics, IEEE Transactions on, Vol. 7, Issue 1, Mar 1971, pp. 102 – 113.
- [2-13] Magnetic Metals, "Data sheets: NAM – Wound magnetics", http://www.magmet.com/nam/images/NAM_cat_combinedCh4.pdf.
- [2-14] Y. Yoshizawa, S. Oguma, and K. Yamaguchi, J. Appl. Phys. 64, 6044, 1988.
- [2-15] K. Suzuki, A. Makino, A. Inoue, and T. Masumoto, J. Appl. Phys. 70, 6232, 1991.
- [2-16] J. Petzold, "Advantages of soft magnetic nanocrystalline materials for modern electronic applications", Journal of Magnetism and Magnetic Materials 242–245, 2002, pp. 84–89.

-
- [2-17] G. Herzer, “Amorphous and nanocrystalline soft magnets”, Kluwer Academic Publishers, 1997.
- [2-18] Hitachi, “Nanocrystalline soft magnetic material Finemet”, <http://www.hitachi-metals.co.jp/e/prod/prod13/pdf/hl-fm10-c.pdf>.
- [2-19] Vaccumschmelze, “Vitroperm 500F - Tape-Wound Cores in Power Transformers for Switched Mode Power Supplies”, http://www.vacuumschmelze.de/dynamic/docroot/medialib/documents/broschuere_n/kbbrosch/Pk003en.pdf.
- [2-20] F. Dong Tan, J. L. Vollin, S. M. Cuk, “A practical approach for magnetic core-loss characterization”, *Power Electronics, IEEE Transactions on*, Vol. 10, March 1995, pp. 124 – 130.
- [2-21] D. Seyoum, D. McKinnon, M. K. Rahman, C. Grantham, “Offset compensation in the estimation of flux in induction machines” *IECON '03*. Vol. 2, Nov. 2003, pp. 1715 – 1720.
- [2-22] Hitachi, “Power electronics component catalog – Finemet F3CC series cut core”, April, 2006.
- [2-23] H. Fukunaga, T. Eguchi, K. Koga, Y. Ohta, H. Kakehashi, “High performance cut cores prepared from crystallized Fe-based amorphous ribbon”, *IEEE Transactions on Magnetics*, Sep. 1990, pp. 2008 – 2010.
- [2-24] O. Ishii, Y. Miyaguchi, S. Kambe, “Application of Fe-based nanocrystalline ribbon as a noise filter”, *Magnetics, IEEE Transactions on* Volume 35, Issue 5, Part 1, Sept. 1999 Page(s):3184 - 3186
- [2-25] W. A. Reass, D. M. Baca, J. D. Doss, R. F. Gribble, “Design technology of high-voltage multi-megawatt polyphase resonant converter modulators”, *IECON '03*, Nov. 2003, pp.: 96 – 101.
- [2-26] University of Birmingham, Applied Alloy Chemistry Group, http://www.aacg.bham.ac.uk/magnetic_materials/type.htm
- [3-1] N. Mohan, T. M. Undeland, and W. P. Robbins, “Power Electronics – Converters, Applications, and Design”, John Wiley & Son, Inc. 1995.

-
- [3-2] G. Bertotti, "Hysteresis in magnetism: for physicists, material scientists and engineers", Academic Press, 1998.
- [3-3] C. P. Steinmetz, "On the law of hysteresis", AIEE Transactions, Vol. 9, pp. 3-64, 1892. Reprinted under the title "A Steinmetz contribution to the ac power revolution", by J. E. Brittain, Proceedings of the IEEE 72(2), 1984, pp. 196-221.
- [3-4] J. Reinert, A. Brockmeyer, and R.W.A.A. De Doncker, "Calculation of losses in ferro- and ferrimagnetic materials based on the modified Steinmetz equation", Industry Applications, IEEE Transactions on Volume 37, Issue 4, July-Aug. 2001 pp.: 1055 – 106.
- [3-5] J. Li; T. Abdallah, and C. R. Sullivan, "Improved calculation of core loss with nonsinusoidal waveforms", Thirty-Sixth IAS Volume 4, 2001 pp.:2203 – 2210.
- [3-6] G. Bertotti, "General properties of power losses in soft ferromagnetic materials", IEEE Transactions on Magnetics, Vol. 24, 1988, pp. 621-630.
- [3-7] W. Roshen, "Ferrite core loss for power magnetic components design", IEEE Transactions on Magnetics, Vol 27, Nov. 1991, pp.4407-4415.
- [3-8] E. F. Gordon, "Soft Magnetic Materials", IEEE Proceedings of the IEEE, Vol. 78, June, 1990, pp.947-972.
- [3-9] D. C. Jiles, D. L. Atherton, "Theory of ferromagnetic hysteresis", Journal of Magnetism and Magnetic Materials, Vol. 61, 1986, pp. 48-60.
- [3-10] Y. Bernard, E. Mendes, and F. Bouillault, "Dynamic hysteresis modeling based on Preisach model", IEEE Transactions on Magnetics, Vol. 38, 2002, pp.885 – 888.
- [3-11] P. M. Gradzki, M. M. Jovanovic, F. C. Lee, "Computer aided design for high-frequency power transformers", APEC 1990, pp. 336-343.
- [3-12] R. Severns, "HF-core losses for non-sinusoidal waveforms", Proceedings of HFPC 1991, pp. 140-148.
- [3-13] S. D. Johnson, and R. W. Erickson, "Steady-state analysis and design of the parallel resonant converter", IEEE Transactions on Power Electronics, Vol. 3, 1988, pp. 93 – 104.

-
- [3-14] V. J. Thottuvelil, T.G. Wilson, H. A. Owen, "High-Frequency Measurement Techniques for Magnetic Cores", IEEE transactions on Power Electronics. Vol. 5. January, 1990, pp. 41-53.
- [3-15] P. M. Gradzki and F. C. Lee, "High Frequency Core Loss Characterization Technique Based on Impedance Measurement," HFPC 1991, pp. 108-115.
- [3-16] M. Sippola and R. E. Sepponen, "Accurate prediction of high-frequency power-transformer losses and temperature rise", IEEE Transactions on Power Electronics, Vol. 17, September, 2002, pp. 835-847.
- [3-17] Y. Han, W. Eberle, and Y. F. Liu, "New measurement methods to characterize transformer core loss and copper loss in high frequency switching mode power supplies", PESC 2004, pp. 1695-1701.
- [3-18] J .A. Ferreira, "Improved analytical modeling of conductive losses in magnetic components", IEEE Transactions on Power Electronics, Vol. 9, 1994, pp.127-133.
- [3-19] P. L. Dowell, "Effects of eddy currents in transformer windings," Proc. Inst. Elect. Eng., vol. 113, pp. 1387–1394, Aug. 1966.
- [3-20] F. Tourkhani, and P. Viarouge, "Accurate analytical model of winding losses in round Litz wire windings", IEEE Transactions on Magnetics, Vol. 37, January 2001, pp. 538-543.
- [3-21] C. R. Sullivan, "Optimal Choice for Number of Strands in a Litz-Wire Transformer Winding", IEEE Transactions on Power Electronics, Vol. 14, March 1999, pp.283-291.
- [3-22] Y. Qiu; B. Lu; B. Yang; D. Fu; F. C. Lee, F. Canales, R. Gean, C. W. Tipton, "A high-frequency high-efficiency three-level LCC converter for high-voltage charging applications", PESC 04, 2004, pp. 4100-4106.
- [3-23] A. J. Batista, J. C. S. ; Fagundes, P. Viarouge, "An automated measurement system for core loss characterization", Instrumentation and Measurement, IEEE Transactions on, Vol. 48, April 1999, pp. 663 – 667.
- [4-1] R. W. Erickson, D. Maksimovic, "Fundamentals of Power Electronics" Kluwaer Academic Publishers, 2001.

-
- [4-2] A. Pokryvailo, and A. Schwarz, "Design of a resonant converter power transformer when using its leakage inductance in oscillatory circuit", Electrical and Electronics Engineers in Israel, 1991. Proceedings, 17th Convention of 5-7 March 1991 Page(s): 316 – 319.
- [4-3] S. D. Johnson, A. F. Witulski, and R. W. Erickson, "Comparison of resonant topologies in high voltage DC applications", IEEE Transactions on Aerospace and Electronic Systems, May 1988, pp. 263-274.
- [4-4] A. M. Pernia, F. Nuno, E. L. Corominas, J. M. Lopera, "Resonant converter controlled by variable leakage inductance in the transformer (LIC)", Power Electronics and Applications, 1993., Fifth European Conference on 13-16 Sep 1993 Page(s):124 - 129 vol.3.
- [4-5] N. Morhan, T. M. Undeland, and W. P. Robbins, "Power Electronics – Converters, Applications, and Design", Wiley 1995.
- [4-6] G. Skutt, F. C. Lee, R. Ridley, D. Nicol, "Leakage inductance and termination effects in a high-power planar magnetic structure", Applied Power Electronics Conference and Exposition, 1994. APEC '94. 13-17 Feb. 1994 Page(s):295 – 301.
- [4-7] J. M. Lopera, M. J. Prieto, A. M. Pernia, and F. Nuno, "A multiwinding modeling method for high frequency transformers and inductors", IEEE Trans. On Power Electronics, Vol. 18, No. 2, May, 2003. pp. 896-906.
- [4-8] P. L. Dowell, "Effects of eddy currents in transformer windings," Proc. Inst. Elect. Eng., vol. 113, pp. 1387–1394, Aug. 1966.
- [4-9] P. S. Venkatraman, "Winding eddy current losses in switch mode power transformer due to rectangular wave currents" Proceedings of Powercon 11, 1984, pp. 1-11.
- [4-10] J. A. Ferreira, "Improved analytical modeling of conductive losses in magnetic components", Power Electronics, IEEE Transactions on, Volume 9, Issue 1, Jan. 1994, Page(s):127 – 131.
- [4-11] B. Carsten, "High frequency conductor losses in switch mode magnetics," PCI Proc., Munich, Germany, 1986, pp. 161-182.

-
- [4-12] J. P. Vandelac and P. D. Ziogas, "A novel approach for minimizing high frequency transformer copper losses," IEEE Trans. Power Electron., vol. 3, pp. 266-276, July 1988.
- [4-13] W. G. Hurley, and D. J. Wilcox, "Calculation of leakage inductance in transformer windings", IEEE Transactions on Power Electronics, Vol. 9, Jan. 1994, pp. 121-126.
- [4-14] A. F. Goldberg, J. G. Kassakian, and M. F. Schlecht, "Issues related to 1-10-MHz transformer design", IEEE Transactions on Power Electronics, Vol. 4, No. 1, Jan. 1989, pp. 113-123.
- [4-15] V. A. Niemela, G. R. Skutt, A. M. Urling, Y. N. Chang, T. G. Wilson, H. A. Jr. Owen, R. C. Wong, "Calculating the short-circuit impedances of a multiwinding transformer from its geometry", Power Electronics Specialists Conference, 1989. PESC '89 Record, 26-29 June 1989, Page(s):607 – 617.
- [4-16] K. W. E. Cheng, "Modelling of solenoidal transformer for the calculation of leakage inductance using eddy-current reaction field", IEEE Transactions on Magnetics, Vol. 41, May 2005, pp. 1996-1999.
- [4-17] K. Fleisch, "Electromagnetics with applications" Fifth Edition, McGraw-Hill Companies, Inc. 1999.
- [4-18] J. A. Ferreira, "Electromagnetic modeling of power electronic converter" Kluwer Academic Publishers, 1989.
- [4-19] R. L. Stoll, "The analysis of eddy current", Clarendon Press, Oxford, 1974.
- [4-20] M. Bartoli, N. Noferi, A. Reatti, M. K. Kazimierczuk, "Modeling Litz-wire winding losses in high-frequency power inductors", PESC '96 Vol. 2, 23-27 June 1996, pp. 1690 – 1696.
- [4-21] C. R. Sullivan, "Cost-constrained selection of strand diameter and number in a litz-wire transformer winding", Power Electronics, IEEE Transactions on Volume 16, Issue 2, March 2001 Page(s):281 – 288.
- [4-22] A. W. Lotfi, F. C. Lee, "A high frequency model for Litz wire for switch-mode magnetics", Industry Applications Society Annual Meeting, 1993, 2-8 Oct. 1993, Page(s):1169 – 1175, vol.2.

-
- [4-23] E. C. Snelling, "Soft Ferrites – Properties and Applications", London, Butterworth, 1988.
- [4-24] H. Y. Lu, J. G. Zhu, and S. Y. R. Hui, "Experimental determination of stray capacitances in high frequency transformers", IEEE Transactions on Power Electronics, Vo. 18, 2003, pp.1105-1112.
- [4-25] B. Cogitore, J. P. Keradec, and J. Barbaroux, "The two-winding transformer: an experimental method to obtain a wide frequency range equivalent circuit", IEEE Transactions on Instrumentation and Measurement, Vo. 43, 1994, pp.364-371.
- [4-26] A. Massarini, M. K. Kazimierczuk, and G. Grandi, "Lumped parameter models for single- and multiple-layer inductors", PESC 1996, pp. 295-301.
- [4-27] Z. Azzouz, A. Foggia, L. Pierrat, and G. Meunier, "3D finite element computation of the high frequency parameters of power transformer windings", IEEE Transactions on Magnetics, Vol. 29, 1993, pp. 1407-1410.
- [4-28] F. de Leon, A. Semlyen, "Complete transformer model for electromagnetic transients", IEEE Transactions on, Volume: 9, Issue: 1, Jan. 1994, pp. 231 – 239.
- [4-29] E. Laveuve, J. P. Keradec, and M. Bensoam, "Electrostatic of wound components: analytical results, simulation and experimental validation of the parasitic capacitance", IAS 1991, pp. 1469-1475.
- [5-1] L. Grajales, J. A. Sabate, K. A. Wang, W. A. Tabisz, and F. C. Lee, "Design of a 10 kW, 500 kHz phase-shift controlled series-resonant inverter for induction heating", IAS 1993, pp. 843-849.
- [5-2] W. E. Frank and R. Lee, "New induction heating transformers", IEEE Transactions on Magnetics, Vol. 18, 1982, pp. 1752-1754.
- [5-3] L. Malesani, P. Mattavelli, L. Rossetto, P. Tenti, W. Marin, A. Pollmann, "Electronic welder with high-frequency resonant inverter", Industry Applications, IEEE Transactions on, Vol. 31, pp. 273-279, 1995
- [5-4] M. A. Kempkes, J.A. Casey, M. P. J. Gaudreau, T. A. Hawkey, I. S. Roth, "Solid-state modulators for commercial pulsed power systems", Power Modulator Symposium 2002, pp. 689 – 693.

-
- [5-5] J. A. Ferreira, J.A.; Roux, "A series resonant converter for arc-striking applications", *Industrial Electronics, IEEE Transactions on*, Vol. 45, 1998, pp. 585 – 592.
- [5-6] Sang-Kyoo Han, Gun-Woo Moon, Myung-Joong Youn, "A high efficiency ZVS PWM asymmetrical half bridge converter for plasma display panel sustaining power module", *PESC 04. 2004*, pp. 776 – 781.
- [5-7] A. Jangwanitlert, J. C. Balda, "Phase-shifted PWM full-bridge DC-DC converters for automotive applications: reduction of ringing voltages", *Power Electronics in Transportation*, 2004, pp. 111 – 115.
- [5-8] W. G. Homeyer, E. E. Bowles, S. P. Lupan, P. S. Walia, M. A. Maldonado, "Advanced power converters for More Electric Aircraft applications", *IECEC-97*. pp. 591 – 596, 1997.
- [5-9] B. Lu, Y. Qiu, C. Wang, Y Kang, J. Sun, W. Dong, F. Canales, P. Barbosa, M. Xu, F. C. Lee, R. Geen, W. C. Tipton, D. Urciuoli, "A high power density high voltage distributed power system for pulse power applications", *APEC 2005*. Vol., 2005 pp.210 – 216.
- [5-10] W. Shen, B. C. Charboneau, H. Wang, H. Sheng, Y Kang, D. Fu, F. Wang, D. Boroyevich, J. D. van Wyk, F. C. Lee, W. C. Tipton, "Design and implementation of a 30kW resonant converter for capacitor charger", *CPES Seminar April 2005*.
- [5-11] F. Canales, P. Barbosa, C. Aguilar, F. C. Lee, "A high-power-density DC/DC converter for high-power distributed power systems", *Power Electronics Specialist Conference, 2003. PESC '03*. Volume 1, 15-19 June 2003 pp.11 – 18.
- [5-12] S. D. Johnson, and R. W. Erickson, "Steady-state analysis and design of the parallel resonant converter", *IEEE Transactions on Power Electronics*, Vol. 3, 1988, pp. 93 – 104.
- [5-13] G. Ivensky, A. Kats, and S. Ben-Yaakov, "An RC load model of parallel and series-parallel resonant DC-DC converters with capacitive output filter", *IEEE Transactions on Power Electronics*, Vol. 14, 1999, pp.515-521.
- [5-14] N. Coonrod, "Transformer computer design aid for high frequency switching power supplies," *IEEE Transactions on Power Electronics*, pp. 248-256, Oct. 1986.

- [5-15] R. Petkov, "Optimal design of a high-power high-frequency transformer", IEEE Transactions on Power Electronics, Vol. 11, No. 1, Jan. 1996, pp. 33-42.
- [5-16] K. D T. Ngo, R. P. Alley, "A. J. Yerman, R. J. Charles, and M. H. Kuo, "Design issues for the transformer in a low-voltage power supply with high efficiency and high power density", IEEE Transactions on Power Electronics, Vol. 7, Jul. 1992, pp. 592 –600.
- [5-17] A. F. Goldberg, J. G. Kassakian, and M. F. Schlecht, "Issues related to 1-10-MHz transformer design", IEEE Transactions on Power Electronics, Vol. 4, No. 1, Jan. 1989, pp. 113-123.
- [5-18] W. G. Hurley, W. H. Wolfle, and J. G. Breslin, "Optimized transformer design: inclusive of high-frequency effects", IEEE Transactions on Power Electronics, Vol. 13, July, 1998, pp. 651-659.
- [5-19] J. P .Holman, "Heat transfer", McGraw-Hill Inc., 1976, Fourth Edition.

-
- [6-1] S. Luo, "A review of distributed power systems part I: DC distributed power system", IEEE Aerospace and Electronic Systems Magazine Vol. 20, Aug. 2005, pp. 5 – 16.
- [6-2] F. C. Lee, P. Barbosa, P. Xu, J. Zhang, B. Yang, F. Canales, "Topologies and design considerations for distributed power system applications", Proceedings of the IEEE, Vol. 89, June 2001, pp. 939 – 950.
- [6-3] X. Feng, J. Liu, F. C. Lee, "Impedance specifications for stable DC distributed power systems", IEEE Transactions on Power Electronics, Vol. 17, 2002, pp. 157 – 162.
- [6-4] W. A. Tabisz, M. M. Jovanovic, F. C. Lee, "Present and future of distributed power systems", APEC '92. pp. 11 – 18.
- [6-5] H. Dai; K. Xing; F. C. Lee, "Investigation of soft-switching techniques for Power Electronics Building Blocks (PEBB)", APEC '98. pp. 633 – 639.
- [6-6] R. Chen, F. Canales, B. Yang, J. D. van Wyk, "Volumetric optimal design of passive integrated power electronics module (IPEM) for distributed power system (DPS) front-end DC/DC converter", Industry Applications, IEEE Transactions on, Vol. 41, 2005, pp. 9 – 17.
- [6-7] R. Chen, F. Canales, B. Yang, J. D. van Wyk, F. C. Lee, "Integration of electromagnetic passive components in DPS front-end DC/DC converter - a comparative study of different integration steps", APEC '03, pp. 1137 – 1142.
- [6-8] W. G. Odendaal, J. A. Ferreira, "Leakage impedance design as function of frequency scaling in power transformer", IAS 1996, pp. 1389-1396.
- [6-9] W. G. Odendaal, J. A. Ferreira, "Effects of scaling high-frequency transformer parameters" IEEE Transactions on Industry Applications, Vol. 35, 1999, pp. 932-940.
- [6-10] W. G. Odendaal, J. A. Ferreira, "A thermal model for high frequency magnetic components", IAS 1997, pp. 1115-1122.
- [6-11] W. J. Gu, R. Liu, "A study of volume and weight vs. frequency for high-frequency transformers", PESC '93 Record, 1993, pp. 1123 – 1129.

Appendix I Arbitrary Waveform Generation

The following Matlab code generates a STS waveform, and outputs the data into a *.txt file. 500 points are used for a period, and both amplitude and frequency have been normalized. To apply the waveform, we can just recall the saved file name from the arbitrary list, and define the amplitude and frequency as we want.

```
% Code to generate a STS waveform with 200 kHz sinusoidal transition  
% portion and 100 kHz repetitive frequency.
```

```
% by Wei Shen (Thanks Jerry Francis for help)  
% CPES, VT  
% 11/20/2005  
% Ver1.0
```

```
HFILE = fopen('c:\arl\STS_200k.txt','w');
```

```
m = linspace(0, 1, 501);
```

```
STRJF = 'DATA VOLATILE, ';
```

```
n = 1;
```

```
for n = 1:65
```

```
    vals(n) = sin(m(n)*2*pi-64/500*pi);
```

```
    STRJF = sprintf( '%s %f',STRJF, vals(n));
```

```
end
```

```
for n=66:251
```

```
    vals(n) = 1.2296/pi;
```

```
    STRJF = sprintf( '%s %f',STRJF, vals(n));
```

```
end
```

```
for n = 252:316
```

```
    vals(n) = -sin(m(n-251)*2*pi-64/500*pi);
```

```
    STRJF = sprintf( '%s %f',STRJF, vals(n));
```

```
end
```

```
for n=317:501
```

```
    vals(n) = -1.2296/pi;
```

```

    STRJF = sprintf( '%s %f;',STRJF, vals(n));
end
STRJF(length(STRJF)) = ''
disp(STRJF);
plot(vals)

fprintf(HFILE, ':SYST:REM\n');
fprintf(HFILE, 'FREQ 50000\n');
fprintf(HFILE, 'VOLT 5\n');
fprintf(HFILE, '%s\n', STRJF );
fprintf(HFILE, 'DATA:COPY STS_200, VOLATILE\n');
fprintf(HFILE, 'FUNC:USER STS_200\n');
fprintf(HFILE, 'FUNC:SHAP USER');

fclose(HFILE);
%=====END=====

```

The generated **200kHz.txt** file is also shown in the flowing. The **200kHz.txt** file can be downloaded to HP function generator through HyperTerminal provided in the Windows.

```

:SYST:REM
FREQ 100000
VOLT 5
DATA VOLATILE, -1.000000, -0.999895, -0.999580, -0.999055, -0.998320, -0.997376, -
0.996221, -0.994858, -0.993285, -0.991503, -0.989513, -0.987314, -0.984907, -0.982292, -0.979471, -
0.976442, -0.973207, -0.969767, -0.966121, -0.962270, -0.958216, -0.953958, -0.949497, -0.944834, -
0.939970, -0.934905, -0.929641, -0.924177, -0.918516, -0.912657, -0.906603, -0.900353, -0.893908, -
0.887271, -0.880441, -0.873420, -0.866209, -0.858809, -0.851221, -0.843447, -0.835488, -0.827344, -
0.819018, -0.810510, -0.801823, -0.792956, -0.783912, -0.774693, -0.765298, -0.755731, -0.745993, -
0.736084, -0.726007, -0.715764, -0.705355, -0.694783, -0.684049, -0.673154, -0.662102, -0.650892, -
0.639528, -0.628011, -0.616342, -0.604524, -0.592559, -0.580448, -0.568193, -0.555796, -0.543259, -
0.530584, -0.517774, -0.504830, -0.491753, -0.478547, -0.465214, -0.451754, -0.438172, -0.424468, -
0.410645, -0.396704, -0.382650, -0.368482, -0.354205, -0.339819, -0.325327, -0.310732, -0.296036, -
0.281241, -0.266350, -0.251364, -0.236286, -0.221120, -0.205866, -0.190527, -0.175106, -0.159606, -
0.144028, -0.128375, -0.112650, -0.096855, -0.080993, -0.065065, -0.049076, -0.033026, -0.016919, -
0.000758, 0.015456, 0.031720, 0.048031, 0.064386, 0.080783, 0.097219, 0.113693, 0.130200, 0.146739,
0.163307, 0.179901, 0.196519, 0.213158, 0.229815, 0.246489, 0.263175, 0.279872, 0.296577, 0.313287,
0.330000, 0.346713, 0.363423, 0.380128, 0.396825, 0.413511, 0.430185, 0.446842, 0.463481, 0.480099,

```


1.000000, -1.000000, -1.000000, -1.000000, -1.000000, -1.000000, -1.000000, -1.000000, -1.000000, -1.000000, -1.000000

DATA: COPY CL_SIN, VOLATILE

FUNC: USER CL_SIN

FUNC: SHAP USER

Appendix II Minimum-size Transformer Design Program

The following Matlab code is developed to find out the minimum transformer size, for a set of given operation conditions. The four parameters of the C-core shown in Fig. 6-10 are changed continuously, and temperature constraints are checked. Finally the minimum size of the design fulfill all requirements are picked out. Four typical high-frequency materials loss Steinmetz coefficients have been integrated into the program.

The leakage inductance can be added as one of the constraints, and the design result will have the expected leakage value. The program itself is flexible, and almost every parameter can be changed, such as core shapes, magnetic materials, operating conditions, design constraints, and so on.

```
% Transformer Design Tool Part I – C- core
% Version 2.1, 15/02/2006

% PRC application requirements: Turns ratio: 1:11; Ambient temperature: T_amb=65 °C;
% Maximum allowed temperature rise: T_rise=55 °C
% Frequency can be 200, 300, 500 kHz; Power rating: 10, 15, 30, 37.5, 50, 100 kW;

% Core Shape: C-core; Magnetic materials: Finemet FT-3M (Hitachi), Ferrite P (Magnetics),
% Amorphous 2705M (Metglas), Supermalloy (Magnetic Metals)

% Wei Shen
% CPES

clear all
%===== Design Specifications =====
N=11;           % Turns ratio
Lemda=0.003;   % Volt*sec for 200 kHz operation
Lemda=0.002;   % Volt*sec for 300 kHz operation
Lemda=0.0012;  % Volt*sec for 500 kHz operation

%Itot=2*57;    % Primary plus secondary (converted) current, A %10kW
%Itot=2*85;    % Primary plus secondary (converted) current, A %15kW
```

Appendix II. Minimum-size Transformer Design Program

$I_{tot}=2*170;$ % Primary plus secondary (converted) current, A %30kW
 $I_{tot}=2*220;$ % Primary plus secondary (converted) current, A %37.5kW
 $I_{tot}=2*295;$ % Primary plus secondary (converted) current, A %50kW
 $I_{tot}=2*430;$ % Primary plus secondary (converted) current, A %75kW
 $I_{tot}=2*600;$ % Primary plus secondary (converted) current, A %100kW

$f=100;$ %equivalent core loss calculation frequency, kHz (for 200 kHz operation
% frequency, after considering average effect of charging period already)
 $f=154;$ %equivalent core loss calculation frequency, kHz (for 300 kHz operation
% frequency, after considering average effect of charging period already)
 $f=257;$ %equivalent core loss calculation frequency, kHz (for 500 kHz operation
% frequency, after considering average effect of charging period already)

$DT=1.1/61.1;$ % charging operation duty cycle of the transformer, here is charging 1.1
second with 60 seconds interval

=====
%=====
Design coefficient =====

$Kr=1.1;$ % Winding AC/DC resistance ratio, after considering average effect of
whole charging period 10kW
 $Kr=1.3;$ % Winding AC/DC resistance ratio, after considering average effect of whole
charging period 15kW
 $Kr=1.6;$ % Winding AC/DC resistance ratio, after considering average effect of whole
charging period 30kW
 $Kr=1.67;$ % Winding AC/DC resistance ratio, after considering average effect of
whole charging period 37.5kW
 $Kr=1.9;$ % Winding AC/DC resistance ratio, after considering average effect of whole
charging period 50kW
 $Kr=2.2;$ % Winding AC/DC resistance ratio, after considering average effect of
whole charging period 75kW
 $Kr=2.5;$ % Winding AC/DC resistance ratio, after considering average effect of
whole charging period 100kW

$Ku=0.2;$ % Core window fill factor

$Rou=1.724e-6;$ % Cu conductivity, Ohm*cm @25 DgrC
 $Rou=2.3e-6;$ % Cu conductivity, Ohm*cm @100 DgrC
 $Mu0=4*pi*1e-7;$ % Permeability, A/m

% ===== Core Demensions =====

% ===== Magnetic Material Characteristics =====

% Finemet FT-3M

*K1=8; % Cole loss coefficient, $mW/cm^3=K1*f^K2*dB^K3$*

K2=1.621; % Cole loss coefficient

K3=1.982; % Cole loss coefficient

Bsat=1.23; % Saturation flux density, Tesla

Bmax=0.8; % Maximum flux density, Tesla

% Ferrite P

*%K1=0.0434*10^2.62; % Cole loss coefficient, $mW/cm^3=K1*f^K2*dB^K3$*

%K2=1.63; % Cole loss coefficient

%K3=2.62; % Cole loss coefficient

%Bsat=0.5; % Saturation flux density, Tesla

%Bmax=0.35; % Maximum flux density, Tesla

% Amorphous 2705M

*%K1=0.726*7.8; % Cole loss coefficient, $mW/cm^3=K1*f^K2*dB^K3$*

%K2=1.883; % Cole loss coefficient

%K3=2.152; % Cole loss coefficient

%Bsat=0.77; % Saturation flux density, Tesla

%Bmax=0.55; % Maximum flux density, Tesla

% Supermalloy

*%K1=0.637*2.205*8.72; % Cole loss coefficient, $mW/cm^3=K1*f^K2*dB^K3$*

%K2=1.7; % Cole loss coefficient

%K3=1.937; % Cole loss coefficient

%Bsat=0.82; % Saturation flux density, Tesla

%Bmax=0.65; % Maximum flux density, Tesla

% ===== Optimization Loop =====

DR=0.1; counter=0; counter1=0;

for ii=15:35

for i=5:15

```

for j=40:60
  for m=40:60
    % C-core construction %
    a(i)=DR*i; b(j)=DR*j; d(m)=DR*m; h(ii)=DR*ii;
    Ac(ii,i,j,m)=a(i)*d(m);
    lc(ii,i,j,m)=2*(b(j)+2*(h(ii)+a(i)));
    Aw(ii,i,j,m)=2*b(j)*h(ii);
    Vc(ii,i,j,m)=2*a(i)*d(m)*(2*h(ii)+2*a(i)+b(j));
    MLT(ii,i,j,m)=2*(a(i)+d(m)+b(j));

    % Optimal flux density calculation %

    Bop(ii,i,j,m)=((Kr*Rou*Lemda^2*Itot^2/2/Ku)*(MLT(ii,i,j,m)/Aw(ii,i,j,m)/Ac(ii,i,j,m)^3/lc(ii,i,j,m))...
    *(1e8/K3/K1/f^K2)*1000)^(1/(K3+2));
    if Bop(ii,i,j,m)>Bmax
      Bop(ii,i,j,m)=Bmax;
    end

    % Turn's number %
    n1(ii,i,j,m)=Lemda/2/Bop(ii,i,j,m)/Ac(ii,i,j,m)*1e4;
    n1(ii,i,j,m)=round(n1(ii,i,j,m));
    n2(ii,i,j,m)=N*n1(ii,i,j,m);

    % Total loss %
    Bop(ii,i,j,m)=Lemda/2/n1(ii,i,j,m)/Ac(ii,i,j,m)*1e4;
    Pfe(ii,i,j,m)=Vc(ii,i,j,m)*K1*f^K2*Bop(ii,i,j,m)^K3/1000;
    Pcu(ii,i,j,m)=Kr*Rou*MLT(ii,i,j,m)*n1(ii,i,j,m)^2*Itot^2/Aw(ii,i,j,m)/Ku;
    Ptot(ii,i,j,m)=Pfe(ii,i,j,m)+Pcu(ii,i,j,m);

    % Thermal Design %
    % Case I: for oil immersion natural convection cooling conditions.
    % Renold number: Ra=Beida*g*deltaT*L^3/(alpha*v)=9.8*0.000547
    % Nusselt number: Nu=h*L/K=c*(Ra)^n
    % thermal resistance: Rth=1/(h*A)

    % Core thermal resistance
  
```

$$Ra_co(ii,i,j,m)=9.8*0.000547*50*(2*(a(i)/100+h(ii)/100))^3/(6.66e-6*0.0032);$$

$$Nu_co(ii,i,j,m)=0.59*Ra_co(ii,i,j,m)^{0.25};$$

$$h_co(ii,i,j,m)=Nu_co(ii,i,j,m)*0.13/(2*(a(i)/100+h(ii)/100));$$

$$\%Rth_co(ii,i,j,m)=1/(h_co(ii,i,j,m)*(4*a(i)/100*(b(j)/100+2*a(i)/100+d(m)/100)+8*h(ii)/100*(d(m)/100+a(i)/100)));$$

$$Rth_co(ii,i,j,m)=1/(h_co(ii,i,j,m)*(4*a(i)/100*(b(j)/100+2*a(i)/100+d(m)/100)+8*h(ii)/100*(d(m)/100+a(i)/100)));$$

% Winding thermal resistance

$$Ra_wd(ii,i,j,m)=9.8*0.000547*50*(2*h(ii)/100)^3/(6.66e-6*0.0032);$$

$$Nu_wd(ii,i,j,m)=0.59*Ra_wd(ii,i,j,m)^{0.25};$$

$$h_wd(ii,i,j,m)=Nu_wd(ii,i,j,m)*0.13/(2*h(ii)/100);$$

$$\%Rth_wd(ii,i,j,m)=1/(h_wd(ii,i,j,m)*4*h(ii)/100*(3*b(j)/100+2*a(i)/100+d(m)/100));$$

$$Rth_wd(ii,i,j,m)=1/(h_wd(ii,i,j,m)*2*h(ii)/100*(5*b(j)/100+4*a(i)/100+d(m)/100));$$

$$Trise_co(ii,i,j,m)=Pfe(ii,i,j,m)*DT*Rth_co(ii,i,j,m);$$

$$Trise_wd(ii,i,j,m)=Pcu(ii,i,j,m)*DT*Rth_wd(ii,i,j,m);$$

if Trise_co(ii,i,j,m)<55 & Trise_wd(ii,i,j,m)<55

counter=counter+1;

$$Llk(counter)=Mu0*n1(ii,i,j,m)^2*b(j)*MLT(ii,i,j,m)/3/(2*h(ii))*1e4/4;$$

*%if Llk(counter)<1.05*10.89/2.5 & Llk(counter)>0.95*10.89/2.5 % for 10kW*

*%if Llk(counter)<1.05*7.26/2.5 & Llk(counter)>0.95*7.26/2.5 % for 15kW*

*%if Llk(counter)<1.05*3.63/2.5 & Llk(counter)>0.95*3.63/2.5 % for 30kW*

*%if Llk(counter)<1.05*2.9/2.5 & Llk(counter)>0.95*2.9/2.5 % for 37.5kW*

*if Llk(counter)<1.05*2.15/2.5 & Llk(counter)>0.95*2.15/2.5 % for 50kW*

*%if Llk(counter)<1.05*1.452/2.5 & Llk(counter)>0.95*1.452/2.5 % for 75kW*

*%if Llk(counter)<1.1*1.075/2.5 & Llk(counter)>0.90*1.075/2.5 % for 100kW*

counter1=counter1+1;

Result(counter1,1)=a(i);

Result(counter1,2)=b(j);

Result(counter1,3)=d(m);

```
Result(counter1,4)=h(ii);
Result(counter1,5)=Bop(ii,i,j,m);
Result(counter1,6)=nI(ii,i,j,m);
Result(counter1,7)=Ptot(ii,i,j,m);
Result(counter1,8)=Trise_co(ii,i,j,m);
Result(counter1,9)=Trise_wd(ii,i,j,m);
Result(counter1,10)=4*(h(ii)+a(i))*(b(j)+a(i))*(b(j)+d(m));
Result(counter1,11)=Llk(counter);
end
end
end
end
end
[Y,I]=sort(Result(:,10));
I(1:20)
%plot(1:counter,Result(:,10))
loglog(1:counter1,Result(:,10))
```

Appendix III C-core Shape Characteristic

C-core used in this work has the advantages of easy to prepare and to achieve balance winding structure, compared with wound core and E core. its surface-to-volume ratio has been studied through changing the C-core dimensions.

```
% C-core shape optimization

clear all
a=1; % normalized core leg width
dF=0.1; % calculation step factor
m=1; % normalized core window height
for i=1:100
    for j=1:100

        Yita_Acore(i,j)=(dF*i+2+dF*j+2*dF*m*(dF*j+1))/(a*(1+dF*i)*(1+dF*m)*(dF*j+dF
        *i));          % core surface to volume factor
        Yita_Awnd(i,j)=dF*m*(3*dF*i+2+dF*j)/(a*(1+dF*i)*(1+dF*m)*(dF*j+dF*i));
        % winding surface to volume factor
    end
end

m=5; % normalized core window height
for i=1:100
    for j=1:100

        Yita_Acore1(i,j)=(dF*i+2+dF*j+2*dF*m*(dF*j+1))/(a*(1+dF*i)*(1+dF*m)*(dF*j+d
        F*i));
        Yita_Awnd1(i,j)=dF*m*(3*dF*i+2+dF*j)/(a*(1+dF*i)*(1+dF*m)*(dF*j+dF*i));
    end
end

m=10; % normalized core window height
for i=1:100
    for j=1:100
```

```

        Yita_Acore2(i,j)=(dF*i+2+dF*j+2*dF*m*(dF*j+1))/(a*(1+dF*i)*(1+dF*m)*(dF*j+d
        F*i));
        Yita_Awnd2(i,j)=dF*m*(3*dF*i+2+dF*j)/(a*(1+dF*i)*(1+dF*m)*(dF*j+dF*i));
    end
end
NormFactor1=Yita_Acore2(10,10);
NormFactor2=Yita_Awnd2(10,10);

m=100; % normalized core window height
for i=1:100
    for j=1:100

        Yita_Acore3(i,j)=(dF*i+2+dF*j+2*dF*m*(dF*j+1))/(a*(1+dF*i)*(1+dF*m)*(dF*j+d
        F*i));
        Yita_Awnd3(i,j)=dF*m*(3*dF*i+2+dF*j)/(a*(1+dF*i)*(1+dF*m)*(dF*j+dF*i));
    end
end

mesh(dF*(1:i), dF*(1:j), Yita_Acore/NormFactor1);
hold on
mesh(dF*(1:i), dF*(1:j), Yita_Acore1/NormFactor1);
mesh(dF*(1:i), dF*(1:j), Yita_Acore2/NormFactor1);
mesh(dF*(1:i), dF*(1:j), Yita_Acore3/NormFactor1);

ylabel('Window width b')
xlabel('Core thickness d')
zlabel('Acore/V Ratio')
grid on

figure(2)
mesh(dF*(1:i), dF*(1:j), Yita_Awnd/NormFactor2);
hold on
mesh(dF*(1:i), dF*(1:j), Yita_Awnd1/NormFactor2);
mesh(dF*(1:i), dF*(1:j), Yita_Awnd2/NormFactor2);
mesh(dF*(1:i), dF*(1:j), Yita_Awnd3/NormFactor2);

```

```
ylabel('Window width b')  
xlabel('Core thickness d')  
zlabel('Awinding/V Ratio')  
grid on
```